Experimental Pool Boiling Investigation of FC-72 on Silicon with Artificial Cavities, Integrated Temperature Micro-Sensors and Heater

Christian Hutter

A thesis submitted for the degree of Doctor of Philosophy.
The University of Edinburgh.
October 2009

Für
Thomas
(1982-2004)

“...any attempt to compare the analyses against growth rate of specific individual bubbles is futile. It is as impossible as trying to predict the growth rate of a particular boy using a universal equation.”

Hsu and Graham, 1987

Abstract

Today nucleate boiling is widely used in numerous industrial applications such as cooling processes because of the high achieved heat transfer rates for low temperature differences. It remains a possible cooling solution for the next generation of central processing units (CPU), which dissipate heat fluxes exceeding the capabilities of today's conventional forced air cooling. However, nucleate boiling is a very complex and elusive process involving many mechanisms which are not fully understood yet and a comprehensive model is still missing.

For this study a new experimental setup was designed, constructed and commissioned to investigate bubble nucleation, growth, departure and interaction during nucleate pool boiling from a silicon device fully immersed in fluorinert FC-72. The location of bubble nucleation is controlled by artificial cavities etched into the silicon substrate. Boiling is initiated with a heater integrated on the back and micro-sensors indicate the wall temperature at the bubble nucleation site. During this work three different silicon test section designs were fabricated and boiling experiments on these substrates successfully conducted.

Bubble growth, bubble departure frequencies and bubble departure diameters for different dimensioned artificial cavities, varied pressure and increasing wall temperature were measured from high-speed imaging sequences. Bubble interactions like vertical and horizontal coalescence were visualised and their impact on the boiling heat transfer investigated. The influence of spacing between two neighbouring artificial cavities on bubble nucleation and departure frequencies, vertical coalescence frequencies and departure diameters was analysed.

The acquired data are used as input for a numerical code developed by our collaborators (Brunel University, UK and Los Alamos National Laboratories, USA) and are a first step to validate the code. The code studies the interactions between bubble nucleation sites on solid surfaces as a network. The simulations will help design boiling substrates utilised for chip cooling applications with optimal artificial cavity distribution to maximise the cooling heat transfer.

Zusammenfassung

Stationäres Blasensieden ist weitverbreitet und spielt eine wichtige Rolle in vielen industriellen Prozessen und Anwendungen als Kühlprozess. Es können sehr hohe Wärmeübergangszahlen bei niedrigen Temperaturdifferenzen erreicht werden. Stationäres Blasensieden bleibt ein möglicher Lösungsansatz für das Kühlen von Computerprozessoren (central processing unit - CPU) der nächsten Generation, dessen Wärmedissipation die Kapazitäten der herkömmlichen Kühlung durch erzwungene Konvektion mit Luft bei weitem übertrifft. Das Blasensieden ist jedoch ein sehr komplizierter und komplexer Prozess, in welchem gleichzeitig viele noch nicht ganz verstandene Mechanismen agieren und ein vollständiges Modell bislang nicht vorhanden ist.

Für die vorliegende Dissertation wurde ein neuer experimenteller Aufbau geplant, entwickelt und aufgebaut, um die Blasenbildung durch Keimbildung, anschliessendes Blasenwachstum, Blasenablösung und Wechselwirkungen zwischen Blasen während dem stationären Blasensieden auf einer Siliziumoberfläche, eingetaucht in fluorinert FC-72, zu untersuchen. Der Ort der Blasenbildung wird durch künstliche, auf der Siedeoberfläche angebrachte, Kavitäten kontrolliert. In diesen bleiben Dampf- oder Gaskeime erhalten. Auf das Siliziumplättchen wurden eine Wiederstandsheizvorrichtung und mehrere Mikrotemperatursensoren aufgedampft. Mit der Heizvorrichtung wird das Sieden initialisiert und mit den Mikrosensoren die Wandtemperaturen bei den künstlichen Kavitäten und somit dem Ort der Blasenbildung gemessen. Während dieser Arbeit wurden drei verschiedene Siedeoberflächen aus Silizium hergestellt und Siedeexperimente erfolgreich durchgeführt.

Blasenwachstumsraten, Blasenablösefrequenzen und Blasendurchmesser bei der Ablösung wurden für unterschiedlich dimensionierte künstliche Kavitäten, variiertem Umgebungsdruck und steigenden Wandtemperaturen von ausgewerteten Hochgeschwindikeitsaufnahmen gemessen. Wechselwirkungen zwischen Blasen, wie vertikale und horizontale Koaleszenz, wurden visualisiert und ihr Einfluss auf den Wärmeübergang während des Siedens untersucht. Der Einfluss der Distanz zwischen zwei benachbarten künstlichen Kavitäten auf die Blasenkeimfrequenz, Blasenablösefrequenz, Frequenz der vertikalen Koaleszenz und den Blasendurchmesser bei der Ablösung wurde analysiert.

Die gemessenen Daten dienen als Eingabe für einen numerischen Code, welcher von weiteren an diesem Projekt beteiligten Person entwickelt wurde (Brunel Universität in Grossbritannien und Los Alamos Nationale Forschungslabore, Vereinigte Staaten) und sind ein erster Schritt zu dessen Validierung. Mit dem Code lassen sich die Wechselwirkungen zwischen Keimbildungsorten von Blasen auf einer festen Oberfläche als Netzwerk studieren. Die Simulation wird helfen optimale Anordnungen der künst-

lichen Kavitäten zu finden, welche den Wärmeübergang während des Kühlens von Computerprozessoren maximieren.

Declaration of originality

I hereby declare that the research recorded in this thesis and the thesis itself was composed and originated entirely by myself in the School of Engineering at the University of Edinburgh.

Christian Hutter

Acknowledgements

The present study was conducted at the Institute of Materials and Processes in the School of Engineering at the University of Edinburgh between 2006 and 2009 and was financially supported by the government of the United Kingdom through the Engineering and Physical Sciences Research Council (EPSRC) with the grant EP/C532813/1.

This dissertation is the outcome of three and a half years of work. During this time I have accumulated a large debt of gratitude to many friends and advisors who helped me during the course of this research. As my main advisor, Dr. Khellil Sefiane provided guidance and advice at every stage of my work and I am very thankful to be given the opportunity to do my PhD in Edinburgh.

The project was in close collaboration with Antonio Sanna, Prof. Tassos G. Karayiannis, Prof. David B.R. Kenning from Brunel University and Dr. Ralph Nelson from the National Laboratories in Los Alamos. I would like to thank Antonio for the helpful discussions about our project, for the time in explaining to me the functioning of his numerical code and for keeping me entertained in the evenings and weekends during my visits in London. Many thanks go to Tassos and Ralph for all their advice and motivation during the project, especially when it came to writing publications. A special word of gratitude and admiration has to go to David. He proved invaluable as a co-author with his wide knowledge and experience in the topic of boiling heat transfer. His great interest in my work and his enthusiasm for research in boiling heat transfer in general kept me motivated and impressed me at the same time. He was always prepared to give advice and no questions remained unanswered.

During the course of this project, I greatly profited from discussions with Dr. Dario Bogojević, who was a colleague and became a dear friend.

As an experimental PhD this project would never have been successful without the help and support of various technicians here at the institute. I would like to thank Mr. Robert

Hogg (Bobby), Mr. Robert Kilgour (Rab), Mr. Kenneth Fee (Kenny) and Mr. Steven Gourlay (Steve) for all their help, ideas, work and especially patience for any request I had. From them, I also learned some special features of the Scottish language, which would be inappropriate to mention here, but belong to the Scottish culture as pubs and haggis do. Many thanks go to Mr David Archibald (Dave) and William Leslie (Bill), who were always prepared to find solutions for electrical and electronic problems I faced during planning, commissioning and running my experimental setup.

I am grateful for my colleagues of the Multiphase Flows and Heat Transfer Laboratory and the Institute of Materials and Processes Alastair, Alessandro, Alex, Andy, Bryony, Carlos, Carmelo, Christoph, Claudia, Dario, Eduardo, Jacqueline, Jan, Jennifer, Joachim, Jose Mario, Jovana, Meropi, Miguel, Paraskevi (Evi), Patricia, Ross, Samuel, Vladimir, Yavor and Yuan and for the shared time in the lab, the office and at lunch. Not to forget all the time we spent together in pubs, flat and birthday parties, Christmas and other dinners, football and badminton games and all the great trips to the Scottish Highlands and sights of Edinburgh and Scotland.

Many thanks go to my relatives and friends in Switzerland, who accepted my decision to go abroad and were always there, whenever I came back home on holidays.

I feel greatly indebted to my parents Cécile and Emil and my brother Philipp for their love and support.

And finally and most importantly I would like to thank Ingrid. She always supported me and all my decisions. She was there for me in good and bad times, patient when I only had my project in my head, expressed great understanding when I came home a little grumpy from a long, hard and stressful day in the lab. I am grateful for her belief in me, her trust and unconditional love.

Nomenclature

Acronyms and abbreviations

AU4G	duraluminium
BNF	bubble nucleation frequency
CHF	critical heat flux
CL	contact line
CMP	chemical mechanical polishing
CPU	central processing unit
DAQ	data acquisition
DI	deionised
DRIE	deep reacting ion etching
EPDM	ethylene propylene diene monomer
EPSRC	Engineering and Physical Sciences Research Council
fps	frames per second
HTC	heat transfer coefficient
ML	micro-layer
Nd:YAG	neodymium-doped yttrium aluminium garnet
PC	personal computer
PECVD	plasma enhanced chemical vapour deposition
PEEK	polyaryletherketone
PIV	particle image velocimetry
PTFE	polytetrafluoroethylene
RMS	root mean square
RTD	resistance temperature detector
SEM	scanning electron microscope
TLC	thermochromic liquid crystal
VCF	frequency of vertical coalescence

Greek letters

α	$^{\mathrm{W}}/_{\mathrm{m^2K}}$	convective heat transfer coefficient
β	$^{1}/_{\mathrm{Pa}}$	compressibility
δ	m	local micro-layer thickness
$\overline{\delta}$	m	average micro-layer thickness
ϕ	deg	contact angle
ϕ	$-$	ratio of contact area and bubble projected area, $(^{d_c}/_{D_b})$
φ	deg	apparent contact angle
κ, α	$^{\mathrm{m^2}}/_{\mathrm{s}}$	thermal diffusivity
μ, η	$\mathrm{Pa\ s}$	dynamic viscosity
ν	$^{\mathrm{m^2}}/_{\mathrm{s}}$	kinematic viscosity
π	$-$	circular constant
$\Delta\theta$	deg	central angle difference
ρ	$^{\mathrm{kg}}/_{\mathrm{m^3}}$	density
σ	$^{\mathrm{N}}/_{\mathrm{m}}$	surface tension
$\Delta\sigma$	$^{\mathrm{N}}/_{\mathrm{m}}$	surface tension difference
τ	s	time delay due to thermal conductance
ψ	deg	cavity side angle
ψ_m	deg	cavity mouth angle

Latin letters

A	$\mathrm{m^2}$	area
b	$-$	constant
C	$-$	constant
$C_{s,f}$	$-$	constant
C_1	$^{\mathrm{J}}/_{\mathrm{kgK}}$	constant boiling liquid property
c_p	$^{\mathrm{J}}/_{\mathrm{kgK}}$	specific heat capacity
D_b	m	bubble diameter
D_b'	$-$	normalised bubble diameter

$\overline{D_b}$	m	average bubble diameter
D_c	m	cavity mouth diameter
D_d	m	bubble departure diameter
$\overline{D_d}$	m	average bubble departure diameter
d_c	m	contact area diameter
f	$1/\mathrm{s}$	bubble departure frequency
$\overline{f}$	$1/\mathrm{s}$	average bubble departure frequency
f_{enh}	$-$	dimensionless factor
f_1, f_2	deg	function of the contact angle ϕ
f_φ	$-$	angle decrease fraction
g	$\mathrm{m^2/s}$	gravitational acceleration
H	$-$	characteristic length
h	$\mathrm{W/m^2K}$	heat transfer coefficient
h_{lg}	$\mathrm{J/kg}$	latent heat of vaporisation
I	A	electric current
K_1	$-$	constant
k	$\mathrm{W/mK}$	thermal conductivity
L	m	thickness
L_c	m	cavity depth
l	m	length
m_1	$-$	constant $(4 < m_1 < 6)$
N	$-$	constant
N_a	$1/\mathrm{m^2}$	nucleation site density
n	$-$	constant
p	Pa, bar	pressure
p_g	Pa, bar	partial pressure of gas or vapour
p_l	Pa, bar	partial pressure of liquid
Q	J	heat energy
$\dot{q}''$	$\mathrm{W/m^2}$	heat flux per unit area
$\dot{q}''_e$	$\mathrm{W/m^2}$	evaporative heat flux per unit area
$\dot{q}''_{MC}$	$\mathrm{W/m^2}$	micro-convection heat flux

$\dot{q}''_{ME}$	$\mathrm{W/m^2}$	micro-layer evaporation heat flux
$\dot{q}''_{TC}$	$\mathrm{W/m^2}$	transient conduction heat flux
$\dot{q}_{cond}$	W	conduction heat flux
$\dot{q}_{conv}$	W	convection heat flux
$\dot{q}_{tot}$	W	overall heat flux
R_a	m	arithmetic average roughness
R_b	m	bubble radius
R_c	m	cavity mouth radius
R_d	m	bubble departure radius
R_g	$\mathrm{J/kgK}$	specific ideal gas constant
r_c	m	contact area radius
S	m	cavity spacing
T	°C, K	temperature
T_∞	°C, K	bulk liquid temperature
ΔT	°C, K	excess temperature or wall superheat
ΔT_{TC}	°C, K	surface and rewetting liquid temperature difference
t	s	time
t_g	s	bubble growth time
t_m	s	micro-layer evaporation time
t_r	s	duration of the surface rewetting event
t_{tot}	s	total bubble growth time $(t_w + t_g)$
t_w	s	waiting time
t'	$-$	normalised time
U	$\mathrm{W/m^2K}$	overall heat transfer coefficient
V	V	potential drop
V_b	$\mathrm{m^3}$	bubble vapour volume
V_{bot}	$\mathrm{m^3}$	bottom bubble vapour volume
V_{coal}	$\mathrm{m^3}$	total vapour volume of coalesced bubbles
V_{top}	$\mathrm{m^3}$	top bubble vapour volume
v	$\mathrm{m^3/kg}$	specific volume
w	m	width

x	m	coordinate
y	m	coordinate

Subscripts

H	characteristic length
g	gas, vapour
l	liquid
max	maximum
min	minimum
NS	nucleation sites
s	surface
sat	saturation
SEN	sensor
Si	silicon
sub	subcooled
w	wall
0	initial condition

Dimensionless numbers

Bo	Bond number
Eo	Eötvös number
Gr	Grashof number
Ja	Jakob number
Nu	Nusselt number
Pr	Prandtl number
Ra	Rayleigh number

Contents

Abstract i
Zusammenfassung ii
Declaration of originality iv
Acknowledgements v
Nomenclature vii
Contents xii
List of figures xiv
List of tables xxviii

1 Introduction **1**
1.1 Motivation 1
1.2 Outline of the thesis 4

2 Nucleate pool boiling heat transfer **6**
2.1 Pool boiling heat transfer fundamentals 6
2.2 Nucleate boiling 8
2.2.1 Heat transfer mechanisms in nucleate pool boiling 8
2.2.2 Effects of system variables 12
2.2.3 Preexisting nuclei, inception and nucleation site density . . . 18
2.2.4 Controlled location of artificial nucleation sites 23
2.2.5 Bubble dynamics 26
2.2.6 Nucleation site interaction and bubble coalescence 36
2.3 Integrated micro-heaters and temperature micro-sensors 41
2.4 Conclusions 43

3 Experimental setup **44**
3.1 Experimental apparatus 44
3.2 Test sections 47
3.2.1 First generation 48
3.2.2 Second generation 50
3.2.3 Third generation 53
3.3 Data acquisition 56
3.4 Calibration and measurement error of the experimental equipment and image processing 58
3.5 Boiling liquid 65
3.6 Experimental procedure 67
3.7 Conclusions 70

4 Single bubble growth **71**
4.1 Bubble growth rate 72

4.2 Bubble departure frequency and departure diameter 89
4.3 The waiting time 106
4.4 Heat removal by vapour generation 111
4.5 Conclusions 117

5 Vertical coalescence **120**
5.1 Bubble nucleation frequency, frequency of vertical coalescence, bubble departure frequency and bubble departure diameter 120
5.2 Vapour volume analysis during vertical coalescence 128
5.3 Conclusions 132

6 Nucleation site interaction **133**
6.1 Two adjacent active artificial cavities 133
6.2 Horizontal coalescence 145
6.3 Conclusions 146

7 Conclusions **147**

8 Future work **150**

A Additional information experimental setup **152**

B General additional information **167**

C Additional results **169**
C.1 Preliminary results 169
C.2 Single bubble growth 173
C.2.1 Equilibrium superheat 173
C.2.2 Bubble growth rate 173
C.2.3 Bubble departure frequency and departure diameter 176
C.2.4 The waiting time 182
C.3 Vertical coalescence 187
C.4 Nucleation site interaction 199
C.4.1 Vertical coalescence 199
C.4.2 Bubble departure diameter 203

List of publications **205**

References **207**

List of figures

1.1 Schematical illustration of a conventional chip stack cooled with an air flow or an other fluid (reprinted with permission of IBM Research Laboratory, Zurich, Switzerland). 2

2.1 Nukiyama's boiling curve for saturated water at atmospheric pressure with corresponding boiling regimes included [1, 2]. 7
2.2 Interrelationships of elementary processes in nucleate boiling (adapted from Hsu and Graham [3]). 9
2.3 Heat transfer mechanisms during nucleate pool boiling, Kenning [4]. . 11
2.4 Left: Schematical view of a bubble with macro- and micro-layer [5]. Right: Macro- and micro-layer including significant phenomena in the micro-region [5]. 30
2.5 Effect factors of nucleation site interaction: 1. Hydrodynamic interaction between bubble and liquid bulk, 2. Hydrodynamic interaction between bubbles, 3. Thermal interaction between nucleation site and heated wall and 4. Thermal interaction between nucleation sites, Zhang and Shoji [6]. 39

3.1 Photograph of the experimental setup including: 1) Boiling chamber, 2) Condenser, 3) Reservoir, 4) Heating bath, 5) High-speed camera, 6) Backlight, 7) Pump, 8) Control system, 9) Power sources, 10) High precision A/V meter, 11) Voltage variac, 12) Data acquisition system (DAQ), 13) Current sources, 14a) PC for DAQ, 14b) PC for high-speed imaging. 45
3.2 Left: Schematic 3D view of the stainless steel boiling chamber with connection fittings and 4 borosilicate glass windows. Right: Schematic 3D view of the inside of the stainless steel boiling chamber with 2 of 4 cartridge heaters visible. 46
3.3 Left: Schematic 3D view of the stainless steel condenser with connection fittings. Right: Schematic 3D view of the inside of the stainless steel condenser including the stainless steel coil. 47
3.4 Arrangement of the 45 cavities etched with DRIE, based on the Bosch process, on a 0.38 mm thick silicon wafer. The coloured area (inner circle) indicates the heated area. 48
3.5 Top: Schematic concept of the jig of the first generation test section. Bottom left: 3D view from the top of the jig holding the first generation test section. Bottom right: 3D view from the bottom of the jig holding the first generation test section. (PTFE transparent for better visibility). 49

3.6 Fabrication sequence of the second generation test section. Fabrication includes micro-cavities, integrated temperature micro-sensors and an integrated resistance heater. 51
3.7 Left: Schematic rear-view of the second generation silicon device, with 5 sensors and one cavity located above each of them. Right: Photograph of the back side of the second generation silicon device. 52
3.8 Top: Schematic concept of the jig of the second generation test section. Bottom left: 3D view from the top of the jig, holding the second generation test section. Bottom right: 3D view from the bottom of the jig, holding the second generation test section (PTFE transparent for better visibility). 53
3.9 Left: Close-up photograph of a third generation micro-sensor. The image shows the square layout of the sensor with an artificial cavity in its centre. Right: Schematic view of the third generation micros-sensor layout with 4 connections indicated. 54
3.10 Top left: Photograph of the front of the third generation silicon device with 16 micro-sensors and 64 connection pads. Top right: Schematic view of the third generation silicon device with numbered sensors and cavities. Bottom left: Photograph of the back of the third generation silicon device with the integrated resistance heater and its two connection pads. Bottom right: Schematic view of the heater layout on the back of the third generation silicon device. 55
3.11 Top: Schematic concept of the jig of the third generation test section. Bottom left: 3D view from the top of the jig, holding the third generation test section. Bottom right: 3D view from the bottom of the jig, holding the third generation test section (PEEK™ transparent for better visibility). 56
3.12 Fabrication sequence of the third generation test section. Fabrication includes micro-cavities, integrated temperature micro-sensors and an integrated resistance heater. 57
3.13 Calibration of the 5 sensors on a second generation silicon device. The data points are plotted with linear trend lines and equations indicated. 59
3.14 Left: SEM image of a section through an elongated cavity. Right: Image of the cavity opening with smooth edges. 61
3.15 Saturation curve of fluorinert FC-72. 67
3.16 Experimental procedure for the high-speed imaging, including the main parts boiling chamber with test section, condenser, high-speed camera and backlight source. 69

4.1 Left: Arrangement of the artificial cavities on the second generation silicon device. Right: Arrangement of the artificial cavities on the third generation silicon device. 72

4.2 High-speed images of a bubble growth sequence from an isolated cavity (S3) with a nominal mouth diameter of 10 μm and a depth of 80 μm, a temporal resolution of 6 ms and a wall superheat of 1.1 K at 1.25 atm. 72
4.3 Average bubble growth of three successive bubbles at a wall superheat of 1.3 K and an applied heat flux of 0.85 $^{kW}/_{m^2}$ at atmospheric pressure from an isolated cavity (S3) with a nominal mouth diameter of 10 μm and depth of 100 μm. A trend line was fitted to the data. 73
4.4 Average bubble growth of three successive bubbles with a wall superheat of 10.1 K and an applied heat flux of 13.4 $^{kW}/_{m^2}$ at atmospheric pressure from an isolated cavity (S3) with a nominal mouth diameter of 10 μm and a depth of 100 μm. A trend line was fitted to the data. . . 74
4.5 Comparison of the bubble growth for two different wall superheats 1.3 K and 10.1 K from the same isolated cavity (S3) with a nominal mouth diameter of 10 μm and a depth of 100 μm at atmospheric pressure. Trend lines were fitted to both sets of data. 75
4.6 Comparison of the average bubble growth of 10 successive bubbles for three different wall superheats 1.4 K, 4.8 K and 8.1 K from the cavity (S8) which is 80 μm deep and has a nominal mouth diameter of 10 μm at 1 bar. Trend lines were fitted to all three sets of data. 76
4.7 Comparison of experimental bubble growth for a wall superheat of 1.3 K at atmospheric pressure from an isolated cavity (S3) with correlations from Forster and Zwick [7], Plesset and Zuber [8], Mikic *et al.* [9] and Fritz and Ende [10]. 78
4.8 Comparison of experimental bubble growth for a wall superheat of 10.1 K at atmospheric pressure from an isolated cavity (S3) with correlations from Forster and Zwick [7], Plesset and Zuber [8], Mikic *et al.* [9] and Fritz and Ende [10]. 78
4.9 Comparison of experimental bubble growth for a wall superheat of 1.4 K at 1 bar from an isolated cavity (S8) with correlations from Forster and Zwick [7], Plesset and Zuber [8], Mikic *et al.* [9] and Fritz and Ende [10]. 79
4.10 Comparison of experimental bubble growth for a wall superheat of 4.8 K at 1 bar from an isolated cavity (S8) with correlations from Forster and Zwick [7], Plesset and Zuber [8], Mikic *et al.* [9] and Fritz and Ende [10]. 79
4.11 Comparison of experimental bubble growth for a wall superheat of 8.1 K at 1 bar from an isolated cavity (S8) with correlations from Forster and Zwick [7], Plesset and Zuber [8], Mikic *et al.* [9] and Fritz and Ende [10]. 80
4.12 Comparison of experimental bubble growth for a wall superheat of 1.3 K at atmospheric pressure from an isolated cavity (S3) with correlations from Cooper [11]. 81

4.13 Comparison of experimental bubble growth for a wall superheat of 10.1 K at atmospheric pressure from an isolated cavity (S3) with correlations from Cooper [11]. 81
4.14 Comparison of experimental bubble growth for a wall superheat of 1.4 K at 1 bar from an isolated cavity (S8) with correlations from Cooper [11]. 82
4.15 Comparison of experimental bubble growth for a wall superheat of 4.8 K at 1 bar from an isolated cavity (S8) with correlations from Cooper [11]. 82
4.16 Comparison of experimental bubble growth for a wall superheat of 8.1 K at 1 bar from an isolated cavity (S8) with correlations from Cooper [11]. 83
4.17 Bubble radii, sensor and nucleation site temperature comparison between experimental and numerical results for case 1A, 1B, 1C, 1D and 1E. 85
4.18 Dimensionless radii comparison between experimental and numerical results with R_b/R_d and t/t_g. 86
4.19 Comparison of the temperature response between experiment (S8) and simulation over a long period at sub-atmospheric pressure of 0.463 bar at an applied heat flux of 8.6 kW/m^2. 87
4.20 Bubble departure frequency as a function of wall superheat from an isolated cavity (S3) with a nominal mouth diameter of 10 μm and a depth of 40 μm at 1 atm. 89
4.21 Bubble departure frequency as a function of wall superheat from an isolated cavity (S3) with a nominal mouth diameter of 10 μm and a depth of 40 μm at 1.25 atm. 90
4.22 Bubble departure frequency as a function of wall superheat from an isolated cavity (S3) with a nominal mouth diameter of 10 μm and a depth of 40 μm at 1.5 atm. 90
4.23 Bubble departure frequency as a function of wall superheat from an isolated cavity (S3) with a nominal mouth diameter of 10 μm and a depth of 80 μm at 1 atm. 91
4.24 Bubble departure frequency as a function of wall superheat from an isolated cavity (S3) with a nominal mouth diameter of 10 μm and a depth of 80 μm at 1.25 atm. 91
4.25 Bubble departure frequency as a function of wall superheat from an isolated cavity (S3) with a nominal mouth diameter of 10 μm and a depth of 80 μm at 1.5 atm. 92
4.26 Bubble departure frequency as a function of wall superheat from an isolated cavity (S3) with a nominal mouth diameter of 10 μm and a depth of 100 μm at 1 atm. 92

4.27 Bubble departure frequency as a function of wall superheat from an isolated cavity (S3) with a nominal mouth diameter of 10 μm and a depth of 100 μm at 1.25 atm. 93
4.28 Bubble departure frequency as a function of wall superheat from an isolated cavity (S3) with a nominal mouth diameter of 10 μm and a depth of 100 μm at 1.5 atm. 93
4.29 Comparison of data from Siedel *et al.* [12] with the measured frequencies of 3 different cavity depths as a function of wall superheat. 95
4.30 Bubble departure diameter as a function of wall superheat from an isolated cavity (S3) with a nominal mouth diameter of 10 μm and a depth of 40 μm at 1 atm. 97
4.31 Bubble departure diameter as a function of wall superheat from an isolated cavity (S3) with a nominal mouth diameter of 10 μm and a depth of 40 μm at 1.25 atm. 97
4.32 Bubble departure diameter as a function of wall superheat from an isolated cavity (S3) with a nominal mouth diameter of 10 μm and a depth of 40 μm at 1.5 atm. 98
4.33 Bubble departure diameter as a function of wall superheat from an isolated cavity (S3) with a nominal mouth diameter of 10 μm and a depth of 80 μm at 1 atm. 98
4.34 Bubble departure diameter as a function of wall superheat from an isolated cavity (S3) with a nominal mouth diameter of 10 μm and a depth of 80 μm at 1.25 atm. 99
4.35 Bubble departure diameter as a function of wall superheat from an isolated cavity (S3) with a nominal mouth diameter of 10 μm and a depth of 80 μm at 1.5 atm. 99
4.36 Bubble departure diameter as a function of wall superheat from an isolated cavity (S3) with a nominal mouth diameter of 10 μm and a depth of 100 μm at 1 atm. 100
4.37 Bubble departure diameter as a function of wall superheat from an isolated cavity (S3) with a nominal mouth diameter of 10 μm and a depth of 100 μm at 1.25 atm. 100
4.38 Bubble departure diameter as a function of wall superheat from an isolated cavity (S3) with a nominal mouth diameter of 10 μm and a depth of 100 μm at 1.5 atm. 101
4.39 Comparison of the measured bubble departure diameter from an isolated cavity (S3) with a nominal depth of 40 μm at 1 atm with correlations from Kutateladze and Gogonin [13], Jenson and Memmel [14], Cole [15] and Gorenflo *et al.* [16] 103
4.40 Comparison of the measured bubble departure diameter from an isolated cavity (S3) with a nominal depth of 80 μm at 1 atm with correlations from Kutateladze and Gogonin [13], Jenson and Memmel [14], Cole [15] and Gorenflo *et al.* [16] 103

4.41 Comparison of the measured bubble departure diameter from an isolated cavity (S3) with a nominal depth of 100 μm at 1 atm with correlations from Kutateladze and Gogonin [13], Jenson and Memmel [14], Cole [15] and Gorenflo *et al.* [16] 104
4.42 Comparison of the product $f^{1/2} \cdot \overline{D_d}$ from an isolated cavity (S3) with a nominal depth of 40 μm at 1 atm with a correlation from Mikic and Rohsenow [17]. 104
4.43 Comparison of the product $f^{1/2} \cdot \overline{D_d}$ from an isolated cavity (S3) with a nominal depth of 80 μm at 1 atm with a correlation from Mikic and Rohsenow [17]. 105
4.44 Comparison of the product $f^{1/2} \cdot \overline{D_d}$ from an isolated cavity (S3) with a nominal depth of 100 μm at 1 atm with a correlation from Mikic and Rohsenow [17]. 105
4.45 Ratio of waiting time and total growth period as a function of wall superheat for bubble growth from an isolated cavity (S3) with a nominal mouth diameter of 10 μm and a depth of 40 μm at 1 atm. 107
4.46 Ratio of waiting time and total growth period as a function of wall superheat for bubble growth from an isolated cavity (S3) with a nominal mouth diameter of 10 μm and a depth of 40 μm at 1.25 atm. 107
4.47 Ratio of waiting time and total growth period as a function of wall superheat for bubble growth from an isolated cavity (S3) with a nominal mouth diameter of 10 μm and a depth of 40 μm at 1.5 atm. 108
4.48 Ratio of waiting time and total growth period as a function of wall superheat for bubble growth from an isolated cavity (S3) with a nominal mouth diameter of 10 μm and a depth of 80 μm at 1 atm. 108
4.49 Ratio of waiting time and total growth period as a function of wall superheat for bubble growth from an isolated cavity (S3) with a nominal mouth diameter of 10 μm and a depth of 80 μm at 1.25 atm. 109
4.50 Ratio of waiting time and total growth period as a function of wall superheat for bubble growth from an isolated cavity (S3) with a nominal mouth diameter of 10 μm and a depth of 80 μm at 1.5 atm. 109
4.51 Ratio of waiting time and total growth period as a function of wall superheat for bubble growth from an isolated cavity (S3) with a nominal mouth diameter of 10 μm and a depth of 100 μm at 1 atm. 110
4.52 Ratio of waiting time and total growth period as a function of wall superheat for bubble growth from an isolated cavity (S3) with a nominal mouth diameter of 10 μm and a depth of 100 μm at 1.25 atm. 110
4.53 Ratio of waiting time and total growth period as a function of wall superheat for bubble growth from an isolated cavity (S3) with a nominal mouth diameter of 10 μm and a depth of 100 μm at 1.5 atm. 111
4.54 Evaporative heat flux $\dot{q}''_e$ and input heat flux $\dot{q}''$ with factor $N = 2$ as functions of wall superheat from an isolated cavity (S3) with a nominal mouth diameter of 10 μm and a depth of 40 μm at 1 atm. 113

4.55 Evaporative heat flux $\dot{q}''_e$ and input heat flux $\dot{q}''$ with factor $N = 2$ as functions of wall superheat from an isolated cavity (S3) with a nominal mouth diameter of 10 μm and a depth of 40 μm at 1.25 atm. 113
4.56 Evaporative heat flux $\dot{q}''_e$ and input heat flux $\dot{q}''$ with factor $N = 2$ as functions of wall superheat from an isolated cavity (S3) with a nominal mouth diameter of 10 μm and a depth of 40 μm at 1.5 atm. 114
4.57 Evaporative heat flux $\dot{q}''_e$ and input heat flux $\dot{q}''$ with factor $N = 2$ as functions of wall superheat from an isolated cavity (S3) with a nominal mouth diameter of 10 μm and a depth of 80 μm at 1 atm. 114
4.58 Evaporative heat flux $\dot{q}''_e$ and input heat flux $\dot{q}''$ with factor $N = 2$ as functions of wall superheat from an isolated cavity (S3) with a nominal mouth diameter of 10 μm and a depth of 80 μm at 1.25 atm. 115
4.59 Evaporative heat flux $\dot{q}''_e$ and input heat flux $\dot{q}''$ with factor $N = 2$ as functions of wall superheat from an isolated cavity (S3) with a nominal mouth diameter of 10 μm and a depth of 80 μm at 1.5 atm. 115
4.60 Evaporative heat flux $\dot{q}''_e$ and input heat flux $\dot{q}''$ with factor $N = 2$ as functions of wall superheat from an isolated cavity (S3) with a nominal mouth diameter of 10 μm and a depth of 100 μm at 1 atm. 116
4.61 Evaporative heat flux $\dot{q}''_e$ and input heat flux $\dot{q}''$ with factor $N = 2$ as functions of wall superheat from an isolated cavity (S3) with a nominal mouth diameter of 10 μm and a depth of 100 μm at 1.25 atm. 116
4.62 Evaporative heat flux $\dot{q}''_e$ and input heat flux $\dot{q}''$ with factor $N = 2$ as functions of wall superheat from an isolated cavity (S3) with a nominal mouth diameter of 10 μm and a depth of 100 μm at 1.5 atm. 117

5.1 Vertical coalescence of succeeding bubbles from an artificial nucleation site. The bubble of the volume V_{top} merges with the bubble of the volume V_{bot} to form a bubble of the volume V_{coal}. The time scale and the bubble volumes depend on the wall superheat. 121
5.2 Bubble growth sequence including vertical coalescence for a wall superheat of 7.9 K (applied heat flux 4.8 kW/m²) from an isolated cavity (S8) at 0.5 bar. The first frame includes a length scale and the temporal resolution between 2 frames is 1 ms. 122
5.3 Bubble nucleation frequency as a function of wall superheat from an isolated cavity (S8) with a nominal mouth diameter of 10 μm and a depth of 80 μm at 0.5 bar. 123
5.4 Bubble nucleation frequency as a function of wall superheat from an isolated cavity (S8) with a nominal mouth diameter of 10 μm and a depth of 80 μm at 0.75 bar. 124
5.5 Bubble nucleation frequency as a function of wall superheat from an isolated cavity (S8) with a nominal mouth diameter of 10 μm and a depth of 80 μm at 1 bar. 124

5.6 Frequency of vertical coalescence as a function of wall superheat from an isolated cavity (S8) with a nominal mouth diameter of 10 μm and a depth of 80 μm at 0.5 bar. 125
5.7 Frequency of vertical coalescence as a function of wall superheat from an isolated cavity (S8) with a nominal mouth diameter of 10 μm and a depth of 80 μm at 0.75 bar. 125
5.8 Frequency of vertical coalescence as a function of wall superheat from an isolated cavity (S8) with a nominal mouth diameter of 10 μm and a depth of 80 μm at 1 bar. 126
5.9 Ratio between frequency of vertical coalescence (VCF) and bubble nucleation frequency (BNF) as a function of wall superheat from an isolated cavity (S8) with a nominal mouth diameter of 10 μm and a depth of 80 μm at 0.5 bar. 126
5.10 Ratio between frequency of vertical coalescence (VCF) and bubble nucleation frequency (BNF) as a function of wall superheat from an isolated cavity (S8) with a nominal mouth diameter of 10 μm and a depth of 80 μm at 0.75 bar. 127
5.11 Ratio between frequency of vertical coalescence (VCF) and bubble nucleation frequency (BNF) as a function of wall superheat from an isolated cavity (S8) with a nominal mouth diameter of 10 μm and a depth of 80 μm at 1 bar. 127
5.12 Bubble volumes immediately before coalescence (V_{bot} and V_{top}) and the total volume just after coalescence (V_{coal}) for 10 cases of vertical coalescence. 129
5.13 Ratio between the volume of the newly nucleated bubble (V_{bot}) and the previously nucleated bubble (V_{top}) for 10 cases of vertical coalescence. 129
5.14 Ratio of the total volume of the top and bottom bubble ($V_{bot} + V_{top}$) immediately before coalescence and the volume of the coalesced bubble (V_{coal}) just after coalescence. 130
5.15 Vapour volume evolution from nucleation, over vertical coalescence to the departure of the coalesced bubble for 10 cases of vertical coalescence. The time at which coalescence occurs was set as the zero point. Vapour production of an isolated cavity (S8) with a nominal mouth diameter of 10 μm and a depth of 80 μm at 0.5 bar and a wall superheat of 7.9 K (applied heat flux 4.8 $^{kW}/_{m^2}$). 131

6.1 Bubble nucleation frequency as a function of wall superheat with a spacing of 1.5 mm between the two cavities S5 and S6 at 0.5 bar. . . . 135
6.2 Bubble departure frequency as a function of wall superheat with a spacing of 1.5 mm between the two cavities S5 and S6 at 0.5 bar. . . . 135
6.3 Bubble departure diameter as a function of wall superheat with a spacing of 1.5 mm between the two cavities S5 and S6 at 0.5 bar. 136
6.4 Bubble nucleation frequency as a function of wall superheat with a spacing of 1.5 mm between the two cavities S5 and S6 at 1 bar. 136

6.5 Bubble departure frequency as a function of wall superheat with a spacing of 1.5 mm between the two cavities S5 and S6 at 1 bar. 137
6.6 Bubble departure diameter as a function of wall superheat with a spacing of 1.5 mm between the two cavities S5 and S6 at 1 bar. 137
6.7 Bubble nucleation frequency as a function of wall superheat with a spacing of 1.2 mm between the two cavities S3 and S4 at 0.5 bar. . . . 138
6.8 Bubble departure frequency as a function of wall superheat with a spacing of 1.2 mm between the two cavities S3 and S4 at 0.5 bar. . . . 138
6.9 Bubble departure diameter as a function of wall superheat with a spacing of 1.2 mm between the two cavities S3 and S4 at 0.5 bar. 139
6.10 Bubble nucleation frequency as a function of wall superheat with a spacing of 1.2 mm between the two cavities S3 and S4 at 1 bar. 139
6.11 Bubble departure frequency as a function of wall superheat with a spacing of 1.2 mm between the two cavities S3 and S4 at 1 bar. 140
6.12 Bubble departure diameter as a function of wall superheat with a spacing of 1.2 mm between the two cavities S3 and S4 at 1 bar. 140
6.13 Bubble nucleation frequency as a function of wall superheat with a spacing of 0.84 mm between the two cavities S1 and S2 at 0.5 bar. . . 141
6.14 Bubble departure frequency as a function of wall superheat with a spacing of 0.84 mm between the two cavities S1 and S2 at 0.5 bar. . . 141
6.15 Bubble departure diameter as a function of wall superheat with a spacing of 0.84 mm between the two cavities S1 and S2 at 0.5 bar. 142
6.16 Bubble nucleation frequency as a function of wall superheat with a spacing of 0.84 mm between the two cavities S1 and S2 at 1 bar. . . . 142
6.17 Bubble departure frequency as a function of wall superheat with a spacing of 0.84 mm between the two cavities S1 and S2 at 1 bar. . . . 143
6.18 Bubble departure diameter as a function of wall superheat with a spacing of 0.84 mm between the two cavities S1 and S2 at 1 bar. 143
6.19 Frequency of horizontal coalescence as a function of increasing wall superheat with a spacing of 0.84 mm between the two cavities S1 and S2 at 0.5 bar. Regions of influence, following Zhang and Shoji [6], are indicated. 145

A.1 Flow and control diagram of the pool boiling experiment. 152
A.2 Technical drawings of the boiling chamber's stainless steel body. . . . 153
A.3 Technical drawings of the condenser's stainless steel body. 154
A.4 Technical drawings of the boiling chamber's top and bottom stainless steel lid. 155
A.5 Technical drawings of the stainless steel window flanges of the boiling chamber and the top and bottom lid of the condenser. 156
A.6 Technical drawing of the silicon device of the second generation with micro-sensors and heater pads. 157
A.7 Technical drawing of the silicon device of the third generation with micro-sensors and heater pads. 158

A.8 Technical drawing of the jig, holding the silicon device of the first generation in place. 159
A.9 Technical drawing of the jig, holding the silicon device of the second generation in place. 160
A.10 Technical drawing of the jig, holding the silicon device of the third generation in place. 161
A.11 Top: LabVIEW user interface for DAQ for the second generation test section. Bottom: LabVIEW visual programming for the second generation test section. 162
A.12 Top: LabVIEW user interface for DAQ for the third generation test section. Bottom: LabVIEW visual programming for the third generation test section. 163
A.13 Drawing of the circuit of the self-made current source. 164
A.14 Drawing of the circuit of the self-made trigger to synchronise the high-speed imaging with the DAQ. 165
A.15 Surface roughness measurement results in 3D for the silicon device of the third generation. 165
A.16 Three steps of image processing to identify the vapour volumes during vertical coalescence. Left: Original image during bubble growth with vertical coalescence. Middle: Processed picture with the assumed shape of the bottom bubble indicated. Right: Area measured with PCO Picture Viewer software. From this area the volume of revolution is calculated. 166
A.17 Influence of the choice of threshold intensity on the bubble volume calculation. 166

C.1 High-speed imaging sequence of bubble growth from the silicon device of the first generation in gas-dissolved saturated FC-72 at atmospheric pressure. Images were acquired at 1000 fps. 170
C.2 Bubble growth of successive bubbles at an applied heat flux of 11.7 $^{kW}/_{m^2}$ at 1.01 bar from an isolated cavity (S3) with a nominal mouth diameter of 2 μm and depth of around 22 μm. The data is compared to a correlation given by Mikic *et al.* [9], Eq. C.3. 171
C.3 Comparison of experimental bubble growth from an isolated cavity (S3) with a nominal mouth diameter of 10 μm and a depth of 100 μm for a wall superheats of 1.3 K at atmospheric pressure with the adjusted empirical correlation of Fritz and Ende [10]. The constant suggested by Fritz and Ende was multiplied by 1.29. 174
C.4 Comparison of experimental bubble growth from an isolated cavity (S3) with a nominal mouth diameter of 10 μm and a depth of 100 μm for a wall superheats of 10.1 K at atmospheric pressure with the adjusted empirical correlation of Fritz and Ende [10]. The constant suggested by Fritz and Ende was multiplied by 0.73. 174

C.5 Comparison of experimental bubble growth from an isolated cavity (S8) with a nominal mouth diameter of 10 μm and a depth of 80 μm for a wall superheat of 1.4 K at atmospheric pressure with the adjusted empirical correlation of Fritz and Ende [10]. The constant suggested by Fritz and Ende was multiplied by 0.92. 175
C.6 Comparison of experimental bubble growth from an isolated cavity (S8) with a nominal mouth diameter of 10 μm and a depth of 80 μm for a wall superheat of 4.8 K at atmospheric pressure with the adjusted empirical correlation of Fritz and Ende [10]. The constant suggested by Fritz and Ende was multiplied by 1.05. 175
C.7 Comparison of experimental bubble growth from an isolated cavity (S8) with a nominal mouth diameter of 10 μm and a depth of 80 μm for a wall superheat of 8.1 K at atmospheric pressure with the adjusted empirical correlation of Fritz and Ende [10]. The constant suggested by Fritz and Ende was multiplied by 2.23. 176
C.8 Comparison of the product $f \cdot \overline{D_d}$ from an isolated cavity (S3) with a nominal mouth diameter of 10 μm and a depth of 40 μm at 1 atm with correlations from Jakob and Fritz [18] and Zuber [19]. 178
C.9 Comparison of the product $f \cdot \overline{D_d}$ from an isolated cavity (S3) with a nominal mouth diameter of 10 μm and a depth of 80 μm at 1 atm with correlations from Jakob and Fritz [18] and Zuber [19]. 178
C.10 Comparison of the product $f \cdot \overline{D_d}$ from an isolated cavity (S3) with a nominal mouth diameter of 10 μm and a depth of 100 μm at 1 atm with correlations from Jakob and Fritz [18] and Zuber [19]. 179
C.11 Comparison of the trend lines of the bubble departure diameter as a function of wall superheat for a pressure of 1 atm. 179
C.12 Comparison of the trend lines of the bubble departure diameter as a function of wall superheat for a pressure of 1.25 atm. 180
C.13 Comparison of the trend lines of the bubble departure diameter as a function of wall superheat for a pressure of 1.5 atm. 180
C.14 Comparison of the trend lines of the bubble departure diameter as a function of wall superheat for a nominal cavity depth of 40 μm. 181
C.15 Comparison of the trend lines of the bubble departure diameter as a function of wall superheat for a nominal cavity depth of 80 μm. 181
C.16 Comparison of the trend lines of the bubble departure diameter as a function of wall superheat for a nominal cavity depth of 100 μm. . . . 182
C.17 Waiting time during bubble growth as a function of wall superheat from an isolated cavity (S3) with a nominal mouth diameter of 10 μm and a depth of 40 μm at 1 atm. 183
C.18 Waiting time during bubble growth as a function of wall superheat from an isolated cavity (S3) with a nominal mouth diameter of 10 μm and a depth of 40 μm at 1.25 atm. 183

C.19 Waiting time during bubble growth as a function of wall superheat from an isolated cavity (S3) with a nominal mouth diameter of 10 μm and a depth of 40 μm at 1.5 atm. 184
C.20 Waiting time during bubble growth as a function of wall superheat from an isolated cavity (S3) with a nominal mouth diameter of 10 μm and a depth of 80 μm at 1 atm. 184
C.21 Waiting time during bubble growth as a function of wall superheat from an isolated cavity (S3) with a nominal mouth diameter of 10 μm and a depth of 80 μm at 1.25 atm. 185
C.22 Waiting time during bubble growth as a function of wall superheat from an isolated cavity (S3) with a nominal mouth diameter of 10 μm and a depth of 80 μm at 1.5 atm. 185
C.23 Waiting time during bubble growth as a function of wall superheat from an isolated cavity (S3) with a nominal mouth diameter of 10 μm and a depth of 100 μm at 1 atm. 186
C.24 Waiting time during bubble growth as a function of wall superheat from an isolated cavity (S3) with a nominal mouth diameter of 10 μm and a depth of 100 μm at 1.25 atm. 186
C.25 Waiting time during bubble growth as a function of wall superheat from an isolated cavity (S3) with a nominal mouth diameter of 10 μm and a depth of 100 μm at 1.5 atm. 187
C.26 Bubble departure frequency as a function of wall superheat from an isolated cavity (S8) with a nominal mouth diameter of 10 μm and a depth of 80 μm at 0.5 bar. 188
C.27 Bubble departure frequency as a function of wall superheat from an isolated cavity (S8) with a nominal mouth diameter of 10 μm and a depth of 80 μm at 0.75 bar. 189
C.28 Bubble departure frequency as a function of wall superheat from an isolated cavity (S8) with a nominal mouth diameter of 10 μm and a depth of 80 μm at 1 bar. 189
C.29 Bubble departure diameter as a function of wall superheat from an isolated cavity (S8) with a nominal mouth diameter of 10 μm and a depth of 80 μm at 0.5 bar. The regions of influence following Zhang and Shoji [6] are indicated. A linear trend line was fitted to the data. . . . 190
C.30 Bubble departure diameter as a function of wall superheat from an isolated cavity (S8) with a nominal mouth diameter of 10 μm and a depth of 80 μm at 0.75 bar. The regions of influence following Zhang and Shoji [6] are indicated. A linear trend line was fitted to the data. . . . 190
C.31 Bubble departure diameter as a function of wall superheat from an isolated cavity (S8) with a nominal mouth diameter of 10 μm and a depth of 80 μm at 1 bar. The regions of influence following Zhang and Shoji [6] are indicated. A linear trend line was fitted to the data. 191

C.32 Comparison of the trend lines of the bubble departure diameter as a function of wall superheat from an isolated cavity (S8) with a nominal mouth diameter of 10 μm and a depth of 80 μm at 0.5, 0.75 and 1 bar. 191
C.33 Evaporative heat flux $\dot{q}''_e$ and input heat flux $\dot{q}''$ with factor $N = 1$ and $N = 4$ as functions of wall superheat from an isolated cavity (S8) with a nominal mouth diameter of 10 μm and a depth of 80 μm at 0.5 bar. . 192
C.34 Evaporative heat flux $\dot{q}''_e$ and input heat flux $\dot{q}''$ with factor $N = 1$ and $N = 4$ as functions of wall superheat from an isolated cavity (S8) with a nominal mouth diameter of 10 μm and a depth of 80 μm at 0.75 bar. 193
C.35 Evaporative heat flux $\dot{q}''_e$ and input heat flux $\dot{q}''$ with factor $N = 1$ and $N = 4$ as functions of wall superheat from an isolated cavity (S8) with a nominal mouth diameter of 10 μm and a depth of 80 μm at 1 bar. . . 193
C.36 Vapour volume evolution from nucleation, over vertical coalescence to the departure of the coalesced bubble for 10 cases of vertical coalescence. The time at which coalescence occurs was set as the zero point and the vapour volume normalised with the volume of the merged bubbles at departure. Vapour production of an isolated cavity (S8) with a nominal mouth diameter of 10 μm and a depth of 80 μm at 0.5 bar and a wall superheat of 7.9 K (applied heat flux 4.8 $^{kW}/_{m^2}$). 194
C.37 Three-dimensional view of the bubble formed by the two-dimensional bubble shape, extracted from the image at 10 ms in Fig. 5.2. 195
C.38 Three-dimensional view of the bubble formed by the two-dimensional bubble shape, extracted from the image at 11 ms in Fig. 5.2. 196
C.39 Three-dimensional view of the bubble formed by the two-dimensional bubble shape, extracted from the image at 12 ms in Fig. 5.2. 196
C.40 Three-dimensional view of the bubble formed by the two-dimensional bubble shape, extracted from the image at 13 ms in Fig. 5.2. 197
C.41 Three-dimensional view of the bubble formed by the two-dimensional bubble shape, extracted from the image at 14 ms in Fig. 5.2. 197
C.42 Three-dimensional view of the bubble formed by the two-dimensional bubble shape, extracted from the image at 15 ms in Fig. 5.2. 198
C.43 Maximum bubble diameter, location of the bubble apex, bubble base diameter and total vapour volume in time measured from Fig. C.37 to C.42. 198
C.44 Frequency of vertical coalescence as a function of wall superheat with a spacing of 1.5 mm between the two cavities S5 and S6 at 0.5 bar. . . 200
C.45 Frequency of vertical coalescence as a function of wall superheat with a spacing of 1.2 mm between the two cavities S3 and S4 at 0.5 bar. . . 200
C.46 Frequency of vertical coalescence as a function of wall superheat with a spacing of 0.84 mm between the two cavities S1 and S2 at 0.5 bar. . 201
C.47 Frequency of vertical coalescence as a function of wall superheat with a spacing of 1.5 mm between the two cavities S5 and S6 at 1 bar. . . . 201

C.48 Frequency of vertical coalescence as a function of wall superheat with a spacing of 1.2 mm between the two cavities S3 and S4 at 1 bar. . . . 202
C.49 Frequency of vertical coalescence as a function of wall superheat with a spacing of 0.84 mm between the two cavities S1 and S2 at 1 bar. . . 202
C.50 Comparison of the trend lines of the bubble departure diameter as a function of wall superheat for cavity spacings of 0.84 mm (S1 and S2), 1.2 mm (S3 and S4) and 1.5 mm (S5 and S6), and an isolated cavity (S8) at 0.5 bar. 203
C.51 Comparison of the trend lines of the bubble departure diameter as a function of wall superheat for cavity spacings of 0.84 mm (S1 and S2), 1.2 mm (S3 and S4) and 1.5 mm (S5 and S6), and an isolated cavity (S8) at 1 bar. 204

List of tables

2.1 Influence intensity of 3 effect factors of nucleation site interaction for different ratios of $S/\overline{D_d}$, Zhang and Shoji [6]. 40

3.1 Properties of fluorinert FC-72 from 3M [20] (part I). 65
3.2 Properties of fluorinert FC-72 from 3M [20] (part II). 66

4.1 Initial contact angle φ_0 and angle decrease factor f_φ used in the simulations A, B, C, D and E. 84

B.1 Values of $C_{s,f}$ and n for various surface/liquid combinations ([21–23]). 167
B.2 Thermal properties of nickel, silicon and titanium at 20 °C. 167
B.3 Summary of the cases calculated with the numerical code. 168
B.4 Applied heat fluxes for experiments at 1, 1.25 and 1.5 atm and nominal cavity depths of 40, 80 and 100 μm and a diameter of 10 μm. 168
B.5 Applied heat fluxes of experiments at 0.5, 0.75 and 1 bar and a nominal cavity depth of 80 μm and mouth diameter of 10 μm. 168

C.1 Theoretically calculated equilibrium superheats for a hemispherical bubble at the mouth of the cavity with a nominal diameter of 10 μm. . 173

Chapter 1
Introduction

1.1 Motivation

Boiling heat transfer is widely used in power and process industries because of the high dissipated heat fluxes at small temperature differences. Due to new developments in silicon-based devices, a strong interest in boiling as a cooling process has arisen. Potential difficulties in cooling by pool boiling are:

- Thermal hysteresis (excessive superheats required to activate nucleation sites).
- Non-uniformity of the temperature due to non-uniform heat sources.
- Random variations in the spatial distribution of sites.
- The deterioration in cooling that accompanies patch-wise transition to film boiling at a high critical heat flux.

The thermal management of electronic circuits and integrated circuits fabricated on silicon is an emerging problem with increasing computing power, miniaturisation of integrated circuits and increasing transistor density. High performing micro-chips can already reach heat dissipation rates above $150\,\mathrm{W/cm^2}$ and will reach around $250\,\mathrm{W/cm^2}$ by the end of 2010. This development was anticipated and will continue further as Moore's law [24] predicts that the number of transistors per area is to double approximately every two years. The maximum operating temperature for an integrated circuit is $85\,^{\circ}\mathrm{C}$, exceeding this limit leads to malfunctions and partial failure and to disintegration if increased further. Commercially available electronics are still cooled with conventional forced convection air cooling illustrated in Fig. 1.1.

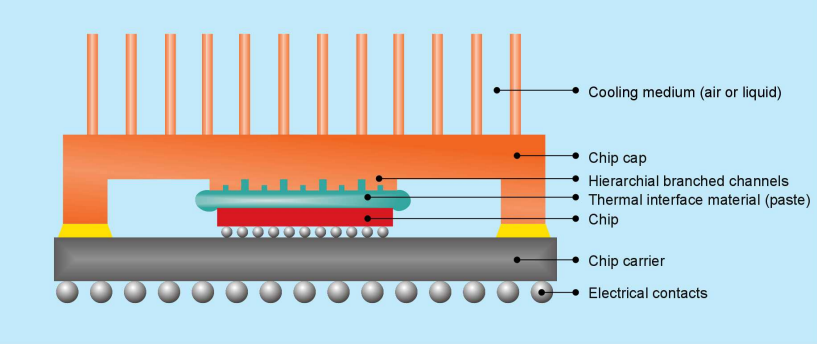

Figure 1.1: *Schematical illustration of a conventional chip stack cooled with an air flow or an other fluid (reprinted with permission of IBM Research Laboratory, Zurich, Switzerland).*

The chip placed on the chip carrier is dissipating heat which conducts through a thermal paste into the chip cap. From the chip cap, which most commonly has a through fin structures increased surface area, the heat is dissipated to a forced flow of air or liquid. The removed heat flux with forced convection air cooling will no longer be sufficient to keep microelectronics at a satisfactory temperature in the near future. It has to be replaced with better performing cooling methods. Pool boiling from a completely immersed microchip is one of this possible solutions with the following advantages:

- Heat transfer during nucleate boiling is very effective.
- The temperature of the bulk liquid is not increasing during boiling.
- The fluid volume is small compared to single phase flow applications, as the heat is removed due to latent heat.
- Direct immersion removes the conduction path and thereby thermal contact resistance from heat source to sink.

An important aspect of cooling with nucleate boiling is the right choice of boiling liquid. The liquid will be in close contact of electronic circuits and close to power supply units. Health and safety during the application and in case of failure, e.g., leaks, must be guaranteed. As electronic devices are short lived and their performance rapidly out-dated, environmental issues such as recycling and waste treatment have to

be considered. This leads to the following necessary criteria identified and summarised by Moghaddam [25]:

- Proper heat transfer properties (high thermal conductivity, large heat of vaporisation)
- Dielectric
- Non-toxic
- Non-corrosive
- Suitable boiling temperature and pressure
- Low freezing point
- Environment friendly

These criteria are reasonably met by FC-72, a fluorinert™ electronic liquid. More important, Bar-Cohen *et al.* [26] recently concluded that passive immersion cooling with natural convection and/or pool boiling of fluorinert™ liquids meets the heat dissipation values anticipated for the portable equipment category and might find application there.

Apart from the importance in engineering there are scientific questions to be elucidated for nucleate pool boiling. Controversies over basic transport mechanisms of bubble coalescence and its effect on the role of micro- and macro-layer, liquid resupply and heater surface are unsolved issues. Therefore, the main purpose of nucleate boiling research is to estimate the role of bubbles and to predict the correlations between the heat transfer and the surface superheat. Despite the beginning of nucleate pool boiling research several decades ago, the understanding of its physics is still not complete and no comprehensive model has been found yet. Nucleate pool boiling remains very complex and elusive.

1.2 Outline of the thesis

This project in boiling heat transfer with controlled arrays of nucleation sites started at the University of Edinburgh in July 2006. It was carried out in collaboration with the Scottish Microelectronic Centre at the University of Edinburgh, Brunel University, Los Alamos National Laboratories and the University of Ljubljana (participating persons: Dr. K. Sefiane, Prof. A. J. Walton, Prof. D. B. R. Kenning, Prof. T. G. Karayiannis, Prof. I. Golobič, Dr. R. Nelson, A. Sanna, Dr. H. Lin and G. Cummins). The objective of the project in Edinburgh was to build an experimental setup to conduct pool boiling experiments from artificial cavities on a silicon substrate with integrated heater and temperature micro-sensors. The investigation on nucleate pool boiling processes and experimental measurements were used as input and are a first step to the validation of a numerical code, currently developed at Brunel University. The code was initially written at Los Alamos National Laboratories by Pasamehmetoglu and Nelson [27] and modified at the University of Ljubljana [28]. An improved version of the code [29] is now used to investigate high heat flux pool boiling on a silicon plate in FC-72 with a large number of artificial cavities; experimental data (i.e., bubble growth time, bubble growth period, departure radius and wall superheat) for an isolated bubble are required as input data. Analysis of the results of simulations, and particularly variation in wall temperature and number of activation of the sites, will guide placement and choice of activation superheat of approximately 100 micro-fabricated cavities (or more) on a new test section. The numerical simulation is investigating the interactions between nucleation sites as a network.

The finished experimental setup was commissioned and tested using silicon wafers with artificial cavities heated from the back with an external heater. The second generation test section already had an integrated heater and temperature micro-sensors. It was used to study single bubble growth. The third and last test section had altered heater and sensor dimension and the artificial cavities were distributed to study bubble interaction during bubble growth.

In chapter 2 the existing literature on boiling heat transfer was reviewed. Chapter 3 explains the experimental setup including the used test sections, materials and adopted experimental procedures. Furthermore the uncertainties involved in measurement techniques and equipment were estimated. In chapter 4, 5 and 6 all the experimental results of this study will be presented and discussed. In chapter 4 bubble growth from a single artificial cavity was investigated. This includes the influence of cavity dimensions, pressure and wall superheat on the bubble departure frequency, bubble departure diameter and the heat flux due to bubble growth. These results are compared to results and models recently published, introduced earlier in chapter 2. In a second series of experiments the occurrence of vertical coalescence, the bubble departure frequency and departure diameter for pressures of 0.5, 0.75 and $1\,\mathrm{bar}$ were investigated. The vapour volume evolution in time during vertical coalescence was calculated from measured bubble areas in image sequences taken with a high-speed camera, chapter 5. In chapter 6 interactions between neighbouring sites were studied. Three different spacings between two cavities, 1.5, 1.2 and $0.84\,\mathrm{mm}$ were used to study the effect of spacing on the bubble departure frequency, the departure diameter and vertical and horizontal coalescence at 0.5 and $1\,\mathrm{bar}$. Final conclusions and a short outlook on future work are given in chapter 7 and 8.

Chapter 2
Nucleate pool boiling heat transfer

In this chapter a review of the existing literature on pool boiling research from the early stage to most recent publications is presented. The first part includes boiling fundamentals explaining the boiling curve and stating the best known nucleate boiling heat transfer correlation. The review continues with a comprehensive summary of mechanisms acting during nucleate pool boiling. System variables which affect the behaviour of pool boiling are followed by boiling inception, control of nucleation site distribution and bubble dynamics including various bubble growth, departure diameter and departure frequency correlations. The chapter closes discussing interactions during boiling and developments of silicon boiling substrates with integrated heaters and temperature sensors.

2.1 Pool boiling heat transfer fundamentals

Boiling is defined as the evaporation at a solid-liquid interface. The temperature of the surface T_s has to exceed the saturation temperature of the liquid. The occurring heat flux can be described by Newton's law of cooling

$$\frac{1}{A}\,\frac{dQ}{dt} = \dot{q}'' = h\ (T_s - T_{sat}) = h\ \Delta T \tag{2.1}$$

where h is the heat transfer coefficient and ΔT the excess temperature or the wall superheat. The process of boiling is characterised by the nucleation, growth and departure of bubbles at a solid-liquid interface. Pool boiling was studied for many decades. Nukiyama [1, 2] was the first who mentioned different boiling regimes, Fig. 2.1 top. He conducted experiments with a horizontal nichrome wire (melting point: $1500\,\mathrm{K}$)

at atmospheric pressure, immersed in saturated water. The heat flux was determined by the measurement of the electrical current I and potential drop V. The wire temperature was measured from the change of the electrical resistance due to changing temperature. First bubbles were observed after the temperature difference between the liquid and the wire reached $5\,^{\circ}\mathrm{C}$, Fig. 2.1 bottom.

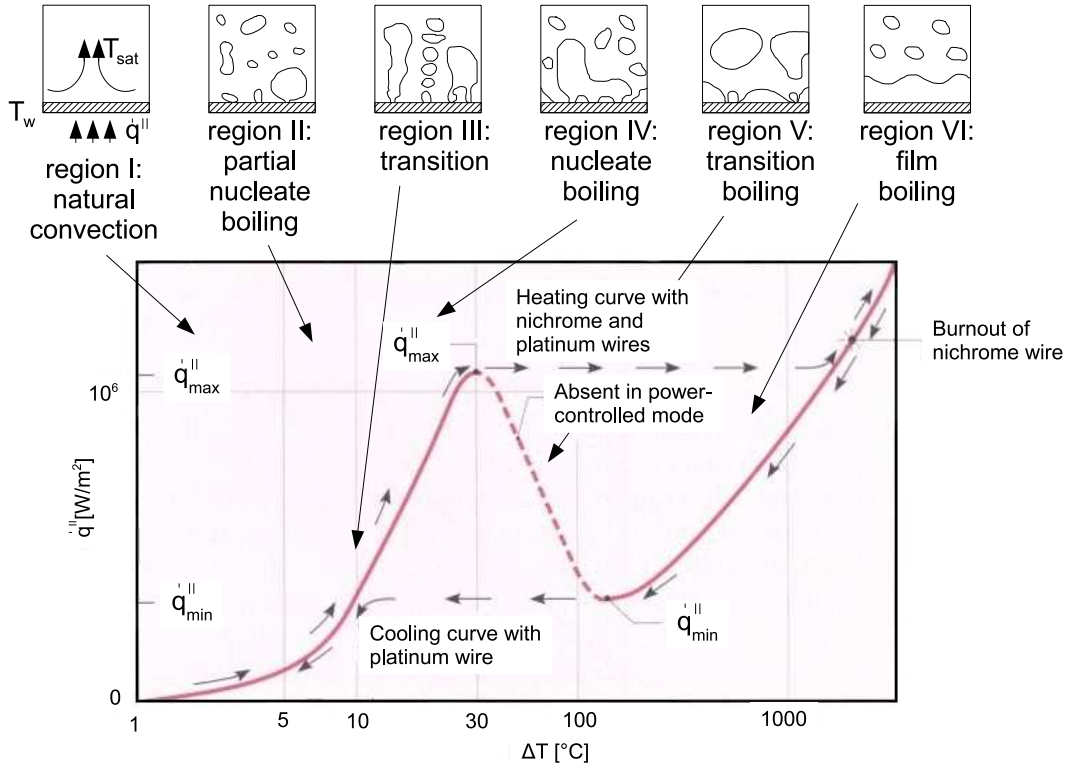

Figure 2.1: *Nukiyama's boiling curve for saturated water at atmospheric pressure with corresponding boiling regimes included [1, 2].*

Increasing the power to the wire slightly beyond the maximum heat flux $\dot{q}''_{max}$ immediately destroyed the wire by burnout. However, when the nichrome was substituted by platinum (melting point: $2045\,\mathrm{K}$), Nukiyama could maintain the heat flux above $\dot{q}''_{max}$ without causing a burnout. By reducing the power to the minimum heat flux $\dot{q}''_{min}$ the excess temperature fell abruptly. Nukiyama was not able to measure the dotted line plotted in Fig. 2.1, but mentioned that with the accurate control of ΔT it was possible to measure the entire boiling curve, as it is known today. Drew and Mueller [30] were the first, who measured the whole boiling curve with the four different boiling regimes,

i.e., natural convection, nucleate, transition and film boiling.

The best known nucleate boiling heat transfer correlation was proposed by Rohsenow [21]

$$\dot{q}'' = \mu_l \, h_{lg} \, \left[\frac{g \, (\rho_l - \rho_g)}{\sigma} \right]^{1/2} \left(\frac{c_{p,l} \, \Delta T}{C_{s,f} \, h_{lg} \, Pr_l^n} \right)^3 \tag{2.2}$$

where σ is the surface tension, h_{lg} the latent heat of evaporation, μ_l the liquid viscosity, ρ_g and ρ_l the vapour and liquid density, $c_{p,l}$ the liquid specific heat capacity and Pr_l the liquid Prandtl number. Parameter $C_{s,f}$ and n are constants, see Table B.1 in appendix A. $C_{s,f}$ takes into account the contact angle and the micro-roughness, and their interaction in determining the nucleation site density.

2.2 Nucleate boiling

Nucleate boiling is a very effective form of heat transfer. It gives high wall heat fluxes at low temperature differences and is widely used in industrial applications, e.g., heat exchanger systems. Nucleate boiling is characterised by the presence of bubbles, which maintain the heat transfer on the macroscopic level. There are many elementary processes involved from the macroscopic down to the microscopic statistical level. The connections and relationships are graphically shown in Fig. 2.2.

A major difficulty is to integrate bubble production behaviour and all involved processes into the correlation predicting the heat transfer from the heated wall, which puts bubble/bubble, bubble/liquid and nucleation site/nucleation site interactions right into the spotlight of pool boiling research.

2.2.1 Heat transfer mechanisms in nucleate pool boiling

One speaks about pool boiling, if the boiling liquid is stationary and only natural convection takes place. During pool boiling, different mechanisms are involved.

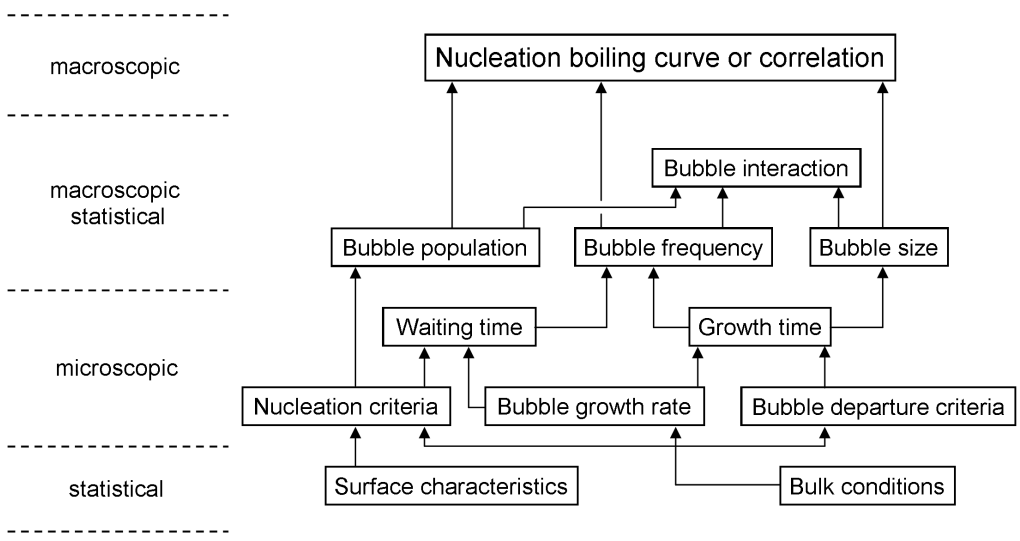

Figure 2.2: *Interrelationships of elementary processes in nucleate boiling (adapted from Hsu and Graham [3]).*

Mikic and Rohsenow [31] mentioned three mechanisms, which contribute to the high heat flux in nucleate boiling:

1) Transient conduction to, and subsequent replacement of, the superheated liquid layer in contact with the heating surface [21, 32, 33].

2) Evaporation of a liquid micro-layer at the base of a growing bubble, e.g., [34, 35].

3) Circulation of liquid in vicinity of a growing bubble due to thermo-capillarity effects on vapor-liquid bubble interface [36].

As the contribution of the micro-layer was without any relative significance and for the last effect no significance could experimentally be shown, they were neglected. However, the model of Mikic and Rohsenow [31], including only transient conduction, was in good agreement with experimental measurements.

Kenning [4] summarised the main mechanisms as following, Fig. 2.3:

a) Latent-heat transport [37]:
   Heat is supplied near the wall to bubbles, which then move away into the bulk

liquid. In subcooled boiling there could be simultaneous evaporation at the base of a bubble and condensation at its tip during growth.

b) Micro-convection [38]:
Bubble growth and/or collapse causes random liquid motion very close to the wall.

c) Vapour-liquid exchange [39]:
A "Reynolds analogy" model in which bubble growth causes an exchange of liquid between the wall and bulk regions.

d) Surface quenching [32, 33]:
A variation of c), assuming transient conduction to the cold liquid contacting the wall after bubble departure.

e) Wake flow [40]:
Liquid motion behind a departing bubble causes convection from the wall.

f) Enhanced natural convection [19]:
Bubble columns produce a cellular flow pattern similar to natural convection above a large horizontal surface.

g) Thermo-capillary flow [41]:
Small variations in surface tension due to temperature differences between the base and the tip of a bubble cause a jet of hot liquid to flow away from the wall. Estimates based on theoretical work by Kao and Kenning [42] suggest that this is not an important mechanism.

However, Kenning [4] argues that all the convective mechanisms have difficulty to explain the insensitivity of the boiling curve to subcooling and are based on the assumption of an self-compensating effect of subcooling on the bubble dynamics. Judd and Merte [43] compared the mechanisms a) to f) with experimental data for the same surface and different magnitudes of gravitational acceleration and found a poor agreement.

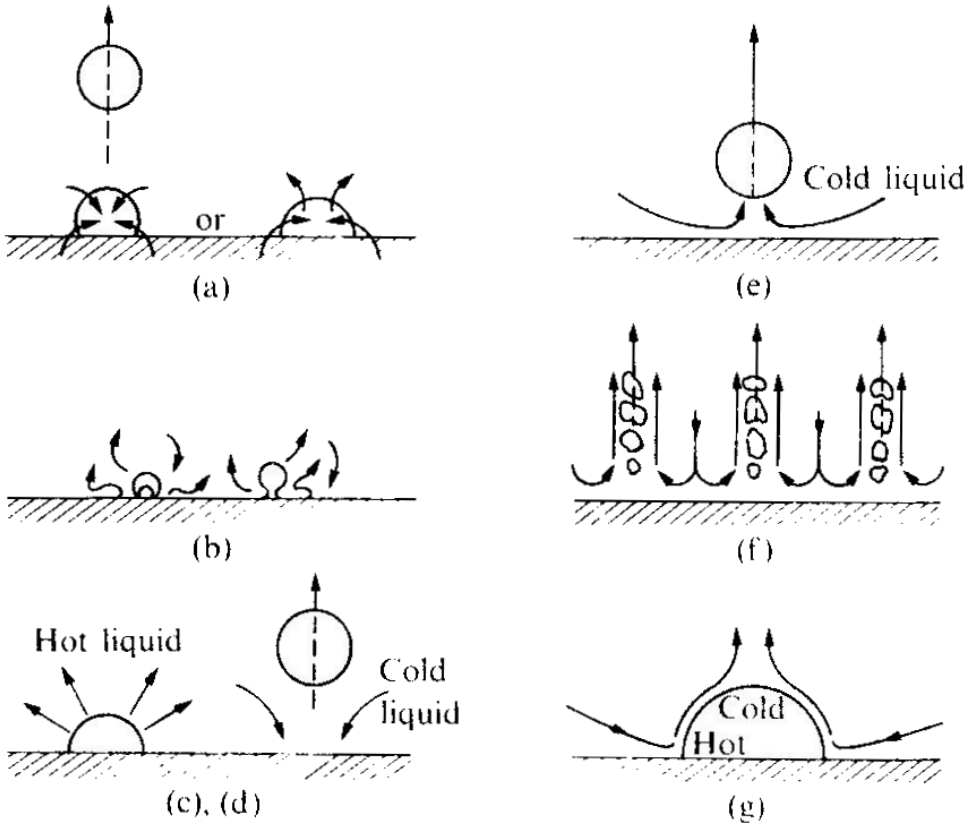

Figure 2.3: *Heat transfer mechanisms during nucleate pool boiling, Kenning [4].*

Dhir [44] identified four main mechanisms:

1) Transient conduction at the area of influence of a bubble growing from a nucleation site.

2) Evaporation (a fraction of which may be included in the transient conduction) at the vapour-liquid interface.

3) Enhanced natural convection on the region in the immediate vicinity of a growing bubble.

4) Natural convection over the area that has no active nucleation sites and is totally free of the influence of the three mechanisms discussed above.

Dhir maintains that the importance of these mechanisms depend on the magnitude of the wall superheat and other system variables such as heater geometry, orientation with respect to gravitational acceleration, magnitude of gravitational acceleration, etc.

Referring to Fujita [45] many researchers propose at least three main mechanisms for the isolated bubble regime:

1) Transient conduction: Involves the bubble-induced removal of the superheat liquid layer formed by transient conduction during the waiting period after bubble departure. This mechanism operates within an influence area of the departing bubble.

2) Micro-layer evaporation mechanism is associated with the evaporation of the micro-layer formed at the base of a growing bubble.

3) Natural convection mechanism operates.

Examples can be found in Mikic and Rohsenow [31], Graham and Hendricks [46], Judd and Hwang [47], Shoukri and Judd [48], Judd and Lavdas [49], and Paul and Abdelkhalik [50].

2.2.2 Effects of system variables

Following Dhir [51] nucleate boiling has several system variables:

- Surface wettability
- Surface finish
- Gravity
- System pressure
- Thermal properties of the solid boiling substrate
- Liquid subcooling

- Heater geometry
- Surface contamination
- Experimental procedure

Examples given by Dhir [51] for the influence of system variables are an increased surface roughness, which moves the boiling curve to the left or a better wettability of the surface, which moves the boiling curve to the right. The following paragraphs only give a choice of examples of how the above mentioned system variables can effect the nucleate boiling regime.

Surface properties The surface micro-geometry and wettability of the boiling surface affects the nucleation process. Heled *et al.* [52] investigated nucleate pool boiling from large arrays of artificial nucleation sites. The brass boiling surface was polished and electroplated with bright nickel and immersed in different organic liquids and water. Different numbers of cylindrical cavities with a mouth diameter of $0.008 \pm 0.0004\,\mathrm{in}$ and a depth of $0.039 \pm 0.001\,\mathrm{in}$ were drilled into the $2\,\mathrm{in}$ in diameter substrate. The boiling heat transfer rate was changed by varying the number of artificial cavities, e.g., the heat flux for methanol at a given average wall temperature superheat $\Delta T = 11.11\,\mathrm{K}$ increased by $75\,\%$, as the artificial cavity density was changed from 8 to 32 per cm^2. However, Heled *et al.* noted that the heat transfer rate cannot be increased indefinitely by increasing the number of cavities.

Experiments by Luke [53] on boiling propane on single horizontal copper and steel tubes with different surface roughness (emery ground, fine or rough sandblasted) showed that the influence of the surface roughness on the heat transfer decreases with increasing pressure and with increasing heat flux. The wall heat flux and superheat are influenced by the number of active nucleation sites and their interactions [54]. Surface properties like surface roughness and wettability influence the availability of nuclei and subsequently potential nucleation sites.

Gravity Early research on the influence of gravitational acceleration on nucleate boiling was mainly sponsored by NASA and performed in drop towers. However, conclusions in the literature are full of contradictions. Some claim an effect of the gravity level on the boiling behaviour, others deny it. The explanation for these discrepancies might be found in the short test times. The natural convection, taking place before the drop was initiated, was not eliminated in this short time periods. The most significant observation was the large increase of bubble size up to a few millimetre at reduced gravity. However, the mechanism which explains the removal of heat from a surface under micro-gravity conditions is still missing [55].

Siegel [56] conducted experiments with saturated distilled water on a very smooth horizontal nickel surface at low heat fluxes with 7 different gravity fields ranging from 1.4 to $100\,\%$ of the earth gravity. A rapid removal of small vapour bubbles merging into a large previously departed bubble, which remains close to the surface due to the low rising velocity, was observed in lower gravity fields. The main bubbling feature was the nucleation of one large bubble followed by several small bubbles before the growth of another large bubble. The product of bubble departure frequency and diameter $f \cdot D_d$ decreased with reduced gravity and tended to become constant below a certain gravity level. The gravity level increases with increasing applied heat flux. The bubble departure diameter and the growth time are increasing with reducing gravitational acceleration. However, the bubble contact angle was not influenced and was independent of gravitation.

Merte [57] and Zell *et al.* [58] showed with experiments using sounding rockets (test time up to $6\,\mathrm{min}$) that a change in the magnitude of the gravity has little effect on nucleate boiling. Zell *et al.* used wires and flat plates immersed in Freon 12, Freon 113, and saturated and subcooled water. Little effect on the overall heat transfer from the flat plate at constant temperature was measured, but a large increase in bubble departure diameter was observed. They concluded that the buoyancy was replaced by surface tension which forced the bubble to depart and evaporation was the main heat transfer.

Dhir [51] claims that the magnitude and direction of gravitational acceleration with re-

spect to the heater surface has an influence on the hydrodynamic and thermal boundary layer and the bubble trajectory.

Kim *et al.* [59] conducted experiments with subcooled FC-72 on micro-scale heater arrays (more details see Rule *et al.* [60] in section 2.3) under low, terrestrial and high gravity fields. At low gravity the bubbles were, as mentioned above, large single bubbles, which work as a sink for small bubbles nucleating in their vicinity. The dryout below the large bubble was held responsible for the significantly lower measured critical heat flux (CHF). Subcooling has a strong effect on the bubble diameter and CHF. Increasing the gravitation and the level of subcooling increased the CHF. However, the heat transfer occurring during small scale boiling was independent.

System pressure By increasing the system pressure the boiling temperature of the liquid will increase and higher temperatures are required to conduct boiling experiments. By reducing the system pressure the opposite will occur. Recently Kim *et al.* [61] compared experimental data obtained by several researchers and found a different, higher bubble growth rate at sub-atmospheric pressure compared to experiments conducted under atmospheric pressure conditions.

Thermal properties of the substrate Stephan and Abdelsalam [62] demonstrated a weak effect on the boiling heat flux which can be steady state or transient by the thermo-physical properties of the boiling surface.

Zhou and Bier [63] conducted boiling experiments on tubes coated with copper immersed in iso-pentane and R-12. The thickness of the copper coat was varied between 2 and $1000\,\mu\mathrm{m}$ and all of them were sandblasted to maintain the same surface roughness conditions. The change of thermal properties with increasing thickness of the copper layer increased the heat transfer coefficient by $80\,\%$.

Subcooling Jacobs and Shade [64] worked with carbon tetrachloride analysed by taking high-speed images using the schlieren optical system. They concluded that

many bubbles at any level of subcooling of the liquid were superheated when leaving the heated surface. Bubbles carried a thin laminar layer of hot liquid at their apex, followed by a long, usually turbulent wake of warm liquid. The authors hypothesised that other mechanisms, such as splashing jets and natural convection in boiling, are responsible for the remaining heat transfer.

A mathematical model for bubble dynamics in subcooled nucleate boiling has been derived by Robin and Snyder [65]. They demonstrated that the main heat transfer mechanism for subcooled boiling is mass transfer. They also found that subcooled boiling is characterised by extremely high heat transfer rates for water systems near atmospheric pressure. Heat fluxes of $4494\,\mathrm{kW/m^2}$ and higher can be achieved.

Kim *et al.* [59] and Demiray and Kim [66] concluded in their work that subcooling strongly affects the primary bubble size and the CHF. The departure diameter of the bubbles and the energy transfer were larger during low subcooled boiling, whereas the departure frequency increased with even lower temperatures, resulting in an overall increased heat transfer. The CHF increases with higher subcooling, however, the heat transfer at small scale boiling is not affected by subcooling.

Furthermore Parker and El-Genk [67] showed in recent experiments with FC-72 boiled on copper and porous graphite that the heat transfer coefficient is increased during subcooled nucleate boiling. The CHF increased linearly with increasing temperature difference ΔT_{sub}.

Heater geometry The effects on the boiling heat transfer of micro-pin-fins on a silicon chip ($10 \times 10 \times 0.5\,\mathrm{mm^3}$) immersed in degassed or gas-dissolved FC-72 have been studied by Wei and Honda [68]. The square micro-pin-fins manufactured by dry etching had dimensions between $30 \times 60\,\mu\mathrm{m}^2$ and $50 \times 270\,\mu\mathrm{m}^2$ (thickness $\times$ height). Experiments were conducted at atmospheric pressure and under subcooled conditions $\Delta T_{sub} = 0$, 3, 25 and $45\,\mathrm{K}$. The micro-pin-fins generally enhanced the heat transfer in the nucleate boiling region. Dissolved gas in the boiling liquid decreases the boiling incipience temperature, which leads to better heat transfer performance in the low heat

flux region compared to degassed FC-72. However, the heat transfer performance in the high heat flux region was almost the same for gas-dissolved and degassed FC-72.

Kim *et al.* [69] conducted experiments on electrically heated platinum wires immersed in saturated FC-72 and water at atmospheric pressure. The effect of the different wire diameters of 25, 75 and $390\,\mu\mathrm{m}$ in FC-72 were investigated by measuring the volume flow rate and the bubble departure frequency. The vapour volume flow rate was calculated through bubble volumes, measured with the consecutive-photo method [70]. Reduced wire diameters led to increased boiling heat transfer due to the reduced surface tension. The bubble size decreased and the bubble departure frequency increased. Therefore, the contribution of the micro-convection increased compared to the contribution of evaporation. The $390\,\mu\mathrm{m}$ wire was also tested in saturated water. Although the bubble frequency was lower and the bubble size larger, the heat transfer in water was higher. This results from the approximately 24 times higher latent heat of vaporisation of water compared to FC-72.

The inclination of the heater surface is found to affect the boiling heat transfer. The effect of the surface configuration on nucleate boiling heat transfer has been investigated by Nishikawa *et al.* [71]. A copper plate immersed in water under atmospheric pressure was used during saturated boiling experiments. The inclination angle was varied between $0\,^\circ$ and $175\,^\circ$. The effect was remarkable in the low heat flux region. The heat transfer coefficient increased with increased inclination . However, no effect was noticeable at high heat fluxes. More information about inclined heater surfaces can be found in Costello *et al.* [72], Githinji and Sabersky [73] and Marcus and Dropkin [74].

Surface contamination Joudi and James [75] investigated the effect of contaminations on stainless steel boiling substrates near the nucleation sites by corrosion products in water and by oxide deposits in methanol during nucleate boiling. Higher temperature differences were continually required for a given value of the heat flux due to surface contaminations. However, for a given wall superheat the wettability is generally enhanced and the nucleate boiling heat transfer reduced by surface contaminations [51].

Experimental procedure Differences in experimental procedures, such as degassing duration, cleaning method of the boiling substrate, ageing of the boiling surface etc., can affect the experimental results.

2.2.3 Preexisting nuclei, inception and nucleation site density

Corty and Foust [76] were the first to postulate a vapour-trapping mechanism in nucleate boiling based on their observation that surface defects serve as nucleation sites. Clark *et al.* [77] confirmed, that vapour or gas trapped in a scratch or cavity can work as nucleus for bubble growth. In order for the nucleus not to shrink, its internal temperature must equal the saturation temperature for the pressure of the vapour phase, calculated from the Young-Laplace equation

$$p_g \; - \; p_l = \frac{2\,\sigma}{R_c} \tag{2.3}$$

where R_c is the cavity mouth radius and p_g and p_l are the partial pressures of the vapour and the liquid. Assuming ideal gas behaviour for the vapour and that the specific volume of the liquid compared to the one of the vapour is negligible, the Clausius-Clapeyron equation can be applied

$$\frac{dp}{dT} = \frac{h_{lg}}{(v_g - v_l)\;T} \tag{2.4}$$

The temperature needed to activate a vapour nucleus is therefore

$$T_g - T_{sat} = \frac{2\,\sigma}{R_c\,h_{lg}\,\rho_g} \tag{2.5}$$

where T_g is the vapour temperature. Smaller cavities can be activated with increasing nucleus vapour temperature.

The first theoretical criterion for preexisting nuclei (gas) was given by Bankoff [78].

A wedge shaped scratch will trap gas as long as the contact angle is greater than the wedge angle. Bankoff showed that the necessary superheats for the onset of boiling for heterogeneous nucleation is much smaller than for those necessary for homogeneous nucleation. The reason for the lower superheat required can be found in the gas and/or vapour trapped in cavities.

Following Wang and Dhir's [79] criterion, a cavity will trap vapour or gas if

$$\phi > \psi_{min} \tag{2.6}$$

where ϕ is the contact angle, ψ_{min} the minimum cavity side angle of a spherical, conical or sinusoidal cavity. For the spherical and the conical cavity, ψ_{min} can be measured at the mouth of the cavity, since it is the same as the cavity mouth angle ψ_m.

Well-wetting liquids, such as R-113 and FC-72, have only few nucleation sites and the wall superheat temperature is expected to approach the homogeneous nucleation temperature ($\approx 90\,\%$ of the critical temperature). The wall superheat is higher than with less wetting liquids, however still much smaller than the corresponding homogeneous nucleation temperature. Barthau [80] suggested that the dissolved gases in the liquid reduce the required superheat.

Kenning [81] described the combined influence of the surface micro-geometry, the surface physico-chemistry and the micro-climate of temperature, temperature gradient and pressure on the bubble nucleation. He concluded that the average roughness is a bad indicator for the nucleation capability of a surface.

There are two approaches to determine the necessary wall superheat for boiling inception from a preexisting nucleus. Hsu [82] stated, that a nucleus becomes a bubble, if the temperature of its furthest point from the heater surface is at least equal to the saturation temperature of the boiling liquid.

The second boiling incipience approach corresponds to the critical point of instability at the vapor-liquid interface. Nucleation starts, if the non-dimensional curvature of the

interface reaches a maximum value, described by Wang and Dhir [79] as

$$\Delta T = \frac{4\,\sigma\,T_{sat}}{\rho_v\,h_{lg}\,D_c}\,K_{max} \tag{2.7}$$

with

$$K_{max} = 1 \quad \text{for } \phi \leq 90\,^\circ \tag{2.8}$$

$$K_{max} = sin\phi \quad \text{for } \phi > 90\,^\circ \tag{2.9}$$

where D_c is the cavity mouth diameter.

According to Wei and Honda [68] and Wei *et al.* [83] dissolved gas can initiate nucleation at lower wall superheat and minimize the hysteresis of the boiling curve. This will also decrease the boiling incipience temperature and confirms previous studies.

Generally an increased wall heat flux or wall superheat will increase the number of active nucleation sites and therefore a deep knowledge of its relations are of importance for industrial applications. Several parameters, such as the heater surface finish, the surface wettability, heater material with its thermo-physical properties and the heater thickness, some of them discussed in detail above, influence the nucleation site density.

Early studies summarised in Hsu and Graham [84] give the nucleation site density as

$$N_a \propto \Delta T^{m_1} \tag{2.10}$$

or

$$N_a \propto \dot{q}''^2 \tag{2.11}$$

where N_a is the nucleation sites density, ΔT the wall superheat and m_1 a constant value between 4 and 6.

Kocamustafaogullari and Ishii [85] derived a correlation (Eq. 2.12) from data of miscellaneous investigators for water on different surfaces and a pressure range between 1 and $198\,\mathrm{atm}$. The heater surface characteristics were not considered in the following correlation

$$N_a^* = \left[D_c^{*-4.4}\ f(\rho^*)\right]^{1/4.4} \tag{2.12}$$

with

$$N_a^* = N_a\ D_d^2 \tag{2.13}$$

$$D_c^* = D_c/D_d \tag{2.14}$$

and

$$f(\rho^*) = 2.157 \cdot 10^{-7}\ \rho^{*-3.2}\ \left(1 + 0.0049\ \rho^*\right)^{4.13} \tag{2.15}$$

where ρ^* and D_c are

$$\rho^* = \frac{\rho_l - \rho_g}{\rho_g} \tag{2.16}$$

$$D_c = 4\,\sigma\ \left[1 + (\rho_l/\rho_g)\right]/p_l \cdot \left\{\exp\left[h_{lg}\ \left(\frac{T_g - T_{sat}}{R_g\ T_g\ T_{sat}}\right)\right] - 1\right\} \tag{2.17}$$

T_g is the vapour temperature and R_g the gas constant for vapour.

Wang and Dhir [79, 86] were first to make a mechanistic approach to correlate the

relationship between existing cavities and active nucleation sites, including the surface wettability. They did not include any thermal interference or seeding between the nucleation sites, however. First they determined the size, shape and mouth angle of cavities on a polished copper surface. The fraction of the vapour or gas trapping cavities is calculated from Eq. 2.10. Most of the vapour or gas trapping cavities are of the reservoir shaped type. A 20-fold reduction in the number of nucleation sites by reducing the contact angle from $90\,^\circ$ to $18\,^\circ$ was shown. Although the model is consistent with empirical data, there is no practical application, since the measurement of the parameters is too time consuming.

The liquid and solid phase vicinity of a nucleation site with its thermal and flow distribution can activate or deactivate nucleation sites, Kenning [87]. Increased heat flux can activate some new nucleation sites, but the existing sites will also be more active and can decrease the activity of other sites as shown by Kenning and Yan [54]. Thermal and flow interactions and their influence on nucleation sites are discussed in more detail in section 2.2.6.

In their experiments Theofanous *et al.* [88] used sub-micron titanium films (thickness: 100 to $140\,\mathrm{nm}$) vapour deposited on borosilicate glass plates (thickness: $130\,\mu\mathrm{m}$) which were heated electrically. They could show that the CHF performance during nucleate pool boiling improved due to increased bubble nucleation densities on aged surfaces. The wall superheat required for boiling incipience on this smooth surface was $10\,\mathrm{K}$. These measurements are not consistent with the general cavity theory, which requires the presence of trapped gas vapour on the heater surface in cavities, scratches, etc. Nano-scale imperfections and defects were assumed to be the reason for the low incipience temperature.

Qi and Klausner [89] compared a coarse (root mean squared (RMS) roughness $1.02\,\mu\mathrm{m}$) and smooth (RMS roughness $0.018\,\mu\mathrm{m}$) brass boiling surface immersed in ethanol. For the smoother surface a slightly higher superheat of $1.7\,\mathrm{K}$ was needed to achieve incipience. However, no difference in the variation of the nucleation site density appeared. They assume that another mechanism than vapour or gas trapped in a cavity is responsible. One reason could be the existence of nano-bubbles on the surface. This theory

and the measurement of these bubbles are still controversial and further research is necessary.

On smooth boiling substrates without cavities other mechanisms are observed. Chen *et al.* [90] immersed a smooth micro-heater (approximately $10\,\mathrm{nm}$ RMS roughness) in degassed FC-72 at ambient properties, $1\,\mathrm{atm}$ and $25\,^{\circ}\mathrm{C}$. A homogeneous nucleation process started when a wall superheat of $80\,\mathrm{K}$ was reached. The vapour expansion process includes initial explosive vapour formation, hemispherical bubble expansion and bubble detachment. After bubble departure a small amount of vapour was left at the surface, which forms a bubble inception point or nucleation site. Single bubble growth was maintained at a wall superheat of $44\,\mathrm{K}$, i.e., much lower than the superheat initially required for incipience.

The nucleation density during pool boiling was investigated by Benjamin and Balakrishnan [91]. Saturated distilled water, carbon tetrachloride, n-hexane and acetone were used. The experiments were conducted on stainless steel and aluminium, polished with different grades of emery paper. The micro-roughness of the boiling substrates was characterised with the arithmetic average roughness R_a, determined by a profilometer. The nucleation site density in this study depended on the surface micro-roughness, the surface tension of the liquid, thermo-physical properties of the heated surface and the liquid and wall superheat.

2.2.4 Controlled location of artificial nucleation sites

Bubble growth is a very rapid process with high departure frequencies. To study single or multiple bubble growth or interaction between nucleation sites with different spacing, using high-speed imaging and temperature sensors integrated into the boiling substrate, the location of the bubble nucleation has to be controlled and fixed.

Gjerkeš and Golobič [92] used laser irradiation to produce controlled nucleation sites. The bottom of a cylindrical stainless steel boiling chamber was closed by a $25\,\mu\mathrm{m}$ thin metal foil, either copper or titanium. The boiling chamber was filled with saturated water and the back was heated by laser irradiation with a Nd:YAG laser. The diam-

eter of the heated area was varied between 2.27 and $9\,\mathrm{mm}$ and the maximum power input was $70\,\mathrm{W}$. The authors were able to produce single and simultaneously active nucleation sites depending on the heat flux, size and material of the heated surface. They concluded that the bubble diameter was increased gradually, while the bubble departure frequency reached a minimum and did not change significantly with further increased laser heat flux.

A second method to produce controlled active nucleation sites is the implementation of artificial cavities on the boiling surface, which will trap gas and/or vapour and act as nuclei for bubble growth.

Rammig and Weiss [93] investigated cryogenic boiling heat transfer with liquid nitrogen and hydrogen. The boiling surface was built with a bottom layer of copper, a layer of soldering tin and coated with a top layer of Au-Pt alloy. They used cylindrical and re-entrant artificial cavities with mouth diameters from 27 to $70\,\mu\mathrm{m}$. The cylindrical cavities had depths between 100 and $200\,\mu\mathrm{m}$ and were arranged in-line on a $10\,\mathrm{mm}$ line with 10 cavities. The re-entrant cavities had a depth of $230\,\mu\mathrm{m}$ and their number density was either $1500\,{}^{1}\!/_{\mathrm{cm}^2}$ or $1800\,{}^{1}\!/_{\mathrm{cm}^2}$. The most important conclusion was that artificial cavities remain active at low wall superheats, whereas on smooth surfaces no bubbles at all were generated for the same superheat. According to the used growth model, they could also demonstrate that the micro-layer is the main part of the heat transfer, except for the first stage of bubble growth.

Mori and Baines [94] studied bubbles by gas diffusion in carbonated water. The main advantage of gas diffusion are the slow growth and large departure diameters, which make the capture and investigation of bubbles easier. On a horizontal plate, built from stainless steel, artificial cylindrical cavities with 0.6, 1.48 and $20.8\,\mathrm{mm}$ in diameter were manufactured. For temperatures between 10 and $50\,^{\circ}\mathrm{C}$ and a pressure range of 1 to $5\,\mathrm{atm}$ bubbles with a departure diameter between 2 and $5\,\mathrm{mm}$ were measured. The surface tension effect forces an earlier departure of the bubble by forming a bubble neck, rather than inhibiting it because of its adherent force, which attaches the bubble to the surface.

The effect of cavity shape on the bubble growth while simultaneously measuring surface temperature fluctuations was investigated by Shoji and Takagi [95]. Conical, cylindrical and re-entrant cavities on a $0.1\,\mathrm{mm}$ thick copper plate were studied. Bubbling from the conical cavity was highly intermittent and larger local temperature fluctuations, requiring higher wall superheats, were measured. The behaviour of the re-entrant cavity was very similar to the cylindrical one, but slightly more complicated.

Chatpun *et al.* [96] arranged three artificial cavities either in an in-line or triangular pattern on a $0.2\,\mathrm{mm}$ thick and $20 \times 20\,\mathrm{mm}^2$ mirror-like silicon wafer. The distance between the cavities was varied between 1, 2, 3 and $4\,\mathrm{mm}$ for both patterns and the silicon substrate was heated by laser irradiation with heat fluxes between 33.8 and $55.6\,\mathrm{kW/m^2}$. Indications were found that both patterns influence the bubble departure frequency, the departure diameter and the temperature distribution on the heated surface. If the optimal cavity spacing for the in-line pattern was chosen, horizontal bubble coalescence could enhance bubble dynamics better than the triangular pattern with the same cavity spacing. The temperatures during the experiment with saturated distilled water at atmospheric pressure were measured with a radiation thermometer with a spatial resolution of $125\,\mu\mathrm{m}$, a temperature resolution of $0.08\,\mathrm{K}$ and a temporal resolution of $3\,\mathrm{ms}$.

Yu *et al.* [97] conducted experiments with a $625\,\mu\mathrm{m}$ thick and $10 \times 10\,\mathrm{mm}^2$ square silicon plate immersed in saturated FC-72 at atmospheric pressure. Cylindrical cavities with diameters of 50, 100 and $200\,\mu\mathrm{m}$ and depths of 110 and $200\,\mu\mathrm{m}$ were microfabricated on the silicon wafer. The boiling incipience and temperature excursion of silicon based surfaces were more significant than on metal based surfaces. The cavity density had more influence at higher applied heat fluxes because of coalescence close to the heated surface. There was no closer focus on the individual bubble growth.

A mechanism worth mentioning in context with artificial cavities is bubble pinning. It is possible that the bubble contact line with the boiling surface is pinned to the edge of the mouth of the artificial cavity acting as nucleation site. This prevents the 3-phase contact line from expanding and receding during growth and affects the heat transfer. There were no specific studies found about this topic, but it was reported in discussions

with other research groups.

2.2.5 Bubble dynamics

Bubble dynamics of a single bubble are divided in three mechanisms: bubble growth, bubble departure and bubble departure frequency which includes the cooling and recovering of the boiling surface between succeeding bubbles.

Bubble growth One of the first models was introduced by Bošnjaković [98], who believed that the heat necessary for the evaporation taking place on the bubble surface is coming from a thin, superheated liquid layer surrounding the bubble. However, Fritz and Ende [10] suggested that the thermal conduction is responsible for the heat transport to the bubble surface. They solved the transient thermal conduction equation and deduced

$$R_b\left(t\right) = \sqrt{4/\pi}\frac{c_p}{h_{lg}}\frac{\rho_l}{\rho_v}\sqrt{k_l}\left(T_s - T_{sat}\right)t^{1/2} \tag{2.18}$$

where $R_b(t)$ is the bubble radius dependent on time t, $T_s - T_{sat}$ the driving temperature difference and k_l the thermal conductivity of the liquid.

However, the bubble growth is not only controlled by heat flow to the bubble surface, i.e., not only by the energy equation. Forces acting on the bubble influence the growth as well and are integrated in the momentum equation. Therefore, Forster and Zuber [7] and Plesset and Zwick [8] took, in addition to the energy equation, the force balance on a growing bubble into account. Compared to Eq. 2.18 the difference is only a factor of a number. Instead of $\sqrt{4/\pi}$ Forster and Zwick obtained $2\sqrt{3/\pi}$ and Plesset and Zuber $2\sqrt{\pi/4}$, respectively. Beer [99] believes the absence of considerable differences is caused by the dominance of the energy equation during bubble growth and suggests the following

$$R_b\left(t\right) = {}^1\!/_2 \left[0.234 \frac{k_l}{\rho_g \, h_{lg}} \left(\frac{\rho_l}{\mu_l^2} \frac{\Delta\sigma}{\Delta\theta}\right)^{0.55} Pr_l^{1/3}\right]^{0.69} \left(T_w - T_{sat}\right)^{0.69} t^{0.69} \quad (2.19)$$

where $\Delta\sigma$ is the change of surface tension and $\Delta\theta$ the change of central angle of the bubble.

In the literature, two different concepts for bubble growth were discussed. First the bubble grows from the evaporation of the interface all around itself. The energy is supplied from the superheated liquid layer around the growing bubble. Mikic *et al.* [9] found a analytical solution for the bubble growth by introducing a geometric factor. With this factor the shape of the growing bubble is related to the perfect sphere and it takes into account the stored energy in a superheated liquid layer before the incipience.

$$R_b\left(t\right) = \left(\frac{12}{\pi}\right)^{1/2} \left\{1 - \frac{T_s - T_\infty}{T_s - T_{sat}} \left[\left(1 + \frac{t_w}{t}\right)^{1/2} - \left(\frac{t_w}{t}\right)^{1/2}\right]\right\} Ja \sqrt{\alpha \, t} \quad (2.20)$$

with the Jakob number as

$$Ja = \frac{\rho_l \, c_{p,l} \, \Delta T}{\rho_g \, h_{lg}} \quad (2.21)$$

where α is the thermal diffusivity, t_w the waiting time and T_∞ the temperature of the bulk liquid. If T_∞ equals T_{sat} and t_w is zero, the bubble radius will be zero, i.e., if there is no waiting time in between succeeding bubbles for the superheated thermal liquid layer to recover, no heat can conduct from the liquid into the bubble and no bubble can grow.

A second considered theory supports a liquid micro-layer at the bubble base between the vapour-liquid interface and the heater surface. Snyder and Edwards [100] were the first to introduce the micro-layer. The existence of the micro-layer with oscilla-

tion in the temperature measurements at nucleation sites was confirmed by Moore and Messler [101]. Cooper and Lloyd [102] confirmed the existence of the micro-layer under an isolated bubble for experiments under low pressure. High heat wall and bulk temperatures tend to promote the formation of a micro-layer. Organic liquids were boiled on glass or ceramic surfaces during experiments. The micro-layer thickness was estimated from temperature measurements with a thermocouple located on the heater surface. The local thickness of the micro-layer is said to be

$$\delta \propto C\sqrt{\nu_l \, t_g} \tag{2.22}$$

where ν_l is the kinematic viscosity, t_g the bubble growth time and $C = 0.8$ for theoretical predictions and between 0.5 and 1 for experimental observations.

Cooper and Lloyd [102] suggested the following two correlations for bubble growth, where the micro-layer evaporation is the main contribution

$$R_b(t) = 2.5 \, \frac{Ja}{Pr_l^{1/2}} \, \left(\alpha_l \, t\right)^{1/2} \qquad \text{(poorly conducting wall)} \tag{2.23}$$

$$R_b(t) = 1.12 \, \left(\frac{k_w \, \rho_w \, c_{p,w}}{k_l \, \rho_l \, c_{p,l}}\right)^{1/2} \, Ja \, \left(\alpha_l \, t\right)^{1/2} \qquad \text{(highly conducting wall)} \tag{2.24}$$

Lee and Nydahl [103] calculated the growth of spherical bubbles with a micro-layer, with the proposed thickness of Cooper and Lloyd [102]. They concluded that the evaporation from the micro-layer contributed significantly to the heat transfer.

The first to visualise the micro-layer was Jawurek [104]. A boiling chamber with a transparent base with parallel monochromatic illumination was used. The micro-layer reflects interference patterns similar to Newton's rings. For methanol and ethanol at system pressures between 0.2 and $0.5\,\mathrm{atm}$, heat fluxes between 30 and $100\,{}^{\mathrm{kW}}/_{\mathrm{m}^2}$ and subcooling between 0 and $20\,\mathrm{K}$, the thickness of the micro-layer at the outer edge of fully grown bubbles ranged from 0.2 to $0.8\,\mu\mathrm{m}$. No trends with varied parameters were

observed.

Plesset and Prosperetti [105] disagreed about the significance of the micro-layer and claimed a contribution from the micro-layer to the heat transfer during boiling of only $20\,\%$.

The experimental results of Kenning and Yan [54] are consistent with the micro-layer model and therefore the cooling of the wall during the bubble growth, but mention that further investigations are required.

Takagi and Yamamoto [106] took photographic images from the side and from the bottom during bubble growth from a micro-scale heater. Analysing the images and simultaneously acquiring local temperature fluctuations, they found that 70 to $80\,\%$ of the generated heat was taken away from the substrate by latent heat of vaporisation and approximately $10\,\%$ through bubble induced flow.

In order to improve the temporal and spatial resolution of temperature and heat flux measurements, Myers *et al.* [107] boiled FC-72 on a micro-heater array consisting of 96 platinum resistance heaters, micro-fabricated on a $500\,\mu\mathrm{m}$ thick silicon substrate. The heater array was $1 \times 1\,\mathrm{mm}^2$ in size. A control circuit was designed to keep the wall heat flux constant. For the studied conditions the micro-layer evaporation and contact-line heat transfer appeared not to be the main heat transfer mechanisms during pool boiling and contributed no more than $23\,\%$. Heat flux due to bubble coalescence only led to small spikes and the change in wall heat flux was small. However, they mentioned that the bubble departure time can be reduced due to the larger size of coalesced bubbles and lead indirectly to a higher wall heat flux.

Sodtke *et al.* [108] studied single bubble growth in a low gravity environment from a $10\,\mu\mathrm{m}$ thin, electrically heated, stainless steel foil covered with thin black tape and a top cover of a layer of thermochromic liquid crystals (TLC). TLC high-speed images have been converted to actual temperature distribution profiles of the downward facing substrate. The profiles indicated increased heat transfer through a temperature drop found near the micro-region, Fig. 2.4 left. The heat transfer in this region of a length in the order of $1\,\mu\mathrm{m}$ was 100 times stronger than in the circumjacent liquid.

A new model, which was qualitatively confirmed with experiments on a stainless steel heater foil in a micro-gravity environment, was developed by Stephan *et al.* [109]. A high resolution dynamic temperature profile was measured on the outside of the boiling substrate. They could show that during bubble growth and detachment period more heat was taken away by evaporation than was supplied to the overall system from the outside. Thus, the temperature in the liquid thermal boundary layer and the foil dropped, especially near the moving apparent 3-phase contact line at the bubble base. During bubble rise and waiting time more heat was supplied to the system then consumed by evaporation and the temperature in the foil and the liquid thermal boundary layer raised again. They concluded that all numerical nucleate boiling models should consider these temperature fluctuations. The single bubble subsystem and the significant phenomena in the micro-region is shown in Fig. 2.4.

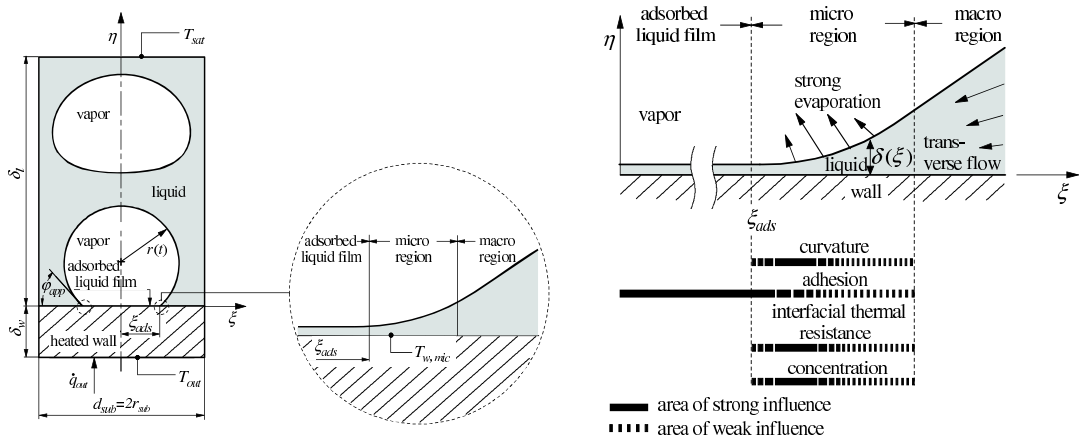

Figure 2.4: *Left: Schematical view of a bubble with macro- and micro-layer [5]. Right: Macro- and micro-layer including significant phenomena in the micro-region [5].*

Moghaddam and Kiger [110, 111] developed a new micro-fabricated device, discussed in more detail in section 2.3, to analyse the dynamics of heat transfer during the nucleation process in saturated FC-72. The study was complemented with simultaneous 8000 frames per second (fps) high-speed imaging. Comparisons of measured surface temperatures from sensors in different quadrants of the radially shaped sensor array at different surface temperature indicated that the temperature distribution during bubble growth is axial-symmetric. If apparent bubble contact areas measured from

high-speed images, taken during bubble growth, are compared with the surface temperature measurements, it can be concluded that the temperature drops at the moment the bubble/surface contact line passes by and micro-layer evaporation takes place. The temperature drop was measured for a second time when the contact line receded and the dried out surface below the bubble was rewetted with cold liquid. For the same wall superheat bubble growth with and without waiting time was observed. No reasons were given for this behaviour, however, a change of bubble shape during bubble growth was reported. The bubble shape was nearly hemispherical during the explosive bubble growth, which was not observed for the case without waiting time. For both cases the heat transfer contributions due to micro-layer evaporation, micro-region heat transfer, transient conduction and micro-convection were discussed. In both cases the micro-layer evaporation resulted in heat flux peaks over the contact area, however, the heat flux was half as high and with a time period of $1\,\mathrm{ms}$ much longer for the bubble growth without waiting time.

The high heat fluxes in the micro-region, reported by Sodtke *et al.* [108], were not observed, but this might be due to the short time period this mode contributed to the overall heat flux. The transient conduction is revealed during rewetting, when the contact line receded and was of the same order of magnitude for both cases. The determined heat flux resulting from transient conduction due to rewetting for the case without waiting time does not include the transient conduction still in progress after bubble formation. It is around $5\,\%$ of the total transient conduction and is negligible for the case with waiting time. Transient conduction started after the micro-layer evaporation, but before the bubble departure, when the contact line begins to recede and took mainly place at the bubble/surface contact area, which is about $0.5 \cdot D_d$. The micro-convection, due to bubble growth, enhances in an almost constant fashion the convection effect close to the contact line. It was significantly higher for the case with waiting time, supposedly due to higher growth rate and earlier departure of the bubble. Micro-layer evaporation, transient conduction and micro-convection were increased with increasing surface temperature, however, the increase was more significant for micro-convection. Micro-layer evaporation was found to be the smallest contribution to the total heat transfer from the surface and its contribution is decreas-

ing with increasing wall superheat. Transient conduction has the largest contribution for low superheats for the case with no waiting time. Micro-convection is largest for high superheats and has the least contribution for low superheats, except for the case with no waiting time. After comparing their results to other heat transfer models, e.g., [21, 31, 39, 47, 91], they pointed out that no exact agreement was found, despite the fact that individual components were predicted rather well. Moghaddam and Kiger proposed an altered model

$$\dot{q}'' = \phi\,\pi\,R_d^2\,N_a\left(\dot{q}''_{ME}\,\frac{t_m}{t_g+t_w}+\dot{q}''_{TC}\frac{t_r}{t_g+t_w}\right)+\left(1-\phi\,\pi\,R_d^2\,N_a\right)\dot{q}''_{MC} \tag{2.25}$$

with

$$\dot{q}''_{ME} = \rho_l\;\left(h_{lg}-C_1\,\Delta T\right)\;\overline{\delta}/t_m \tag{2.26}$$

$$\begin{aligned}\dot{q}''_{TC} = \frac{8\,k\,\Delta T_{TC}\,\nu}{3\,\sqrt{\pi\,\alpha}\,r_c^2\,t}\Big\{&r_c\,t_r^{3/2}-{}^2\!/_5\,\nu\,t_r^{5/2}+r_c\;\left(t^{3/2}-t_r^{3/2}\right)\\&-\left(r_c-\nu\,t_r\right)\;\left(t-t_r\right)^{3/2}-\frac{2\,\nu}{5}\;\left[\left(t^{5/2}-t_r^{5/2}\right)-\left(t-t_r\right)^{5/2}\right]\Big\}\end{aligned} \tag{2.27}$$

where ϕ is the ratio of contact area d_c and bubble projected area D_b, R_d the bubble departure radius, N_a the nucleation site density, t_m the micro-layer evaporation time, t_w the bubble waiting time, t_r the duration of the surface rewetting event, t_g the bubble growth time period, r_c the radius of the contact area, $C_1 = 1098.4\,{}^{\mathrm{J}}\!/_{\mathrm{kgK}}$ the coefficient for saturated FC-72 and $\overline{\delta}$ the average micro-layer thickness. However, Moghaddam and Kiger state that this model is not recommended for large surfaces, as bubble interactions probably add secondary effects, which are not included in the model yet.

Bubble departure The bubble departure diameter results from the balance of forces acting on the bubble. This includes the inertia of the liquid and vapour, the liquid drag on the bubble, buoyancy and surface tension. Fritz [112] proposed the following correlation which balances the surface tension and buoyancy acting on the bubble

$$D_d = 0.0208\ \phi \sqrt{\frac{\sigma}{g\ (\rho_l - \rho_g)}} \tag{2.28}$$

where ϕ is the contact angle in degrees. The correlation predicts the correct length scale, but many deviations are reported in the literature, especially for high pressure. Many more expressions obtained empirically or analytically reported in the literature are, however, not consistent. In some sources the bubble departure diameter is increasing with wall superheat, in others it is insensitive to or it even decreases with increasing wall superheat.

Cole [15] found for pressures between 60 and $760\,\mathrm{mmHg}$

$$D_d = 0.04 \sqrt{\frac{\sigma}{g\ (\rho_l - \rho_g)}}\ Ja \tag{2.29}$$

Kutateladze and Gogonin [13] and Jenson and Memmel [14] proposed correlations, where the departure diameter is a weaker function of the Jakob number Ja

$$D_d = \sqrt{\frac{0.0625\ \sigma}{g\ (\rho_l - \rho_g)}\ (1 + 10^5\ K_1)} \quad \text{(for } K_1 < 0.06\text{)} \tag{2.30}$$

and

$$D_d = \sqrt{\frac{0.0361\ \sigma}{g\ (\rho_l - \rho_g)}\ (1.8 + 10^5\ K_1)^{2/3}} \tag{2.31}$$

with

$$K_1 = \left(\frac{Ja}{Pr_l}\right)\left\{\left[\frac{g\ \rho_l\left(\rho_l-\rho_g\right)}{\mu_l^2}\right]\left[\frac{\sigma}{g\ \left(\rho_l-\rho_g\right)}\right]^{3/2}\right\}^{-1} \tag{2.32}$$

Gorenflo *et al.* [16] proposed for high heat fluxes

$$D_d = C_1\ \left(\frac{Ja^4\ k_l^2}{g}\right)^{1/3}\ \left[1+\left(1+\frac{2\ \pi}{3\ Ja}\right)^{1/2}\right]^{4/3} \tag{2.33}$$

The Jakob was defined in Eq. 2.21 and C_1 is a constant for different liquids.

Waiting time is the time period in between two bubbles when the superheated liquid layer around the nucleation site has to reform after a bubble has departed. Hsu and Graham [84] concluded from schlieren pictures that an area of twice the bubble departure diameter is influenced by bubble motion. Han and Griffith [32, 33] obtained an analytical expression for the waiting time by assuming the liquid layer to be semi-infinite and by substituting the expression for the thermal layer thickness from the wall superheat

$$\Delta T = \left(\frac{4\ f_1\ \sigma\ T_{sat}}{\rho_g\ h_{lg}\ D_c}\right)\left[1-\frac{f_2\ D_c}{f_1\ 2\ \delta}\right] \tag{2.34}$$

where f_1 and f_2 are functions of the contact angle ϕ and D_c is the cavity mouth diameter. This results in

$$t_w = \left[\frac{f_2\ D_c}{2\ \sqrt{\pi\ \kappa_l}\ f_1\ \left(1-\frac{4\ f_1\ \sigma\ T_{sat}}{\Delta T\ \rho_g\ h_{lg}\ D_c}\right)}\right]^2 \tag{2.35}$$

The waiting time will first decrease and then increase with cavity size. However, it will continuously decrease as the wall superheat is increased.

Bubble departure frequency The bubble departure frequency represents the inverted sum of bubble growth time and waiting time. Jakob and Fritz [18] proposed for water and hydrogen

$$f \cdot D_d = 0.078 \tag{2.36}$$

Zuber et. al [19] also suggested a correlation, where $f \cdot D_d$ is constant.

$$f \cdot D_d = 0.59 \left[\frac{\sigma \; g \; (\rho_l - \rho_g)}{\rho_l^2} \right]^{1/4} \tag{2.37}$$

However, in the correlation of Mikic and Rohsenow [31] the product of frequency and departure diameter is not constant with increasing wall superheat

$$f^{1/2} \cdot D_d = \left(\frac{4}{\pi} \right) \; Ja \; \sqrt{3 \; \pi \; \alpha_l} \left[\left(\frac{t_g}{t_w + t_g} \right)^{1/2} + \left(1 + \frac{t_g}{t_w + t_g} \right)^{1/2} - 1 \right] \tag{2.38}$$

where t_g is the bubble growth time.

If bubble departure frequencies are determined from predicted growth and waiting times, the results are in poor agreement with experimental measurements. Usually, growth models only consider evaporation at the bubble base or at the liquid/vapour interface of the bubble, but interactions between nucleation sites can strongly influence the bubble waiting time. This could be the reason for the discrepancies observed when predicting bubble departure frequencies. Furthermore, larger cavities produce larger bubbles, which changes the bubble growth time and the bubble shape is also continuously changing during growth.

2.2.6 Nucleation site interaction and bubble coalescence

Zuber [19] divided nucleate boiling into two regions, the regime of isolated bubbles and the region of interference. The isolated bubble regime in nucleate pool boiling has been discussed in many publications [51]. In this regime, bubbles are produced intermittently and do not interfere with each other. When the wall superheat increases, the waiting time between the nucleation of a new bubble and the departure of the previous bubble, grown from the same site, becomes shorter. If a certain critical temperature is reached, succeeding bubbles merge to form a mushroom-like bubble. This merger can also involve pairs, consisting of a large bubble followed by a small one, departing from the same nucleation site. This is known as the region of interference; bubbles interfere with each other and form continuous vapour columns and patches.

Buyevich and Webbon [113] investigated the limit of the isolated bubble regime. They identified four contributing mechanisms that lead to this limit, a) the upward flow of the rising bubble, which obstructs the downward flow of liquid required to compensate for the vapour removal from the wall, b) lateral coalescence of bubbles from several nucleation sites to form large bubbles and extended vapour patches on the surface, c) longitudinal coalescence close to the wall, which results in the departure of dissimilar sized bubble pairs as mentioned before, d) longitudinal coalescence in the bulk, which leads to the formation of vapour columns. Buyevich and Webbon identified the last case as the most important effect for the termination of the isolated bubble region, as it can lead to the boiling crisis and trigger the critical heat flux.

Chekanov [114] was the first to conduct experiments with two artificial nucleation sites spaced close enough to make interactions between nucleation sites visible. The artificial nucleation sites were created by two heated copper rods in contact with a perm-alloy plate immersed in water. The time between two departed bubbles from neighbouring nucleations sites followed a gamma distribution. He introduced three regions of interaction determined by the dimensionless cavity spacing S/D_d, where S is the distance between two cavity centres and D_d the bubble departure diameter.

- $S/D_d < 3$: The formation of a bubble at one nucleation site inhibits the formation of a vapour bubble at the neighbouring nucleation site.
- $S/D_d > 3$: The formation of a bubble at one nucleation site promotes the formation of a vapour bubble at the neighbouring nucleation site.
- $S/D_d >> 3$: No interaction between two nucleation sites is taking place.

Chekanov suggested acoustic and hydrodynamic effects as responsible mechanisms for the observed inhibition and promotion of bubble growth from closely spaced nucleation sites.

Judd *et al.* [49, 115–117] studied in their experiments interaction phenomena between adjacent nucleation sites. They used a transparent glass surface, $3.6\,\mathrm{mm}$ thick and coated with a $0.3\,\mu\mathrm{m}$ stannic oxide layer, acting as heater. To decrease the number of active nucleation sites, to increase the bubble size and to prevent any damage of the boiling surface, the system pressure was reduced. Like Chekanov they introduced three regions of interaction between nucleation sites:

- $S/\overline{D_d} < 1$ "promotive" region: When a nucleation site that is unable to capture vapour nuclei lies within the area influenced by a continually active nucleation site that can deposit or "seed" vapour nuclei in it, bubbles will form at the adjacent nucleation site more frequently than would otherwise be the case.
- $1 < S/\overline{D_d} < 3$ "inhibitive" region: When a nucleation site that is unable to capture vapour nuclei lies within the area influenced by an intervening active nucleation site capable of depositing/displacing nuclei in it, that is itself under the influence of a continually active nucleation site, bubbles will form at the adjacent nucleation site less frequently than would otherwise be the case.
- $S/\overline{D_d} > 3$ "independent" region: When bubble formation at one nucleation site is in no way influenced by bubble formation at another nucleation site.

Judd *et al.* suggested the mechanism of "site seeding" as responsible for these phenomena.

Kenning and Yan [54] investigated temperature fluctuations in the heated wall during bubble growth. A direct electrically heated stainless steel plate was immersed in water. The plate, $0.13\,\mathrm{mm}$ thick and $46 \times 103\,\mathrm{mm}^2$ in cross-section, was carefully cleaned and the surface was well wetting, with a contact angle less than $20\,^\circ$. The water was degassed in a separated tank, but since the boiling chamber was opened to the atmosphere, the amount of dissolved gas was uncertain. On the back of the plate a TLC layer, which had a visual colourplay from 104 to $123\,^\circ\mathrm{C}$, was deposited. The importance of wall temperature variations for bubble growth and activity of nucleation sites was confirmed. The cooling effect on the wall surface was considerable. It was limited to the maximum contact area of the bubble on the heated surface. The cooling effect decreased closer to the outer limit of the "area of influence". They concluded that nucleation sites inside the maximum occurring diameter of a growing bubble influence each other through thermal fluctuations on the wall surface. This interaction caused intermittency that had a large influence on the productivity of bubbles at the sites.

Golobič and Gjerkeš [118] activated nucleations sites with a laser beam (diameter of heated spot area between 1.66 and $5.23\,\mathrm{cm}$) on a $25\,\mu\mathrm{m}$ thin copper or titanium foil immersed in saturated water. The laser power output was tuned with an attenuator. The applied heat flux was up to $560\,{}^{\mathrm{kW}}/_{\mathrm{m}^2}$. Spacings between the three or four simultaneously active nucleation sites were ranging from 2.6 to $4.1\,\mathrm{mm}$. They concluded that interactions between two artificially activated sites decrease the overall activity of both sites. The activity at both sites may decrease or increase at one site and simultaneously decrease at the other. If there is more than one active site in its vicinity, they influence each others activity.

Zhang and Shoji [6] conducted experiments on a thin silicon surface with a thickness of $0.2\,\mathrm{mm}$ and a diameter of $15\,\mathrm{mm}$ with cylindrical artificial cavities $10\,\mu\mathrm{m}$ in diameter and $80\,\mu\mathrm{m}$ deep. The cavities where arranged as single or twin cavities with different spacing of 1, 2, 3, 4, 6 and $8\,\mathrm{mm}$. Boiling liquid was distilled water and the silicon surface was heated by Nd:YAG laser irradiation. Temperature fluctuations were measured beneath and around cavities with radiation thermometers (spatial resolution $120\,\mu\mathrm{m}$, temperature resolution $0.08\,\mathrm{K}$ and temporal resolution $3\,\mathrm{ms}$). All pictures

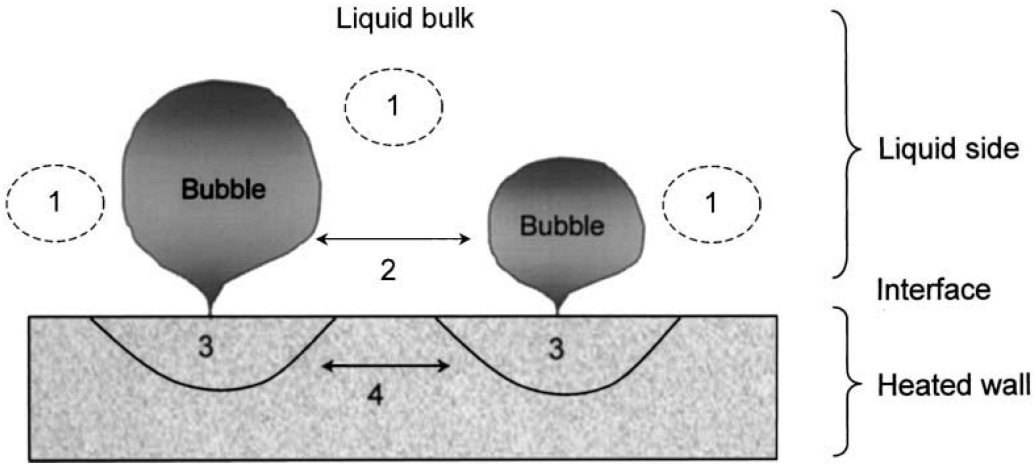

Figure 2.5: *Effect factors of nucleation site interaction: 1. Hydrodynamic interaction between bubble and liquid bulk, 2. Hydrodynamic interaction between bubbles, 3. Thermal interaction between nucleation site and heated wall and 4. Thermal interaction between nucleation sites, Zhang and Shoji [6].*

were captured with a high-speed camera ($1297\,\mathrm{fps}$). In Figure 2.5 the effect factors of nucleation site interactions from this experiments are summarised and illustrated by Zhang and Shoji. Interaction 1 and 3 can be found in single and multiple cavity experiments, whereas interaction 2 and 4 can only be found in multiple cavity conditions.

From their experiments Zhang and Shoji found three crucial effect factors:

A Hydrodynamic interaction between bubbles.

B Thermal interaction between nucleation sites.

C Horizontal and declining bubble coalescence.

They proposed four intensity regions for the three effect factors. An overview can be found in Table 2.1. In the 'I' region ($S/\overline{D_d} > 3$) none of the three interactions can be observed, meaning that the two artificial cavities are independent and behave like single cavities would. The 'H' region ($2 < S/\overline{D_d} \leq 3$) is influenced by the factor A and has a higher bubble departure frequency than region 'I'. In the 'H+T' region

Table 2.1: *Influence intensity of 3 effect factors of nucleation site interaction for different ratios of $S/\overline{D_d}$, Zhang and Shoji [6].*

Main effect factors	$S/\overline{D_d}$				
	Effect on $\overline{f}$	$S/\overline{D_d} > 3$	$2 < S/\overline{D_d} \leq 3$	$1.5 < S/\overline{D_d} \leq 2$	$S/\overline{D_d} \leq 1.5$
Hydrodynamic interaction between bubbles (A)	promotive	×	○	○	○
Thermal interaction between nucleation sites (B)	inhibitive	×	×	○	○
Horizontal and declining bubble coalescence (C)	promotive	×	×	×	○

×: negligible; ○: should be considered

($1.5 < S/\overline{D_d} \leq 2$) effect A and B are both dominant. The dominance of the effect B leads to a lower bubble departure frequency. In region 'H+T+C' ($S/\overline{D_d} \leq 1.5$) all the three effects have an influence on the behaviour of the process resulting in an increased bubble departure frequency. However, the authors point out that the influence range of thermal interactions is also related to the thermal properties and the thickness of the boiling substrate.

Nimkar *et al.* [119] compared different spacings between artificial micro-pyramidal, re-entrant cavities, with a characteristic size of $40\,\mu\mathrm{m}$ etched in silicon, during boiling from vertically oriented surfaces immersed in saturated FC-72 under atmospheric pressure. For a spacing of $0.5\,\mathrm{mm}$ the boiling substrate underperformed compared to a plain surface, what the authors believe is caused by nucleation site interactions. The second surface ($S = 0.75\,\mathrm{mm}$) showed the highest heat transfer augmentation. Bubble departure diameter and frequency were increased with higher applied heat fluxes. No effect of cavity spacing on departure diameter and frequency was found. However, the density of active nucleation sites was strongly affected by the spacing and decreased with decreasing heat flux. A cavity spacing in the region of $0.75\,\mathrm{mm}$ was suggested as optimum and most of the artificial nucleation sites stay active for a wide range of heat fluxes.

Direct bubble/bubble interaction or bubble coalescence was classified by Williamson and El-Genk [120] and Buyevich and Webbon [121] into three different types:

a) Lateral coalescence far away from the heated wall, which had no effect on boil-

ing heat transfer.

b) Vertical coalescence between consecutive bubbles near the wall.

c) Lateral coalescence between adjacent bubbles near the wall.

Yang *et al.* [122] confirmed the three types with a numerical simulation. Zhang and Shoji [6] proposed a forth type:

d) Lateral coalescence between adjacent declining bubbles near the wall.

Types c) and d) are important for the heat transfer, but only occur when the distance between two nucleation sites is less than 1.5 times the bubble departure diameter.

Bonjour *et al.* [123] characterized the thermal effect of coalescence by conducting experiments with artificial nucleation sites. A duraluminium (AU4G) vertical, heated boiling surface was immersed in either pentane, to study the influence of coalescence on the boiling curve and bubble departure diameter as a function of the wall superheat, or R-113 for the study of the influence of coalescence on bubble frequency. Heat fluxes between 0.1 and $1\,{}^{\mathrm{kW}}/_{\mathrm{cm}^2}$ or wall superheats between 5 to $35\,\mathrm{K}$ were applied. For moderate heat fluxes, the bubble frequency decreased, but for low or high heat fluxes it increased. Coalescence improved the heat transfer coefficient, which was attributed to a supplementary micro-layer evaporation, forming below two merging bubbles. However, the highest heat transfer coefficient was measured for an optimal site distance, where no coalescence took place.

2.3 Integrated micro-heaters and temperature micro-sensors

The first micro-fabricated temperature sensors were reported in the literature with the emerging semiconductor technology, e.g., [124–133]. One of the first boiling substrate with integrated temperature sensors and heater was fabricated by Miller [134]. On

the non-planar walls of inverted pyramids, used as artificial cavities and etched on a $1.27 \times 1.27\,\mathrm{cm}^2$ silicon boiling substrate, 81 temperature micro-sensors with a size of $12 \times 24\,\mu\mathrm{m}^2$ were fabricated. These micro-sensors were the smallest, and the number of sensors per area was the largest, found in the known literature at the time. Three types of sensors were fabricated, a Si-RTD, a diode sensor and a germanium thin film thermistor. The sensors were connected to a pin-grid by gold wire bonding. A titanium film resistance heater was deposited on the back of the silicon. The substrate was placed vertically inside a boiling chamber filled with FC-72. The magnitude of temperature fluctuations observed during bubble growth was 0.5 to $1.5\,^\circ\mathrm{C}$. A frequency analysis indicated that the dominant bubble departure frequency was insensitive to changes in heat flux. The average frequency was $27.6\,\mathrm{Hz}$ with a standard deviation of $3.2\,\mathrm{Hz}$.

Rule and Kim [60] used a micro-fabricated device with an array of 96 temperature-controlled heaters to investigate the heat transfer behaviour during pool boiling using FC-72. The array provided a controlled local heat flux and measured the temperature during boiling at the same time. The array of 96 platinum resistance heaters was deposited on a quartz wafer. Each element had an area of $0.26 \times 0.26\,\mathrm{mm}^2$, a nominal resistance of $1\,\mathrm{k}\Omega$ and a nominal temperature coefficient of resistance of $0.002\,^\circ\mathrm{C}^{-1}$. With this array it was possible to keep the superheat on the boiling surface constant by controlling the power output of each heater element individually by detecting resistance changes due to temperature changes caused by bubble growth. As artificial nucleation sites were not fabricated, bubble growth could occur anywhere on the heated surface.

The same heater array was adopted by Yin *et al.* [135], but they only used one heater. Bubble growth experiments in FC-72 for heat fluxes between 3 and $44\,\mathrm{MW/m^2}$ were conducted. The heater was pulse powered for periods between 1 and $10\,\mathrm{ms}$. For low heat fluxes, a single bubble formed rapidly, then started to decrease in size and stabilised while still attached to the heater surface. For high heat fluxes, a thin layer of vapour formed initially, shrank and was followed by high vapour production. It was concluded that due to the quick growth at higher heat fluxes, not enough thermal energy was stored in the surrounding liquid to sustain a bubble on the heater surface.

More experiments using the same temperature-controlled array of micro-heaters are described in [59, 66, 69, 107, 136–139].

Moghaddam *et al.* [140] developed a novel $60\,\mu\mathrm{m}$ thick dual-layer silicon and benzocyclobutene test section with an array of 44 embedded temperature micro-sensors. The Ni/Cr sensors were distributed radially around three artificial cavities with diameters of 0.7, 1.3 and $2.4\,\mu\mathrm{m}$ and covered a circle with a diameter of $1\,\mathrm{mm}$. The radial resolution of the sensors was 22 to $44\,\mu\mathrm{m}$ and each of them had a nominal resistance of $1\,\mathrm{k}\Omega$. The array was heated with a $3 \times 3\,\mathrm{mm}^2$ chromium heater, deposited on an Al layer. They successfully measured the temperature distribution in the substrate during bubble growth in degassed FC-72. The results were already discussed in detail in section 2.2.5.

2.4 Conclusions

Since nucleate pool boiling research has its origins in the early 20$^{\text{th}}$ century, the amount of available publications is vast. In consequence of its long history many contradictions between models, experiments and authors remain. Irakli G. Shekriladze [141] recently concluded: "A history of boiling heat transfer research represents an impressive example how unwillingness to deconstruct internal contradictions of applicable approaches leads to theoretical deadlock." However, the reason for the high number of controversies is more likely to be found in the characteristics of boiling being a very complex and elusive process. This and the continuous effort of going behind the involved physics during nucleate boiling, proven by the amount of publications these days, keep boiling research challenging and interesting.

An overview of the important subjects concerning this study are given. These are mainly nucleate boiling mechanisms, bubble dynamics and interactions between bubbles, liquid and boiling substrate including nucleation sites. Nevertheless, the reader may keep in mind that this literature review does not claim to be complete.

Chapter 3
Experimental setup

This chapter describes the design, assembly and commissioning of the experimental setup built for this experimental study. The main objective of the setup was to successfully conduct nucleate pool boiling experiments on silicon substrates with integrated temperature micro-sensors and a heater over a wide range of conditions and to investigate bubble growth, nucleation and interaction from artificial cavities distributed on the boiling substrate. Other specifications for the experimental setup were to prevent any contamination from the ambient environment and to use only materials, which in contact with the boiling liquid are non-corrosive and undissolvable. The amount of fluid used to conduct experiments had to be kept minimal due to its high price. The test section had to be completely immersed in the boiling liquid to allow experiments at different pressures and saturated temperatures. It was important to design the boiling chamber as accessible as possible to allow rapid alternations between different test sections. The same applies to the jig holding the silicon device in place.

3.1 Experimental apparatus

The designed and completed experimental rig is shown in Fig. 3.1. The setup was built into an aluminium frame from suitable materials to prevent any contamination by corrosion or other impurities, such as dissolved molecules from insulations and gaskets. The used materials are stainless steel, synthetic ethylene propylene diene momomer (EPDM), borosilicate glass, medical silicone rubber, neoprene rubber, polytetrafluoroethylene (PTFE) and polyaryletheretherketone (PEEK™). The system is designed to withstand a pressure range from 0.5 to $3\,\mathrm{bar}$ and temperatures between $0\,^{\circ}$ and $160\,^{\circ}\mathrm{C}$.

The main part of the setup is the boiling chamber (Cortassa & Co.), Fig. 3.2. The boiling chamber has four borosilicate glass windows (Borofloat®33, Schott Jenaer Glas

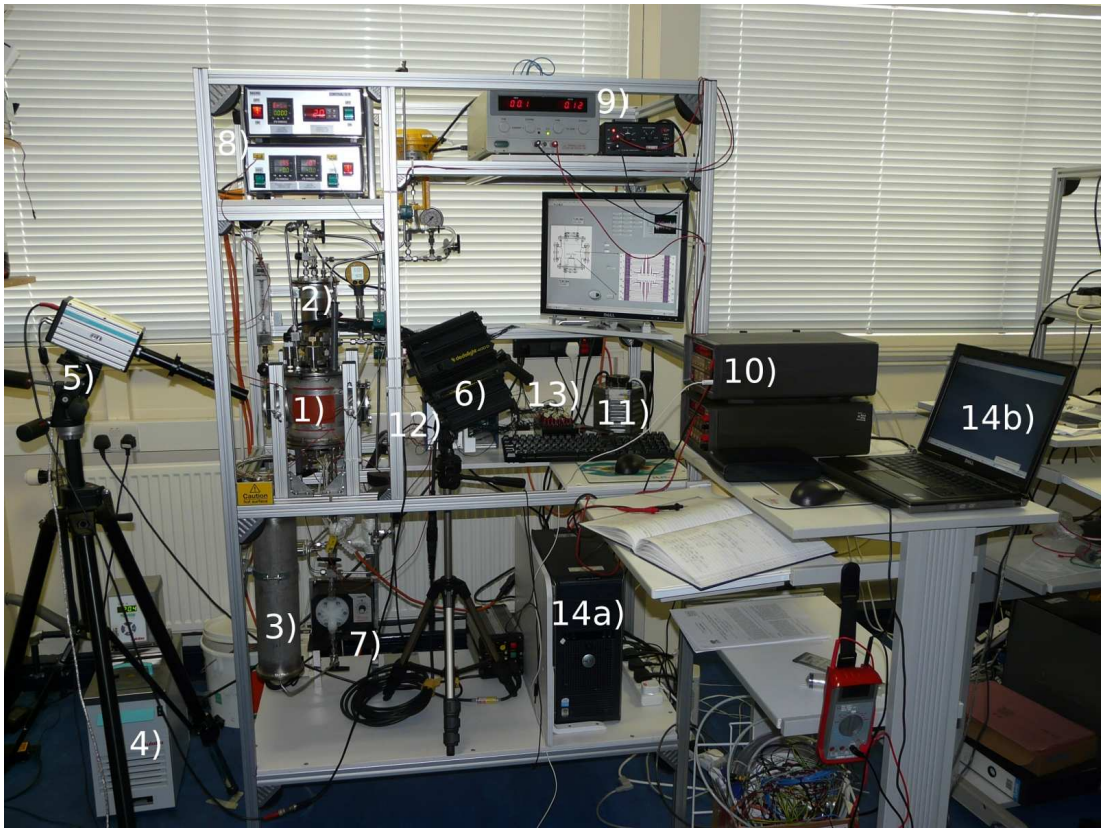

Figure 3.1: *Photograph of the experimental setup including: 1) Boiling chamber, 2) Condenser, 3) Reservoir, 4) Heating bath, 5) High-speed camera, 6) Backlight, 7) Pump, 8) Control system, 9) Power sources, 10) High precision A/V meter, 11) Voltage variac, 12) Data acquisition system (DAQ), 13) Current sources, 14a) PC for DAQ, 14b) PC for high-speed imaging.*

GmbH), which allow optical access to the boiling substrate. To reduce heat losses through the boiling chamber wall two temperature controlled, small flexible silicone rubber insulated resistance heaters (SRFG series, Omega Engineering Ltd.), with a maximum power output of $320\,\mathrm{W}$ were wrapped around it. Four heater cartridges (Cartridge heater, RS Components Ltd.) with a maximum power of $880\,\mathrm{W}$, were implemented into the bottom lid of the chamber. The power was controlled with a voltage variac (Chemical Technology & Chemical Engineering) and always held below $190\,\mathrm{W}$ ($110\,\mathrm{V}$) to prevent the boiling liquid from decomposing, see section 3.5 for more details. These heater cartridges are used to degas the boiling liquid and to heat it up to the saturation temperature. Two T-type thermocouples (TMTSS-IM050U-150, Omega En-

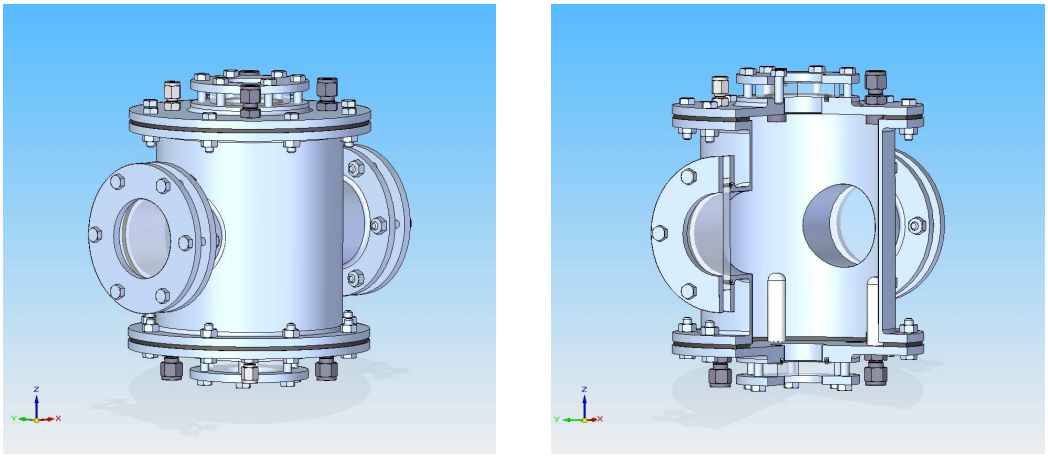

Figure 3.2: *Left: Schematic 3D view of the stainless steel boiling chamber with connection fittings and 4 borosilicate glass windows. Right: Schematic 3D view of the inside of the stainless steel boiling chamber with 2 of 4 cartridge heaters visible.*

gineering Ltd.) were used to measure the vapour and liquid temperature. Initially the pressure inside the boiling chamber was measured with a pressure transducer (PX603, Omega Engineering Ltd.) connected to the data acquisition system (DAQ) system, for more details see section 3.3. Later this transducer was replaced with a digital manometer (Leo2, Keller Druck AG). The boiling substrate was positioned inside the boiling chamber and all its necessary wires connected to the ambient with three sealed feedthroughs (Amatron Ltd.) implemented into the top lid of the chamber.

The vapour is led through stainless steel piping (SS-T4-S-035-6ME, Swagelok™) with $^1/_4$-inch outer diameter to the external condenser (Cortassa & Co.), Fig. 3.3. The condenser and the condenser coil within were built from stainless steel. The condenser is connected to a heating bath (F12-EH, Julabo Labortechnik GmbH) with adjustable cooling water temperature and flow, which allowed to control the condenser performance and therefore the system pressure by adjusting these two properties and the power input from the support heating system. A T-type thermocouple (TMTSS-IM050U-150, Omega Engineering Ltd.) was installed to monitor the condensate temperature. From the bottom of the condenser, the boiling liquid is led back into the boiling chamber by gravitation. The boiling fluid circulation is solely due to evaporation and condensation and no pump was needed.

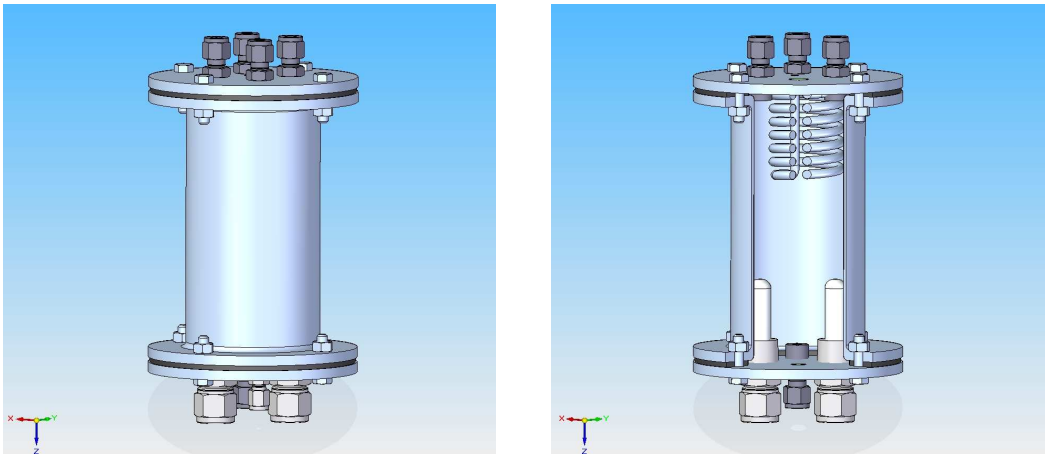

Figure 3.3: *Left: Schematic 3D view of the stainless steel condenser with connection fittings. Right: Schematic 3D view of the inside of the stainless steel condenser including the stainless steel coil.*

For safety reasons both, the boiling chamber and the condenser have a pressure gauge (110-826, RS components Ltd.) and a low pressure relief valve (SS-RL3S4, Swagelok™) installed.

More detailed technical drawings of the boiling chamber and the condenser and a process flow diagram can be found in appendix A.

3.2 Test sections

During this study three different generations of boiling substrates were fabricated and used for experiments. All substrates were fabricated from 3-inch ($76.2\,\mathrm{mm}$) double-side polished n-type (100), single-crystalline silicon wafers with a thickness of $380\,\mu\mathrm{m}$. The measured average surface roughness for an area of $25 \times 25\,\mu\mathrm{m}^2$ of the finished top surface, where boiling will take place, is $0.5\,\mathrm{nm}$. An image of the surface roughness measurement of a third generation silicon device is presented in Fig. A.15 in appendix A. The test sections were held in place by jigs, which had to be altered for each generation of the chip. The design of the boiling substrates and the corresponding jigs are described in the following three sections 3.2.1, 3.2.2 and 3.2.3.

3.2.1 First generation

On the substrate of the first generation 45 cylindrical cavities were etched into the substrate, using deep reactive ion etching (DRIE), based on the Bosch process, Fig. 3.4. The cavities have a diameter of $2\,\mu\mathrm{m}$. Due to the etching process there are holding marks, whose depths were measured as $22\,\mu\mathrm{m}$. The wafer is heated from the back with a separate heater, covering a circular area with a diameter of $50.8\,\mathrm{mm}$. Inside the boiling chamber the silicon boiling substrate is placed in a PTFE jig, which stands on three adjustable stainless steel legs, Fig. 3.5. Between the table and the silicon wafer a kapton insulated resistance heater (KH-303/10, Omega Engineering Ltd.) is positioned and connected to the power supply. The maximum power output is $31.4\,\mathrm{W}$ ($1.55\,\mathrm{W/cm^2}$). The wall temperature of the boiling substrate was not measured during boiling experiments. This test section was mainly used for the commissioning of the experimental setup. However, the first bubble growth was measured and these preliminary results are presented in section C.1, in appendix C.

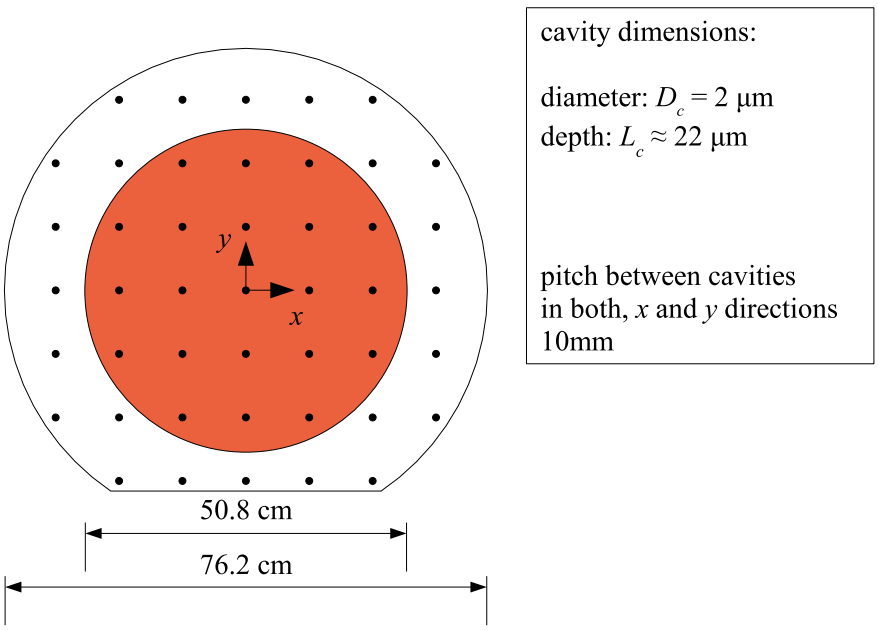

Figure 3.4: *Arrangement of the 45 cavities etched with DRIE, based on the Bosch process, on a 0.38 mm thick silicon wafer. The coloured area (inner circle) indicates the heated area.*

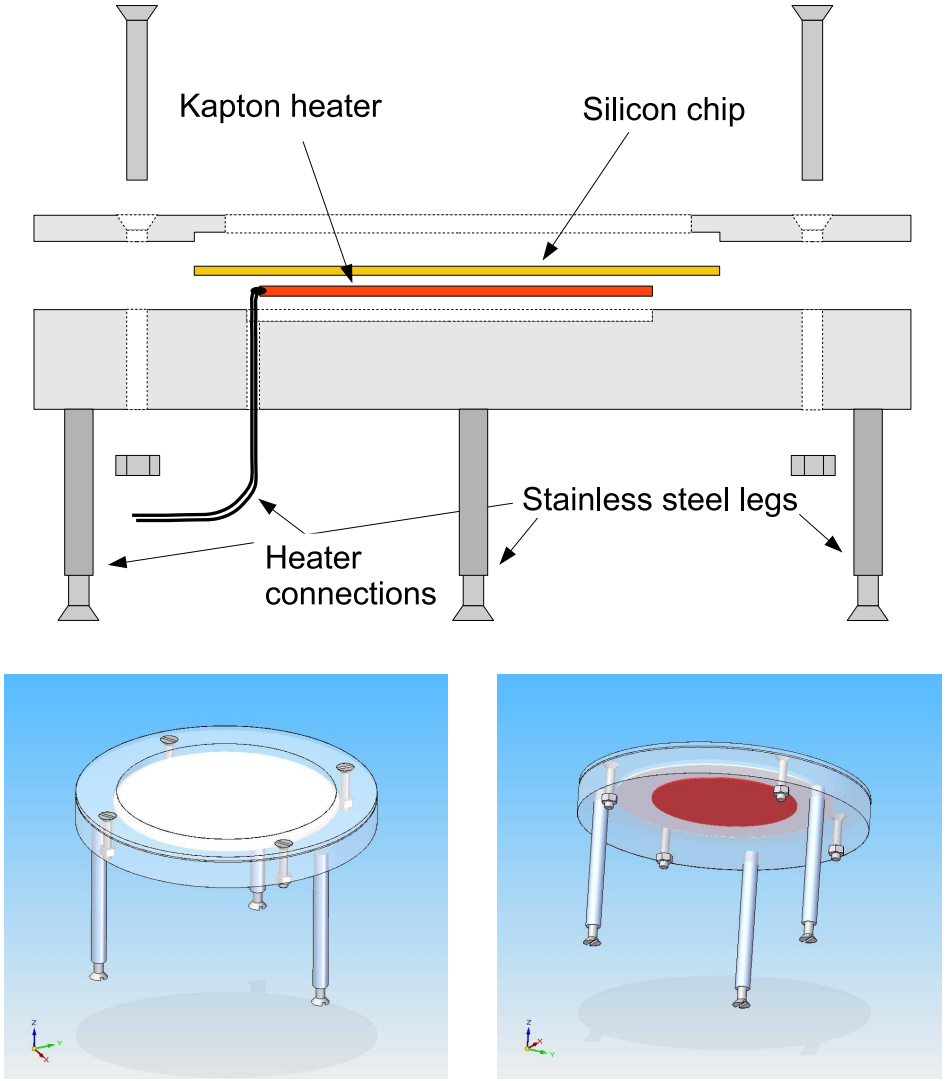

Figure 3.5: *Top: Schematic concept of the jig of the first generation test section. Bottom left: 3D view from the top of the jig holding the first generation test section. Bottom right: 3D view from the bottom of the jig holding the first generation test section. (PTFE transparent for better visibility).*

3.2.2 Second generation

The fabrication of the silicon chip of the second generation started from a 3-inch wafer. A thermal silicon dioxide layer of $0.3\,\mu\mathrm{m}$ was grown on both sides of the wafer to electrically isolate the temperature sensors from the silicon substrate on the back side of the wafer and to prevent any damage occurring to the front side of the wafer during the fabrication, Fig. 3.6 (a). A lift-off process was used to form temperature sensors on the back side of the wafer. A negative photo-resist AZ5214E was used to define sensor tracks, and the patterned photo-resist was then used as a shadow mask for the subsequent Ti/Ni deposition, as shown in Fig. 3.6 (b). A combined $0.02\,\mu\mathrm{m}$ Ti and $0.25\,\mu\mathrm{m}$ Ni layer was then deposited using a Balzers BAS450M sputterer, Fig. 3.6 (c). The wafer was immersed in acetone solvent, followed by ultrasonic agitation. The photo-resist dissolved in the acetone and the thin metal film on top of the photo-resist broke into small pieces and was carried away by acetone, as shown in Fig. 3.6 (d). The lift-off process finished with a DI (deionised) water rinse (15 minutes) and wafer drying. A $3\,\mu\mathrm{m}$ plasma enhanced chemical vapour deposition oxide (PECVD) layer was deposited on Ti/Ni layers using STS PECVD Multiplex, and a Presi E460 employed to planarise the surface using chemical mechanical polishing (CMP) technology, Fig. 3.6 (e). To create the Al heater, a $1\,\mu\mathrm{m}$ layer of Al was deposited using a Balzers sputterer and patterned using a Karl Suss MA8 wafer aligner with the Al being dry etched using a STS RIE metal etcher. PECVD oxide was then deposited on the heater and the top surface, planarised using CMP, Fig. 3.6 (f). The silicon dioxide layer on the front side of the wafer was then dry etched using a Plasmatherm PK 2440 RIE etcher, Fig. 3.6 (g). The cavities were then patterned using a thick photo-resist SPR220-7 ($7\,\mu\mathrm{m}$) and were etched using a STS Multiplex ICP deep etcher, Fig. 3.6 (h). The nominal depth of the cavities was controlled by the etching time, so all the cavities on the chip had the same depth. Three different versions of the chip were fabricated, with nominal cavity depths of 40, 80 and $100\,\mu\mathrm{m}$. The test devices were completed by removing the photo-resist and dicing the wafer.

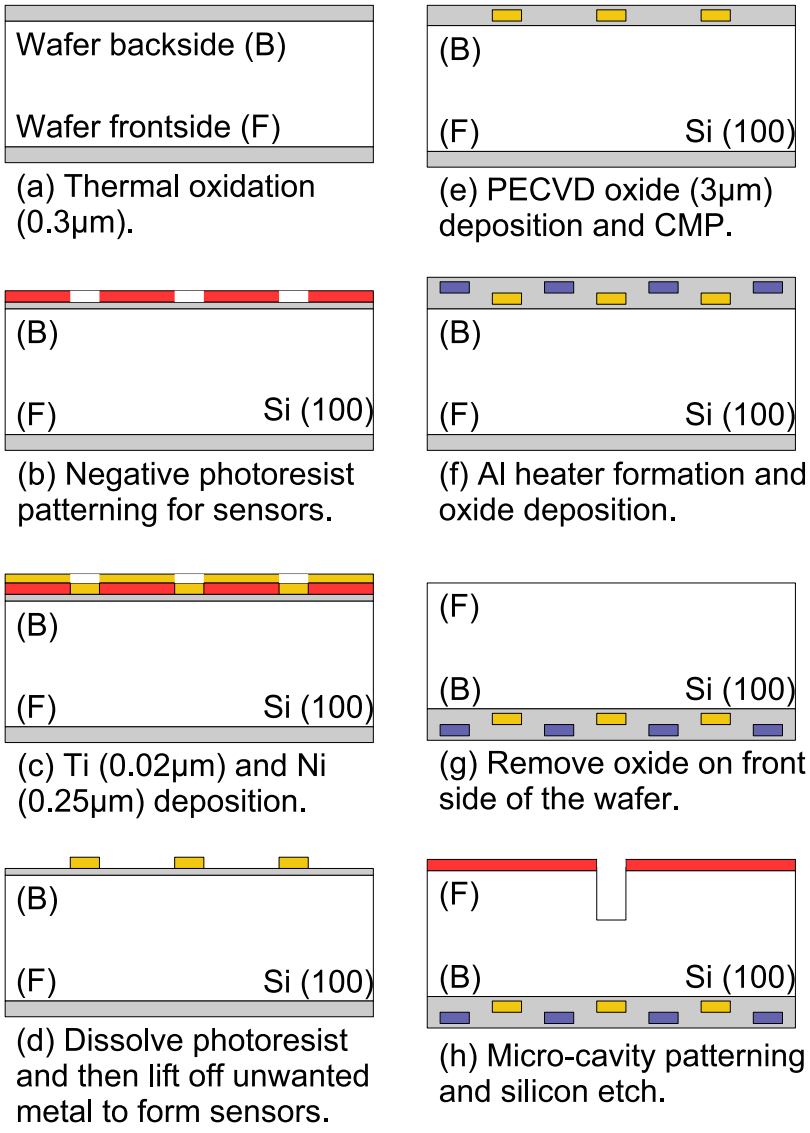

Figure 3.6: *Fabrication sequence of the second generation test section. Fabrication includes micro-cavities, integrated temperature micro-sensors and an integrated resistance heater.*

Figure 3.7 shows the arrangement of the heater, the five sensors and the connection pads on the silicon wafer. The artificial cavities etched into the boiling substrate are located above the geometrical centre of each sensor. The chip size was $19 \times 39.5\,\mathrm{mm}^2$, whereas the heater has a size of $15 \times 10\,\mathrm{mm}^2$. The heater has a serpentine layout with 17 turns. Each sensor has four connections, with two used to pass a constant current through the sensor and the remaining two to measure the voltage change due to varying temperature and resistance. This configuration allows a ”four point” resistance

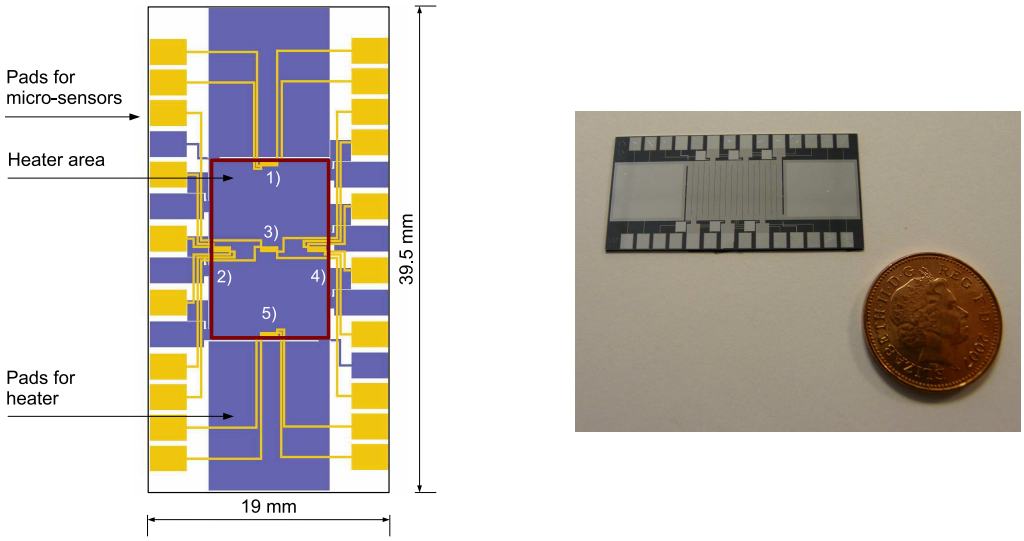

Figure 3.7: *Left: Schematic rear-view of the second generation silicon device, with 5 sensors and one cavity located above each of them. Right: Photograph of the back side of the second generation silicon device.*

measurement with a higher accuracy. The second generation micro-sensors cover an area of $435 \times 1500\,\mu\mathrm{m}^2$ and have a serpentine layout with 13 turns. At each sensor a cavity with different nominal mouth diameter was etched 1) $2\,\mu\mathrm{m}$, 2) $5\,\mu\mathrm{m}$, 3) $10\,\mu\mathrm{m}$, 4) $20\,\mu\mathrm{m}$ and 5) $50\,\mu\mathrm{m}$. A jig with spring probes (P6FS, Coda Systems Ltd.) was used to provide electrical connection to each pad. These probes were embedded in a $49 \times 69.5 \times 10\,\mathrm{mm}^3$ PTFE plate with the chip being held in position with a polycarbonate frame tightened down from the top with 12 screws, Fig. 3.8. Between the PTFE plate and the polycarbonate frame a thin medical silicone rubber gasket was placed to seal the gap between the silicon device and frame. This gap can act as artificial nucleation cavity and disturbing secondary bubble growth was reduced remarkably after the sealing was implemented.

More detailed technical drawings of the silicon device layout and the jig can be found in appendix A.

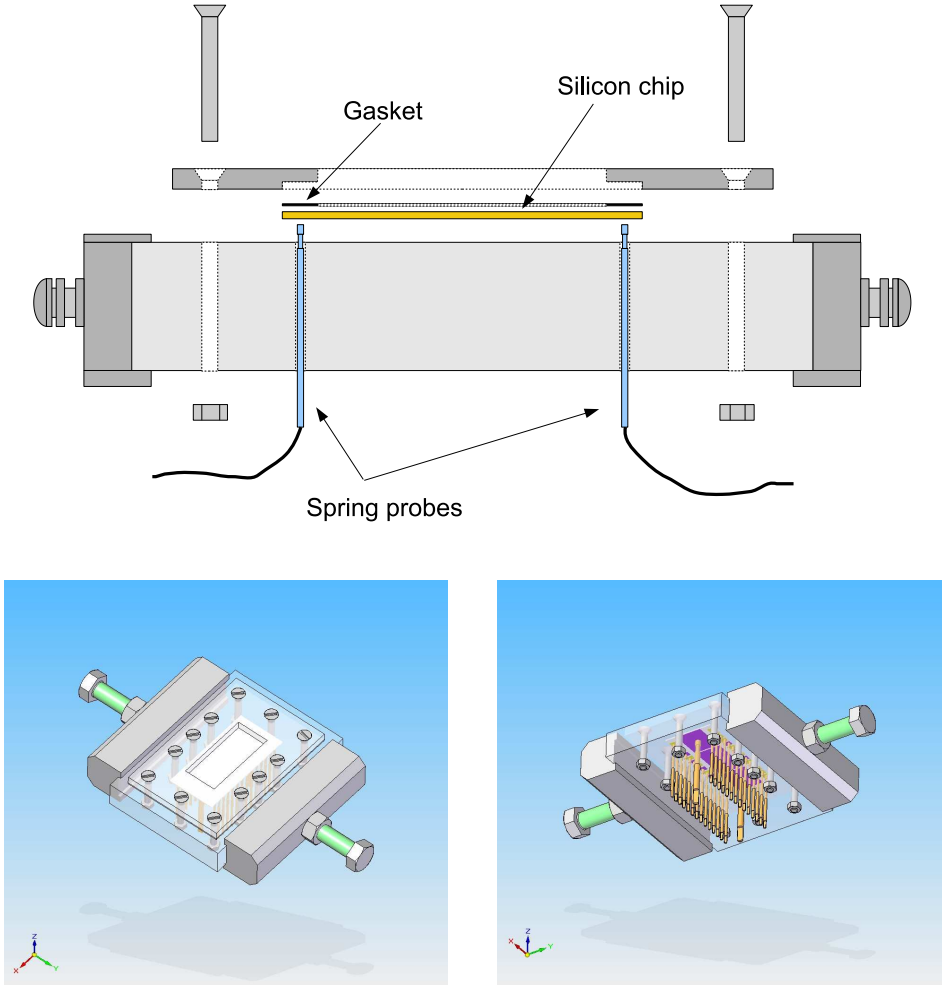

Figure 3.8: *Top: Schematic concept of the jig of the second generation test section. Bottom left: 3D view from the top of the jig, holding the second generation test section. Bottom right: 3D view from the bottom of the jig, holding the second generation test section (PTFE transparent for better visibility).*

3.2.3 Third generation

In the test section design of the third generation the size of the boiling surface was increased, there are new 16 temperature micro-sensors integrated on the top surface with artificial cavities etched at their geometrical centre. The geometry of the sensors was changed from rectangular to square. They cover an area of $0.84 \times 0.84\,\mathrm{mm}^2$, however, the same metals, Ni and Ti, were used, Fig. 3.9. The resistance heater is made from Al, rectangular and deposited on the back of the silicon wafer.

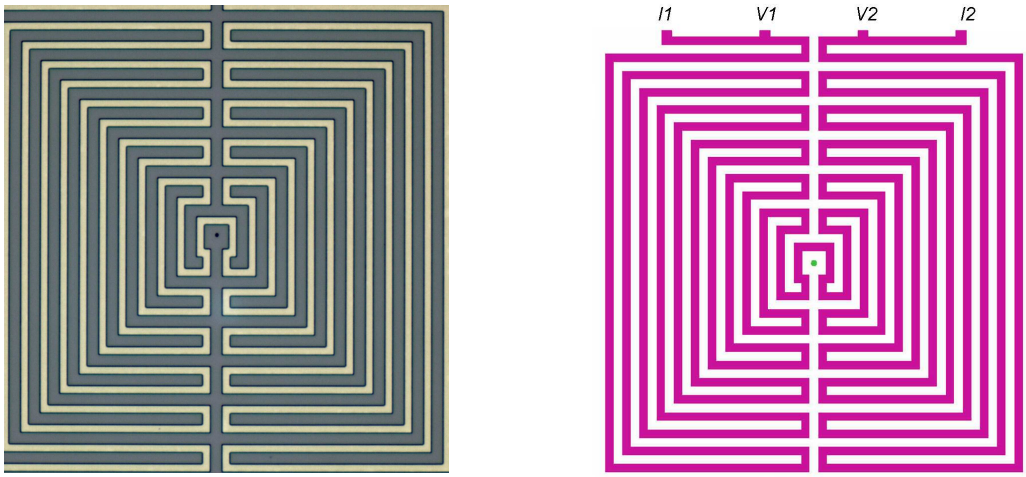

Figure 3.9: *Left: Close-up photograph of a third generation micro-sensor. The image shows the square layout of the sensor with an artificial cavity in its centre. Right: Schematic view of the third generation micros-sensor layout with 4 connections indicated.*

Figure 3.10 shows the arrangement of the heater, the 16 sensors and all the connection pads on the silicon wafer. The chip size was $50 \times 50\,\mathrm{mm}^2$, whereas the heater has a size of $40 \times 37\,\mathrm{mm}^2$. The heater has a serpentine layout with 8 turns. Again, each sensor has four connections. There were two rows of micro-sensors and artificial cavities, the top row with a diameter of $10\,\mu\mathrm{m}$ and the bottom row with $2\,\mu\mathrm{m}$. A set of devices with a cavity depth of $80\,\mu\mathrm{m}$ was fabricated. To tighten the gap between silicon device and the top frame of the jig, a neoprene gasket was placed in between. The fabrication steps in Fig. 3.12 (a)-(e) are the same as in Fig. 3.6 (a)-(e), only that all steps were done on the front side of the wafer. To create the Al heater the silicon wafer was flipped over. PECVD oxide was then deposited on the heater and the back surface planarised using CMP, Fig. 3.12 (f). To clean the silicon wafer it was rinsed with DI water and dried in the Marangoni drier, Fig. 3.12 (g). The last step in Fig. 3.12 (h) is the same as in Fig. 3.6 (h) with the difference that previous to the silicon etch, oxide etching has to be done. The connection pads to micro-sensors and heater are not on the same side of the wafer due to micro-fabrication limitations. The new jig, holding the wafer in position and guarantying a good physical connection to the pads, has to be changed accordingly to fulfil the new requirements.

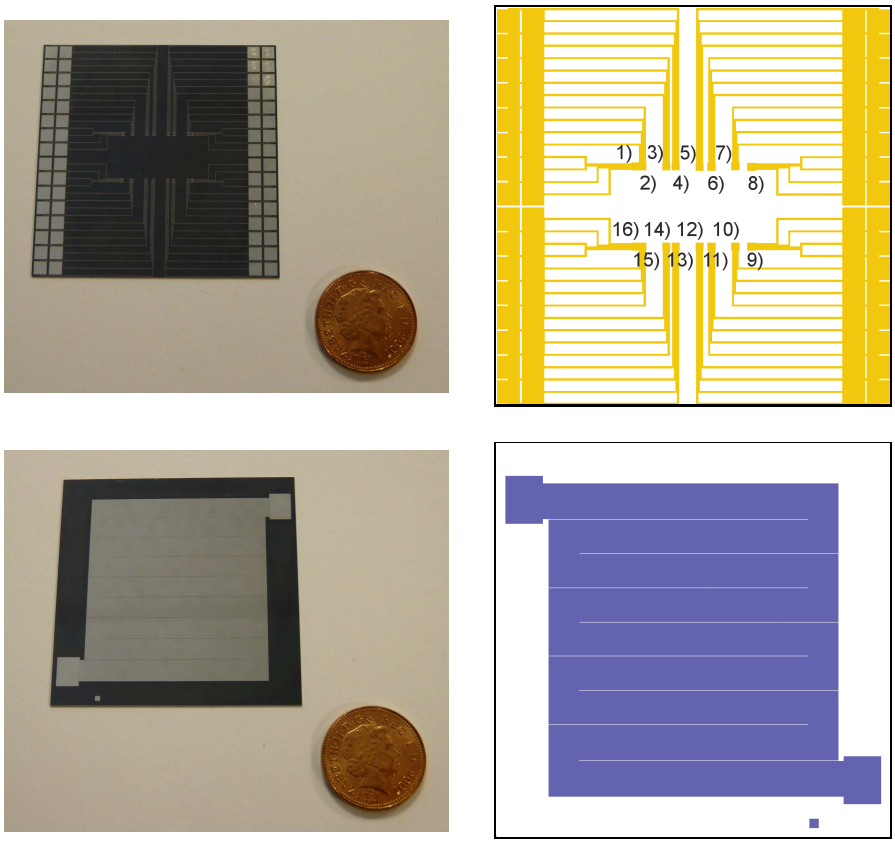

Figure 3.10: *Top left: Photograph of the front of the third generation silicon device with 16 micro-sensors and 64 connection pads. Top right: Schematic view of the third generation silicon device with numbered sensors and cavities. Bottom left: Photograph of the back of the third generation silicon device with the integrated resistance heater and its two connection pads. Bottom right: Schematic view of the heater layout on the back of the third generation silicon device.*

More detailed technical drawings of the silicon device layout and the jig can be found in appendix A.

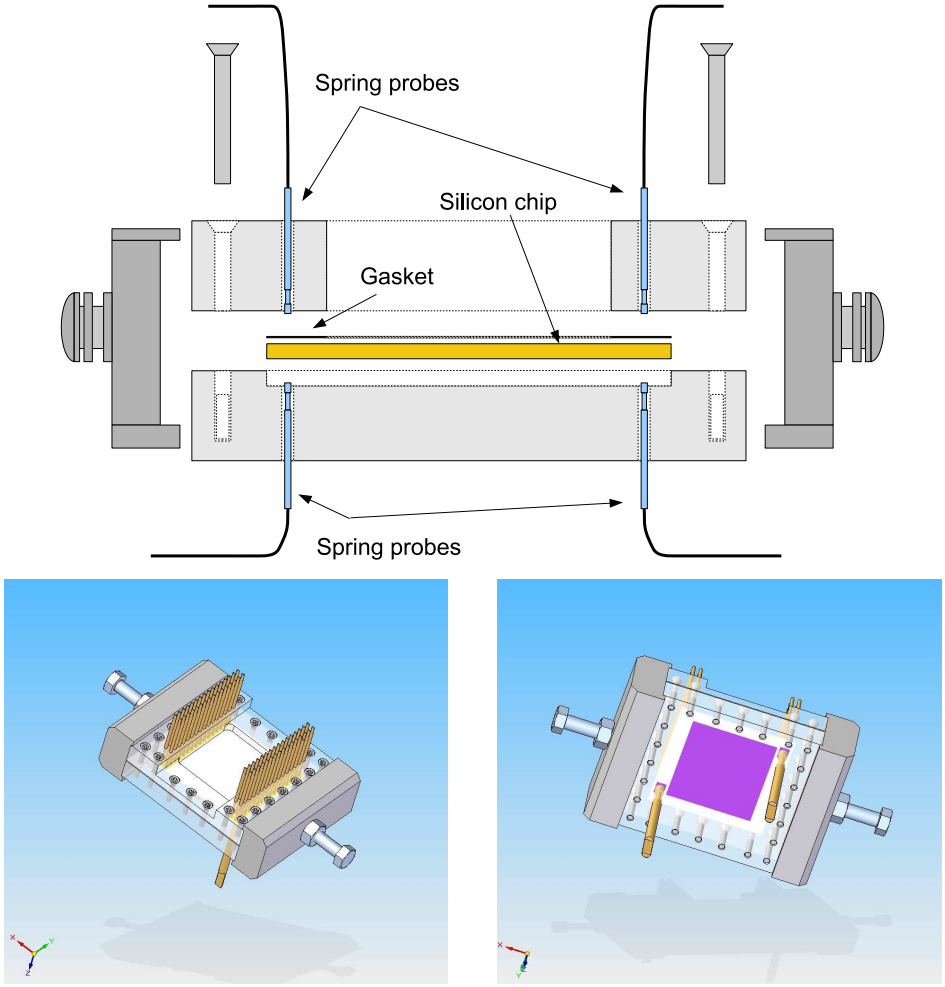

Figure 3.11: *Top: Schematic concept of the jig of the third generation test section. Bottom left: 3D view from the top of the jig, holding the third generation test section. Bottom right: 3D view from the bottom of the jig, holding the third generation test section (PEEK™ transparent for better visibility).*

3.3 Data acquisition

Voltage signals from thermocouples and the micro-sensors were acquired and recorded with a DAQ system (16-bit SCXI-1600 with SCXI-1100 analog input module, National Instruments) using the LabVIEW 8.6 (National Instruments) software interface. Screen shots of the actual programs with the user interfaces for the second and third generation test sections are shown in appendix A. In this configuration the DAQ system can sample at a maximum rate of $166\,{}^{\mathrm{kS}}/_{\mathrm{s}}$, scanning all 32 channels of the SCXI-1100

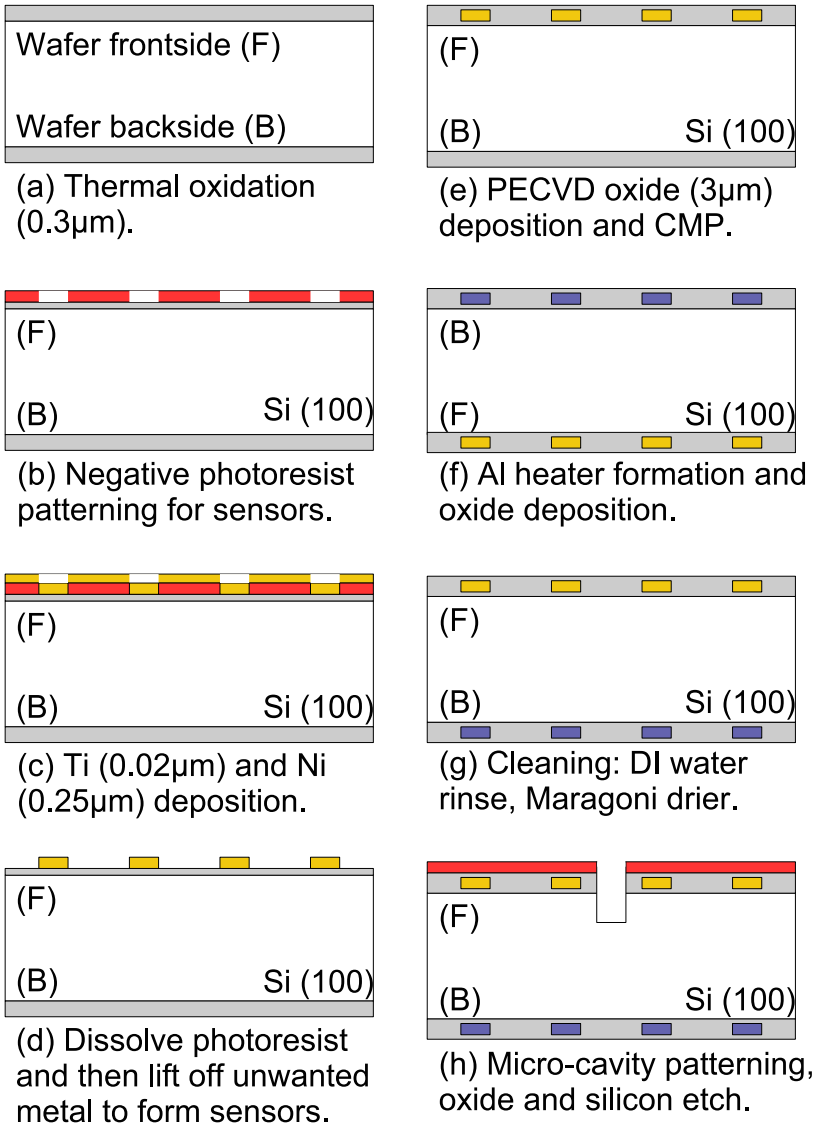

Figure 3.12: *Fabrication sequence of the third generation test section. Fabrication includes micro-cavities, integrated temperature micro-sensors and an integrated resistance heater.*

module with a resolution of $0.15\,\mathrm{mV}$ and an input range of 0 to $10\,\mathrm{V}$. All measured signals were ungrounded-floating, connected and measured differentially.

As mentioned earlier, the micro-sensors are temperature dependent resistors. To measure the voltage across the resistance changing with temperature, a constant current source had to be connected to each sensor. Initial tests showed that a current of $0.5\,\mathrm{mA}$ was suitable and would not lead to Joule heating (i.e., self heating) of the sensor. First

temperature measurements with the sensors were not satisfactory due to the high signal to noise ratio. It was found, that the common high precision current source was the main source because of its connection to the power grid. After replacing the common current source with a self-made current source, the signal to noise ratio was reduced to acceptable amplitudes. The layout of the self-made current source is presented in Fig. A.13 in appendix A. The current source circuit includes two resistors, a voltage regulator and a transistor. To prevent a new source of noise, four $1.5\,\mathrm{V}$ batteries were connected in series resulting in a voltage of $6\,\mathrm{V}$. The current was measured and controlled with a high precision multimeter (196 System DMM, Keithley Instruments Inc.) before, during and after each experiment. The resistance calculations were always corrected with the actual current reading of the experiment. The variations in current was typically below $0.0001\,\mathrm{mA}$. The accuracy of the current readings for a range of 0 to $20\,\mathrm{mA}$ is $\pm 0.038\,\%$.

First calibration attempts indicated a non-linear behaviour of the resistance with temperature. The problem was solved after the thickness of the thermal oxide layer between the heater and the sensor was increased because of detected current "leaks". These first tests were all conducted with the second generation silicon device.

3.4 Calibration and measurement error of the experimental equipment and image processing

Pressure measurement Both pressure indicators were calibrated by the manufactures. The pressure transducer has an accuracy of $\pm 0.4\,\%$ for the full range and the pressure was indicated relatively. The digital manometer has an accuracy of $\pm 0.1\,\%$ at room temperature and the pressure was indicated absolutely.

Thermocouples The T-type thermocouples have an accuracy of $\pm 0.5\,^{\circ}\mathrm{C}$ and the readings were checked with a high precision thermometer (F250 MkII, Automatic Systems Laboratories), which has an accuracy of $\pm 0.01\,^{\circ}\mathrm{C}$, between 20 and $85\,^{\circ}\mathrm{C}$. The

thermocouples were placed in a temperature controlled heating bath together with the platinum probe of the thermometer. The temperature was increased in steps of $10\,\mathrm{K}$ and after equilibrium was reached, the temperature was measured simultaneously. The difference between the thermometer and the thermocouples was below $0.45\,\mathrm{K}$ for the measured range.

Temperature micro-sensor including DAQ The sensors were calibrated in-situ with the thermocouple mounted at the bottom of the boiling chamber for the single phase region and with both thermocouples above the boiling temperature. The sensors of each silicon device were calibrated whenever it was newly mounted inside the boiling chamber, even if they were in use previously. The behaviour of the sensors resistance with temperature was near-linear. The limit of error for the thermocouples and therefore the sensors is $0.5\,\mathrm{K}$. According to the manufacturer specifications the absolute accuracy of the used DAQ system is $8.2469\,\mathrm{mV}$ for a signal range from -10 to $10\,\mathrm{V}$. Calibration curves of five sensors of a second generation silicon device are plotted with linearly fitted trend lines in Fig. 3.13.

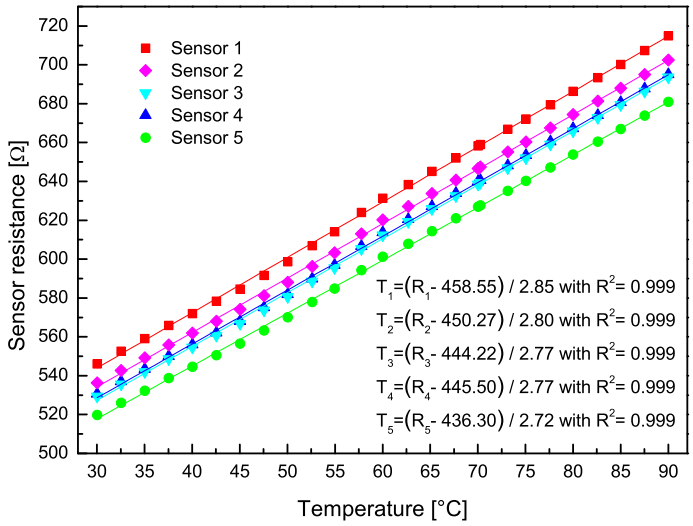

Figure 3.13: *Calibration of the 5 sensors on a second generation silicon device. The data points are plotted with linear trend lines and equations indicated.*

The sensors had a typical sensitivity of around $3\,\Omega/\mathrm{K}$. For the second generation silicon device the sensor are on the back. The time delay due to thermal conductance is calculated from

$$\tau = \frac{L_{Si}^2}{\kappa} \tag{3.1}$$

where L_{Si} is the silicon wafer thickness and κ the thermal diffusivity of silicon. The determined time delay at $20\,^{\circ}\mathrm{C}$ is $1.6 \cdot 10^{-3}\,\mathrm{s}$. The time-averaged temperature drop due to thermal conduction through the silicon for the second generation test section was calculated from

$$T_s = T_{SEN} - \frac{\dot{q}''\, L_{Si}}{k_{Si}} \tag{3.2}$$

where T_s is the temperature on the silicon surface on which boiling takes place, T_{SEN} the temperature measured with the integrated micro-sensor, $\dot{q}''$ the applied heat flux and k_{Si} the thermal conductivity of silicon. The temperature difference for steady conduction of the net heat flux (after allowance for losses) between the back side, where the sensor is situated, and the front side of the second generation silicon wafer was $0.1\,\mathrm{K}$ for the highest heat flux applied during experiments. This is within the limit of error of $0.5\,\mathrm{K}$ and therefore negligible.

The time delay was also calculated just for the sensor itself, Eq. 3.1. For the Ni/Ti sensor τ is equal to $2.8 \cdot 10^{-9}\,\mathrm{s}$ at $20\,^{\circ}\mathrm{C}$. Thermal properties of materials are given in Table B.2 in appendix B.

Artificial cavities The artificial cavities were etched into the silicon. Fig. 3.14 left shows a scanning electron microscope (SEM) image of a section through an elongated cavity with a nominal depth of $40\,\mu\mathrm{m}$ and width of $10\,\mu\mathrm{m}$, in order to check the specified dimensions of the micro-fabricated cavities. The depth measured from the SEM image is $35.4\,\mu\mathrm{m}$ with the width of the cavity tapering from $9.7\,\mu\mathrm{m}$ (top) to $10\,\mu\mathrm{m}$

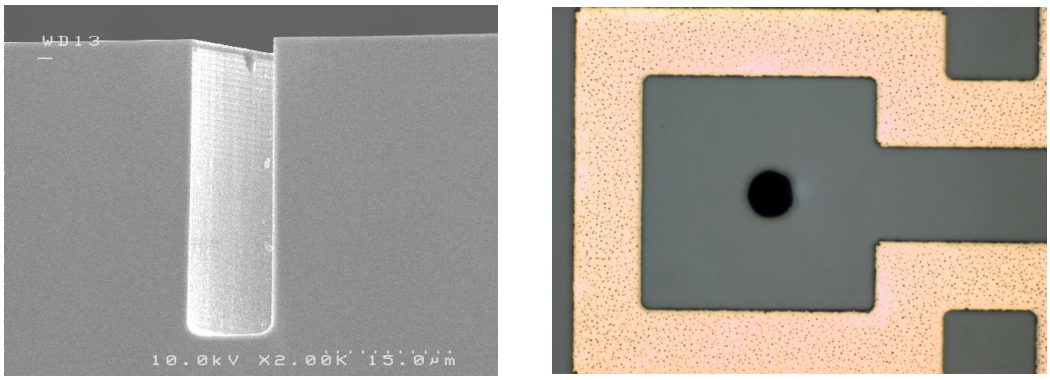

Figure 3.14: *Left: SEM image of a section through an elongated cavity. Right: Image of the cavity opening with smooth edges.*

(bottom). The edge of the cavity is rather smooth as seen in Fig. 3.14 right.

Applied heat flux The applied heat flux is determined from the current and voltage readings indicated by the power supply connected to the integrated heater. The limit of error for the applied heat flux is $\pm 0.7\,\%$. The readings were checked with a high precision multimeter (196 System DMM, Keithley Instruments Inc.) with an accuracy of $\pm 0.058\,\%$ for a current of $1\,\mathrm{A}$ and $\pm 0.0035\,\%$ for a voltage of $10\,\mathrm{V}$. The loss of heat by conduction through the $10\,\mathrm{mm}$ thick PTFE back side insulation for the second generation jig and the $10\,\mathrm{mm}$ PEEK™ for the third generation to the surrounding saturated liquid by natural convection is driven by a temperature difference approximately equal to the wall superheat.

An empirical correlation for natural convection for a downward facing heated plate [142] was used to estimate the heat loss.

$$Nu_H = \frac{\alpha\, H}{k_w} = 0.27\, Ra_H^{1/4} \qquad \text{for} \qquad \left(10^5 < Ra_H < 10^{10}\right) \tag{3.3}$$

where α is the convective heat transfer coefficient, k_w the conductive heat transfer coefficient of PTFE or PEEK™ and H the characteristic length given as

$$H = \frac{\text{area}}{\text{circumference of area}} = \frac{l\ w}{2\ l + 2\ w} \tag{3.4}$$

The Rayleigh number Ra is the product of the Grashof number Gr and the Prandtl number Pr

$$Ra_H = Gr_H\ Pr = \frac{g\ \beta\ (T_w - T_\infty)\ H^3}{\nu\ \kappa} \tag{3.5}$$

where g is the gravitational acceleration, T_w the wall temperature, T_∞ the fluid temperature, in this case the saturation temperature of FC-72, ν the kinematic viscosity, κ the thermal diffusivity and β the volumetric thermal expansion coefficient given as

$$\beta = -\frac{1}{\rho}\ \left(\frac{\partial \rho}{\partial T}\right)_p \tag{3.6}$$

where ρ is the density of FC-72. From the equations above the overall heat transfer coefficient was calculated as

$$U = \frac{\alpha\ k}{k + \alpha\ L_w} \tag{3.7}$$

where L_w is the wall thickness of either the PTFE or PEEK™ plate. The wall temperature T_w was found through iteration until $\dot{q}_{tot}$, $\dot{q}_{conv}$ and $\dot{q}_{cond}$ from the following three equations were equal

$$\dot{q}_{tot} = l\ w\ U\ (T_{SEN} - T_\infty) \tag{3.8}$$

$$\dot{q}_{conv} = l\ w\ \alpha\ (T_w - T_\infty) \tag{3.9}$$

$$\dot{q}_{cond} = \frac{k}{L_w}\ l\ w\ (T_{SEN} - T_w) \tag{3.10}$$

where T_{SEN} is the temperature measured with the micro-sensors, l the length and w

the width of the plate. The liquid properties were implemented temperature dependent and can be found in section 3.5 in Table 3.1 and 3.2. The thermal conductivity of PTFE and PEEK™ was implemented as constant with $0.25\,{}^{\mathrm{W}}/_{\mathrm{mK}}$ at $25\,^{\circ}\mathrm{C}$, because it is only varying little for the applied temperature range. The estimated heat loss for the second generation jig is less than $10\,\%$ at the lowest applied heat flux of $0.7\,{}^{\mathrm{kW}}/_{\mathrm{m^2}}$, falling to less than $4\,\%$ at heat fluxes above $17.5\,{}^{\mathrm{kW}}/_{\mathrm{m^2}}$. This estimate does not allow for lateral conduction inside the PTFE, but the measured rear temperature of the silicon plate does not vary more than $2\,\mathrm{K}$ at the highest heat flux. If the same estimation is done for the third jig the heat loss is below $10\,\%$ for the lowest applied heat flux of $0.5\,{}^{\mathrm{kW}}/_{\mathrm{m^2}}$ and less than $5.5\,\%$ at heat fluxes above $7.1\,{}^{\mathrm{kW}}/_{\mathrm{m^2}}$.

Image processing Most experimental results of this study were obtained by analysing high-speed images. Measurements and resulting deductions have to be made carefully as they are easily more generally applied than justified, Kenning [143]. The high temperature gradients involved during boiling experiments, especially close to the boiling surface, lead to high refractive index gradients and a phenomenon known as “mirage” effect can distort the observations, Minnaert [144]. A cold fluid is denser than a warm fluid and has therefore a greater refractive index. As light passes this colder fluid across a sharp boundary to significantly warmer fluid layer, in the case of boiling experiments from saturated liquid into a superheated liquid layer, the light rays bend away from the direction of the temperature gradient. This results in the light ray being bent in a concave, upward trajectory. If the light reaches the camera sensor it can be interpreted as if it traces back a perfectly straight “line of sight”. This line is ,however, at a tangent to the path the ray takes at the point it reaches the eye. Therefore observations very close to the heated surface have to be treated very carefully.

The camera was always set to acquire at $1000\,\mathrm{fps}$ resulting in a temporal resolution of $1\,\mathrm{ms}$. The bubble diameter during bubble growth and the bubble departure diameter represent the apparent diameter, the widest horizontal distance or equator of the bubble. The estimated accuracy is $\pm 2\,\mathrm{px}$. In experiments with the second generation test section the bubble departure frequency was calculated from measured bubble growth

times of five succeeding bubbles. The accuracy of this measurements is $\pm 2\,\mathrm{ms}$, however this was only indicated as error bar for the data points, where the standard deviation of the average of the five bubble growth times was smaller. For the third generation test section high-speed image sequences events like bubble nucleation, departure and interactions were counted. To estimate the accuracy of these measurements is difficult. For the nucleation, departure and vertical coalescence frequency it was set to ± 2 events for the observation time of $0.815\,\mathrm{s}$. Due to the smaller numbers of occurred horizontal coalescence the measurement error was estimated to be ± 1 events for the observation time of $0.815\,\mathrm{s}$. These measurements are not influenced by the camera inclination.

The vapour volume of bubbles was calculated from measured areas of bubbles. With a commercial image processing program (PCO Picture Viewer, SchnitzeSoft) the vapour boundary was detected with thresholding. All pixels with a grey-level below the threshold are assigned to the background. The threshold was chosen so that manually measured apparent bubble diameters result in the same value. The influence of the chosen threshold intensity (12-bit scale) on the calculated vapour volume is shown in Fig. A.17 in appendix A. A reasonable estimated threshold error of around ± 100 is well below the estimated accuracy of $\pm 2\,\mathrm{px}$ for each horizontal and vertical row of pixels, including the camera inclination. Each pixel row is then rotated around its centre and the volumes of all rows summed up with

$$V_b = \pi \int_0^y R_b(y)^2 dy \tag{3.11}$$

where $R_b(y)$ is the bubble radius depending on the vertical position.

For the calibration of the images taken during boiling from the second generation test sections, screws of the jigs at same horizontal height as the artificial cavities were used. For experiments with the third generation test section the connection patterns of the micro-sensor, located around the artificial cavity, were used to calibrate the length scale of the images.

3.5 Boiling liquid

The working fluid for all experiments was fluorinert FC-72 (perfluorohexane C_6F_{14}, IUPAC: 1,1,1,2,2,3,3,4,4,5,5,6,6,6-tetradecfluorhexane). It is a clear, colourless, thermally and chemically stable, compatible with sensitive materials, non-flammable, practically non-toxic liquid and is widely used for boiling experiments. Its low boiling temperature ($T_{sat} = 57.15\,^{\circ}\mathrm{C}$ at $p = 1\,\mathrm{bar}$, 3M [20]) and dielectric properties make it possible to completely immerse the bare electrical connections to the silicon test section. This is an important practical consideration, because of the large number of connections. It is important to keep the temperature of the boiling liquid always below the decomposition temperature of around $200\,^{\circ}\mathrm{C}$. The decomposed liquid may form hydrofluoric acid with the solved water, which can lead to destruction of materials and test sections and be seriously harmful.

In Figure 3.15 the saturation temperature is plotted against saturation pressure and in Table 3.1 and 3.2 important thermal and physical properties of fluorinert FC-72 are summarised.

Table 3.1: *Properties of fluorinert FC-72 from 3M [20] (part I).*

Temperature $T\,[^{\circ}\mathrm{C}]$	Temperature $T\,[\mathrm{K}]$	Specific heat capacity $c_p\,[\mathrm{J/kgK}]$	Prandtl number $Pr\,[-]$
0	273.15	1014	15.98704
10	283.15	1029.54	14.03476
20	293.15	1045.08	12.47870
30	303.15	1060.62	11.22535
40	313.15	1076.16	10.20787
50	323.15	1091.70	9.376993
60	333.15	1107.24	8.695609
70	343.15	1122.78	8.135228

Table 3.2: *Properties of fluorinert FC-72 from 3M [20] (part II).*

Temperature T [°C]	Liquid density ρ_l [kg/m³]	Vapour density ρ_v [kg/m³]	Kinematic viscosity ν [m²/s]
0	1740	1.36220	$5.44 \cdot 10^{-7}$
10	1713.9	2.21956	$4.68 \cdot 10^{-7}$
20	1687.8	3.46255	$4.09 \cdot 10^{-7}$
30	1661.7	5.19778	$3.61 \cdot 10^{-7}$
40	1635.6	7.54132	$3.22 \cdot 10^{-7}$
50	1609.5	10.61606	$2.91 \cdot 10^{-7}$
60	1583.4	14.70080	$2.65 \cdot 10^{-7}$
70	1557.3	20.11167	$2.43 \cdot 10^{-7}$

Temperature T [°C]	Thermal conductivity k [W/mK]	Compressibility β [1/K]	Surface tension σ [dynes/cm]
0	0.0600	0.001500	12.66597
10	0.0589	0.001523	11.77936
20	0.0578	0.001546	10.90541
30	0.0567	0.001571	10.04475
40	0.0556	0.001596	9.198045
50	0.0545	0.001622	8.366092
60	0.0534	0.001648	7.549774
70	0.0523	0.001676	6.750113

Temperature T [°C]	Vapour pressure p_{sat} [kPa]	Heat of vaporisation h_{lg} [kJ/kg]	Dynamic viscosity μ [kg/ms]
0	10.236	99.77355	0.000946
10	16.298	97.39592	0.000803
20	25.138	94.93161	0.000690
30	37.681	92.36824	0.000600
40	55.041	89.70579	0.000527
50	78.535	86.91951	0.000468
60	109.691	84.03417	0.000419
70	150.252	81.03737	0.000379

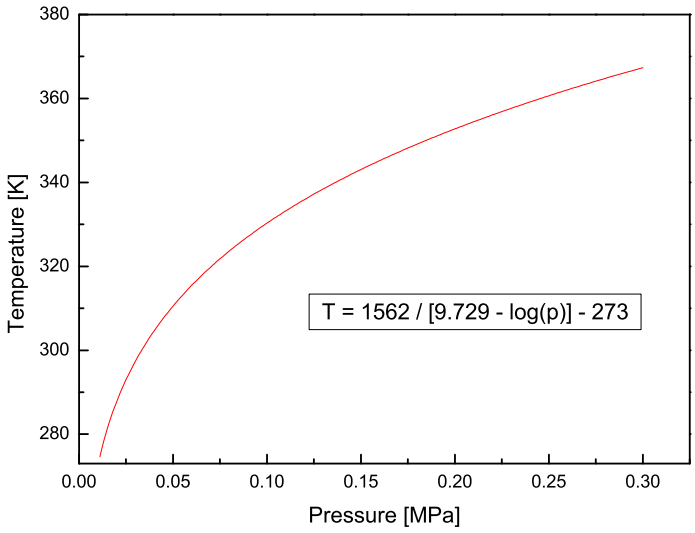

Figure 3.15: *Saturation curve of fluorinert FC-72.*

3.6 Experimental procedure

After the construction of the experimental setup was completed, pressure tests were conducted. The system was pressurised to $3\,\mathrm{bar}$ with air and closed. Potential leaks were located with leak detector foam and eliminated. To successfully pass the pressure test, the system had to hold a pressure of $3\,\mathrm{bar}$ for 30 minutes. This pressure test was conducted every time the system was opened and closed. The setup was then flushed for 8 hours with DI water and dried with pure nitrogen for 4 hours. In a second step the system was filled with a small amount of FC-72, which was circulated for 8 hours. After draining the FC-72, the system was flushed and dried with pure nitrogen for 4 hours, before it was filled again with pure FC-72.

Before the test section was positioned in its holder, it was always cleaned for 30 minutes in an ultrasonic bath, rinsed with DI water for 10 minutes and dried with pure nitrogen. Through a particle filter the boiling chamber was filled with 3 litres of FC-72. In case the boiling chamber had to be opened for changing the test section, the

liquid was stored in a separate welded stainless steel reservoir. After the work on the boiling chamber, or the condenser, the liquid was pumped back into the chamber with a pump (PHP-600 series dosing pump, Omega Engineering Ltd.). A particle filter (Swagelok™), which was built in between the pump and the boiling chamber, removed possible impurities. The liquid was usually circulated between boiling chamber and reservoir for 20 minutes.

The heating up was started with increasing the power output to the four heater cartridges and the silicone heater, wrapped around the wall of the boiling chamber, in small steps. After $1.2\,\mathrm{bar}$ was reached the heating bath was switched on to supply cooling liquid to the condenser. Approximately every 5 minutes incondensable gases, accumulated in the top of the condenser, were released through an instrument plug valve (SS-4P4T, Swagelok™). The liquid was degassed for at least 2 hours prior to each experiment.

The pressure inside the chamber was adjusted with the temperature and flow of the cooling liquid supplied to the condenser. When the set pressure was reached, boiling from the substrate was initiated by switching on the power to the integrated or separate heater on the back of the substrates. The heaters of all three generations of test sections were connected to a D.C. power supply (IPS-1820HD, Iso-tech) with A/C input circuit and transformer. The option of a power supply using a transformer instead of a switched-mode power supply was preferred because of considerable signal to noise ratio reduction in the acquired signals of the micro-sensors. Up to $37.8\,\mathrm{kW/m^2}$ were used to start saturated nucleate boiling on the substrate. After the onset of boiling the power was decreased to $21.3\,\mathrm{kW/m^2}$ and kept at this power for 30 minutes to degas the test section. The power supply was then switched off and after a waiting time of 15 minutes, boiling was initiated again, but the power was immediately reduced to reach the chosen wall superheat. Bubble growth was now limited to the location of the artificial cavities.

The set power must provide a wall superheat which is always above the equilibrium superheat for a hemispherical bubble at the mouth of the cavity, which may be deduced from Eq. 2.3. The equilibrium superheat values for the cavity dimensions and

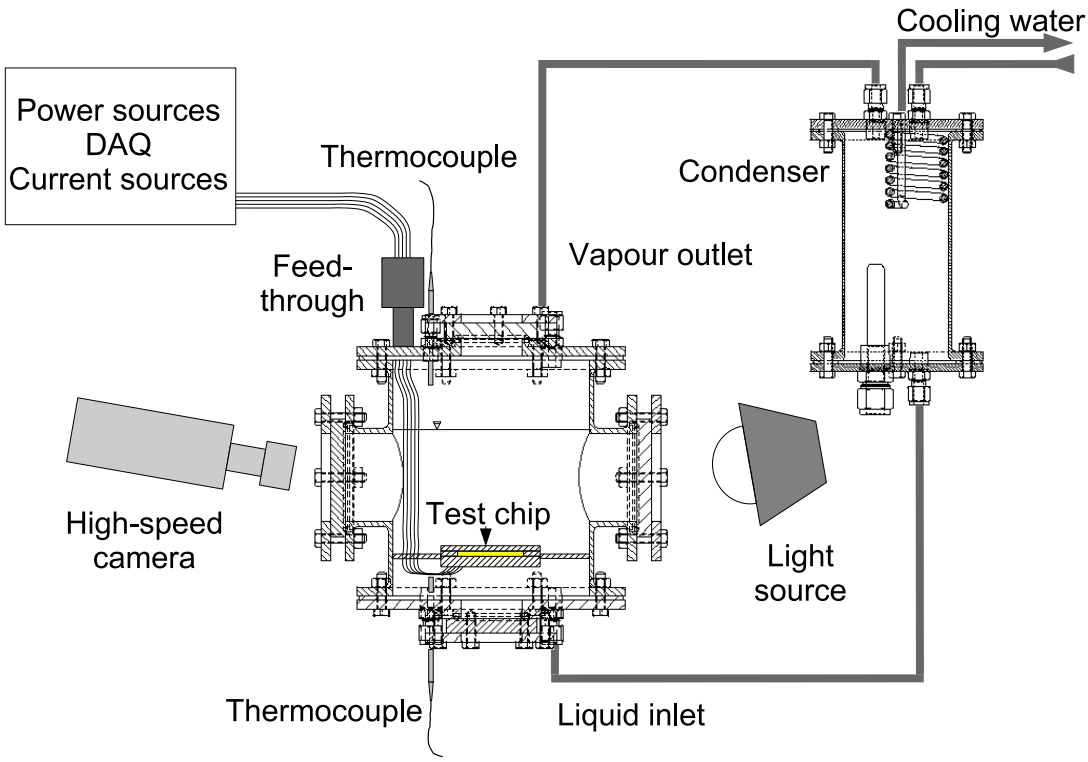

Figure 3.16: *Experimental procedure for the high-speed imaging, including the main parts boiling chamber with test section, condenser, high-speed camera and backlight source.*

set pressures used during experiments are given in Table C.1 in appendix C. The wall superheat was increased up to the point, where unwanted bubble growth from new nucleation sites appeared. This is the limitation of wall superheat for boiling experiments in the present study.

In Figure 3.16 a schematic view of the experimental procedure for the high-speed imaging is presented. Bubble growth is observed with a high-speed camera (IDT Nanosense MkIII) working at $1000\,\mathrm{fps}$. The camera has a CMOS sensor with a size of $1280 \times 1024\,\mathrm{pixel}$ and takes 10-bit images. A lens (VZM™450i) including an extender lens ($\times 0.5$ for VZM™450i), with a working distance of around $20\,\mathrm{cm}$, a field of view of $3\,\mathrm{mm}$ and a field of depth of $0.5\,\mathrm{mm}$ was mounted on the camera. The boiling substrate was illuminated by a continuously working incoherent light source (Dedolight 400D) opposite to the camera. Due to the design of all jigs, holding the test section in

position, the high speed camera had to be inclined at an angle of approximately $20\,°$.

All experiments were conducted at saturated conditions. As soon as the thermocouples, measuring the vapour and liquid temperature, indicated the same temperature, saturated boiling was taking place. Simultaneously to the imaging, the wall temperature was measured with the integrated temperature micro-sensors and the power supplied to the integrated heater indicated at the power supply. The micro-sensors were connected to the DAQ and with a self-made trigger, as shown in Fig. A.14 in appendix A, the start of capture was indicated in the DAQ output file with a step response of $0.5\,\mathrm{V}$. The trigger separates the DAQ side from the camera electrically with an opto-isolator to protect the DAQ signals from high frequency noise from the high-speed camera. A voltage of $5\,\mathrm{V}$ from an ungrounded power supply (Farnell Technology) had to be applied to power the trigger. After one sequence was recorded, the integrated heater was switched off for 15 minutes before a new wall superheat was set for further measurements and recording.

3.7 Conclusions

A new experimental setup was designed, built and commissioned to investigate pool boiling from a horizontal boiling substrate. It was possible to conduct boiling experiments for a pressure range between 0.5 and $3\,\mathrm{bar}$. Three different boiling substrates were micro-fabricated, including the jigs to hold them in place. The accuracy of the micro-fabrication and the used equipment was discussed in detail and the DAQ system including the program is presented. Important properties of the used boiling liquid are introduced. The chapter closes with a detailed experimental procedure including commissioning, cleaning of the setup and test sections, pressure tests, boiling liquid degassing and conducting experiments.

Chapter 4
Single bubble growth

For an artificial cavity to qualify as a nucleation site for single bubble growth certain requirements have to be fulfilled. The spacing between two neighbouring cavities or nucleation sites has to be wide enough, so that no thermal interactions within the substrate or the liquid phase, no physical interactions between bubbles and no bubble induced liquid motions occur. In chapter 2, in section 2.2.6, regions of interaction were generally determined by $S/\overline{D_d}$, where S is the spacing between two active nucleation sites and $\overline{D_d}$ the average departure diameter. For $S/\overline{D_d} > 3$ no interactions between two sites were reported in the literature, Zhang and Shoji [6].

Bubble growth was measured during boiling from artificial cavities at S3 on the second generation device and from the cavity at S8 on the third generation device, Fig. 4.1. Experiments with different artificial cavity depths and varied pressures of 1, 1.25 and $1.5\,\mathrm{atm}$ were all conducted on second generation test sections (S3 only). The nominal cavity mouth diameter was for all measurements $10\,\mu\mathrm{m}$ and three different silicon wafers, each with a different cavity depth of 40, 80 and $100\,\mu\mathrm{m}$, were used. The distance from the cavities above sensor S2 and S4 to sensor S3 is $4.25\,\mathrm{mm}$, while the dimension between the cavities above sensors S1 and S5 and the one above S3 is $7.065\,\mathrm{mm}$. S3 can be treated as an isolated nucleation site for bubble departure diameters smaller than $1.42\,\mathrm{mm}$. On the third generation device the two rows of artificial cavities (S1-S8 and S9-S16) are $10\,\mathrm{mm}$ afar from each other. In between the cavities S7 and S8 is a distance of $2\,\mathrm{mm}$. The maximum bubble departure diameter for isolated bubble growth is $0.67\,\mathrm{mm}$ following the above specifications.

For the remaining experiments, including bubble growth at pressures of 0.5, 0.75 and $1\,\mathrm{bar}$, vertical and horizontal coalescence and nucleation site interactions, presented in this and the following two chapters, only third generation test sections were used. Only bubble growth from the cavity at sensor S8 was observed, see Fig. 4.1 right.

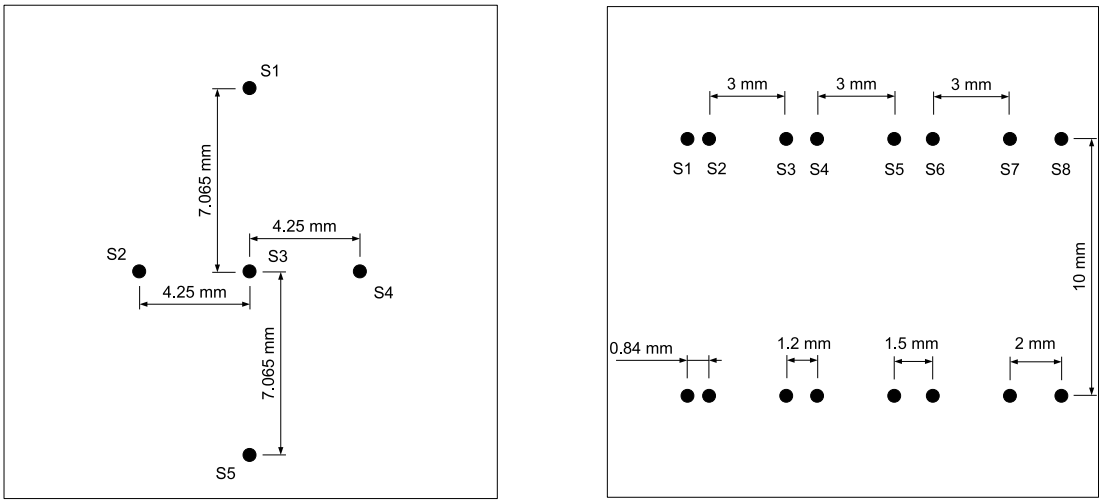

Figure 4.1: *Left: Arrangement of the artificial cavities on the second generation silicon device. Right: Arrangement of the artificial cavities on the third generation silicon device.*

4.1 Bubble growth rate

The bubble diameter was measured from images taken by the high-speed camera as the maximum apparent diameter of the bubble or bubble equator. In Figure 4.2 a sequence of images with a temporal resolution of 6 ms for bubble growth from the $80\,\mu\mathrm{m}$ deep cavity with a mouth diameter of $10\,\mu\mathrm{m}$ and a wall superheat of $1.1\,\mathrm{K}$ at $1.25\,\mathrm{atm}$ is shown.

In Figure 4.3 the average bubble growth of three successive bubbles from S3 of the second generation test section is presented. The diameters were measured from images taken for a wall superheat of $1.3\,\mathrm{K}$ and an applied heat flux of $0.85\,\mathrm{kW/m^2}$ at atmospheric pressure from the $100\,\mu\mathrm{m}$ deep artificial cavity. The error bars indicate the standard deviation of the average of the three successive bubbles. It was replaced by the uncertainty of the apparent diameter measurement of $\pm 2\,\mathrm{px}$ if the standard devia-

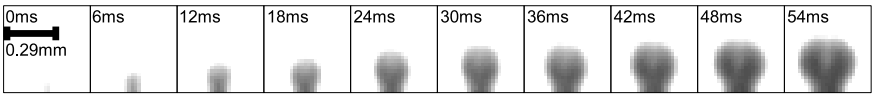

Figure 4.2: *High-speed images of a bubble growth sequence from an isolated cavity (S3) with a nominal mouth diameter of 10 μm and a depth of 80 μm, a temporal resolution of 6 ms and a wall superheat of 1.1 K at 1.25 atm.*

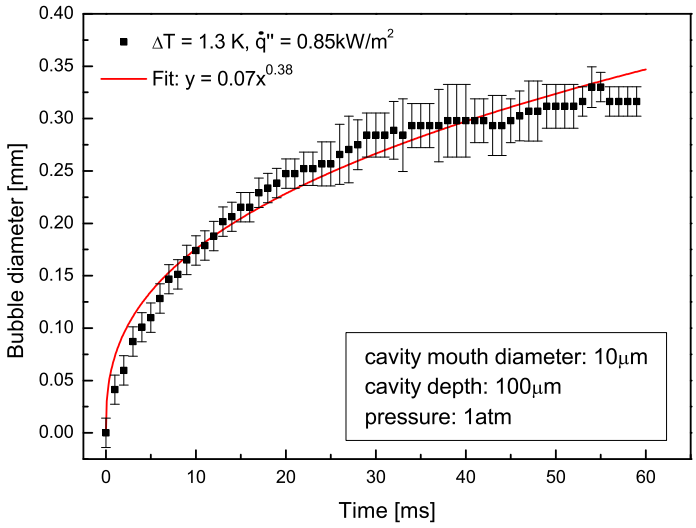

Figure 4.3: *Average bubble growth of three successive bubbles at a wall superheat of 1.3 K and an applied heat flux of 0.85 $^{kW}/_{m^2}$ at atmospheric pressure from an isolated cavity (S3) with a nominal mouth diameter of 10 μm and depth of 100 μm. A trend line was fitted to the data.*

tion was smaller. The uncertainty is given here only in pixels, as the calibration always varies slightly with the magnification and position of the high-speed camera.

During the initial fast bubble growth period, the agreement of the diameter measurement of the three individual bubbles is very good. After $10\,\mathrm{ms}$, the difference in the diameter of the bubbles increases. The departure diameter is between $0.3\,\mathrm{mm}$ and $0.34\,\mathrm{mm}$.

Contrary to findings for liquid nitrogen, reported by Rammig and Weiss [93], the waiting time between successive bubbles depends on the wall superheat. For the lowest superheats, waiting times of up to $70\,\mathrm{ms}$ were measured, whereas for the high superheat it was below $1\,\mathrm{ms}$, and therefore below the time resolution of the measurements. Despite this different behaviour for the waiting time, bubble growth in FC-72 at a wall superheat of $1.3\,\mathrm{K}$ and in nitrogen are very similar, in that the radii are dependent on time to the power of 0.38 and 0.40 respectively.

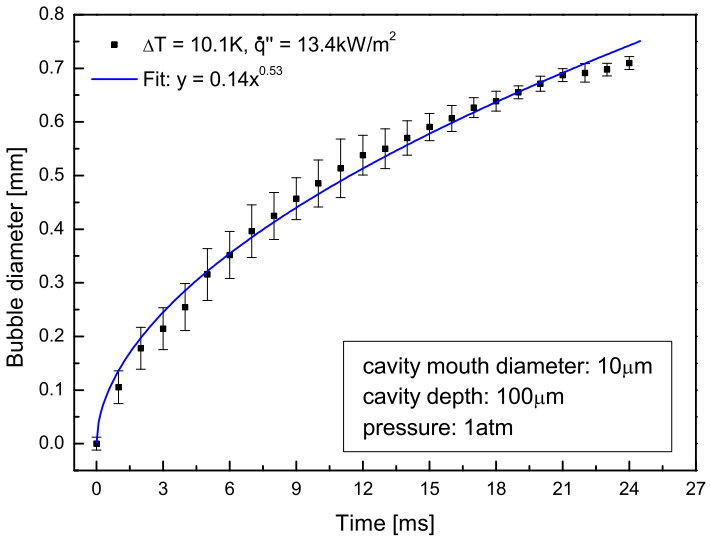

Figure 4.4: *Average bubble growth of three successive bubbles with a wall superheat of 10.1 K and an applied heat flux of 13.4 kW/m² at atmospheric pressure from an isolated cavity (S3) with a nominal mouth diameter of 10 μm and a depth of 100 μm. A trend line was fitted to the data.*

In Figure 4.4 the bubble growth of three successive bubbles for a wall superheat of $10.1\,\mathrm{K}$ and applied heat flux of $13.4\,\mathrm{kW/m^2}$ is presented. As for the lower superheat, the data were fitted by a power law. The departure diameter is between $0.68\,\mathrm{mm}$ and $0.72\,\mathrm{mm}$. The fast initial growth seen for the lower wall superheat is less distinctive. The empirical law found for a wall superheat of $10.1\,\mathrm{K}$, where the diameter is proportional to the time to the power of 0.53, is in agreement with the growth rate found in most analytical studies.

In Figure 4.5 the growth rates for both superheats are shown normalised to allow a comparison. Time t was normalised with the total bubble growth time t_g and the average bubble diameter $\overline{D_b}$ with the average departure diameter $\overline{D_d}$. For the low superheat, the bubble growth rate becomes very small before lift-off, which may be a consequence of the reduction in contact area. For the higher wall superheat, the bubble growth rate decreases less, the bubble lifts off faster and departs more suddenly. The normalisation is only for shape comparison of the bubble growth from the two different cavities,

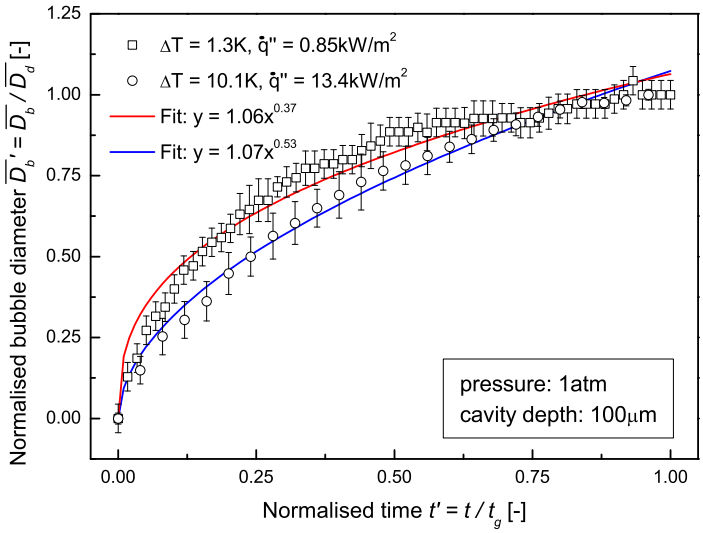

Figure 4.5: *Comparison of the bubble growth for two different wall superheats 1.3 K and 10.1 K from the same isolated cavity (S3) with a nominal mouth diameter of 10 μm and a depth of 100 μm at atmospheric pressure. Trend lines were fitted to both sets of data.*

as irregularities of the departure time caused by random disturbances during the slow final bubble growth may distort the shape of the curves.

Bubble growth from S8 on the third generation test section was measured for applied heat fluxes of 0.46, 2.36 and $4.48\,{}^{\mathrm{kW}}/_{\mathrm{m}^2}$, resulting into wall superheats of 1.4, 4.8 and $8.1\,\mathrm{K}$ at $1\,\mathrm{bar}$, and are presented in Fig. 4.6. Each curve represents the average of 10 successive bubbles at each wall superheat. The general behaviour of the bubble growth from the $80\,\mu\mathrm{m}$ deep cavity on the third generation test section is very similar to observations of bubble growth from the $100\,\mu\mathrm{m}$ deep cavity on the second generation device. The bubble growth time is decreasing with increasing wall superheat and for higher wall superheats the bubbles departed before the growth rate could slow down significantly. However, the bubble growth time at the low wall superheat was for the $100\,\mu\mathrm{m}$ deep cavity considerably longer compared to that of the $80\,\mu\mathrm{m}$ deep cavity at the lowest superheat, despite the similar departure diameter. Comparing the waiting times for bubble growth at the lowest wall superheat from the two different cavities, re-

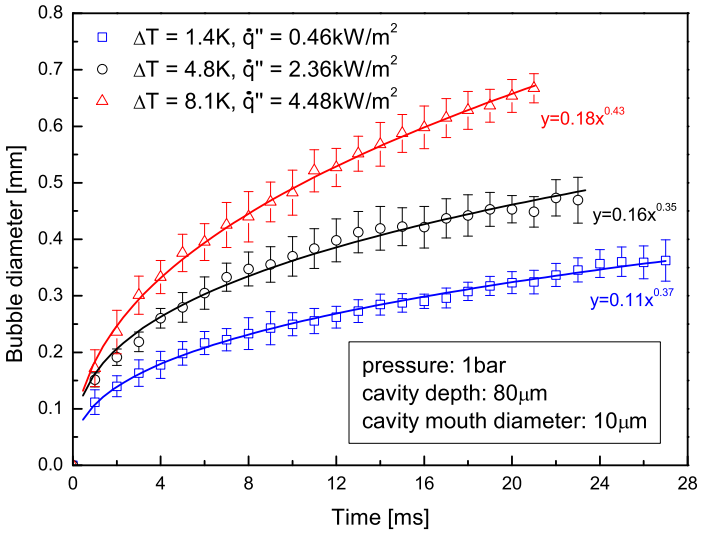

Figure 4.6: *Comparison of the average bubble growth of 10 successive bubbles for three different wall superheats 1.4 K, 4.8 K and 8.1 K from the cavity (S8) which is 80 μm deep and has a nominal mouth diameter of 10 μm at 1 bar. Trend lines were fitted to all three sets of data.*

veals that for the slower bubble growth it is around three times longer, which is almost the same ratio as for the bubble growth times. Although the wall superheat and the pressure were slightly different, it does not explain the observed discrepancy between the two cavities. Moghaddam and Kiger [110, 111] found for bubble growth from an artificial cavity cases with and without waiting time, despite not varying the wall superheat. As discussed in section 2.2.5, differences in the evolution of heat transfer and bubble shape during growth were reported, no explanation for the occurrence of cases with and without waiting time was, however, given.

Bubble growth presented in Fig. 4.3 and 4.4 was compared to common correlations in the existing literature and plotted in Fig. 4.7 and 4.8. The correlation in Eq. 2.20 suggested by Mikic *et al.* [9] followed the assumption of Bošnjaković [98] that all the energy necessary for bubble growth is supplied from the relaxation layer, a superheated liquid layer surrounding the bubble dome. Heat is transferred from the heated wall to the bulk liquid through transient thermal conduction. The correlation predicts the bubble growth for the low wall superheat very closely. For the higher superheat the correlation fails to match the initial growth rate, despite predicting an equal departure diameter.

Mikic *et al.* take the waiting time between succeeding bubbles into account, which is the time needed for the superheated layer to recover after the substrate was rewetted by cooler bulk liquid. Throughout our experiments the waiting time for high wall superheats was generally shorter than the temporal resolution of the high-speed imaging sequence, i.e., $1\,\mathrm{ms}$.

The correlation of Fritz and Ende [10] discussed in Eq. 2.18 and with slightly different parameters suggested by Forster and Zwick [7] and Plesset and Zuber [8], section 2.2.5, were compared to our experimental measurements. The correlations, as in the case of Mikic *et al.* [9], are based on transient thermal conduction. The latter authors took additionally into account the forces acting on the growing bubbles, which were determined from the impulse equations including inertia force. This leads to small changes for the numerical constant calculated by Fritz and Ende. Forster and Zwick, and Plesset and Zuber both over predict the bubble growth for the low and high wall superheat. Fritz and Ende are closer, they, however, over predict the experiment at the higher superheat and under predict it for the lower. If the constant $\sqrt{4/\pi}$ suggested by Fritz and Ende is multiplied by 1.29 to fit the experimentally measured departure diameter, the correlation fails to follow the curve between 5 and $45\,\mathrm{K}$. For the experiment at $10.1\,\mathrm{K}$ Fritz and Ende's correlation was multiplied by 0.73, in which case the correlation predicts the bubble growth almost perfectly, Fig. C.3 and C.4 in appendix C.

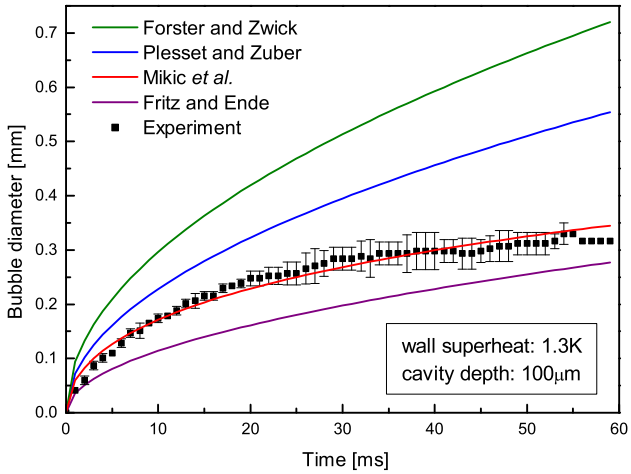

Figure 4.7: *Comparison of experimental bubble growth for a wall superheat of 1.3 K at atmospheric pressure from an isolated cavity (S3) with correlations from Forster and Zwick [7], Plesset and Zuber [8], Mikic et al. [9] and Fritz and Ende [10].*

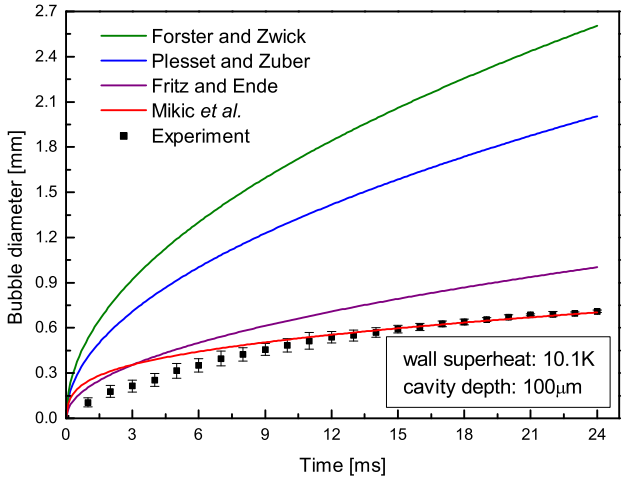

Figure 4.8: *Comparison of experimental bubble growth for a wall superheat of 10.1 K at atmospheric pressure from an isolated cavity (S3) with correlations from Forster and Zwick [7], Plesset and Zuber [8], Mikic et al. [9] and Fritz and Ende [10].*

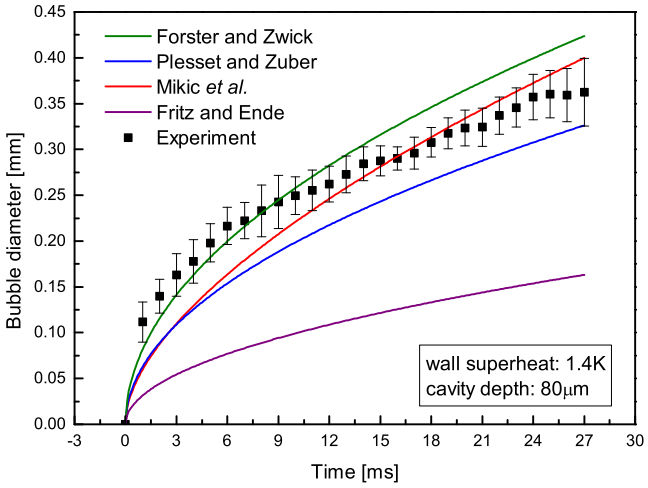

Figure 4.9: *Comparison of experimental bubble growth for a wall superheat of 1.4 K at 1 bar from an isolated cavity (S8) with correlations from Forster and Zwick [7], Plesset and Zuber [8], Mikic et al. [9] and Fritz and Ende [10].*

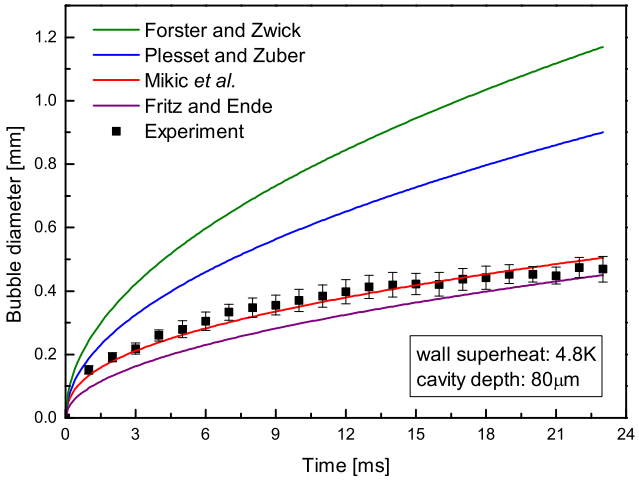

Figure 4.10: *Comparison of experimental bubble growth for a wall superheat of 4.8 K at 1 bar from an isolated cavity (S8) with correlations from Forster and Zwick [7], Plesset and Zuber [8], Mikic et al. [9] and Fritz and Ende [10].*

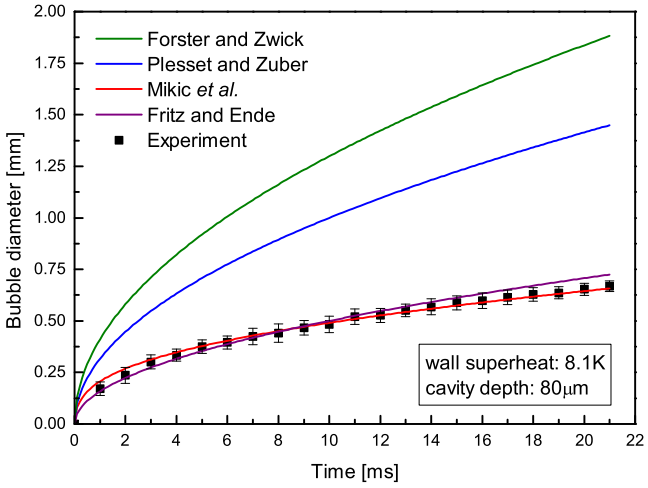

Figure 4.11: *Comparison of experimental bubble growth for a wall superheat of 8.1 K at 1 bar from an isolated cavity (S8) with correlations from Forster and Zwick [7], Plesset and Zuber [8], Mikic et al. [9] and Fritz and Ende [10].*

In Figure 4.9, 4.10 and 4.11 the same correlations as above were compared to the experimental measurements presented in Fig. 4.6. The correlation of Mikic *et al.* is best in predicting the bubble growth. The prediction improves with increasing wall superheat.

For the lowest superheat, the bubble growth is enclosed by the correlation curves of Forster and Zwick and Plesset and Zuber. Fritz and Ende's correlation fails to predict the bubble growth. However, for the two higher superheats Fritz and Ende's correlation predicts the shape almost as well as Mikic *et al.*, whereas the other two correlations are over predicting the experiment. If the constant in Fritz and Ende's correlation was multiplied by 0.92, 1.05 and 2.23 to fit the departure diameter, the agreement is satisfying, Fig. C.5, C.6 and C.7 in appendix C.

The bubble growth correlation by Cooper [11], presented in Eq. 2.23 and 2.24, is suggesting that the main heat energy for bubble growth is supplied by an evaporating micro-layer forming below the growing bubble.

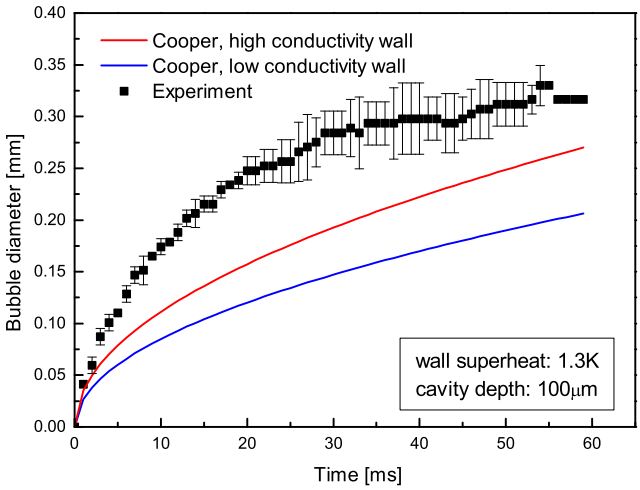

Figure 4.12: *Comparison of experimental bubble growth for a wall superheat of 1.3 K at atmospheric pressure from an isolated cavity (S3) with correlations from Cooper [11].*

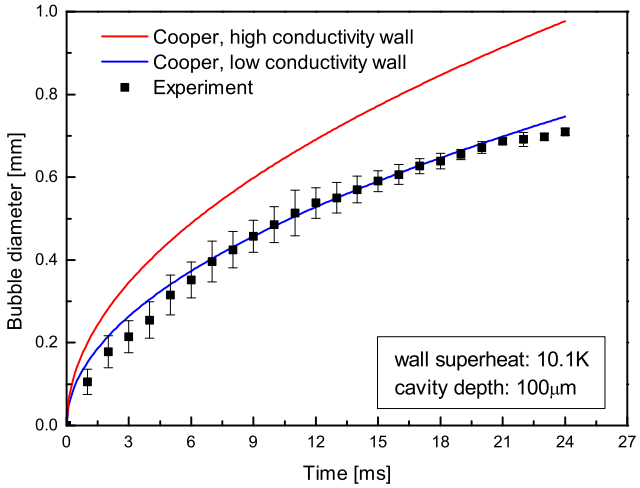

Figure 4.13: *Comparison of experimental bubble growth for a wall superheat of 10.1 K at atmospheric pressure from an isolated cavity (S3) with correlations from Cooper [11].*

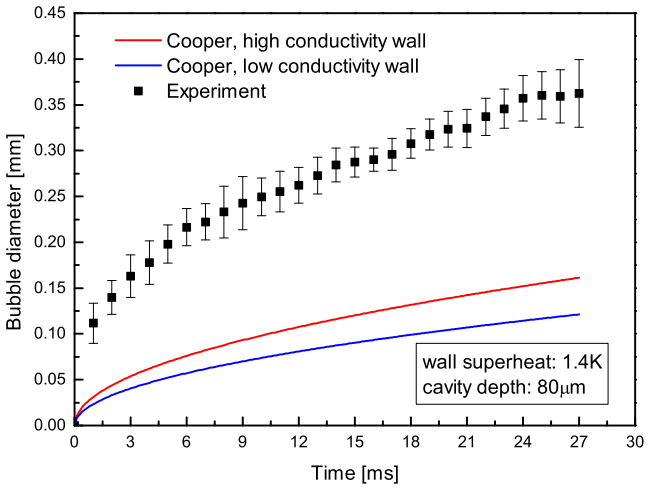

Figure 4.14: *Comparison of experimental bubble growth for a wall superheat of 1.4 K at 1 bar from an isolated cavity (S8) with correlations from Cooper [11].*

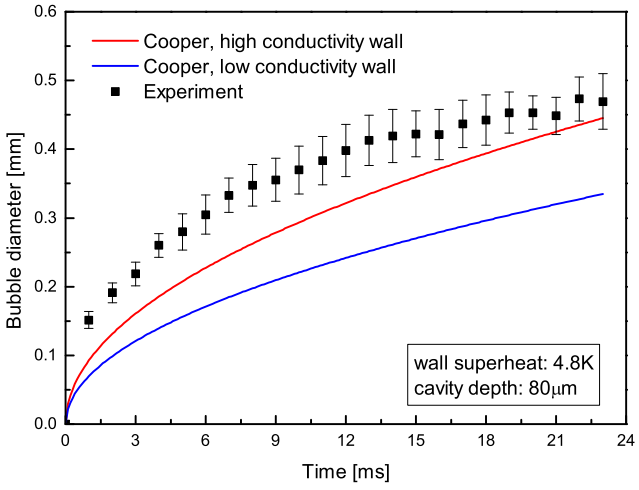

Figure 4.15: *Comparison of experimental bubble growth for a wall superheat of 4.8 K at 1 bar from an isolated cavity (S8) with correlations from Cooper [11].*

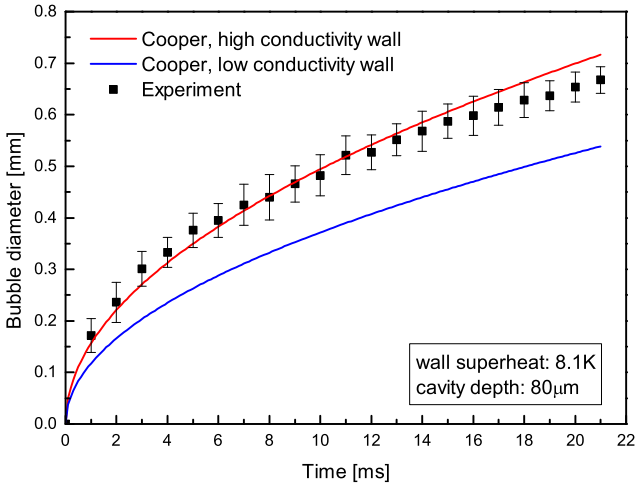

Figure 4.16: *Comparison of experimental bubble growth for a wall superheat of 8.1 K at 1 bar from an isolated cavity (S8) with correlations from Cooper [11].*

Comparison of the obtained data presented in Fig. 4.3 and 4.4 reveals that for the lower superheat the correlations for a highly and poorly conducting wall under predict the experimentally determined bubble growth, Fig. 4.12 and 4.13. However, for the higher wall superheat, the correlation for the poorly conducting wall is in agreement with the experiment. This is surprising, as the silicon boiling substrate is thermally highly conductive.

A possible impact of the substrate thickness, however, was mentioned by Cooper. In this experiment the substrate was $380\,\mu\mathrm{m}$ thin. Comparing Cooper's correlation to the bubble growth presented in Fig. 4.14, 4.15 and 4.16, shows a similar result. For the lower two superheats both of Cooper's equations under predict the bubble growth. For the highest superheat the correlation for a highly conductive wall is in good agreement with the experiment. This is in agreement with the observation of Cooper and Lloyd [102], that higher wall temperatures tend to promote the formation of a micro-layer between the heated wall and the growing bubble.

Table 4.1: *Initial contact angle φ_0 and angle decrease factor f_φ used in the simulations A, B, C, D and E.*

	φ_0	f_φ	HTC model
A	$32°$	0.60	CL
B	$64°$	0.60	CL
C	$64°$	0.90	CL
D	$64°$	0.97	CL
E	$32°$	0.60	ML

As mentioned earlier, experimental data collected during this study are used as input and are the first step to validate a numerical simulation developed at Brunel University [29, 145]. The code, based on the FORTRAN language, solves the temperature three-dimensional space and time equation in a solid plate horizontally immersed in a liquid at saturated conditions, so that pool nucleate boiling may occur at fixed locations, called nucleation sites, that simulate artificial cavities on the top surface. The code combines the exact explicit solution of the temperature field in the solid plate with simplified models for heat removal from the top surface, for bubble growth mechanisms and for interactions between sites, including coalescence. Code flexibility includes the use of different plate materials and fluids (i.e., different heat transfer mechanisms) as well as variable potential activation site distributions on the upper surface with volumetric heat source or heat flux applied on the back of the plate.

A brief summary of compared results from 5 experimental cases at variable heat fluxes and superheats is shown in Table B.3 in appendix B. Five different simulations (A, B, C, D and E) have been run for each case, using for the heat transfer coefficient models (HTC) the contact-line (CL) or micro-layer (ML) model, with variable initial apparent contact angle φ_0 and angle decrease fraction f_φ. The vapour bubble is supposed to grow as a truncated sphere. The apparent contact angle is constant for the initial stage of bubble growth, i.e., until the bubble radius reaches a fixed angle decrease fraction of the bubble departure radius, and will then linearly decrease to zero by the ratio of bubble volume and maximum bubble volume afterwards. The CL model was hypothesised by Stephan and Hammer [146] assuming that the highest heat transfer coefficients are reached in the micro-region due to surface tension and adhesion forces acting in this region. The ML model was incorporated as suggested by Golobič [147].

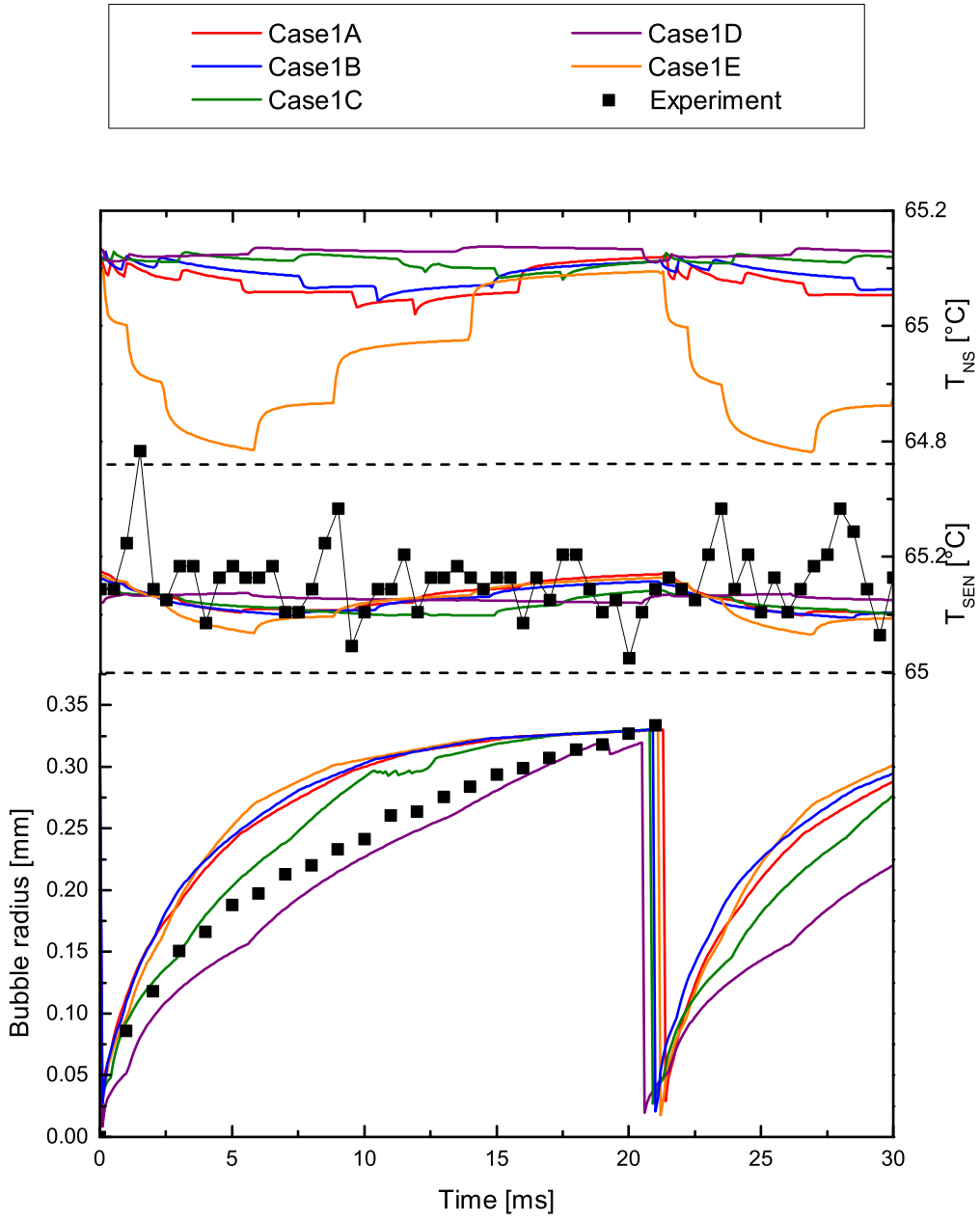

Figure 4.17: *Bubble radii, sensor and nucleation site temperature comparison between experimental and numerical results for case 1A, 1B, 1C, 1D and 1E.*

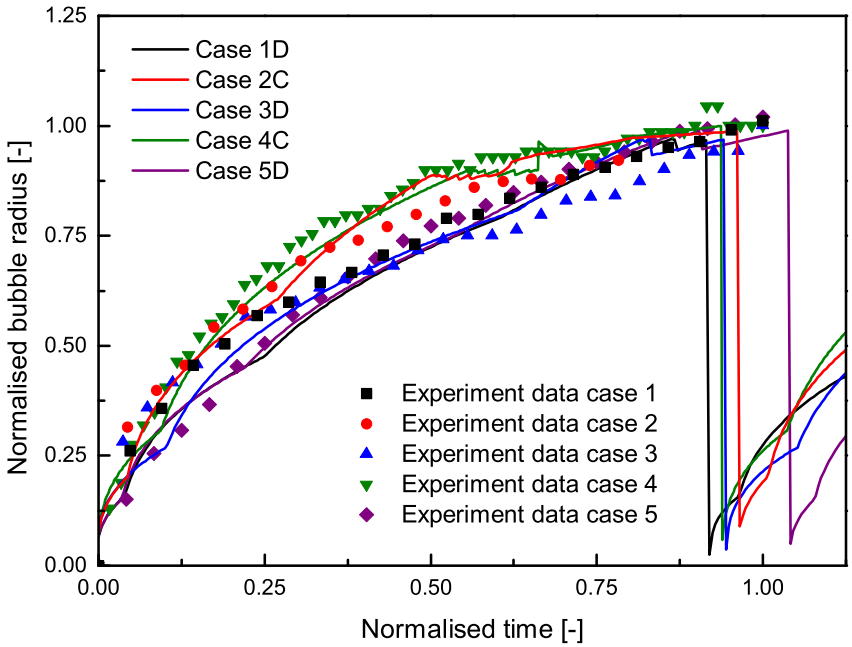

Figure 4.18: *Dimensionless radii comparison between experimental and numerical results with* R_b/R_d *and* t/t_g.

Table 4.1 shows the variation of φ_0 and f_φ for the CL model (A, B, C and D). This variation influences the heat transfer coefficient of the CL model (automatically adjusted by the code during simulations to match the experimental bubble growth times); the values of the heat transfer coefficient are only illustrative, since they strongly depend on the refined cell sizes of the mesh (and then indirectly on the bubble radius, initial contact angle and angle decrease factor) but they show a decrease with increasing φ_0 and f_φ.

Figure 4.17 compares the different numerical and experimental results for case 1, Table B.3 in appendix C. The bubble radius history shows that the different apparent contact angle does not sensibly affect the bubble growth in simulations, while the final stage of the bubble growth is severely flattened by increasing f_φ. The best matching simulations for case 1 are C for the initial stage of bubble growth and D during the second stage, i.e., for $\varphi_0 = 64°$ and f_φ between 0.9 and 0.97. The temperature T_{SEN}, averaged

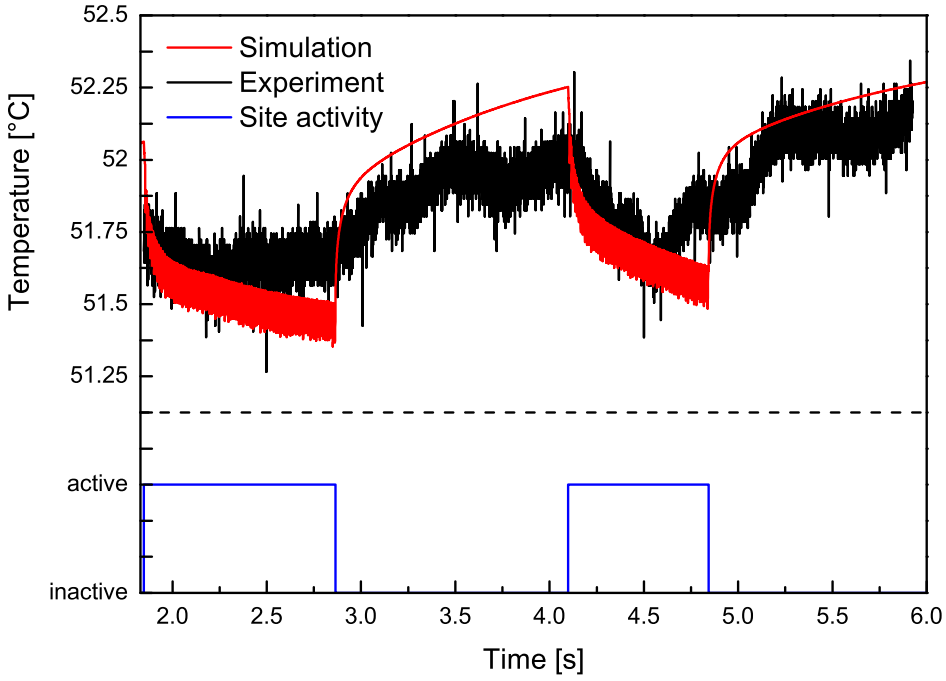

Figure 4.19: *Comparison of the temperature response between experiment (S8) and simulation over a long period at sub-atmospheric pressure of 0.463 bar at an applied heat flux of 8.6* $^{kW}/_{m^2}$.

temperature over an area equal to the size of the sensor (chapter 3, sections 3.2.2 and 3.2.3), shows good agreement with experimental data when the temperature is lowered by $0.42\,\mathrm{K}$ in the graph, an adjustment that is lower than the measurable error. No sensible variations in temperatures between the different simulations are evident due to the large measuring area, at least twice the size of the maximum contact area. An additional simulation with $\varphi_0 = 32°$ and $f_\varphi = 0.6$ but applying the ML model is also shown in Fig. 4.17 (case 1E). This case shows much larger temperature variation at the nucleation site T_{NS} but a similar trend for T_{SEN}. The simulations suggest that it will not be possible to define the most appropriate HTC model from measurements with the present size of sensors.

Figure 4.18 shows a very good agreement between numerical and experimental results for the dimensionless bubble radius R_b/R_d versus dimensionless time t/t_g. The case shown for each simulation represents the best matching simulation, i.e., C for cases 2 and 4, and D for cases 1, 3 and 5. No waiting time or horizontal coalescence have been predicted in any of the simulated cases, contrary to experimental observations of significant waiting time for low heat fluxes (cases 3 and 4). Vertical bubble coalescence has not been simulated, since it did not occur during the considered experiments. The effect of this phenomenon on heat transfer must be experimentally verified and implemented in the future if necessary. However, results presented in section 5 show that this phenomenon did not affect the bubble volume at bubble departure.

Experiments at sub-atmospheric pressure have been run for the third generation test section to obtain larger bubble departure radii and consequent larger contact areas with possibly larger variations in the measured temperature. Analysis of the temperature response of the sensor located at the same cavity over a long period (S8), approximately $4\,\mathrm{s}$ (with applied heat flux of $8.6\,\mathrm{kW/m^2}$), is shown in Fig. 4.19. The pressure was reduced to $0.463\,\mathrm{bar}$, leading to departure radii of approximately $0.45\,\mathrm{mm}$ and bubble growth time of approximately $10\,\mathrm{ms}$. The cavity experimentally demonstrated large-period intermittent irregularities in activity, which could be reproduced artificially in the simulations by manually changing the activation temperature according to the experimental activity curve. Comparison with numerical results (case 1A) shows a good agreement, although variations in the simulations are faster and larger than in experiments, possibly due to hydrodynamic effects in the liquid that are not modelled. This still does not explain why the site becomes active or recovers slower when inactive. However, the period with no bubble nucleation increases with wall superheat and does not show any regular behaviour.

4.2 Bubble departure frequency and departure diameter

Figure 4.20 to 4.28 show measured bubble departure frequencies for an isolated artificial cavity (S3, on the second generation test section) with a nominal mouth diameter of $10\ \mu\mathrm{m}$ and nominal depths of 40, 80 and $100\ \mu\mathrm{m}$ for pressures of 1, 1.25 and $1.5\ \mathrm{atm}$. The minimum and maximum applied heat flux for each case can be found in Table B.4 in appendix B. Bubble departure frequency is the reciprocal of the sum of waiting time and bubble growth time. Each point represents the average value for five successive bubbles and the error bars indicate the variation between each bubble.

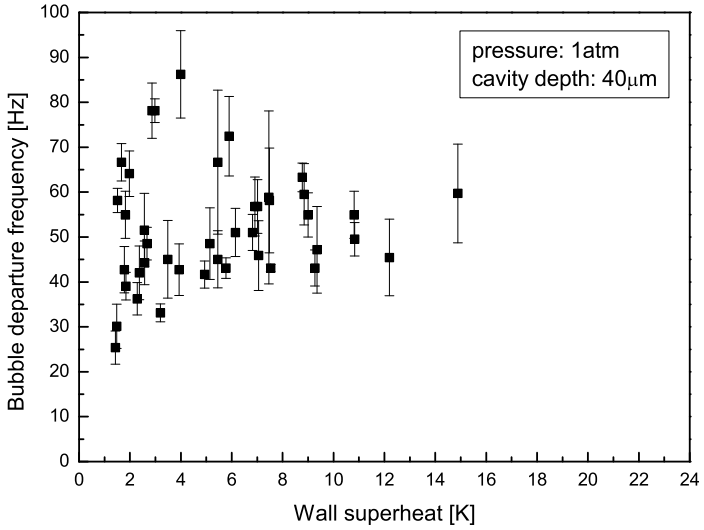

Figure 4.20: *Bubble departure frequency as a function of wall superheat from an isolated cavity (S3) with a nominal mouth diameter of 10 μm and a depth of 40 μm at 1 atm.*

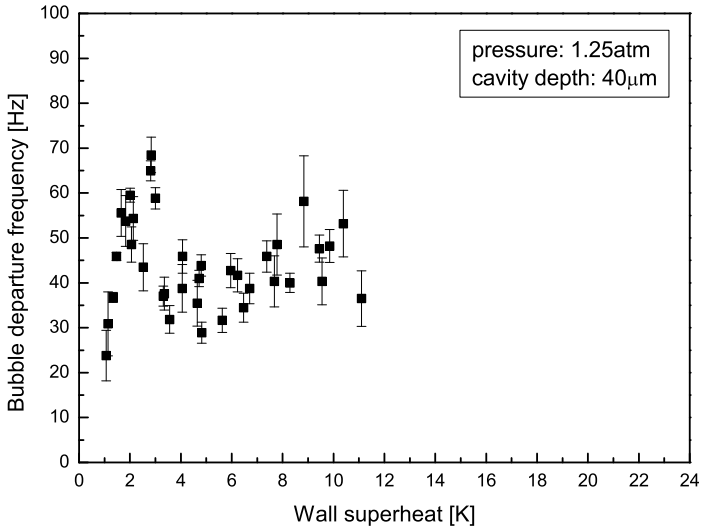

Figure 4.21: *Bubble departure frequency as a function of wall superheat from an isolated cavity (S3) with a nominal mouth diameter of 10 μm and a depth of 40 μm at 1.25 atm.*

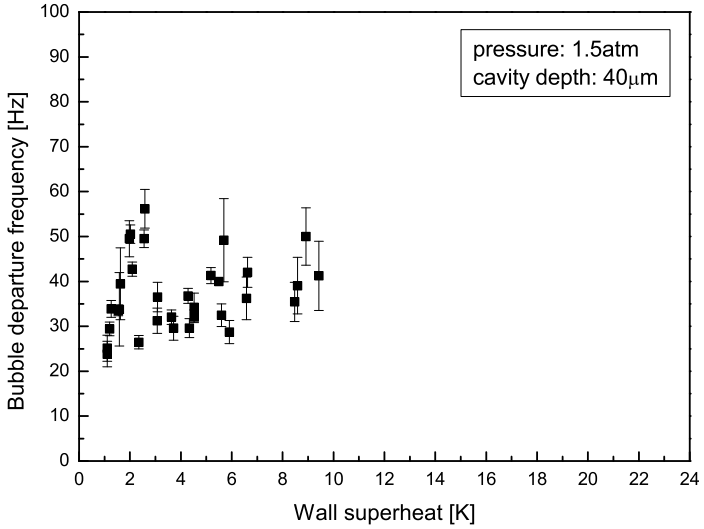

Figure 4.22: *Bubble departure frequency as a function of wall superheat from an isolated cavity (S3) with a nominal mouth diameter of 10 μm and a depth of 40 μm at 1.5 atm.*

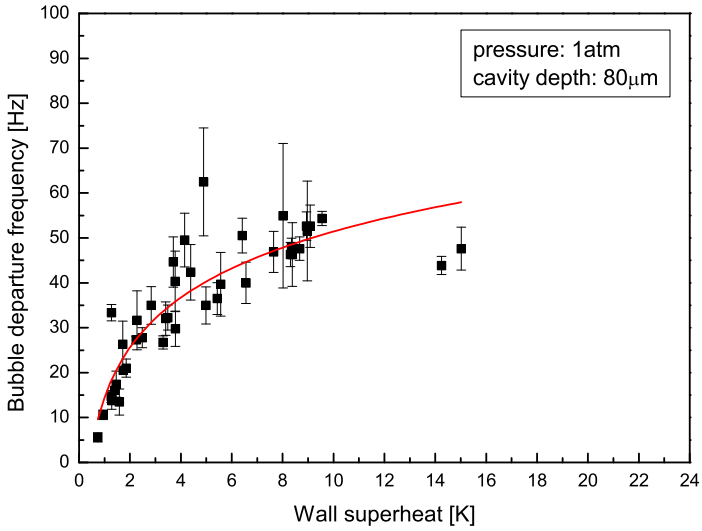

Figure 4.23: *Bubble departure frequency as a function of wall superheat from an isolated cavity (S3) with a nominal mouth diameter of 10 μm and a depth of 80 μm at 1 atm.*

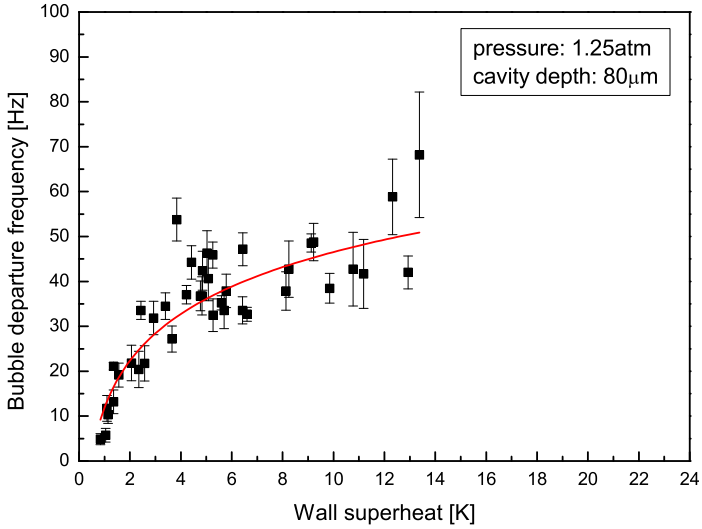

Figure 4.24: *Bubble departure frequency as a function of wall superheat from an isolated cavity (S3) with a nominal mouth diameter of 10 μm and a depth of 80 μm at 1.25 atm.*

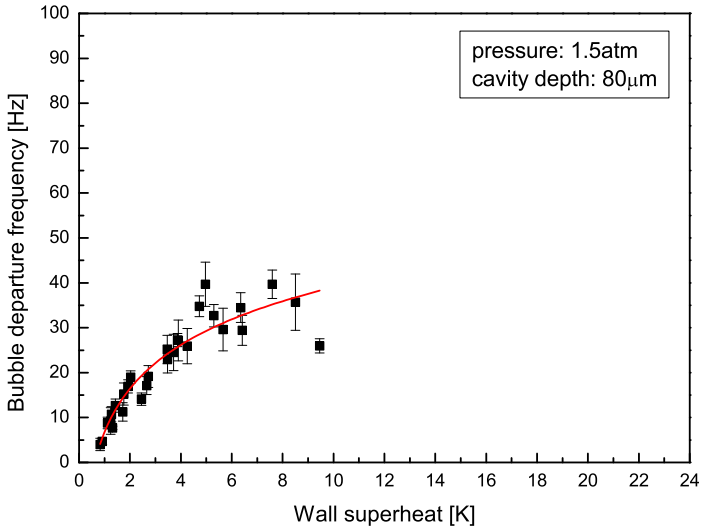

Figure 4.25: *Bubble departure frequency as a function of wall superheat from an isolated cavity (S3) with a nominal mouth diameter of 10 μm and a depth of 80 μm at 1.5 atm.*

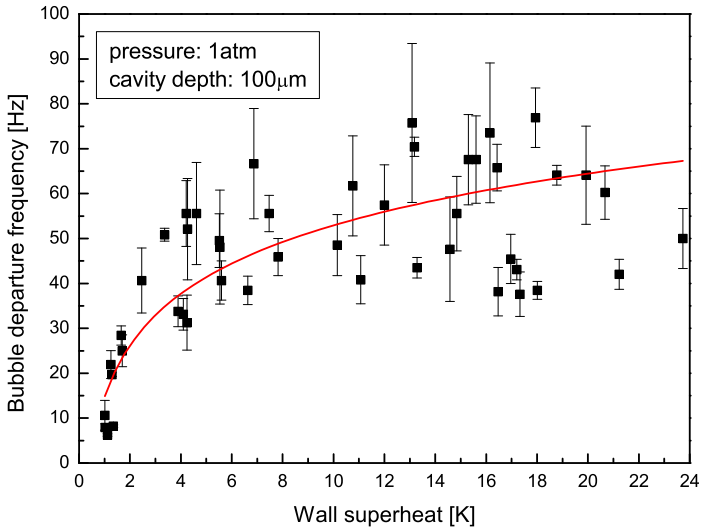

Figure 4.26: *Bubble departure frequency as a function of wall superheat from an isolated cavity (S3) with a nominal mouth diameter of 10 μm and a depth of 100 μm at 1 atm.*

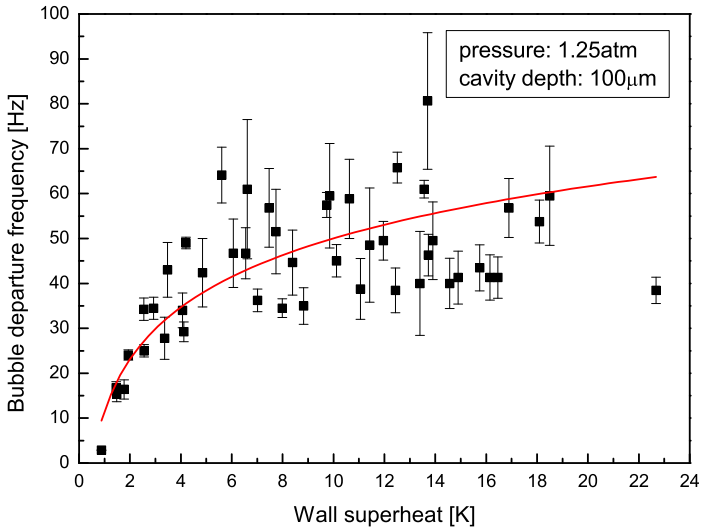

Figure 4.27: *Bubble departure frequency as a function of wall superheat from an isolated cavity (S3) with a nominal mouth diameter of 10 μm and a depth of 100 μm at 1.25 atm.*

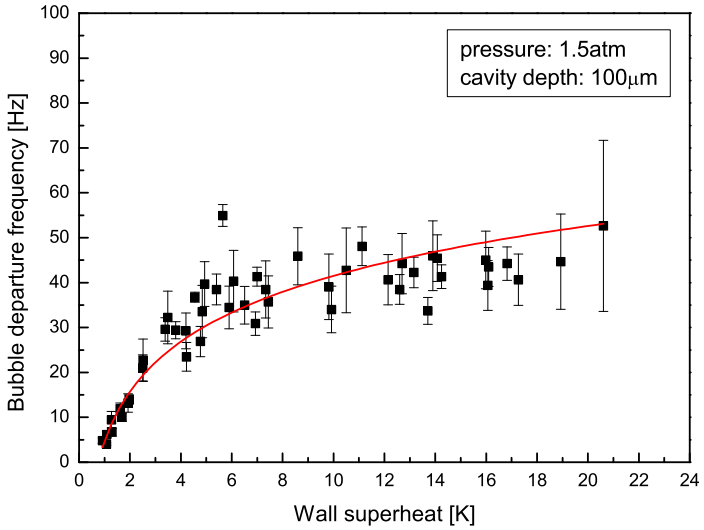

Figure 4.28: *Bubble departure frequency as a function of wall superheat from an isolated cavity (S3) with a nominal mouth diameter of 10 μm and a depth of 100 μm at 1.5 atm.*

For the $40\,\mu\mathrm{m}$ deep cavities, Fig. 4.20, 4.21 and 4.22, the lowest possible wall superheat that could maintain bubble production was about $1\,\mathrm{K}$ for all three pressures, consistent with the theoretically determined equilibrium superheats in Table C.1 in appendix C and is within the experimental uncertainty of $0.5\,\mathrm{K}$. It was possible to measure frequencies for temperatures up to $15\,\mathrm{K}$ for the lowest pressure and up to almost $10\,\mathrm{K}$ for the highest pressure before any unwanted nucleation sites were activated, i.e., with increasing pressure unwanted nucleation sites on the substrate appear earlier. No strong dependence of frequency on wall superheat was found. A slight decrease in frequency with increasing pressure is obscured by the scatter in the data.

In Figure 4.23, 4.24 and 4.25 the bubble departure frequencies for an isolated artificial cavity (S3, on the second generation test section) with a nominal mouth diameter of $10\,\mu\mathrm{m}$ and a nominal depth of $80\,\mu\mathrm{m}$ for the same three different pressures are presented. The frequency increases in a near-linear fashion up to wall superheats of 4 to $5\,\mathrm{K}$. For higher wall superheats the frequency increases only slightly with increasing wall superheat up to the wall superheat, just before any unwanted bubble nucleation appears. Frequencies decrease with increasing pressure and the data is generally less scattered.

For the same three pressures but for an isolated artificial cavity (S3, on the second generation test section) depth of $100\,\mu\mathrm{m}$ and mouth diameter of $10\,\mu\mathrm{m}$ measured frequencies are presented in Fig. 4.26, 4.27 and 4.28. The frequency is initially found to increase rapidly with increasing superheat. This dependency is less noticeable above wall superheats between 4 to $5\,\mathrm{K}$ and is similar to the cavity depth of $80\,\mu\mathrm{m}$. As the frequency measurements were possible up to higher superheats, the trend after 4 to $5\,\mathrm{K}$ is clearer. The data seem to scatter less with increasing pressure and the possible superheat without any unwanted nucleation sites on the substrate decreases, but less distinctive as for the $80\,\mu\mathrm{m}$ deep cavity. The frequencies at 1 and $1.25\,\mathrm{atm}$ are initially very similar. The decrease of the frequencies for the same superheats with increasing pressure is more remarkable.

Both, the 80 and $100\,\mu\mathrm{m}$ deep cavity, show initially a quick increase of the frequency with increasing superheat, this is not the case for a $40\,\mu\mathrm{m}$ cavity, where frequencies

for all superheats are similar. All measured frequencies for the two deeper cavities level off after a wall superheat of $4\,\mathrm{K}$, however, this behaviour is more pronounced for the $100\,\mu\mathrm{m}$ cavity. The standard deviation tends to be smaller for lower superheats as the growth time is longer and variations of even a few milliseconds represent a relatively small change in frequency. This is especially the case for Fig. 4.23 to 4.28. Comparing the FC-72 frequency measurements for different cavity depths shows that there is less scatter for the $80\,\mu\mathrm{m}$ than the $100\,\mu\mathrm{m}$ deep cavity, whereas the shortest cavity indicates the largest scatter. The deepest cavity reaches the highest superheats without other nucleation sites appearing on the substrate.

In Figure 4.29 the measured bubble departure frequencies for FC-72 from the $40\,\mu\mathrm{m}$, $80\,\mu\mathrm{m}$ and $100\,\mu\mathrm{m}$ cavity at atmospheric pressure are plotted together with experimental measurements published in Siedel *et al.* [12]. Siedel *et al.* measured the bubble frequency for n-pentane on copper at atmospheric pressure. There were two identical artificial cavities with a spacing of $660\,\mu\mathrm{m}$ in between. The cavities were $500\,\mu\mathrm{m}$ deep and had a mouth diameter of $180\,\mu\mathrm{m}$.

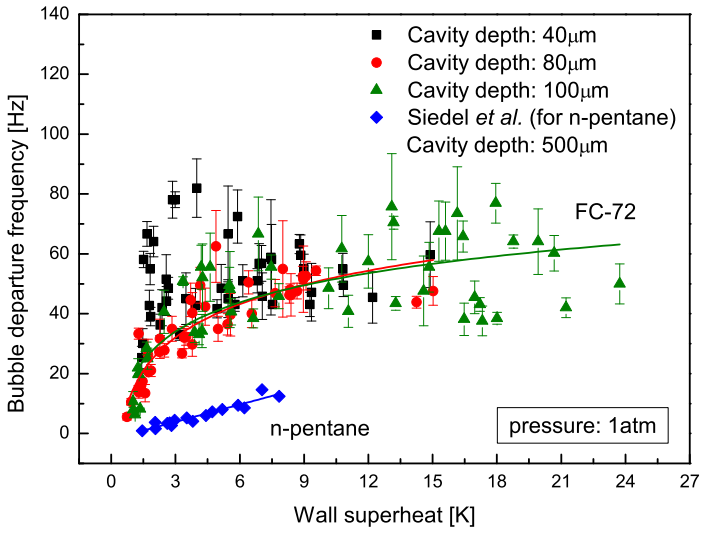

Figure 4.29: *Comparison of data from Siedel et al. [12] with the measured frequencies of 3 different cavity depths as a function of wall superheat.*

Following the criteria from Zhang and Shoji [6], this arrangement cannot be considered as two isolated cavities for bubble departure diameters above $0.22\,\mathrm{mm}$. The bubble departure diameters for all applied wall superheats exceed this limit. The given values for wall superheats above $6\,\mathrm{K}$ represent the frequency of two, prior to departure coalesced, bubbles. The departure frequency of n-pentane increases linearly with increasing wall superheat and is lower than for FC-72. The difference between the two liquids increases for higher wall superheats.

For high wall superheats there was occasional vertical coalescence at the observed cavity, but for the present measurements only sequences of frames without coalescence were considered. Nucleation only occurred at the artificial cavity on the silicon surface. However, there is unavoidable minor bubble growth at the gap between the silicon chip and the device holder, which occurs at least $7.5\,\mathrm{mm}$ for S3 and $10.725\,\mathrm{mm}$ for S8 away from the observed artificial nucleation site. Interference would only occur for bubble departure diameters larger than $2.5\,\mathrm{mm}$ for S3 and $3.575\,\mathrm{mm}$ for S8. No interference with the studied artificial site was observed at any time.

In Figures 4.30 to 4.38 bubble departure diameters for the above presented frequencies are shown. The error bars indicate the standard deviation of measured departure diameters of five successive bubbles for each wall superheat. The bubble departure diameter increases in a near-linear fashion with increasing wall superheat. There is no obvious influence of the cavity depth and pressure for all measured diameters. However, if the trend lines are compared with each other, small differences are revealed, Fig. C.11 to C.16 in appendix C. Only the regions of wall superheat where all curves have data points are discussed. In Figure C.11, C.12 and C.13 departure diameters for 40, 80 and $100\,\mu\mathrm{m}$ are compared for pressures at 1, 1.25 and $1.5\,\mathrm{atm}$. For low wall superheats the bubble diameter is largest for the $80\,\mu\mathrm{m}$ deep cavity, smallest for the $40\,\mu\mathrm{m}$ deep one and in the middle for $100\,\mu\mathrm{m}$. This is the case for all three pressures. At higher wall superheats the $100\,\mu\mathrm{m}$ deep cavity produces the smallest bubbles for all three pressures.

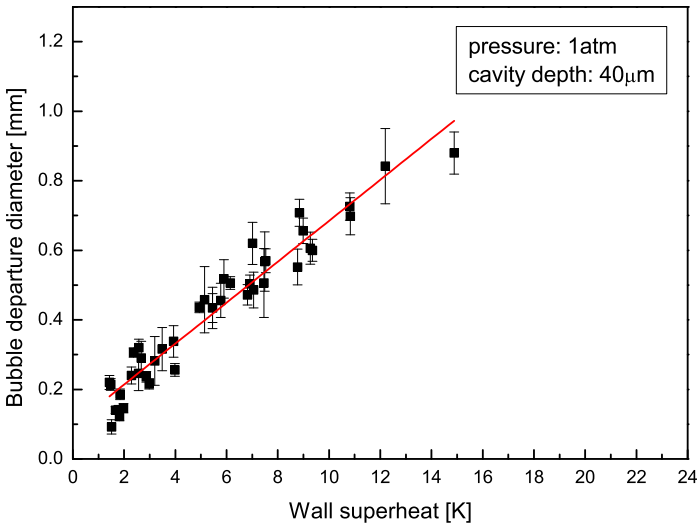

Figure 4.30: *Bubble departure diameter as a function of wall superheat from an isolated cavity (S3) with a nominal mouth diameter of 10 μm and a depth of 40 μm at 1 atm.*

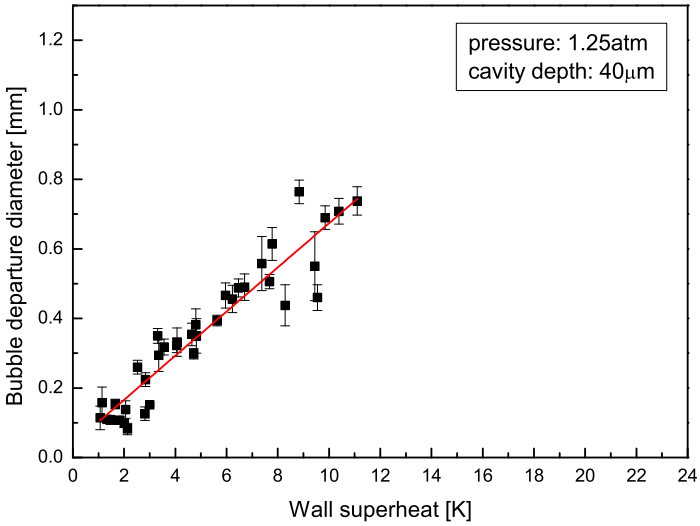

Figure 4.31: *Bubble departure diameter as a function of wall superheat from an isolated cavity (S3) with a nominal mouth diameter of 10 μm and a depth of 40 μm at 1.25 atm.*

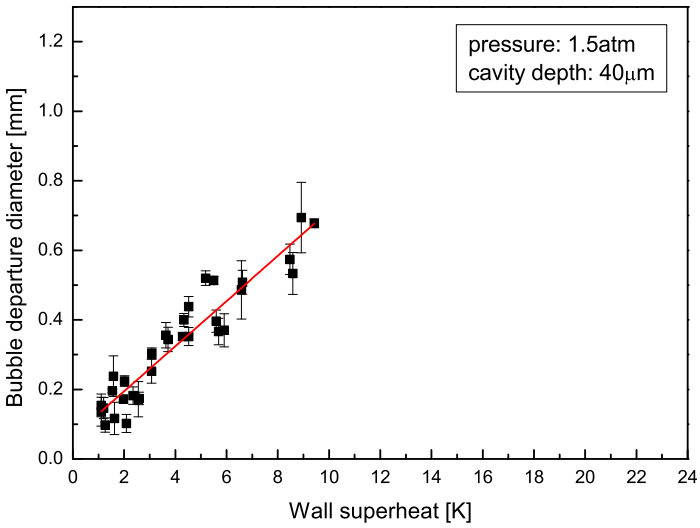

Figure 4.32: *Bubble departure diameter as a function of wall superheat from an isolated cavity (S3) with a nominal mouth diameter of 10 μm and a depth of 40 μm at 1.5 atm.*

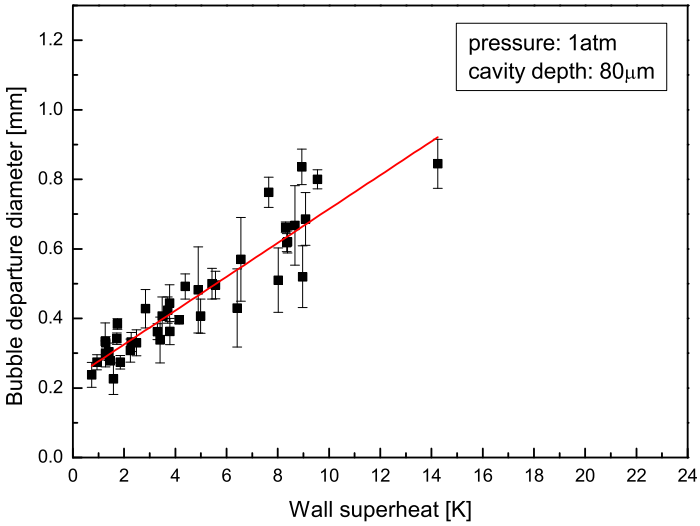

Figure 4.33: *Bubble departure diameter as a function of wall superheat from an isolated cavity (S3) with a nominal mouth diameter of 10 μm and a depth of 80 μm at 1 atm.*

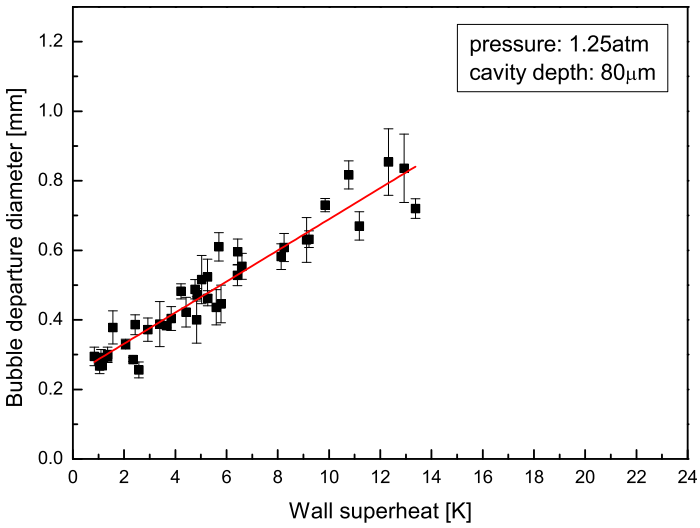

Figure 4.34: *Bubble departure diameter as a function of wall superheat from an isolated cavity (S3) with a nominal mouth diameter of 10 μm and a depth of 80 μm at 1.25 atm.*

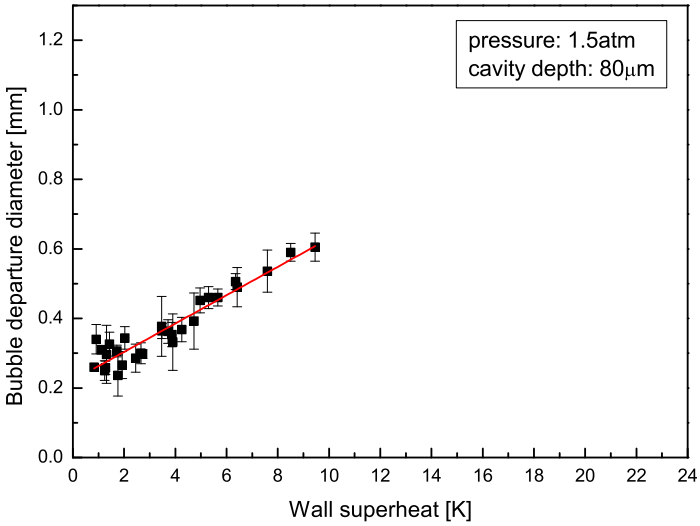

Figure 4.35: *Bubble departure diameter as a function of wall superheat from an isolated cavity (S3) with a nominal mouth diameter of 10 μm and a depth of 80 μm at 1.5 atm.*

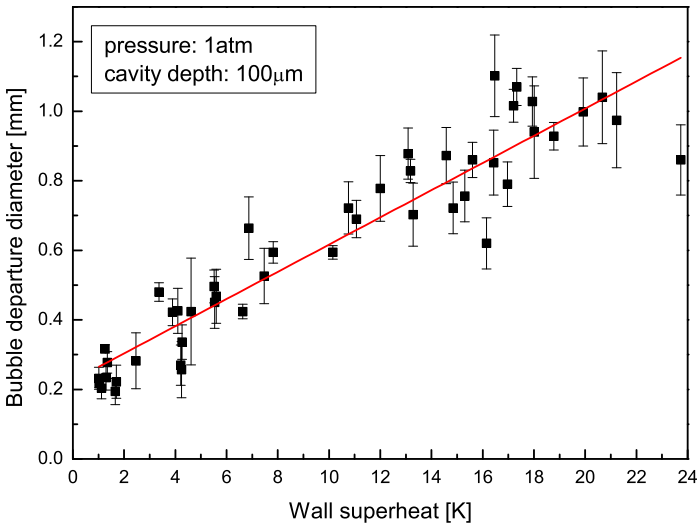

Figure 4.36: *Bubble departure diameter as a function of wall superheat from an isolated cavity (S3) with a nominal mouth diameter of 10 μm and a depth of 100 μm at 1 atm.*

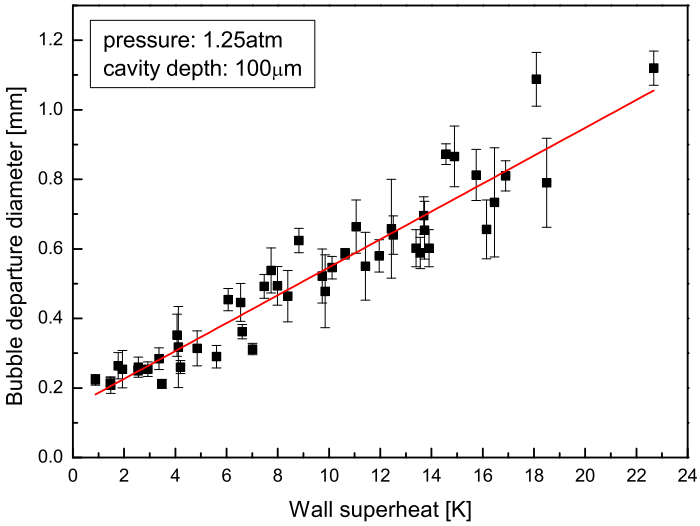

Figure 4.37: *Bubble departure diameter as a function of wall superheat from an isolated cavity (S3) with a nominal mouth diameter of 10 μm and a depth of 100 μm at 1.25 atm.*

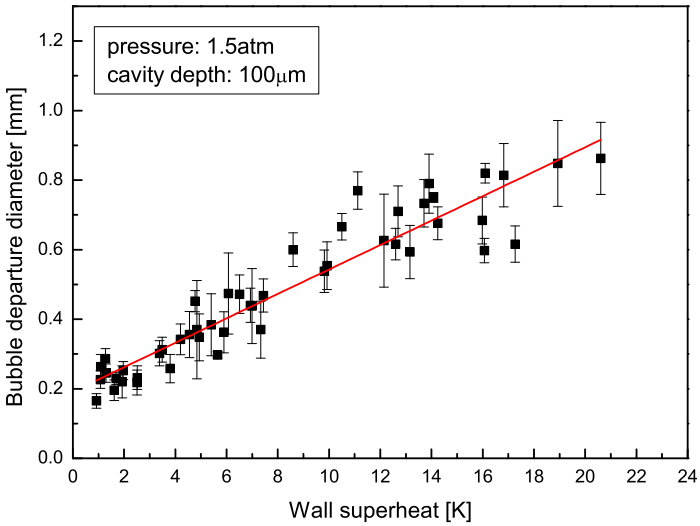

Figure 4.38: *Bubble departure diameter as a function of wall superheat from an isolated cavity (S3) with a nominal mouth diameter of 10 μm and a depth of 100 μm at 1.5 atm.*

The influence of pressure on the bubble departure diameters, presented in Fig. C.14, C.15 and C.16, is small as the trend lines lie very close. However, the differences are slightly increasing with increasing cavity depth. For the two deeper cavities the lowest pressure setting tends to produce the largest departing bubbles. The above comparison has to be treated with care, as the trend lines were fitted to rather scattered data. Here only a few important points were discussed, for a more detailed description see appendix C.

Many correlations for the bubble departure diameter exist in the literature. They cover the effect of a wide range of parameters, such as liquid and vapour properties, wall superheat, applied heat flux and thermal properties of the boiling substrate. Only a few of them were chosen to compare them to the bubble departure diameter with increasing wall superheat for the three different cavity depths, measured at $1\,\mathrm{atm}$.

Correlations from Kutateladze and Gogonin [13], Jenson and Memmel [14], Cole [15] and Gorenflo *et al.* [16] are plotted for the experimental conditions in Fig. 4.39, 4.40, 4.41 and were already discussed in section 2.2.5.

The correlations of Kutateladze and Gogonin and Jenson and Memmel under predict the experimental data. The trend of the data was different and not captured by the models. Cole's correlation is the only correlation which predicts no bubble growth for wall superheats of zero. In contrast to the previous two models, Cole's is of a stronger function of the Jakob number. Although the correlation fails to predict the correct departure diameter, it comes closest to representing the trend or shape of the curves for all three cavity depths, especially for the higher wall superheat reached with the deepest cavity. The departure diameters calculated with the Gorenflo *et al.* model are too small and follow the trend of curve only up to 6 to $8\,\mathrm{K}$. For higher superheats the slope increases more sharply than the experimental data.

In addition to the predictions for the bubble diameter during bubble growth and the bubble departure diameter, many researchers are interested in the relation between bubble departure diameter and bubble release or departure frequency. Mikic and Rohsenow [17] suggested a correlation for $f^{1/2} \cdot \overline{D_d}$, which includes the bubble growth time and the waiting time. In Figure 4.42, 4.43 and 4.44 the experimental results are compared to this correlation. Only the origin of the curve is in agreement, as with increasing wall superheat the correlation is over predicting the experimental data strongly for all cavity depths. Jakob and Fritz [18], and Zuber *et al.* [19] suggested a constant product $f \cdot \overline{D_d}$ with increasing wall superheat. The product calculated from the experimental data is not constant and increases with wall superheat in a near-linear fashion. Both correlations over predict even the largest value of the product of departure diameter and frequency determined from experiments. For Jakob and Fritz this is not surprising as the empirical correlation was given for experiments conducted in water and hydrogen. The two constants are compared to experiments in Fig. C.8, C.9 and C.10 in appendix C. None of the above suggested correlations is in agreement with the experimental data.

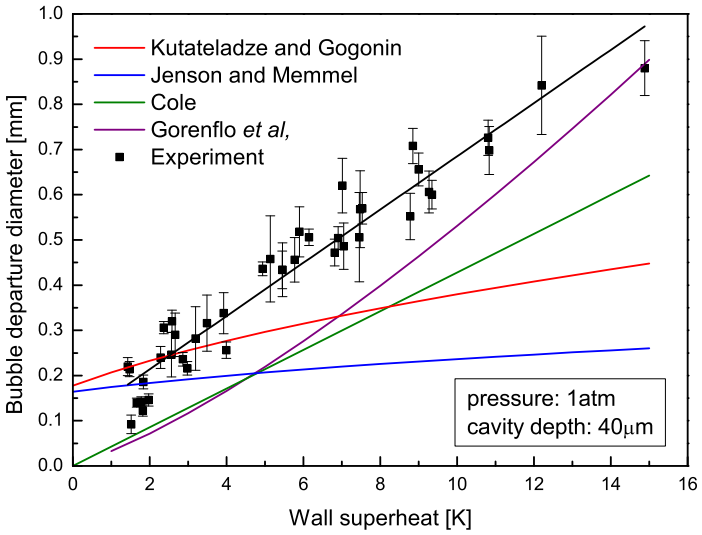

Figure 4.39: *Comparison of the measured bubble departure diameter from an isolated cavity (S3) with a nominal depth of 40 μm at 1 atm with correlations from Kutateladze and Gogonin [13], Jenson and Memmel [14], Cole [15] and Gorenflo et al. [16]*

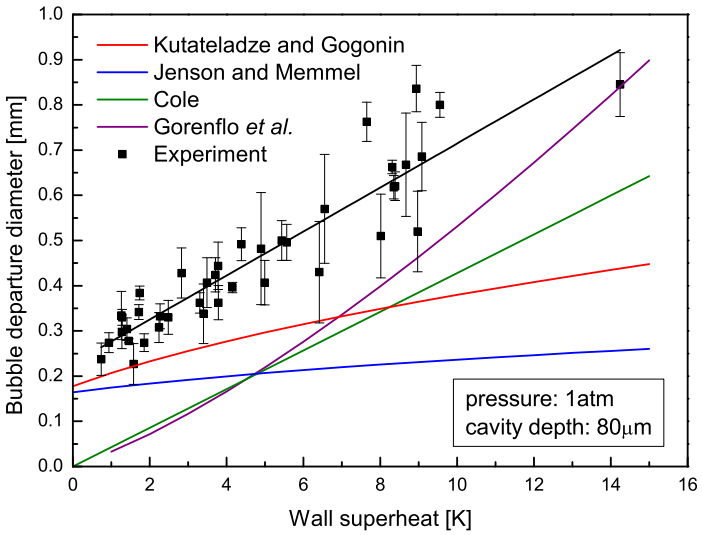

Figure 4.40: *Comparison of the measured bubble departure diameter from an isolated cavity (S3) with a nominal depth of 80 μm at 1 atm with correlations from Kutateladze and Gogonin [13], Jenson and Memmel [14], Cole [15] and Gorenflo et al. [16]*

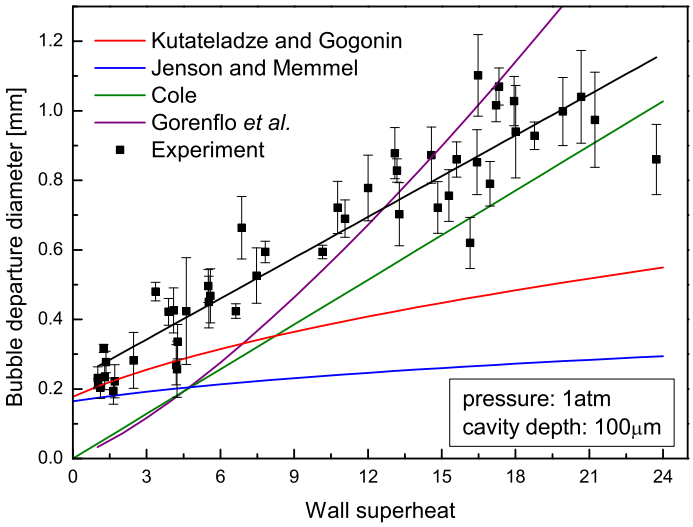

Figure 4.41: *Comparison of the measured bubble departure diameter from an isolated cavity (S3) with a nominal depth of 100 μm at 1 atm with correlations from Kutateladze and Gogonin [13], Jenson and Memmel [14], Cole [15] and Gorenflo et al. [16]*

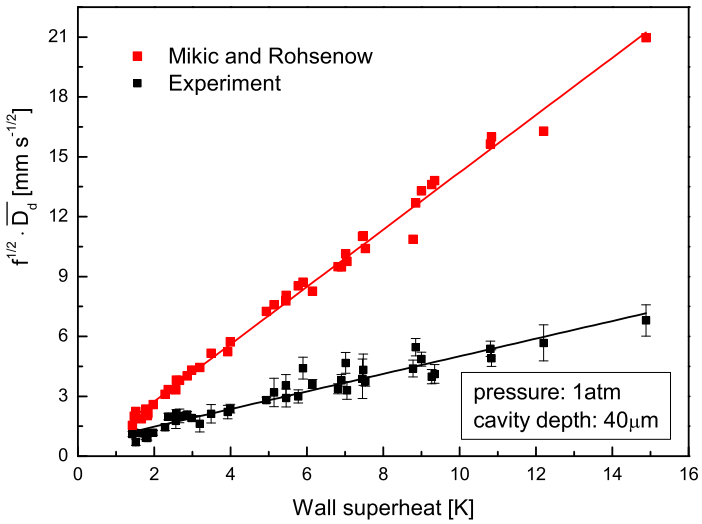

Figure 4.42: *Comparison of the product $f^{1/2} \cdot \overline{D_d}$ from an isolated cavity (S3) with a nominal depth of 40 μm at 1 atm with a correlation from Mikic and Rohsenow [17].*

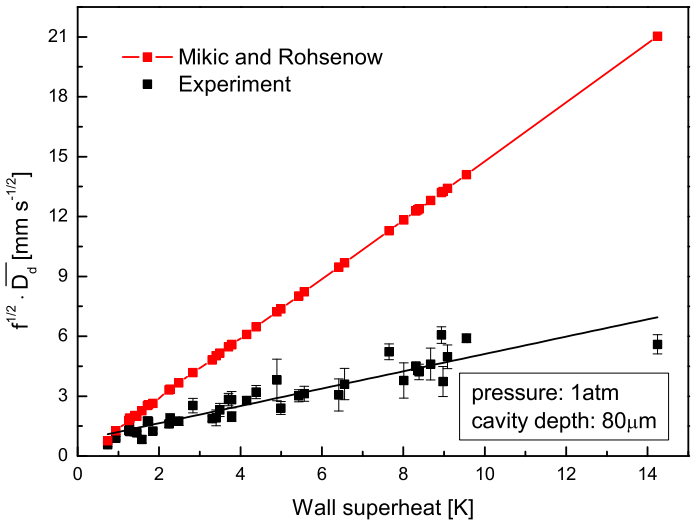

Figure 4.43: *Comparison of the product $f^{1/2} \cdot \overline{D_d}$ from an isolated cavity (S3) with a nominal depth of 80 μm at 1 atm with a correlation from Mikic and Rohsenow [17].*

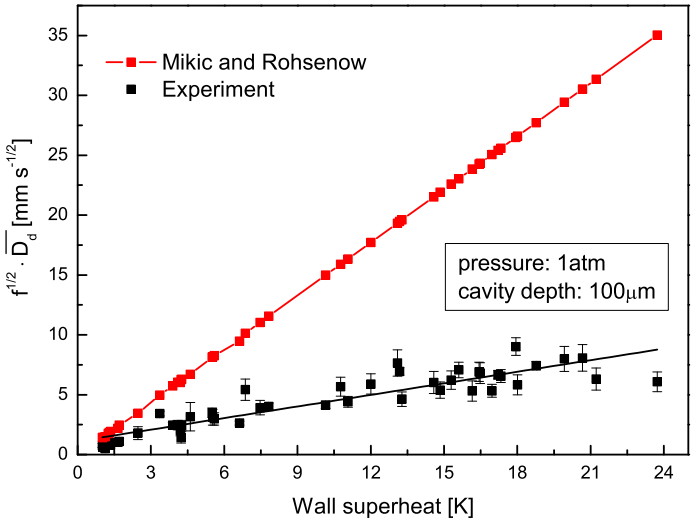

Figure 4.44: *Comparison of the product $f^{1/2} \cdot \overline{D_d}$ from an isolated cavity (S3) with a nominal depth of 100 μm at 1 atm with a correlation from Mikic and Rohsenow [17].*

4.3 The waiting time

The ratio between waiting time and total growth period of bubbles, for which the frequency and the departure diameters were discussed above, are presented in Fig. 4.45 to 4.53. The ratio is calculated from

$$\text{ratio} = \frac{t_w}{t_{tot}} = \frac{t_w}{t_w + t_g} \tag{4.1}$$

where t_w is the waiting time and t_{tot} the sum of the bubble growth time t_g and the waiting time t_w. The values of t_w as a function of wall superheat for 40, 80 and $100\,\mu\mathrm{m}$ deep cavities and for pressures of 1, 1.25 and $1.5\,\mathrm{atm}$ can be found in Fig. C.17 to C.25 in appendix C. Close to equilibrium superheat, the ratio of waiting time and total growth period can be very high occasionally, up to $45\,\%$ at $1\,\mathrm{atm}$ for the $80\,\mu\mathrm{m}$ deep cavity, $56\,\%$ at $1\,\mathrm{atm}$ and $62\,\%$ at $1.5\,\mathrm{atm}$ for the $100\,\mu\mathrm{m}$ deep cavity. The ratio decreases rapidly at higher wall superheats, becoming a very small fraction of the total bubble growth period when the superheat is 2 to 4 times the equilibrium value. There are occasional examples of longer waiting times. The large waiting time may be associated with penetration of the residual liquid-vapour interface into the cylindrical cavity but the effect of cavity depth in the range of 40 to $100\,\mu\mathrm{m}$ is inconclusive. The greatly reduced waiting times at measured time-averaged wall superheats, that are much higher than the calculated equilibrium superheats, may depend on the rate of recovery of the local superheat during bubble detachment, as discussed in Sanna *et al.* [145], which may reverse the collapse of the residual vapour nucleus before it enters the cavity.

Local temperature variations in time and local space could neither be detected by the sensors on the back of the second generation test section, nor the sensors located on the boiling surface surrounding the artificial cavities for the third generation test section.

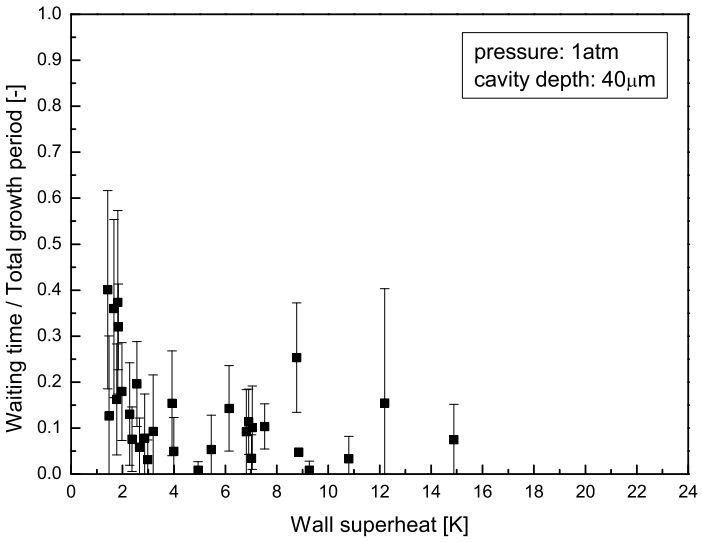

Figure 4.45: *Ratio of waiting time and total growth period as a function of wall superheat for bubble growth from an isolated cavity (S3) with a nominal mouth diameter of 10 μm and a depth of 40 μm at 1 atm.*

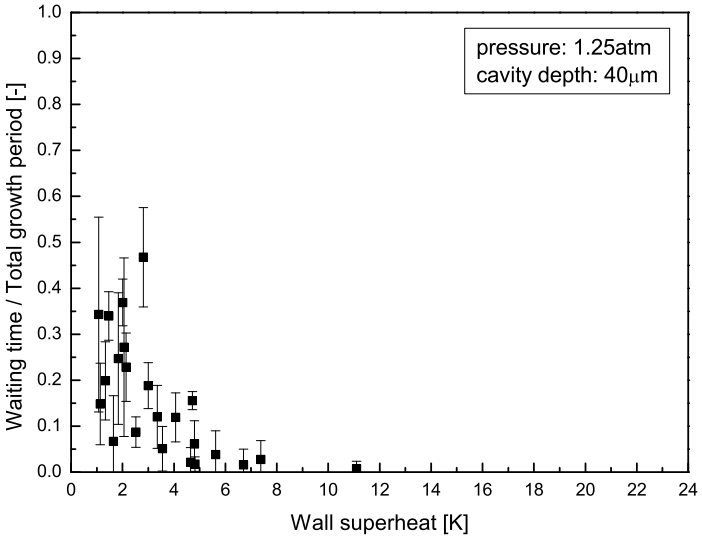

Figure 4.46: *Ratio of waiting time and total growth period as a function of wall superheat for bubble growth from an isolated cavity (S3) with a nominal mouth diameter of 10 μm and a depth of 40 μm at 1.25 atm.*

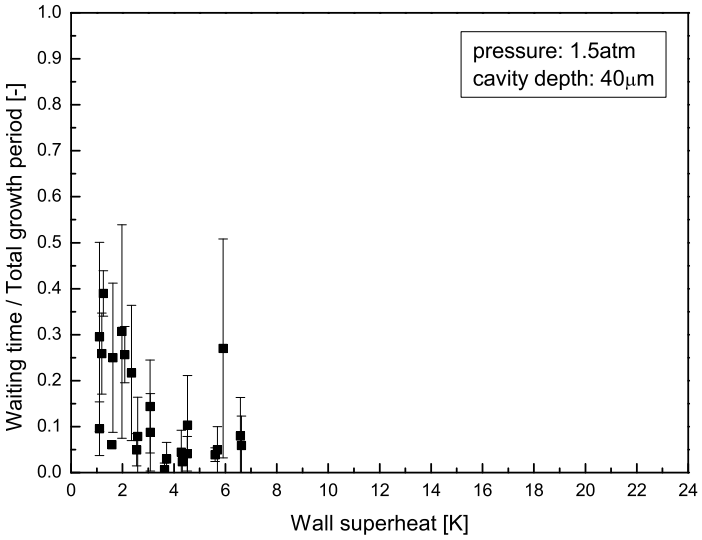

Figure 4.47: *Ratio of waiting time and total growth period as a function of wall superheat for bubble growth from an isolated cavity (S3) with a nominal mouth diameter of 10 μm and a depth of 40 μm at 1.5 atm.*

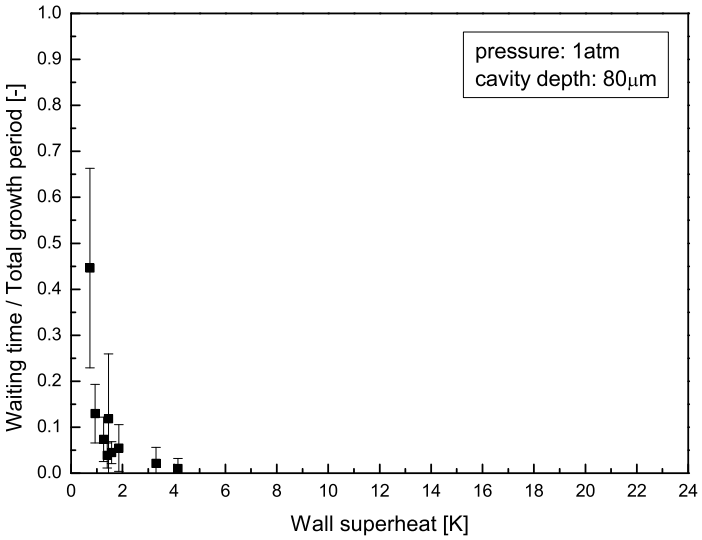

Figure 4.48: *Ratio of waiting time and total growth period as a function of wall superheat for bubble growth from an isolated cavity (S3) with a nominal mouth diameter of 10 μm and a depth of 80 μm at 1 atm.*

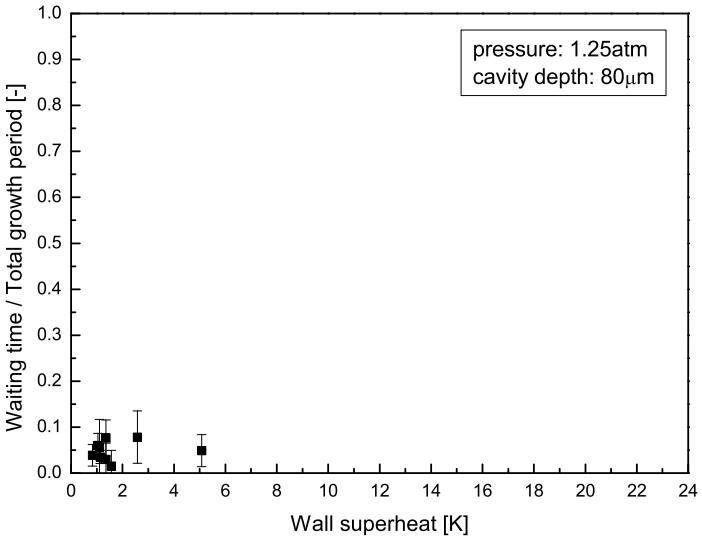

Figure 4.49: *Ratio of waiting time and total growth period as a function of wall superheat for bubble growth from an isolated cavity (S3) with a nominal mouth diameter of 10 μm and a depth of 80 μm at 1.25 atm.*

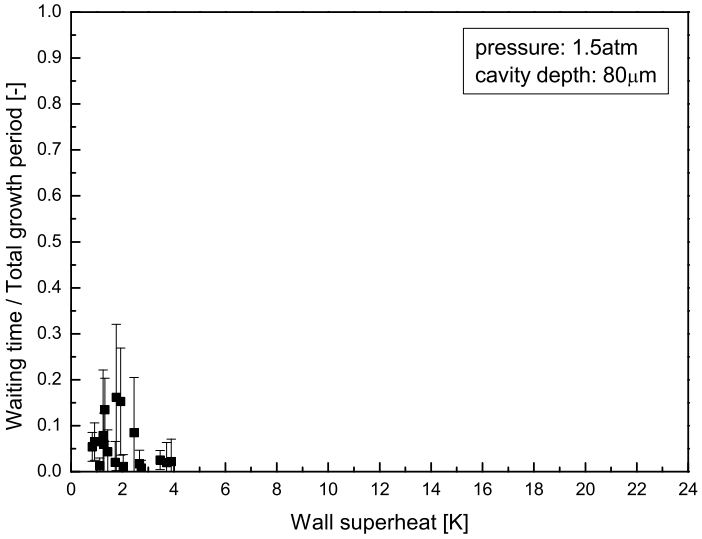

Figure 4.50: *Ratio of waiting time and total growth period as a function of wall superheat for bubble growth from an isolated cavity (S3) with a nominal mouth diameter of 10 μm and a depth of 80 μm at 1.5 atm.*

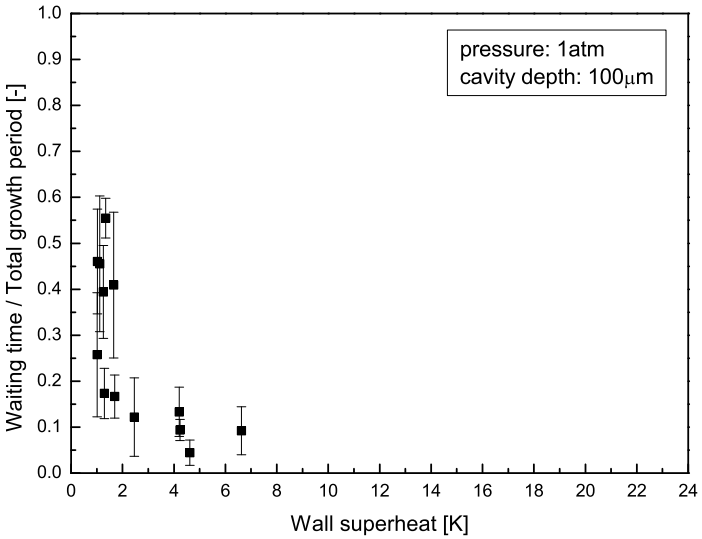

Figure 4.51: *Ratio of waiting time and total growth period as a function of wall superheat for bubble growth from an isolated cavity (S3) with a nominal mouth diameter of 10 μm and a depth of 100 μm at 1 atm.*

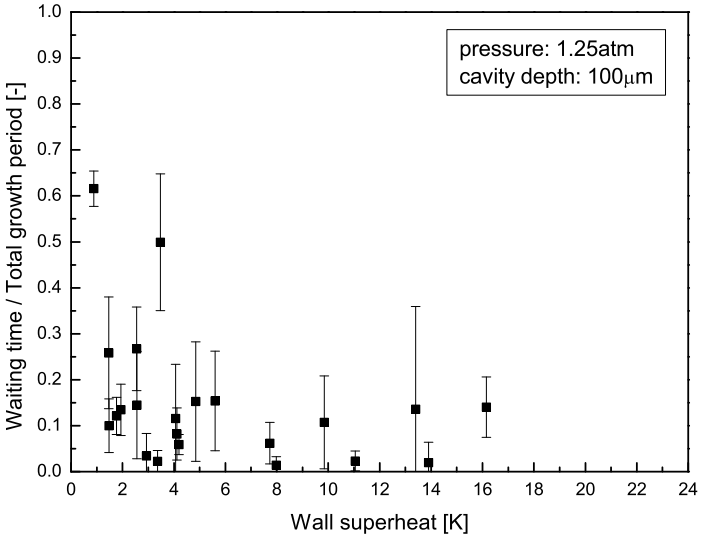

Figure 4.52: *Ratio of waiting time and total growth period as a function of wall superheat for bubble growth from an isolated cavity (S3) with a nominal mouth diameter of 10 μm and a depth of 100 μm at 1.25 atm.*

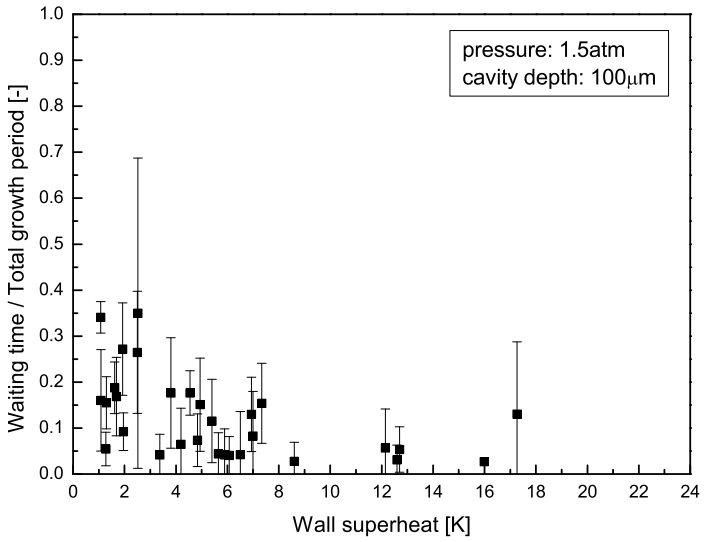

Figure 4.53: *Ratio of waiting time and total growth period as a function of wall superheat for bubble growth from an isolated cavity (S3) with a nominal mouth diameter of 10 μm and a depth of 100 μm at 1.5 atm.*

4.4 Heat removal by vapour generation

The transport of heat by enthalpy of evaporation is estimated from the product of the measured bubble frequency and the volume of a sphere, the latter calculated from the bubble departure diameter. This is then expressed as an evaporative heat flux (based nominally on the projected area of the bubble), which is a factor N times the input heat flux

$$\dot{q}''_e = \frac{2}{3} f D_d \rho_g h_{lg} = N \dot{q}'' \tag{4.2}$$

where f is the measured bubble departure frequency and D_d the measured departure diameter. The saturated vapour density ρ_g and the latent heat of vaporisation h_{lg} can be found in Table 3.1 and 3.2 in chapter 3. The input heat flux and the evaporative heat flux increase linearly with increasing wall superheat over a considerable range, with

$N = 2$, Fig. 4.54 to 4.62. The fitting line on all plots has a slope of $1.4\,{}^{\mathrm{kW}}/_{\mathrm{m^2K}}$. For the $100\,\mu\mathrm{m}$ deep cavity the evaporative heat flux tends to drop below the added line for wall superheats above $10\,\mathrm{K}$. This might be the case only for the deepest cavity, because considerably higher wall superheats were reached before the appearance of any unwanted nucleations. Evaporation may not occur entirely at the triple contact line or micro-layer below a bubble. Some of the wall heat flux may be transferred to a layer of superheated liquid by bubble-induced convection and then to the dome of the bubble. Simulation studies for these conditions by Sanna *et al.* [145] and experiments by Demiray and Kim [66] have suggested that this heat transfer mechanism is a significant fraction of the total heat flow to a growing bubble. Recent studies from Moghaddam and Kiger [110, 111] show that the contribution of different heat transfer mechanisms is changing with increasing wall superheat and that the occurrence or non-occurrence of waiting time has an important influence as well. In case of no waiting time and a surface temperature range of 80 to $97\,^{\circ}\mathrm{C}$ ($\Delta T = 24$ to $41\,\mathrm{K}$) for an surface area equal to the projected bubble area, the contributions were: 28.8 to $16.3\,\%$ for micro-layer, 45.4 to $32.1\,\%$ for transient conduction and 25.8 to $51.6\,\%$ for micro-convection. For a case with waiting time at low surface temperature the contribution was distributed as following: $26.5\,\%$ for micro-layer, $32\,\%$ for transient conduction and $41.4\,\%$ for micro-convection. However, comparison with this work is difficult as Moghaddam and Kiger's low surface temperature is the upper limit of wall superheat for the here presented experiments. Estimations of the heat transfer coefficient for natural convection or laminar forced convection for the measured temperatures undervalue the heat transfer coefficient calculated from experiments. Other mechanisms or convective flows introduced by the auxiliary heating to keep the boiling liquid at saturated conditions may be the reason for this discrepancy. This does not, however, affect the main conclusions derived from the presented work.

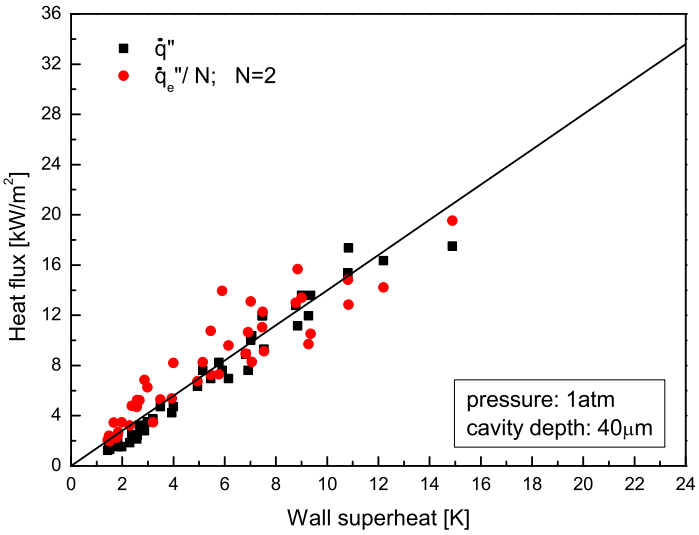

Figure 4.54: *Evaporative heat flux $\dot{q}_e''$ and input heat flux $\dot{q}''$ with factor $N = 2$ as functions of wall superheat from an isolated cavity (S3) with a nominal mouth diameter of 10 μm and a depth of 40 μm at 1 atm.*

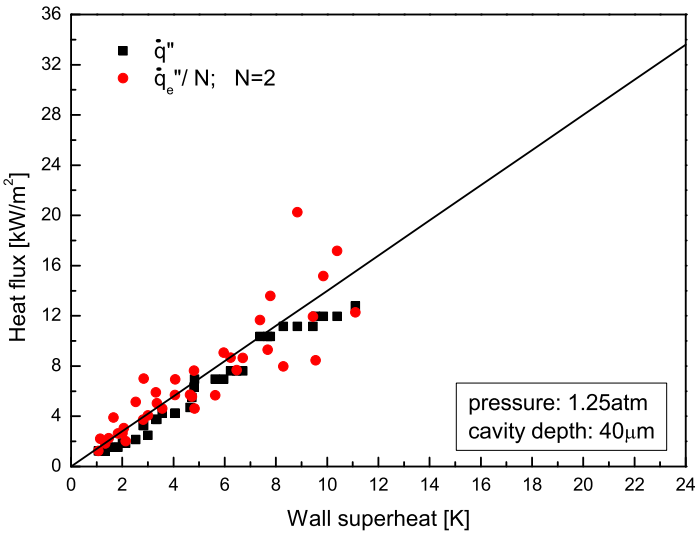

Figure 4.55: *Evaporative heat flux $\dot{q}_e''$ and input heat flux $\dot{q}''$ with factor $N = 2$ as functions of wall superheat from an isolated cavity (S3) with a nominal mouth diameter of 10 μm and a depth of 40 μm at 1.25 atm.*

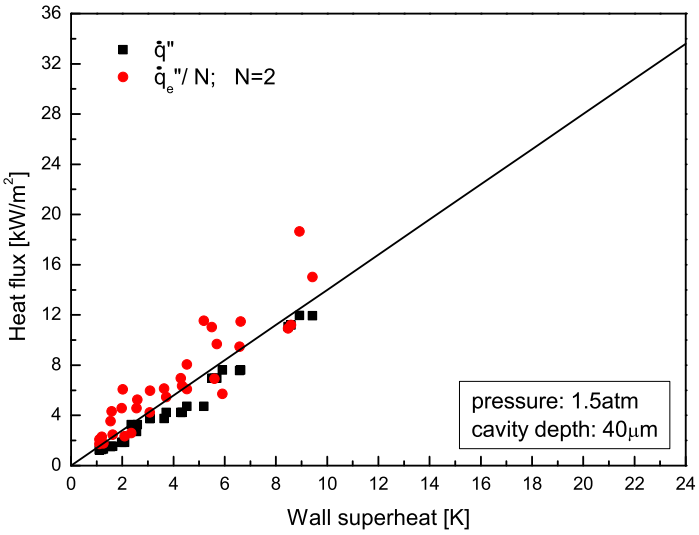

Figure 4.56: *Evaporative heat flux $\dot{q}''_e$ and input heat flux $\dot{q}''$ with factor $N = 2$ as functions of wall superheat from an isolated cavity (S3) with a nominal mouth diameter of 10 μm and a depth of 40 μm at 1.5 atm.*

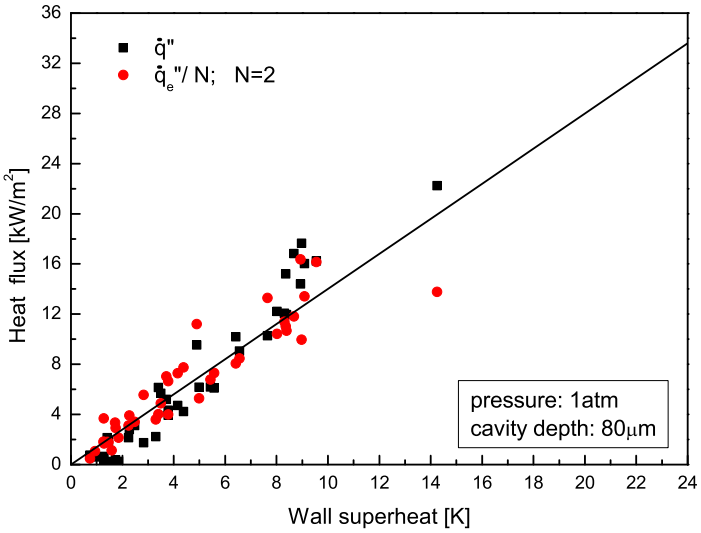

Figure 4.57: *Evaporative heat flux $\dot{q}''_e$ and input heat flux $\dot{q}''$ with factor $N = 2$ as functions of wall superheat from an isolated cavity (S3) with a nominal mouth diameter of 10 μm and a depth of 80 μm at 1 atm.*

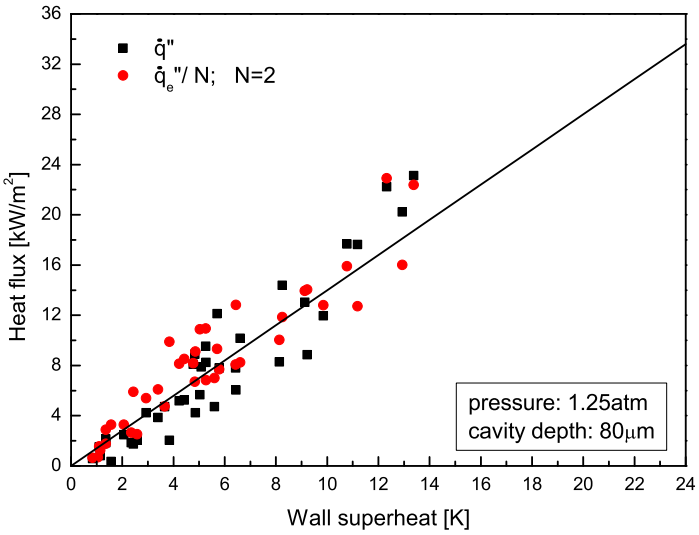

Figure 4.58: *Evaporative heat flux $\dot{q}''_e$ and input heat flux $\dot{q}''$ with factor $N = 2$ as functions of wall superheat from an isolated cavity (S3) with a nominal mouth diameter of 10 μm and a depth of 80 μm at 1.25 atm.*

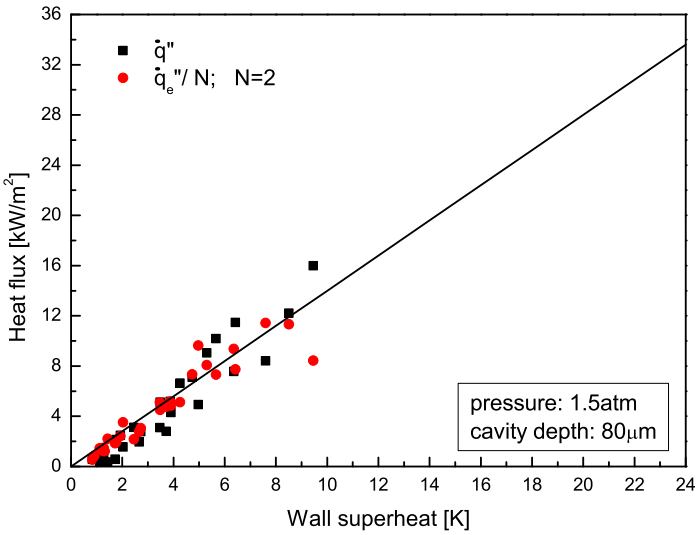

Figure 4.59: *Evaporative heat flux $\dot{q}''_e$ and input heat flux $\dot{q}''$ with factor $N = 2$ as functions of wall superheat from an isolated cavity (S3) with a nominal mouth diameter of 10 μm and a depth of 80 μm at 1.5 atm.*

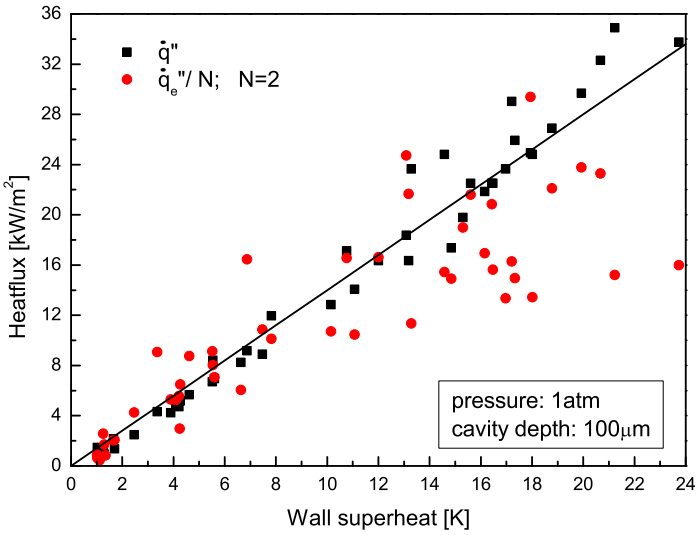

Figure 4.60: *Evaporative heat flux $\dot{q}''_e$ and input heat flux $\dot{q}''$ with factor $N = 2$ as functions of wall superheat from an isolated cavity (S3) with a nominal mouth diameter of 10 μm and a depth of 100 μm at 1 atm.*

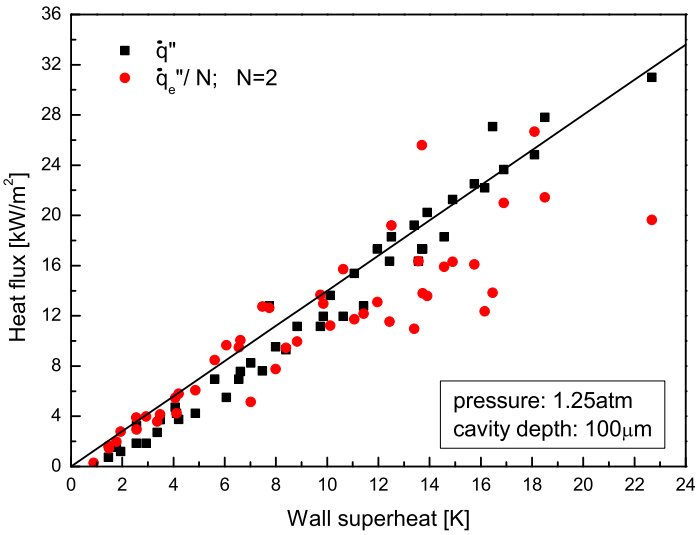

Figure 4.61: *Evaporative heat flux $\dot{q}''_e$ and input heat flux $\dot{q}''$ with factor $N = 2$ as functions of wall superheat from an isolated cavity (S3) with a nominal mouth diameter of 10 μm and a depth of 100 μm at 1.25 atm.*

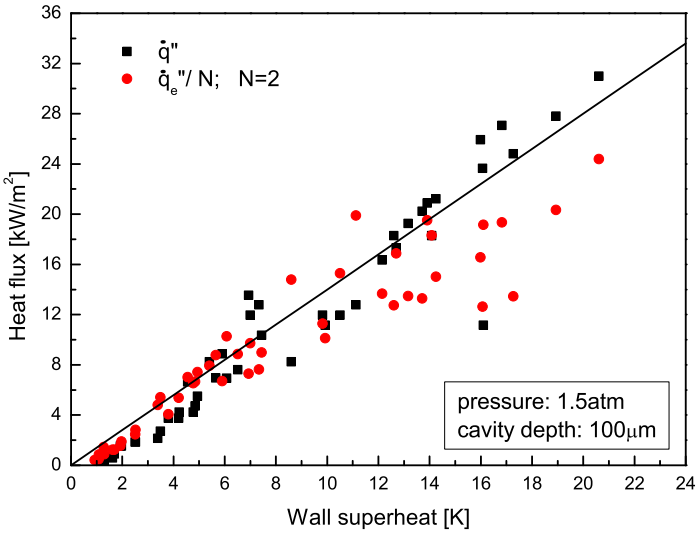

Figure 4.62: *Evaporative heat flux $\dot{q}''_e$ and input heat flux $\dot{q}''$ with factor $N = 2$ as functions of wall superheat from an isolated cavity (S3) with a nominal mouth diameter of 10 μm and a depth of 100 μm at 1.5 atm.*

4.5 Conclusions

Experiments were conducted from isolated artificial cylindrical cavities (S3 and S8) with a nominal mouth diameter of $10\,\mu\mathrm{m}$ and depths of 40, 80 and $100\,\mu\mathrm{m}$ on the second and third generation test section. All cavities produced bubbles for a range of wall superheats, with limits defined by the minimum superheat needed to produce a bubble at all and the onset of boiling from uncontrolled new nucleation sites.

Bubble growth from isolated cavities with a nominal depth of $80\,\mu\mathrm{m}$ at $1\,\mathrm{bar}$ and $100\,\mu\mathrm{m}$ at atmospheric pressure for different wall superheats was measured. The bubble growth rate becomes very small before lift-off for the lowest studied wall superheats, which may be a consequence of the reduction in contact area. For higher wall superheats, the bubble growth rate decreases less, the bubble lifts off faster and departs more suddenly. Generally the bubble growth time is decreasing with increasing wall superheat and for higher wall superheats the bubbles depart before the significant de-

crease in growth rate, mentioned above, was observed. However, the bubble growth time for the lowest wall superheat was for the $100\,\mu\mathrm{m}$ cavity much longer compared to that of the $80\,\mu\mathrm{m}$ deep cavity, despite similar departure diameters. Comparing the waiting times of the two experiments at low wall superheat reveals that for the slower bubble growth it is around three times longer, which is almost the same ratio as for the bubble growth times. Although the wall superheat and the pressure were slightly different, this does not explain the observed discrepancy between the two cavities. The experimental results for bubble growth were compared to common correlations found in the literature. The correlation of Mikic *et al.* predicts the bubble growth generally closest if results for all measured conditions are considered. For this correlation all energy is supplied from a relaxation layer surrounding the bubble dome. However, as different correlations occasionally predict the bubble growth better, it may be a combination of several heat transfer mechanisms. The collected data is used as input for a numerical simulation developed at Brunel University and is the first step for its validation.

Bubble departure frequencies were measured for all cavities for different wall superheats and pressures. The departure frequency is slightly decreased for all cavity depths with increasing pressure and becomes at all measurement conditions almost constant for high wall superheats.

The departure diameter increases in a near-linear fashion with wall superheat. Common correlations generally under predict the measured departure diameters. No influence of cavity depth and pressure was observed.

Waiting times between bubbles decrease rapidly with increasing wall superheat. There are occasional examples of longer waiting times. The large waiting time may be associated with penetration of the residual liquid-vapour interface into the cylindrical cavity but the effect of cavity depth in the range of 40 to $100\,\mu\mathrm{m}$ is inconclusive. Again, there is no visible influence of cavity depth and pressure.

The evaporative heat flux due to bubble growth was estimated from measured bubble departure frequencies and diameters. Both the input and evaporative heat flux increase

linearly with increasing wall superheat over a wide range. An influence area of twice the projected bubble area indicates that evaporation may not occur entirely at the triple contact line or micro-layer below a bubble. Some of the wall heat flux may be transferred to a layer of superheated liquid by bubble-induced convection and then to the dome of the bubble.

Chapter 5
Vertical coalescence

Vertical coalescence of succeeding bubbles is schematically shown in Fig. 5.1. Below a single bubble (V_{top}), which has still not departed from the surface, a second bubble nucleates (V_{bot}) and is vertically lifting off the first bubble and pushing it away from the substrate. The two bubbles then merge into one (V_{coal}) and will further lift off and finally depart as one larger bubble from the boiling surface. The time scale for this process depends on the wall superheat, as do bubble volumes, as shown in chapter 4, section 4.1. Horizontal coalescence happens between two or more adjacently growing bubbles, which merge to form one large bubble. The merger of a growing bubble from an adjacent nucleation site with an already departed bubble is called declining coalescence [6]. Zhang and Shoji [6] concluded that bubble coalescence near the heated wall promotes growing bubbles to depart from the nucleation site. They only considered horizontal and declining coalescence in their analysis. Indeed, vertical coalescence is acknowledged in several publications, but is not employed in the analysis of boiling heat transfer in all examined cases.

5.1 Bubble nucleation frequency, frequency of vertical coalescence, bubble departure frequency and bubble departure diameter

The average frequency of nucleated bubbles and vertical coalescence from an isolated single cavity were measured analysing sequences of high-speed images taken during bubble growth at absolute pressures of 0.5, 0.75 and $1\,\mathrm{bar}$ with increasing wall superheat. Figure 5.2 presents such a sequence taken during bubble growth with vertical coalescence at $0.5\,\mathrm{bar}$ absolute pressure and a wall superheat of $7.9\,\mathrm{K}$ (applied heat

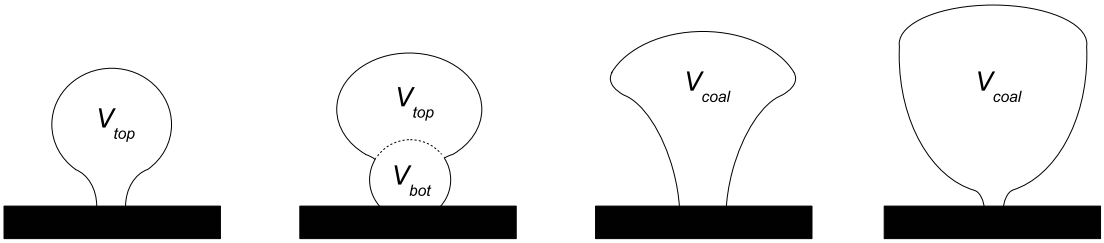

Figure 5.1: *Vertical coalescence of succeeding bubbles from an artificial nucleation site. The bubble of the volume V_{top} merges with the bubble of the volume V_{bot} to form a bubble of the volume V_{coal}. The time scale and the bubble volumes depend on the wall superheat.*

flux $4.8\,\mathrm{kW/m^2}$ with the camera set to $1000\,\mathrm{fps}$). Bubble nucleation occurs at $0\,\mathrm{ms}$ and for the first $11\,\mathrm{ms}$ the bubble growth follows the usual behaviour of a single bubble. At $11\,\mathrm{ms}$ a second bubble nucleates from the same artificial cavity and completely merges within $3\,\mathrm{ms}$ with the previously departed upper bubble. At $15\,\mathrm{ms}$ a third bubble nucleates, but does not coalesce with its predecessor during growth. The occasionally visible widening of the bubble base is due to reflection of the bubble on the silicon surface.

The average nucleation frequency (BNF) with increasing wall superheat for the above three pressures is shown in Fig. 5.3, 5.4 and 5.5. In all plots the isolated bubble regime is indicated. As mentioned in section 2.2.6, bubbles in this regime are produced intermittently and do not interfere with each other. When the wall superheat increases, the waiting time between the nucleation of a new bubble and the departure of the previous bubble, grown from the same site, becomes shorter. The number of nucleations per second decreases with increasing pressure. With increasing wall superheat this number of nucleations initially increases sharply and seems to level off, with this behaviour being more pronounced for the $0.5\,\mathrm{bar}$ pressure case. The results for $0.75\,\mathrm{bar}$ are rather scattered and for $1\,\mathrm{bar}$ the initial increase is less noticeable.

Figure 5.6, 5.7 and 5.8 present the average frequency of vertical coalescence (VCF) for the same three pressures with increasing wall superheat. Reducing the pressure or increasing the wall superheat increases the occurrence of coalescence.

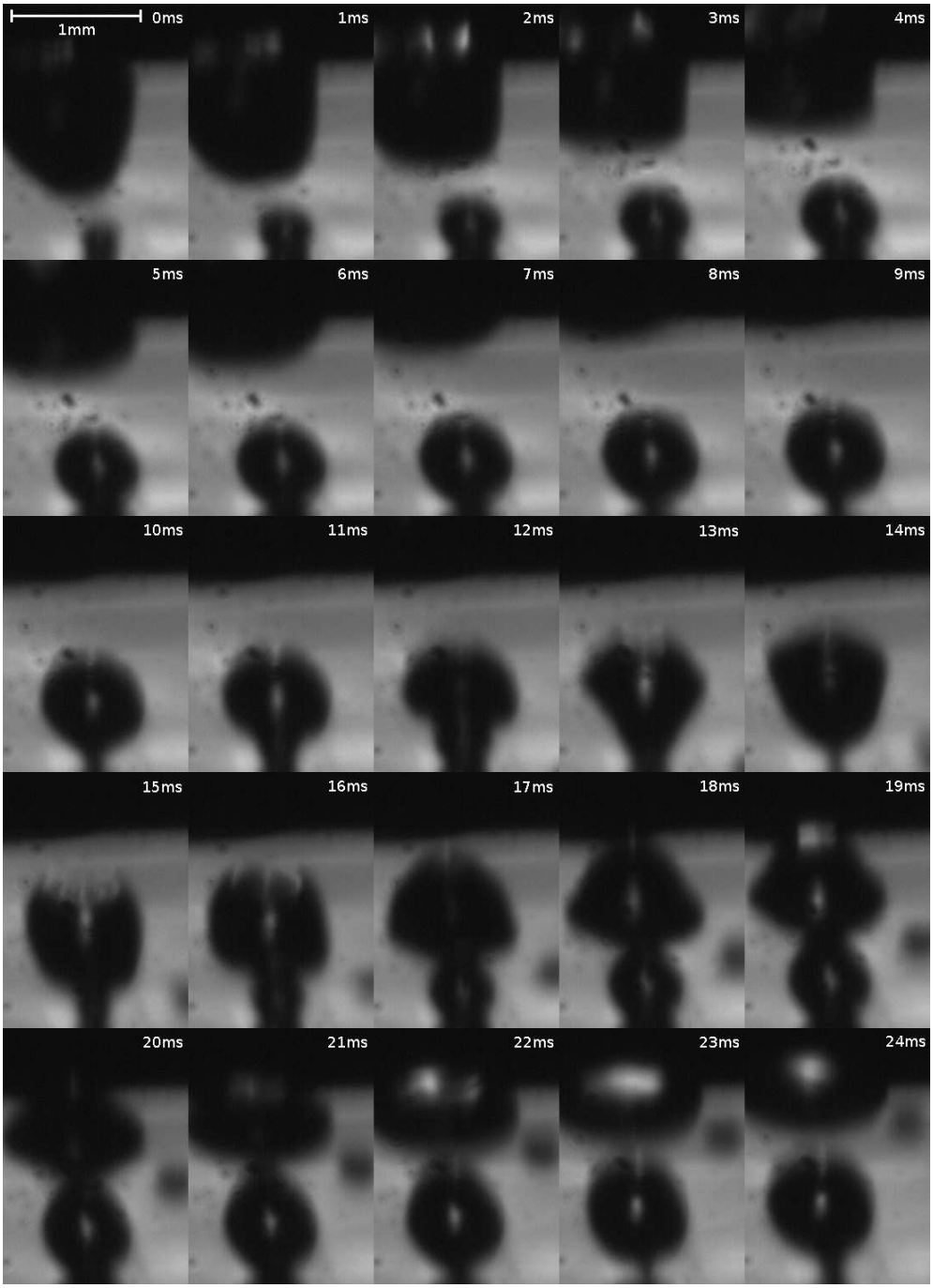

Figure 5.2: *Bubble growth sequence including vertical coalescence for a wall superheat of 7.9 K (applied heat flux 4.8 kW/m^2) from an isolated cavity (S8) at 0.5 bar. The first frame includes a length scale and the temporal resolution between 2 frames is 1 ms.*

The average frequency of bubble nucleation corresponds to an increase in the average frequency of vertical coalescence, as coalescence tends to reduce the bubble growth time. Bubbles are pulled away from the surface at much smaller size and this increases the number of nucleations for the same time period but increases the total growth time of the two bubbles only by a few milliseconds.

If the frequency of vertical coalescence is subtracted from the average nucleation frequency, the bubble departure frequency can be presented, Fig. C.26, C.27 and C.28 in appendix C.

The ratio between the average frequency of vertical coalescence and the bubble nucleation frequency (VCF/BNF) is compared in Fig. 5.9, 5.10 and 5.11. At $0.5\,\mathrm{bar}$ approximately $45\,\%$ of the bubbles coalesce for higher wall superheats. The ratio remains at this level even with increasing wall superheat. A possible explanation for this behaviour may be the fact that vertical coalescence most commonly appears only in pairs, i.e., only very rarely does a third or more bubbles coalesce with already vertically coalesced bubbles.

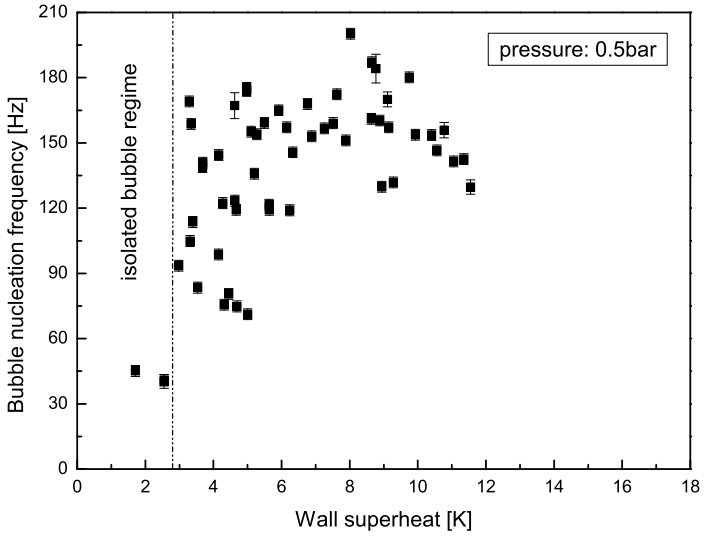

Figure 5.3: *Bubble nucleation frequency as a function of wall superheat from an isolated cavity (S8) with a nominal mouth diameter of 10 μm and a depth of 80 μm at 0.5 bar.*

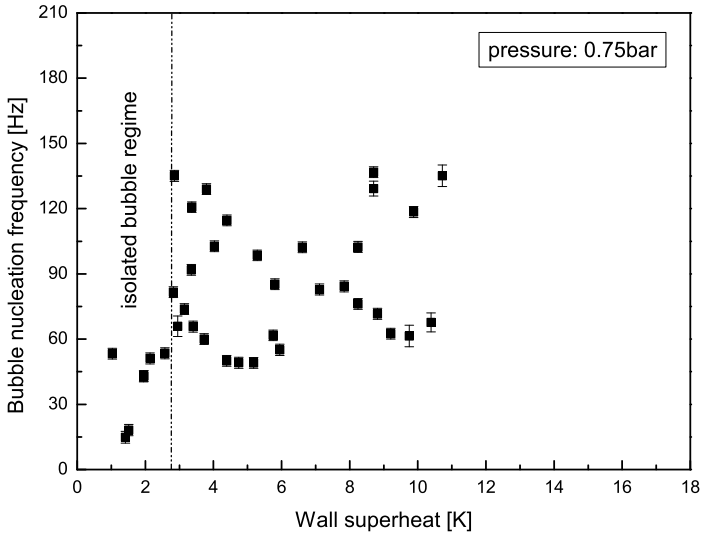

Figure 5.4: *Bubble nucleation frequency as a function of wall superheat from an isolated cavity (S8) with a nominal mouth diameter of 10 μm and a depth of 80 μm at 0.75 bar.*

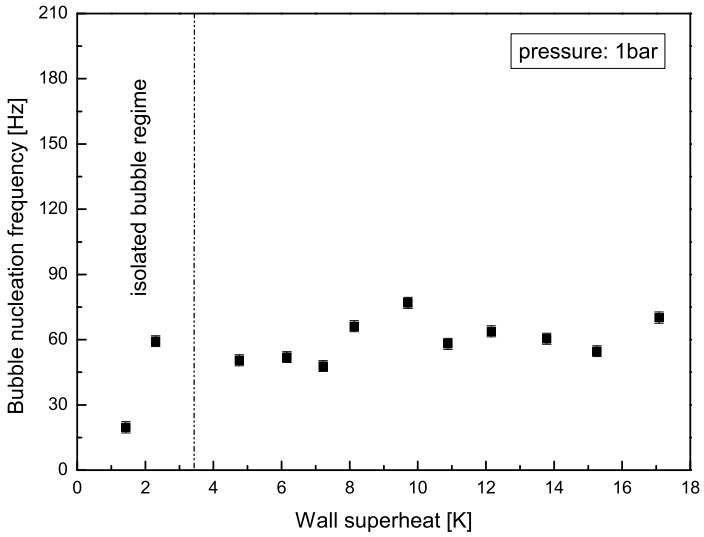

Figure 5.5: *Bubble nucleation frequency as a function of wall superheat from an isolated cavity (S8) with a nominal mouth diameter of 10 μm and a depth of 80 μm at 1 bar.*

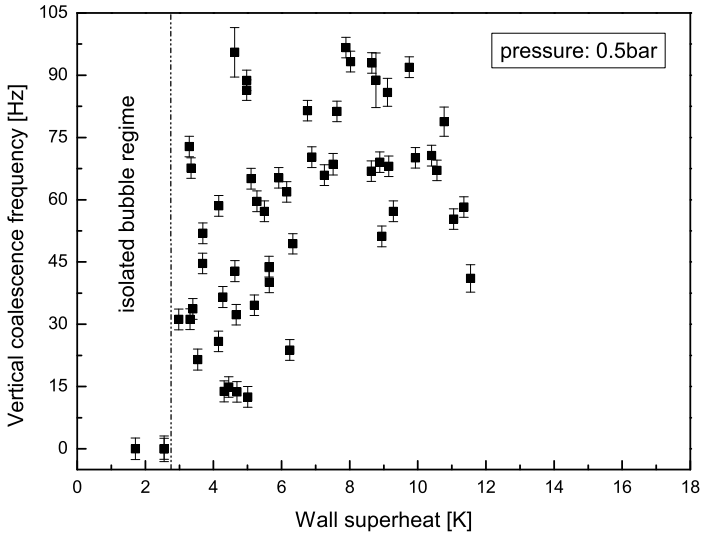

Figure 5.6: *Frequency of vertical coalescence as a function of wall superheat from an isolated cavity (S8) with a nominal mouth diameter of 10 μm and a depth of 80 μm at 0.5 bar.*

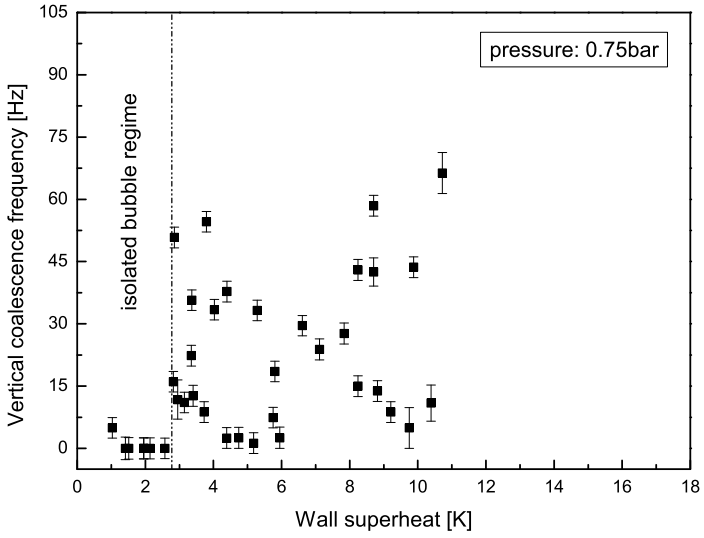

Figure 5.7: *Frequency of vertical coalescence as a function of wall superheat from an isolated cavity (S8) with a nominal mouth diameter of 10 μm and a depth of 80 μm at 0.75 bar.*

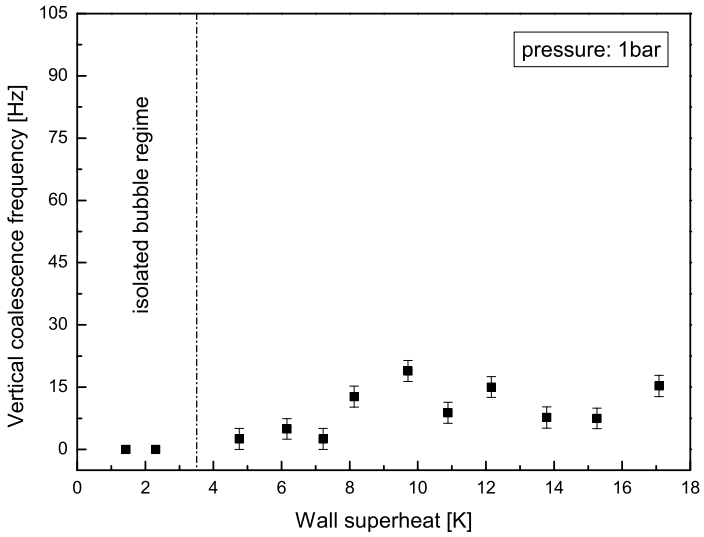

Figure 5.8: *Frequency of vertical coalescence as a function of wall superheat from an isolated cavity (S8) with a nominal mouth diameter of 10 μm and a depth of 80 μm at 1 bar.*

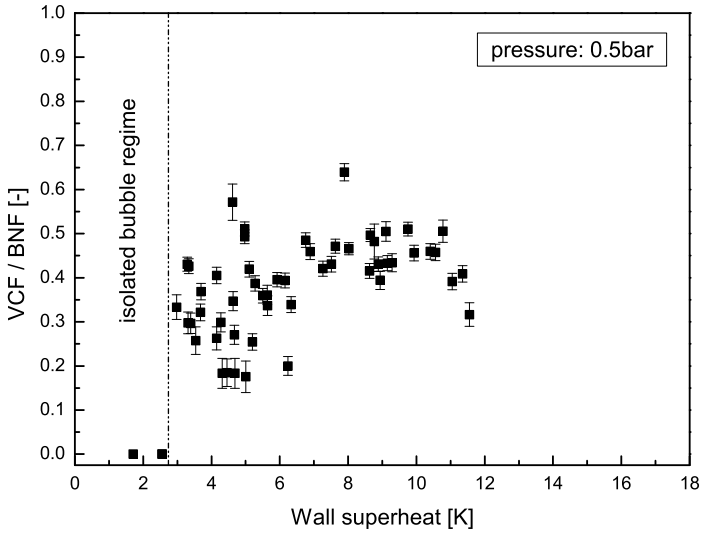

Figure 5.9: *Ratio between frequency of vertical coalescence (VCF) and bubble nucleation frequency (BNF) as a function of wall superheat from an isolated cavity (S8) with a nominal mouth diameter of 10 μm and a depth of 80 μm at 0.5 bar.*

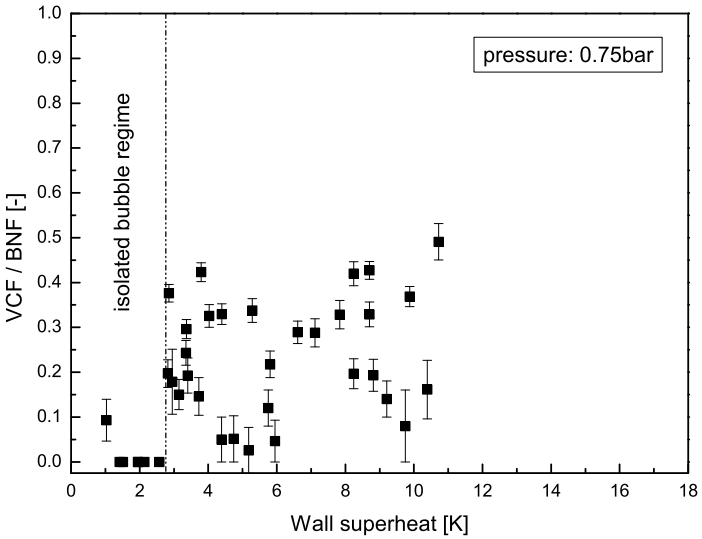

Figure 5.10: *Ratio between frequency of vertical coalescence (VCF) and bubble nucleation frequency (BNF) as a function of wall superheat from an isolated cavity (S8) with a nominal mouth diameter of 10 μm and a depth of 80 μm at 0.75 bar.*

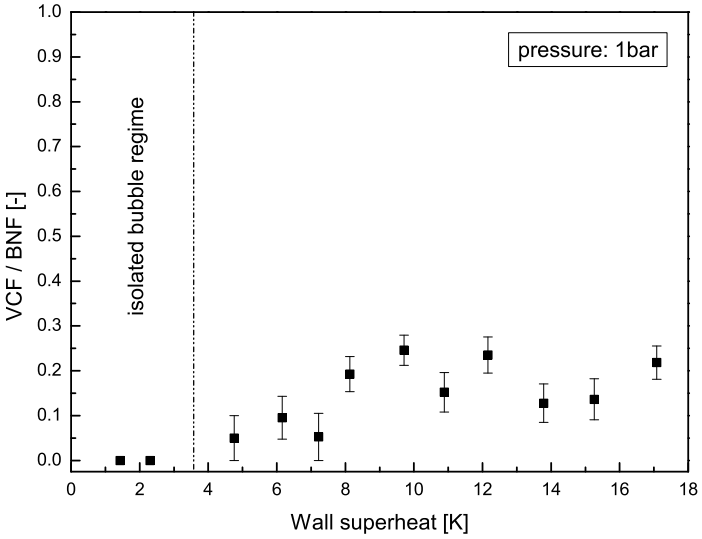

Figure 5.11: *Ratio between frequency of vertical coalescence (VCF) and bubble nucleation frequency (BNF) as a function of wall superheat from an isolated cavity (S8) with a nominal mouth diameter of 10 μm and a depth of 80 μm at 1 bar.*

As the pressure increases, the ratio between vertical coalescence and nucleations decreases. For $1\,\mathrm{bar}$ the maximum ratio is around $20\,\%$ for high wall superheats. This means that around three bubbles depart as single bubbles before vertical coalescence occurs between the two that follow. Measurements at $0.75\,\mathrm{bar}$ tend to lie in between the results for the lower and higher pressure.

As in subsection 4.2 and 4.4 the bubble departure diameter and the evaporative heat flux were measured and calculated for 0.5, 0.75 and $1\,\mathrm{bar}$. The results are presented in Fig. C.29, C.30, C.31, C.33, C.34 and C.35 with a detailed description in appendix C.

5.2 Vapour volume analysis during vertical coalescence

The vapour volumes of ten bubble pairs immediately before and just after coalescence were measured and are presented in Fig. 5.12, 5.13 and 5.14. The pressure was $0.5\,\mathrm{bar}$ with a wall superheat of $7.9\,\mathrm{K}$ (applied heat flux $4.8\,\mathrm{kW/m^2}$). The original images, Fig. 5.2, were processed with the software PCO Picture Viewer™.

A suitable threshold helped to identify the bubble area and Eq. 3.11 was used to calculate the vapour volume. Due to the invisibility of the intersection between the top and bottom bubble, the shape of the bottom bubble was assumed to be spherical. Since small single bubbles have a small Eötvös or Bond number, gravitational effects are negligible and the shape is near-spherical.

Figure 5.12 shows that the newly nucleated bubble (bottom bubble) is always smaller than the previously nucleated one (top bubble) just before coalescence and the total volume immediately after coalescence is larger than the sum of volumes before coalescence.

Figure 5.13 presents the ratio between the volume of the bottom bubble V_{bot} and the top bubble V_{top} with error bars indicating the propagated systematic measurement error. The volume of the bottom bubble never exceeds one third of the volume of the top one. The smallest bottom bubble compared to its top one is 10 times smaller than its predecessor.

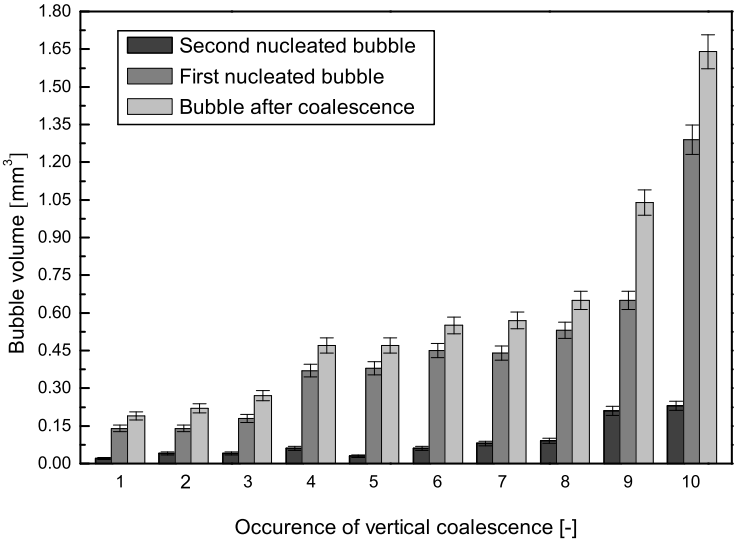

Figure 5.12: *Bubble volumes immediately before coalescence (V_{bot} and V_{top}) and the total volume just after coalescence (V_{coal}) for 10 cases of vertical coalescence.*

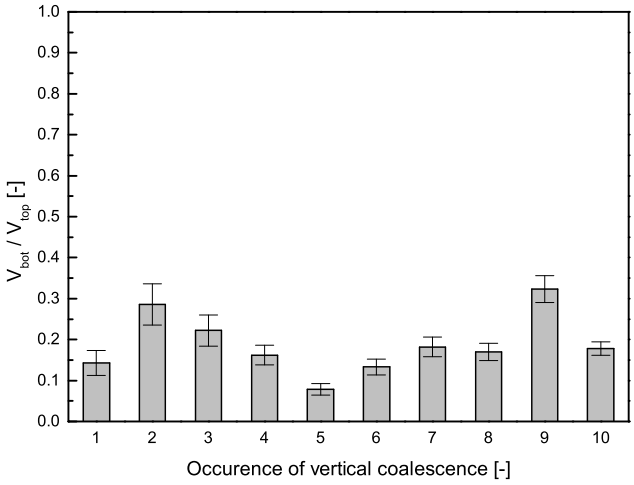

Figure 5.13: *Ratio between the volume of the newly nucleated bubble (V_{bot}) and the previously nucleated bubble (V_{top}) for 10 cases of vertical coalescence.*

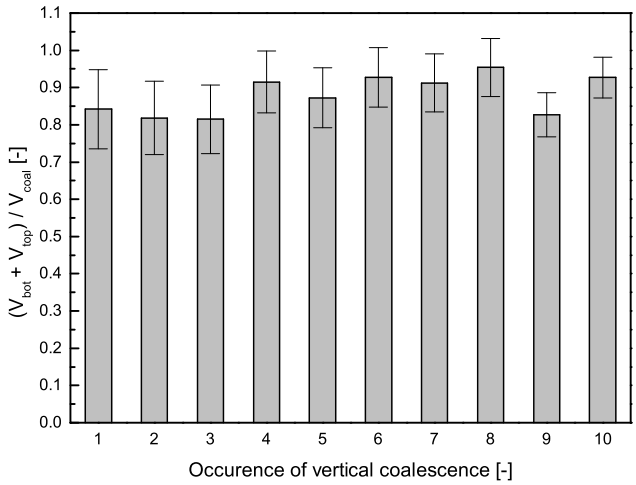

Figure 5.14: *Ratio of the total volume of the top and bottom bubble ($V_{bot} + V_{top}$) immediately before coalescence and the volume of the coalesced bubble (V_{coal}) just after coalescence.*

The ratio between the sum of the volumes of the two bubbles $V_{bot} + V_{top}$ immediately before coalescence and the total volume V_{coal} just after (maximum temporal resolution is $1\,\mathrm{ms}$) is illustrated in Fig. 5.14. After coalescence the total volume is 5 to $18\,\%$ larger than before. This suggests that the process of coalescence causes a brief increase in heat transfer to the liquid-vapour interface. This may occur at the base of the second bubble, or by heat transfer from a thin superheated liquid layer trapped between the bubbles, or by rapid motion close to the line of coalescence.

However, if the evolution of the vapour volume during vertical coalescence from nucleation of the first bubble to the departure of the two merged bubbles is analysed, it is obvious that the vapour production is not increasing or decreasing during vertical coalescence. This vapour volume evolution of the previously illustrated ten cases of vertical coalescence is presented in Fig. 5.15. The time at which coalescence occurs was set as the zero point. The ten cases of occurrence of vertical coalescence are numbered the same way as previously. The slope of increase of vapour production for the two cases with the largest final vapour volumes (9 and 10) is generally slightly increasing, whereas for the other cases the vapour volume is increasing in a near-linear fashion. To allow better comparison between the different cases, the vapour volume was nor-

malised with the volume of the merged bubbles at departure, Fig. C.36 appendix C. The comparison reveals that for smaller bubbles the vapour volume is increasing faster to reach the normalised departure volume.

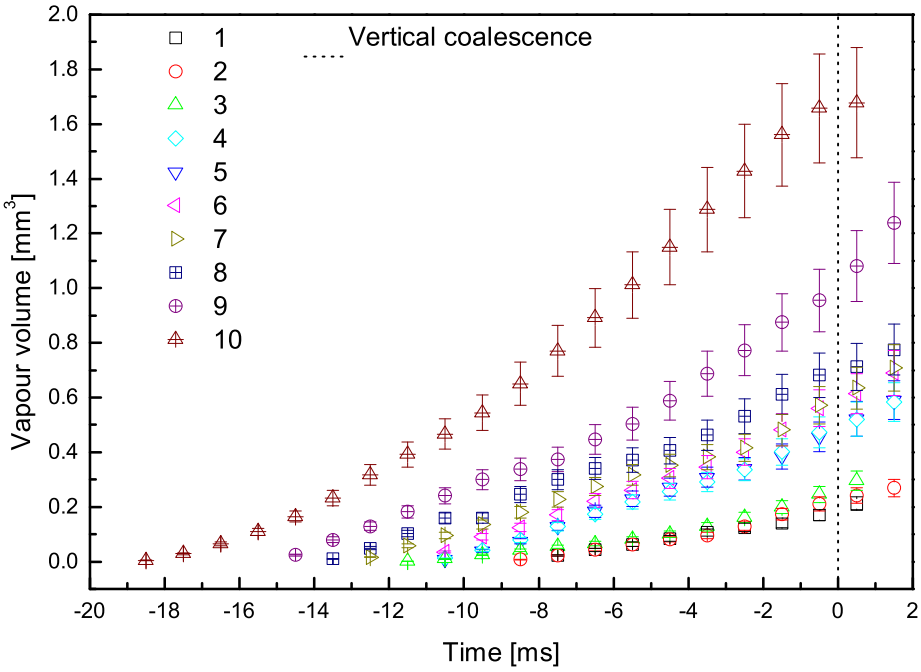

Figure 5.15: *Vapour volume evolution from nucleation, over vertical coalescence to the departure of the coalesced bubble for 10 cases of vertical coalescence. The time at which coalescence occurs was set as the zero point. Vapour production of an isolated cavity (S8) with a nominal mouth diameter of 10 μm and a depth of 80 μm at 0.5 bar and a wall superheat of 7.9 K (applied heat flux 4.8 kW/m^2).*

5.3 Conclusions

Bubble growth from an isolated artificial cavity (S8) on the third generation test section at the end of the isolated bubble regime and the beginning of the regime of interference, where vertical coalescence appears, has been experimentally investigated. Studies of bubble growth as a function of wall superheat and at different pressures of 0.5, 0.75 and $1\,\mathrm{bar}$ revealed the dependence of vertical coalescence on these properties. Bubble growth changes from the isolated bubble regime into the regime of interference with increasing wall superheat. The average frequency of bubble nucleation and vertical coalescence increased with the wall superheat. Decreasing the pressure, increases the average frequency of vertical coalescence and therefore subsequently the average frequency of nucleated bubbles from the artificial cavity. At $0.5\,\mathrm{bar}$ every two nucleated bubble pairs merge into one for high wall superheats. At $1\,\mathrm{bar}$ up to three single bubbles depart from the artificial cavity, before two coalesce. The equivalent volume of a sphere was calculated for ten pairs of bubbles immediately before and just after they coalesced. The second nucleating bubble is always smaller than its departed predecessor. During coalescence the vapour volume still increases, as the merged bubble is between 5 and $18\,\%$ larger than the summarised volumes of the two bubbles before coalescence. However, the measured evolution of vapour volume during vertical coalescence shows that the vapour production is neither increasing nor decreasing during vertical coalescence.

Chapter 6
Nucleation site interaction

In this part the interaction between two nucleation sites was studied. In a first step the influence of spacing between two cavities on the bubble nucleation frequency, the bubble departure frequency and the bubble departure diameter at 0.5 and $1\,\mathrm{bar}$ was investigated. As vertical coalescence is involved, the number of departed bubbles is not the same as nucleated bubbles. The bubble departure frequency is the difference between the bubble nucleation frequency and the vertical coalescence frequency. Later, direct horizontal bubble interaction between two cavities was analysed. Horizontal coalescence was only observed for the closest spacing between two artificial cavities. Bubble growth from cavities S1 to S6 was observed to study the nucleation site interactions, Fig. 4.1 right.

6.1 Two adjacent active artificial cavities

In Figure 6.1 to 6.18 the bubble nucleation frequency, the bubble departure frequency and the bubble departure diameter are plotted as a function of wall superheat for a cavity spacing of 1.5, 1.2 and $0.84\,\mathrm{mm}$ at 0.5 and $1\,\mathrm{bar}$. The frequency of vertical coalescence is presented in Fig. C.44 to C.49 in appendix C. The wall superheat represents the average temperature during the captured time period from the sensor at the corresponding cavity. The limit for the lowest wall superheat was the temperature to keep the cavities active, which is in good agreement with the theoretical minimum temperature for a cavity to trap vapour nuclei calculated from the Laplace-Young equation, Eq. 2.3. The wall superheat was increased until unwanted new nucleation sites became active. The interaction regions suggested by Zhang and Shoji [6] were included in the bubble departure diameter plots Fig. 6.3, 6.6, 6.9, 6.12, 6.15 and 6.18. From

the intersection points between the limits of these regions (horizontal lines in the bubble departure diameter plots) and the linear trend lines for bubble departure diameter for each cavity, the two corresponding wall superheats for the two cavities were determined and averaged (wherever there was a discrepancy). The difference between the two superheats for the two cavities was always below $1\,\mathrm{K}$. From this it was possible to determine the interaction region limits (vertical lines) due to spacing on the bubble nucleation frequency and the bubble departure frequency at corresponding temperatures, Fig. 6.1, 6.2, 6.4, 6.5, 6.7, 6.8, 6.10, 6.11, 6.13, 6.14, 6.16 and 6.17.

The measured parameters of the neighbouring cavities behave very similarly at 0.5 and $1\,\mathrm{bar}$ for a cavity spacing of $1.5\,\mathrm{mm}$, Fig. 6.1 to 6.6. As observed in previous studies, chapter 5, section 5.1, the bubble nucleation frequency initially increases rapidly, then appears to level off, before it slightly drops for the highest wall superheats. This behaviour is more pronounced and the small drop of frequency only noted at $0.5\,\mathrm{bar}$, Fig. 6.1 and 6.4. The initial rapid increase, which flattens with higher superheats, can also be seen for the bubble departure frequency at $0.5\,\mathrm{bar}$, Fig. 6.2. Frequency measurements are less scattered if vertical coalescence is not considered. The bubble departure diameter increases in a near-linear fashion with increasing superheat for both cases, Fig. 6.3 and 6.6. The departure diameters for the same wall superheats are slightly larger at lower pressure but this is only apparent when the linear trend lines are compared, as the data are rather scattered for high superheats at $0.5\,\mathrm{bar}$.

In Figure 6.7 to 6.12 the bubble nucleation frequency, the bubble departure frequency and the bubble departure diameter for two cavities, spaced $1.2\,\mathrm{mm}$ from each other, are plotted for the same two pressures with increasing wall superheat. The two neighbouring cavities, again, behave very similarly. After the sharp initial increase, the bubble nucleation frequency at $0.5\,\mathrm{bar}$ reaches a maximum, before it starts to decrease for superheats above $8\,\mathrm{K}$, Fig. 6.7. The slight decrease for higher wall superheats is still noticeable if the vertical coalescence is not considered, Fig. 6.8. The departure frequency appears constant for superheats above $4\,\mathrm{K}$ at $1\,\mathrm{bar}$, Fig. 6.11.

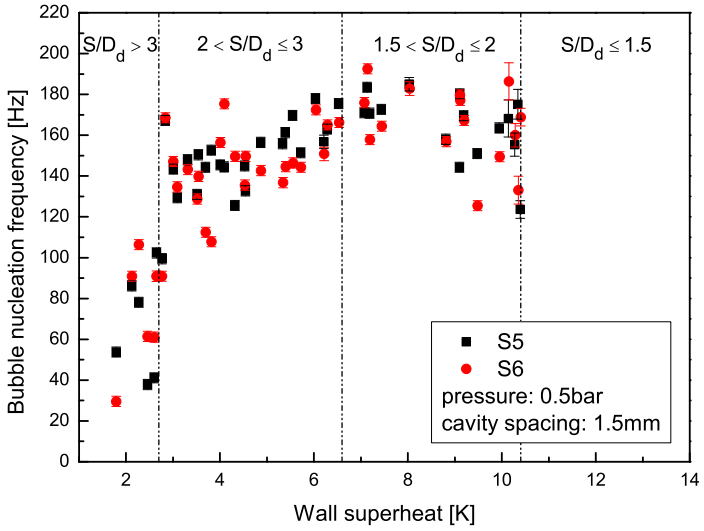

Figure 6.1: *Bubble nucleation frequency as a function of wall superheat with a spacing of 1.5 mm between the two cavities S5 and S6 at 0.5 bar.*

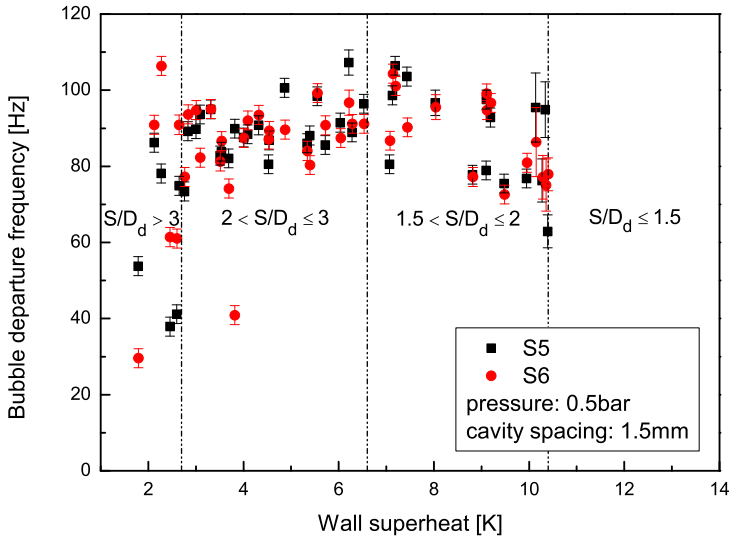

Figure 6.2: *Bubble departure frequency as a function of wall superheat with a spacing of 1.5 mm between the two cavities S5 and S6 at 0.5 bar.*

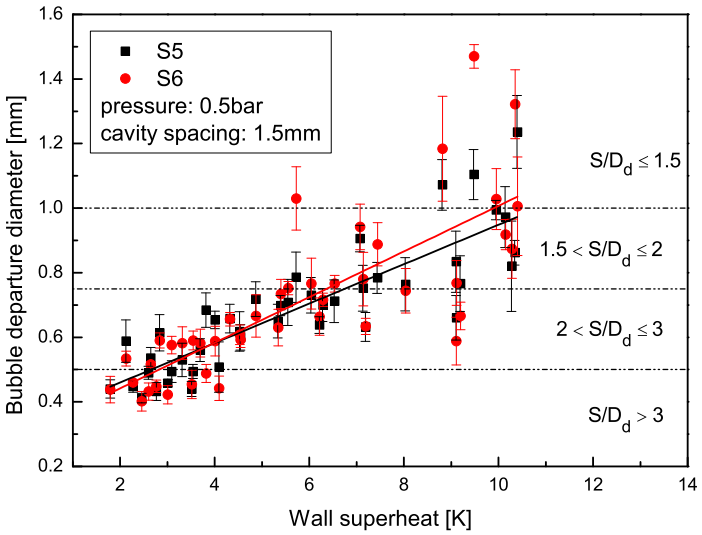

Figure 6.3: *Bubble departure diameter as a function of wall superheat with a spacing of 1.5 mm between the two cavities S5 and S6 at 0.5 bar.*

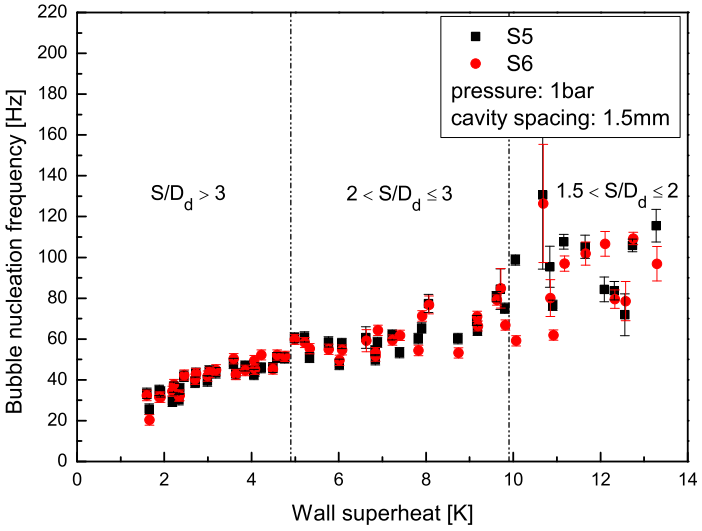

Figure 6.4: *Bubble nucleation frequency as a function of wall superheat with a spacing of 1.5 mm between the two cavities S5 and S6 at 1 bar.*

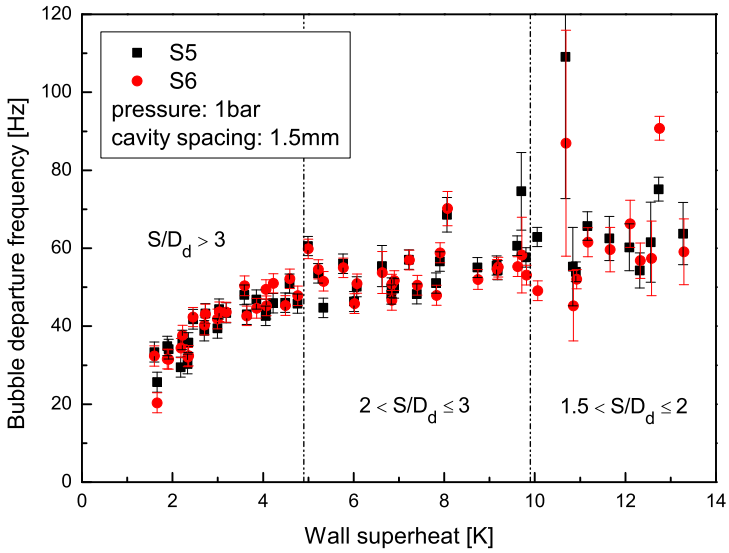

Figure 6.5: *Bubble departure frequency as a function of wall superheat with a spacing of 1.5 mm between the two cavities S5 and S6 at 1 bar.*

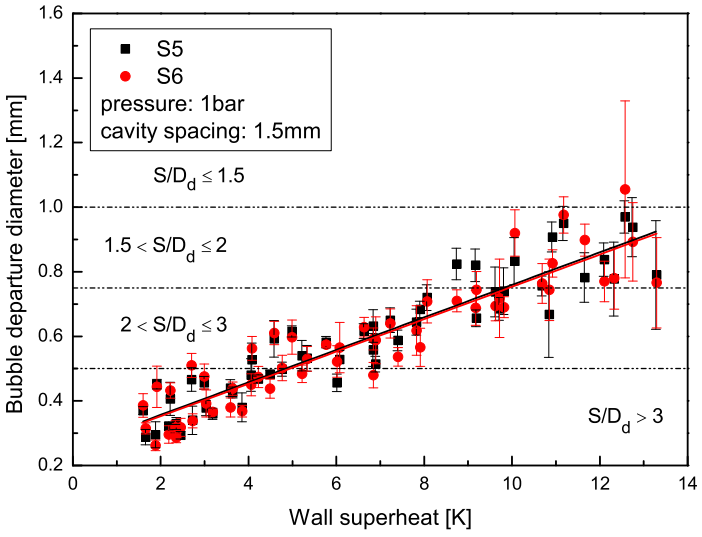

Figure 6.6: *Bubble departure diameter as a function of wall superheat with a spacing of 1.5 mm between the two cavities S5 and S6 at 1 bar.*

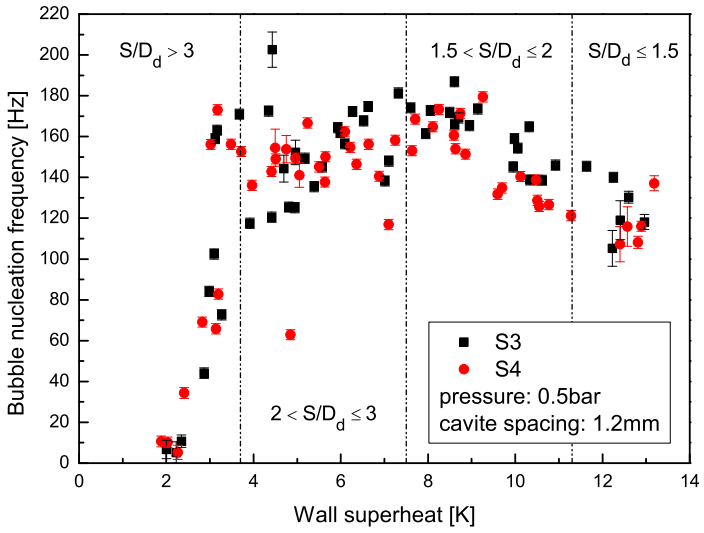

Figure 6.7: *Bubble nucleation frequency as a function of wall superheat with a spacing of 1.2 mm between the two cavities S3 and S4 at 0.5 bar.*

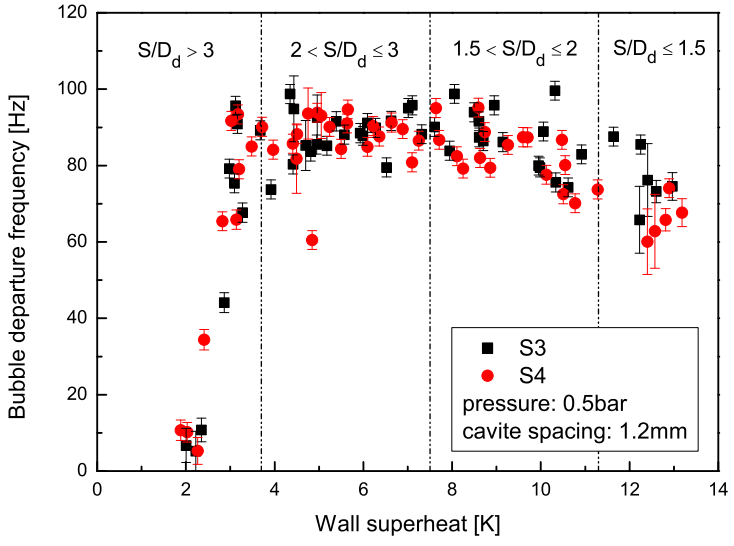

Figure 6.8: *Bubble departure frequency as a function of wall superheat with a spacing of 1.2 mm between the two cavities S3 and S4 at 0.5 bar.*

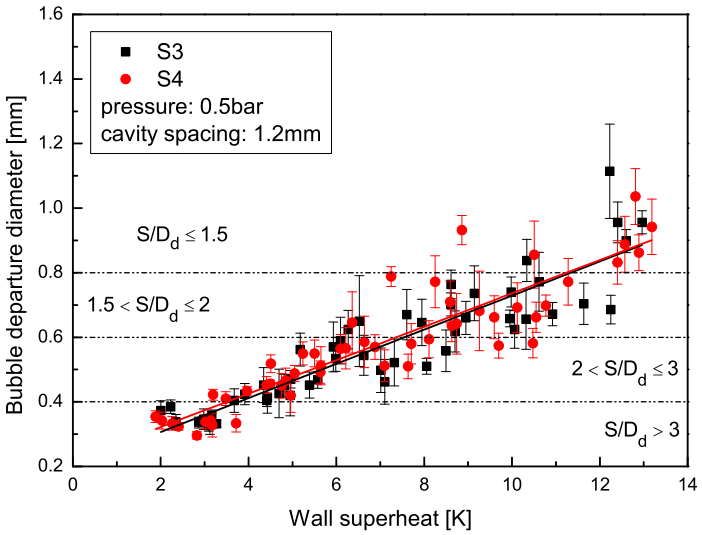

Figure 6.9: *Bubble departure diameter as a function of wall superheat with a spacing of 1.2 mm between the two cavities S3 and S4 at 0.5 bar.*

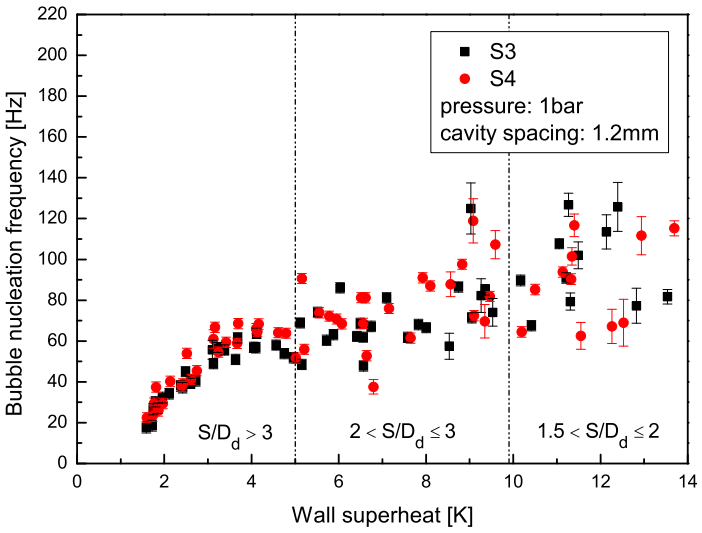

Figure 6.10: *Bubble nucleation frequency as a function of wall superheat with a spacing of 1.2 mm between the two cavities S3 and S4 at 1 bar.*

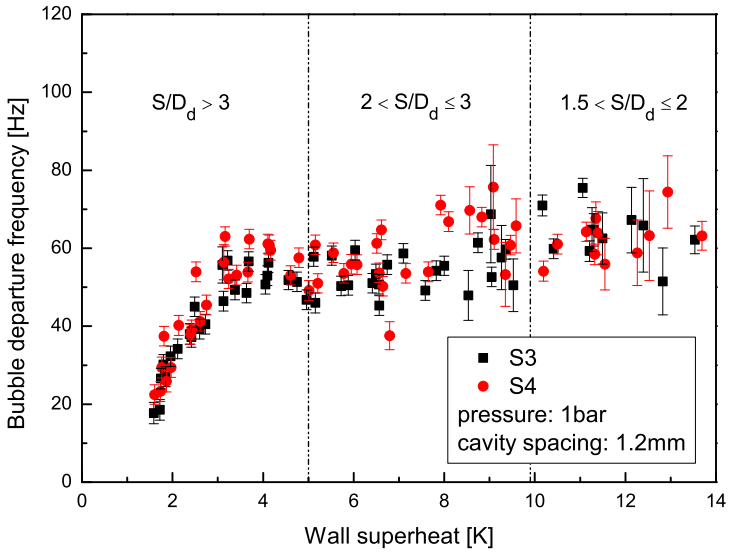

Figure 6.11: *Bubble departure frequency as a function of wall superheat with a spacing of 1.2 mm between the two cavities S3 and S4 at 1 bar.*

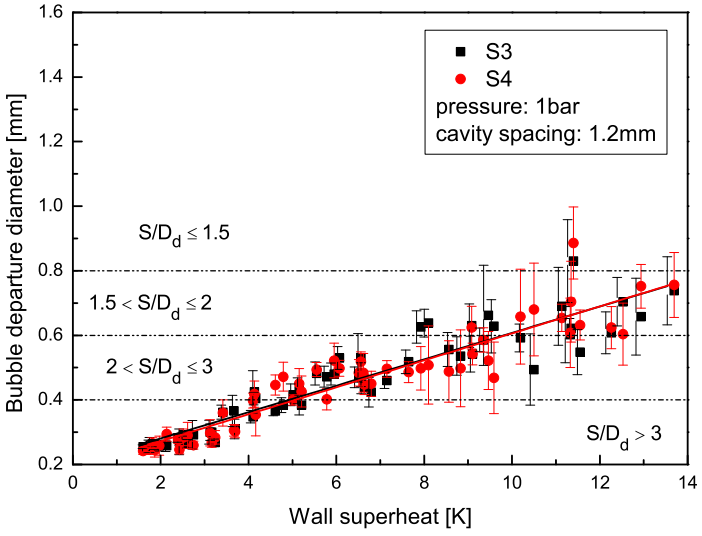

Figure 6.12: *Bubble departure diameter as a function of wall superheat with a spacing of 1.2 mm between the two cavities S3 and S4 at 1 bar.*

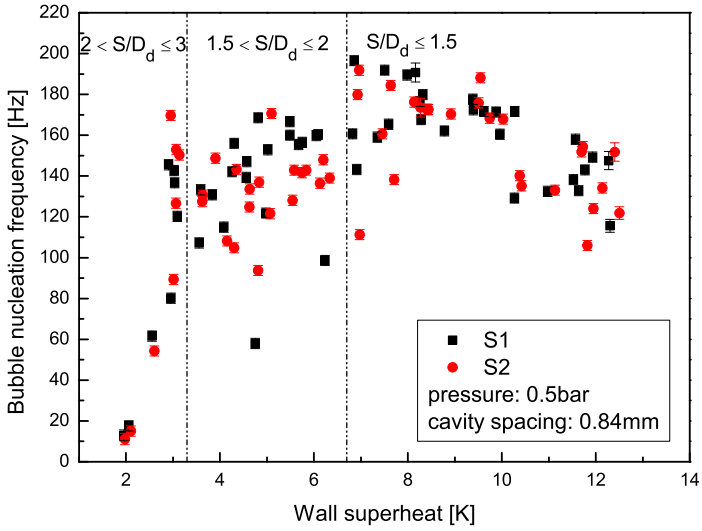

Figure 6.13: *Bubble nucleation frequency as a function of wall superheat with a spacing of 0.84 mm between the two cavities S1 and S2 at 0.5 bar.*

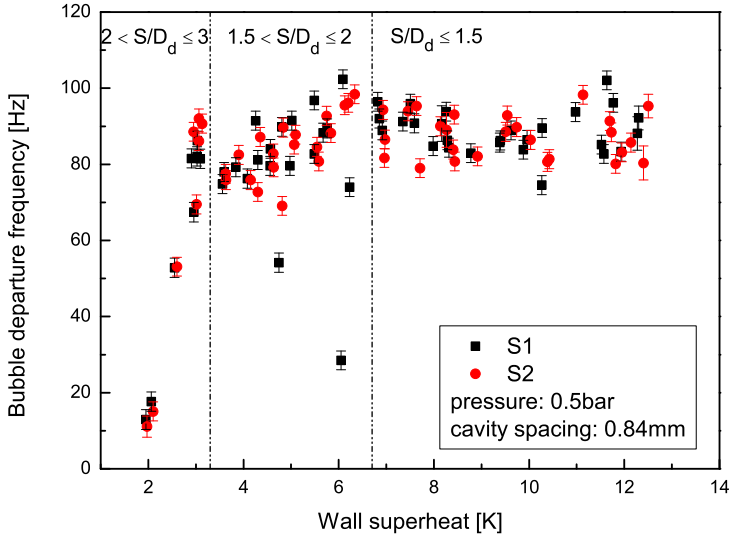

Figure 6.14: *Bubble departure frequency as a function of wall superheat with a spacing of 0.84 mm between the two cavities S1 and S2 at 0.5 bar.*

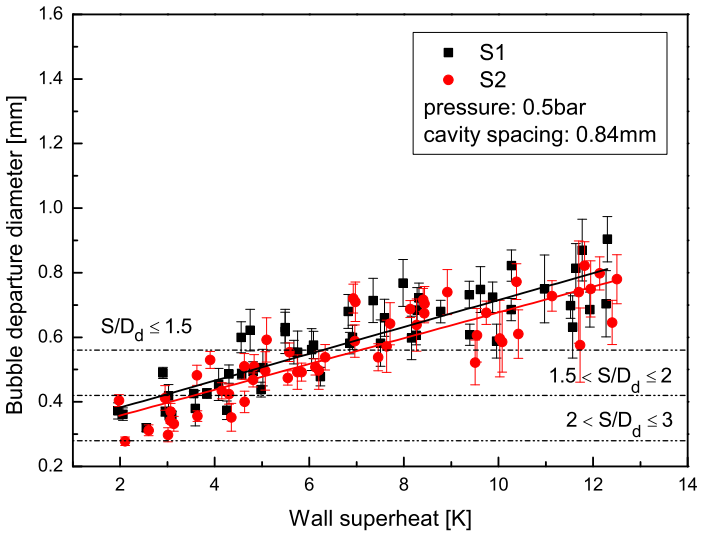

Figure 6.15: *Bubble departure diameter as a function of wall superheat with a spacing of 0.84 mm between the two cavities S1 and S2 at 0.5 bar.*

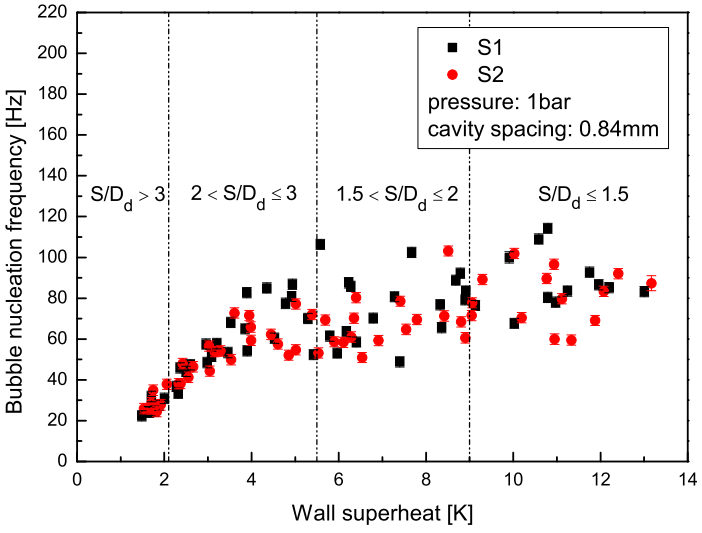

Figure 6.16: *Bubble nucleation frequency as a function of wall superheat with a spacing of 0.84 mm between the two cavities S1 and S2 at 1 bar.*

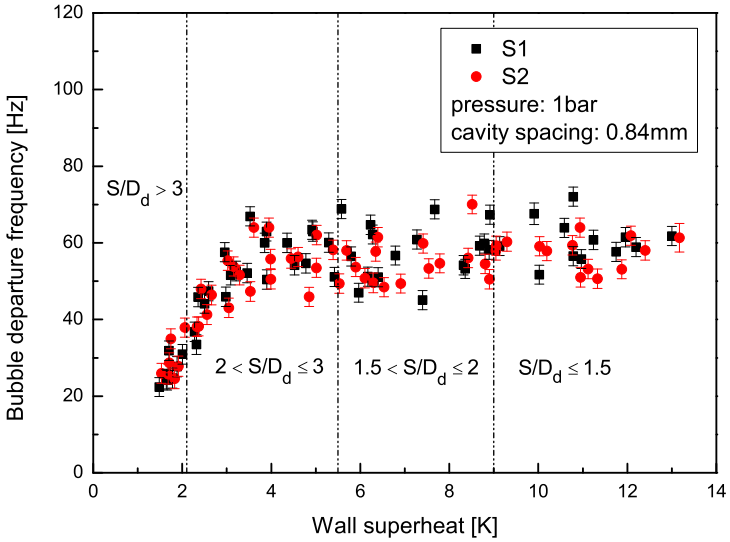

Figure 6.17: *Bubble departure frequency as a function of wall superheat with a spacing of 0.84 mm between the two cavities S1 and S2 at 1 bar.*

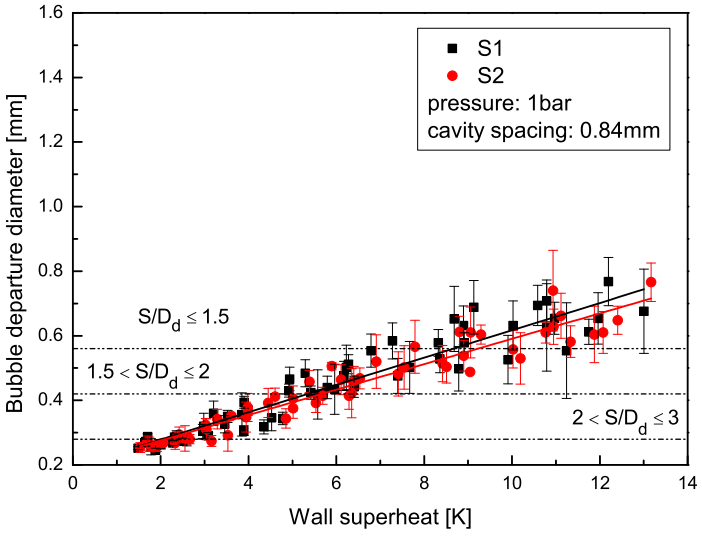

Figure 6.18: *Bubble departure diameter as a function of wall superheat with a spacing of 0.84 mm between the two cavities S1 and S2 at 1 bar.*

The departure diameter increases for both pressures in a near-linear fashion and reaches slightly higher departure diameters for the same superheat at $0.5\,\mathrm{bar}$, only visible, however, if the trend lines are compared, Fig. C.50 and C.51.

In Figure 6.13 to 6.18 the same parameters are presented for two neighbouring cavities with a spacing of $0.84\,\mathrm{mm}$ for 0.5 and $1\,\mathrm{bar}$. The bubble nucleation frequency seems to drop above $9\,\mathrm{K}$, however, if the vertical coalescence is not considered, the frequency appears to be almost constant above $4\,\mathrm{K}$ wall superheat at $0.5\,\mathrm{bar}$, Fig. 6.13 and 6.16. Figure 6.16 and 6.17 are very similar to Fig. 6.10 and 6.11 and no influence of the spacing is apparent. The departure diameters increase in a near-linear fashion for both pressures, Fig. 6.15 and 6.18; unlike Fig. 6.3, 6.6, 6.9 and 6.12 for larger spacing, where no significant difference in size is detectable.

Experimental bubble frequencies measured by Zhang and Shoji [6] were strongly influenced by the variation of $S/\overline{D_d}$ at their applied heat fluxes. The heat fluxes applied in this study are typically one order of magnitude smaller as compared to that of Zhang and Shoji, but the latent heat of vaporisation at the normal boiling temperature is around 24 times smaller for FC-72 as compared to that of water. For $S/\overline{D_d}$ equal to 0.5 the frequency was about three times higher than for 1.5 and around 1.75 times higher than at 2.5 for the highest applied heat flux of $37.2\,\mathrm{kW/m^2}$. The measured nucleation and departure frequency seem not to be influenced by decreasing spacing, or any interactions for the applied heat flux are minor and hidden in the rather scattered data.

For the departure diameter there is a small increase for the two widest spacings between two cavities. For cavity spacings of 0.84 and $1.2\,\mathrm{mm}$ the difference in departure diameter is very small and can be treated as insignificant. The difference between the two shorter spaced cases and the widest spacing is increasing with wall superheat and ranges from 0.05 to $0.24\,\mathrm{mm}$ for $0.5\,\mathrm{bar}$ and from 0.07 to $0.16\,\mathrm{mm}$ for $1\,\mathrm{bar}$. These differences are very small and are only valid for the comparison of the linear trend lines of the departure diameter measurement with increasing wall superheat for each cavity, Fig. C.50 and C.51 in appendix C.

6.2 Horizontal coalescence

In this chapter the occurrence of horizontal coalescence was investigated. Horizontal coalescence took place only for the two closest spaced cavities S1 and S2 at $0.5\,\mathrm{bar}$. In Figure 6.19 the frequency of horizontal coalescence is presented as a function of increasing wall superheat. Bubbles growing from S1 and S2 only merged above a wall temperature superheat of $8\,\mathrm{K}$ and the frequency of horizontal coalescence increases with further increasing superheat. At the highest measured superheat the frequency reached its maximum slightly above $60\,\mathrm{Hz}$. Zhang and Shoji [6] reported horizontal coalescence for $S/\overline{D_d}$ smaller than 1.5. Measured frequencies for $S/\overline{D_d}$ equal to 1 are higher than frequencies at $12\,\mathrm{K}$, the corresponding temperature for $S/\overline{D_d}$ equal to 1.1 for these experiments.

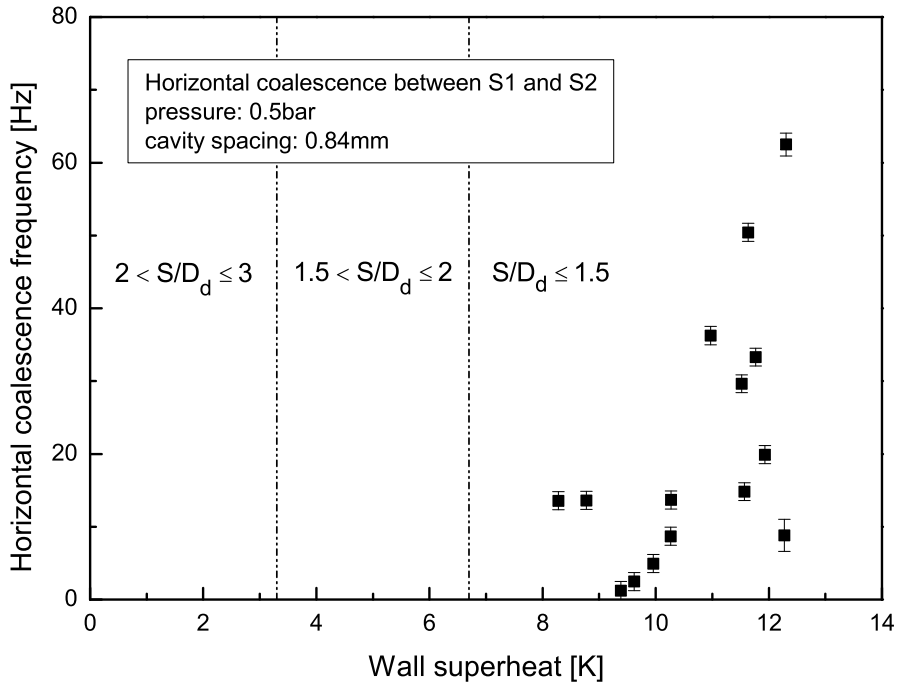

Figure 6.19: *Frequency of horizontal coalescence as a function of increasing wall superheat with a spacing of 0.84 mm between the two cavities S1 and S2 at 0.5 bar. Regions of influence, following Zhang and Shoji [6], are indicated.*

However, Zhang and Shoji do not report what wall superheats were reached nor distinguish between horizontal and declining coalescence, and the latter was not considered here.

6.3 Conclusions

Experimentally measured bubble nucleation frequency, departure frequency, frequency of horizontal coalescence and bubble departure diameter of bubble growth from pairs of artificial cavities with three different values of spacing were measured with increasing wall superheat at pressures of 0.5 and $1\,\mathrm{bar}$. Interaction between neighbouring cavities was investigated by considering the behaviour of bubble growth. Bubble nucleation frequency, departure frequency and bubble departure diameter were very similar for the pairs of artificial cavities. The lower pressure shifted slightly the regions of influence suggested by Zhang and Shoji [6] to lower superheat, due to the small increase in departure diameter at $0.5\,\mathrm{bar}$. The strong "inhibitive" and "promotive" regions for the departure frequency with decreasing spacing between cavities have not been observed in the present study. An increase in departure diameter with increasing spacing was observed. This increase was more significant for the widest spacing of $1.5\,\mathrm{mm}$. However, to compare the above results with those of Zhang and Shoji is difficult because they applied different heat fluxes. Further they used a different boiling liquid than that employed in the present study, which can affect the region of influence boundaries. Horizontal coalescence of bubbles from neighbouring cavities was only observed for the closest spacing at $0.5\,\mathrm{bar}$ for superheats above $8\,\mathrm{K}$.

Chapter 7
Conclusions

In this study the design, construction and commissioning of a pool boiling experimental setup and subsequently conducted pool boiling experiments in fluorinert FC-72 are presented. The setup consists of a temperature and pressure controlled boiling chamber, a condenser with adjustable performance and a DAQ system for liquid and vapour temperatures and micro-sensor signals. It also includes controllable power sources for the support heating system and the integrated sensors and heater in the boiling substrate. Optical observations were accomplished with a high-speed camera synchronised with the DAQ system and an adequate backlight. The experimental setup was constructed to allow a rapid alternation between differently designed silicon boiling substrates with varied artificial cavity and temperature sensor dimensions and locations.

For this investigation three different versions of boiling substrates with appropriate jigs were designed and implemented. The first was used to test the boiling chamber and condenser, the temperature control system and the DAQ. Preliminary experiments were conducted on this first test section. On the second design single bubble growth, bubble departure frequency and the influence of increasing pressure and cavity depth was investigated. The third generation test section was used to study vertical coalescence during single bubble growth and simultaneous bubble growth from differently spaced pairs of artificial cavities.

Bubble growth from isolated cavities with a nominal depth of $80\,\mu\mathrm{m}$ at $1\,\mathrm{bar}$ and $100\,\mu\mathrm{m}$ at atmospheric pressure for different wall superheats was measured. The bubble growth rate becomes very small before lift-off for the lowest studied wall superheat, which may be a consequence of the reduction in contact area. For higher wall superheats, the bubble growth rate decreases less, the bubble lifts off faster and departs

more suddenly. Generally, bubble growth time is found to decrease with increasing wall superheat and for higher wall superheats the bubbles departed before a significant decrease in growth rate was observed. The collected data is used as input for a numerical code developed at Brunel University and is a first step to validate the code. Bubble growth was compared to common correlations found in the literature. The correlation of Mikic *et al.* is found to be the closest in predicting the bubble growth overall, if results for all measured conditions are considered. Occasional close predictions of other correlations leave the contribution of distinctive mechanisms inconclusive.

In experiments with the second generation test section, bubble departure frequencies were measured for different cavity depths and pressures as a function of wall superheat. The departure frequency slightly decreases for all cavity depths with increasing pressure and becomes almost constant for high wall superheats at all measured conditions. The corresponding departure diameter increases in a near-linear fashion with wall superheat and no influence of cavity depth and pressure was observed. Common correlations generally under predict the measured departure diameters.

Waiting times between bubbles decrease rapidly with increasing wall superheat and again, there is no visible influence of cavity depth and pressure.

The evaporative heat flux due to bubble growth was estimated from measured bubble departure frequencies and diameters. Both the input and evaporative heat flux increase linearly with increasing wall superheat over a wide range.

In experiments from an isolated cavity on the third generation test section the phenomenon of vertical coalescence was visualised and quantified using high-speed imaging. The average frequency of bubble nucleation and vertical coalescence increased with wall superheat and decreasing pressure. The evolution of the vapour volume during vertical coalescence from nucleation of the first bubble to the departure of the merged bubbles was analysed. The results indicate that the vapour production is nearly constant during vertical coalescence.

To investigate potential interactions between differently spaced nucleation sites, bubble nucleation frequencies, departure frequencies, frequencies of horizontal coalescence

and bubble departure diameters during bubble growth from pairs of artificial cavities with increasing wall superheat at 0.5 and $1\,\mathrm{bar}$ were experimentally measured. All measured parameters, however, were very similar for the pairs of artificial cavities. Only an increase in departure diameter with increasing spacing was observed. This increase was most significant for the widest spacing of $1.5\,\mathrm{mm}$. Horizontal coalescence of bubbles from neighbouring cavities was only observed for the closest spacing at $0.5\,\mathrm{bar}$ for superheats above $8\,\mathrm{K}$.

Chapter 8
Future work

The present study can be further developed into two possible directions. To provide input and validation data for a numerical code, under development parallel to this investigation at Brunel University, a new silicon boiling substrate design is required. The objective of this simulation is to study nucleation sites on various boiling substrate materials as interacting network and finally, working as a design tool of boiling substrates for the implementation in pool boiling cooling applications. Therefore, empirical input of large numbers of active and stable nucleation sites on a substrate are essential. For a configuration containing hundreds or more artificial cavities, specific optical observations are impossible. That is why the sensitivity of temperature sensors has to be improved or FC-72 replaced with another boiling liquid, exhibiting a higher heat of vaporisation or reaching larger bubble departure diameters and hence leading to larger local temperature variations during bubble growth. Dielectric liquids meeting this specifications are very expensive, on the other hand are changes to the experimental setup time consuming and would come with major expenses.

Another requirement for the improvement of the numerical code is to control the activation of single nucleation sites individually. This feature was added to the boiling substrate by integrating small resistance heaters below each artificial cavity. Possible problems are the complexity of the control system, regulating each heater individually and the electrical insulation between temperature sensors and micro-heaters to prevent interference and signal noise. To handle this large amount of wiring, it is suggested to use gold wire bonding, which ensures a proper connection between test section and instrumentation.

Further fundamental investigations concerning, bubble nucleation, interactions for single or multiple nucleations sites, is another direction this project may take. Sensors of

the kind developed by Moghaddam *et al.* [140] are required, though. The large number of small sensors entangling a single artificial cavity, gives a high spatial and temporal resolution of the temperature field and a deep insight of involved mechanisms. An elaborate distribution of such sensors between two or more artificial cavities could reveal thermal interactions between closely spaced nucleation sites during bubble growth. Again, adding micro-heaters below each cavity would allow us to control the moment of activation.

To increase the visualisation of single bubbles and bubble interactions, such as coalescence, a sophisticated arrangement of mirrors is a potential solution. Positioning mirrors behind an artificial cavity with a certain angle, allows us to record simultaneously different sides of one or more bubbles. Similar techniques are already extensively used in combustion research. Special image processing software corrects the distortion due to the angle between mirror and camera and reproduces a clear image of the bubble. For the current experimental setup the purchase of a better performing long-distance lens would be inevitable.

It is important to prevent or reduce liquid motion induced by natural convection due to the heating system, keeping the boiling liquid saturated. A small transparent fence around the artificial cavities is a possible solution. The distance between cavities and fence has to be considered carefully, as it needs to be wide enough to exclude any thermal or direct hydrodynamic interaction.

A certainly challenging, but most interesting idea is the implementation of the particle image velocimetry (PIV) technique to visualise the flow field around a growing bubble, [148, 149]. Especially obtaining a better insight and understanding of hydrodynamic interactions between two or more simultaneously growing bubbles would be rather exciting. A drawback is the addition of particles to the boiling liquid. This will have an impact on heat transfer and nucleation mechanisms, however, simultaneous measurements of the temperature field inside the boiling substrate would allow to estimate this impact.

Appendix A
Additional information experimental setup

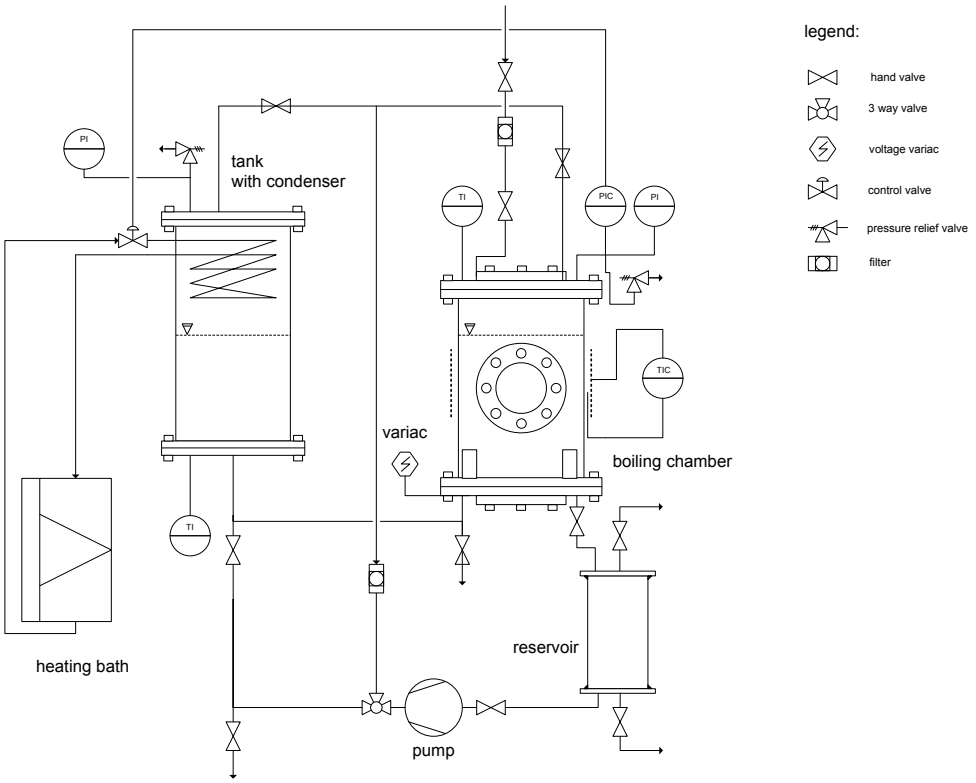

Figure A.1: *Flow and control diagram of the pool boiling experiment.*

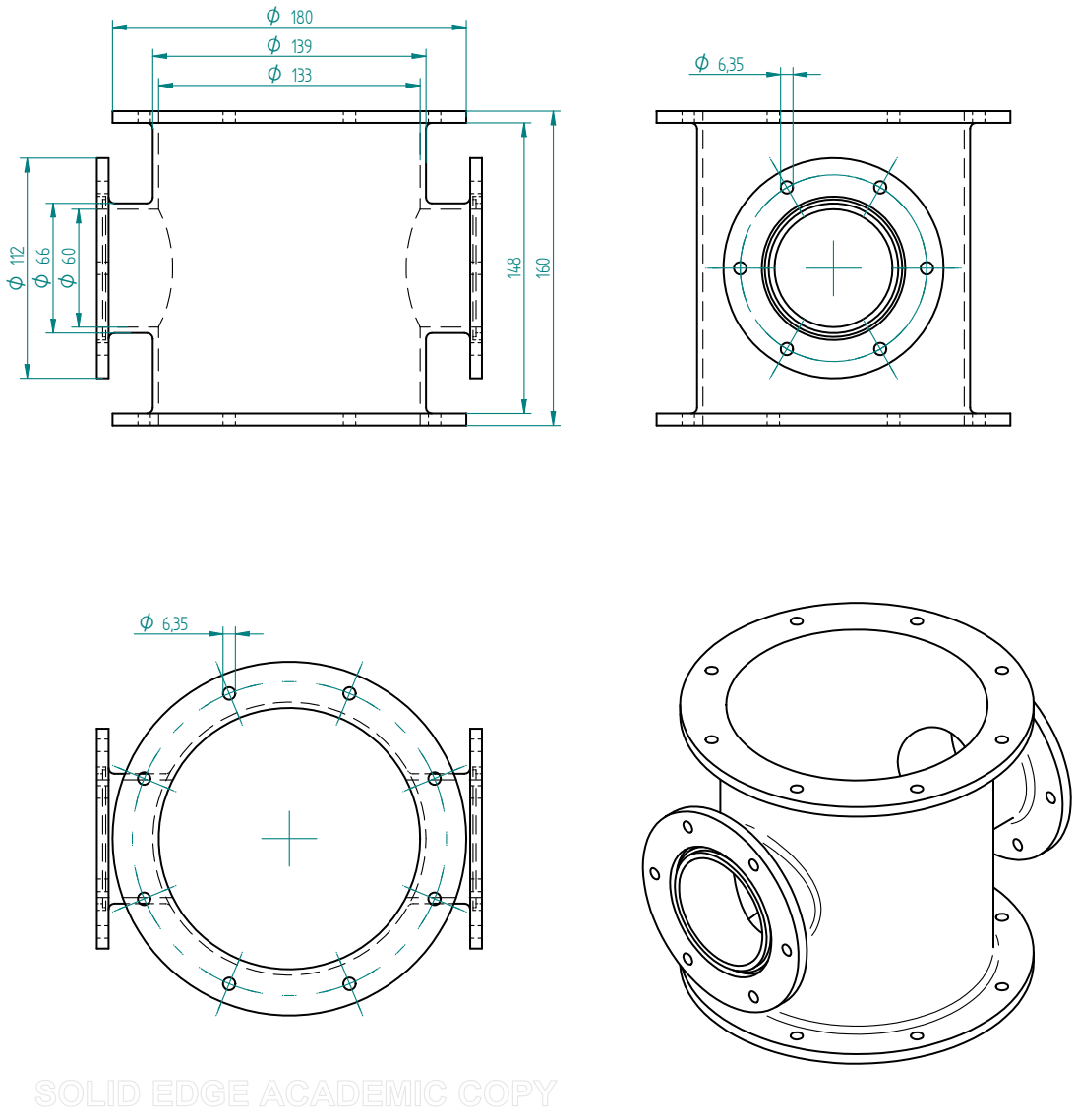

Figure A.2: *Technical drawings of the boiling chamber's stainless steel body.*

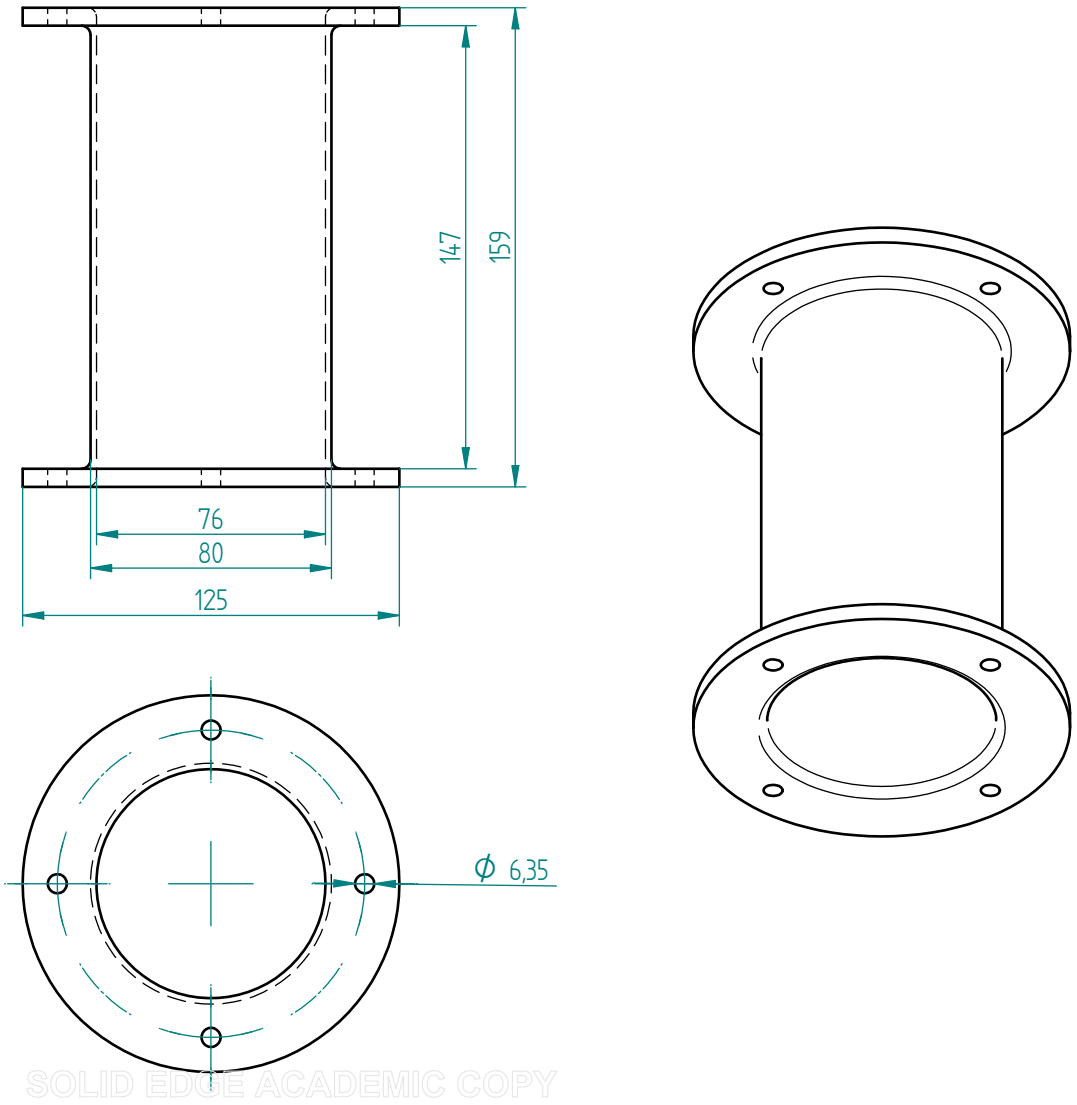

Figure A.3: *Technical drawings of the condenser's stainless steel body.*

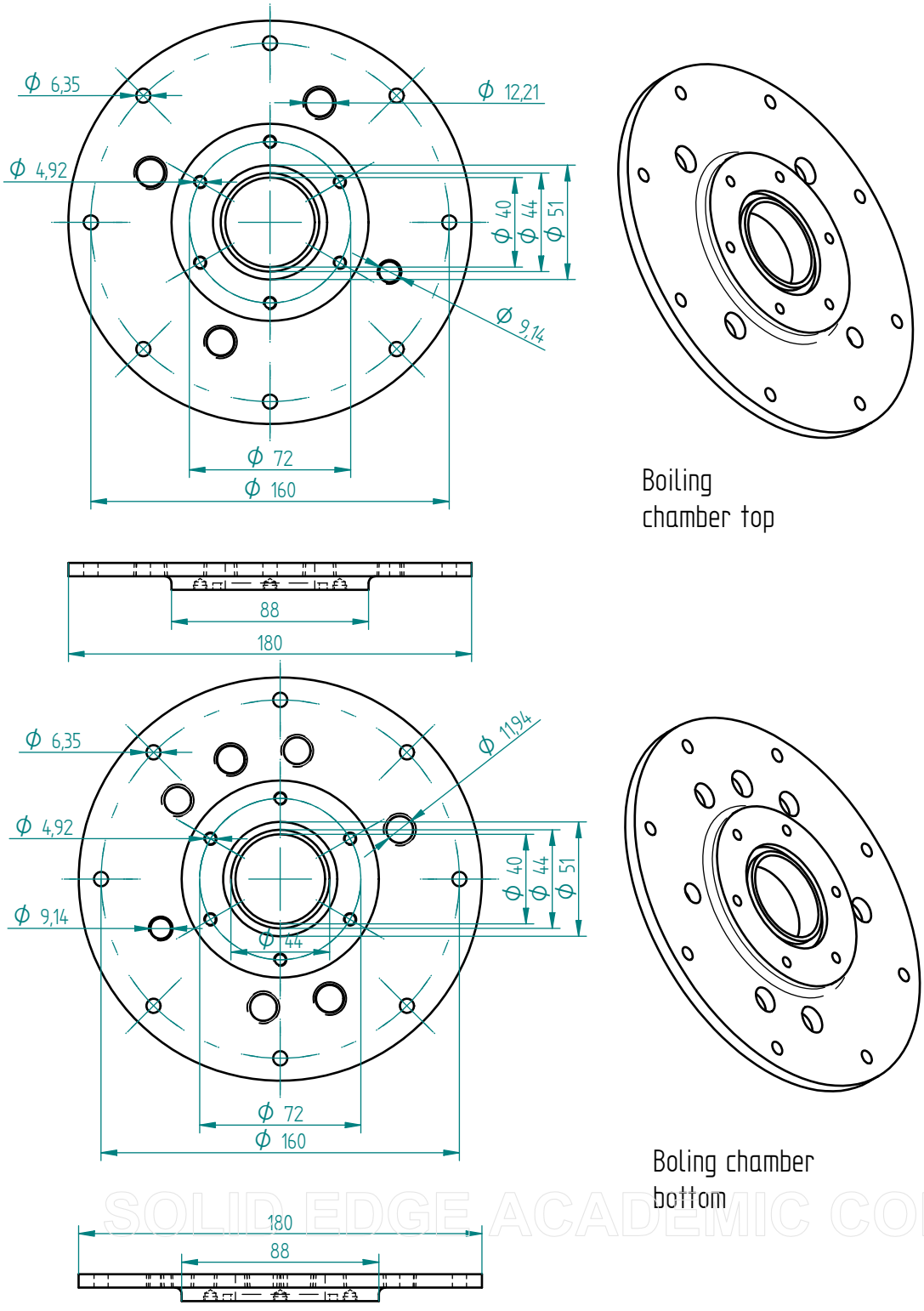

Figure A.4: *Technical drawings of the boiling chamber's top and bottom stainless steel lid.*

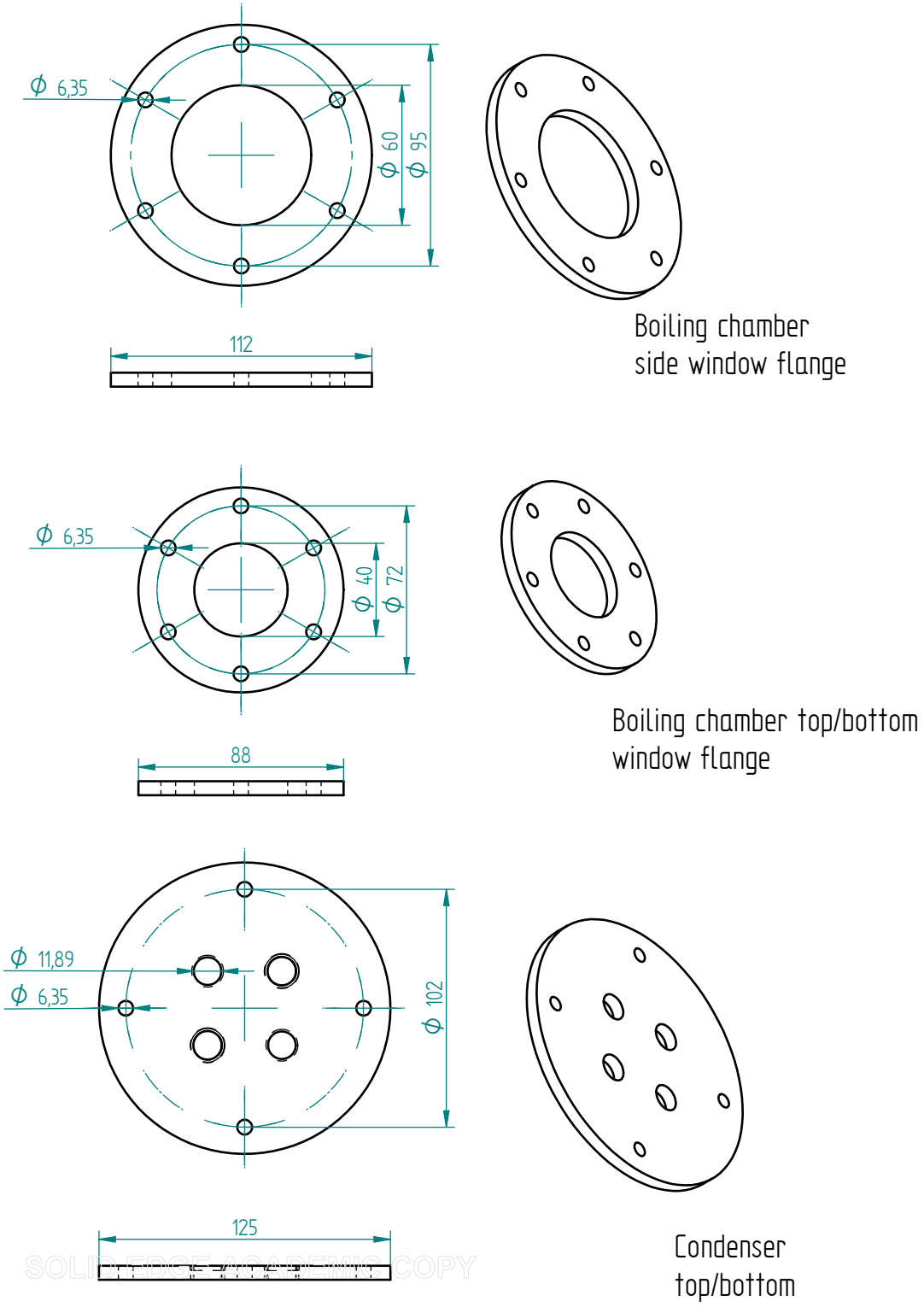

Figure A.5: *Technical drawings of the stainless steel window flanges of the boiling chamber and the top and bottom lid of the condenser.*

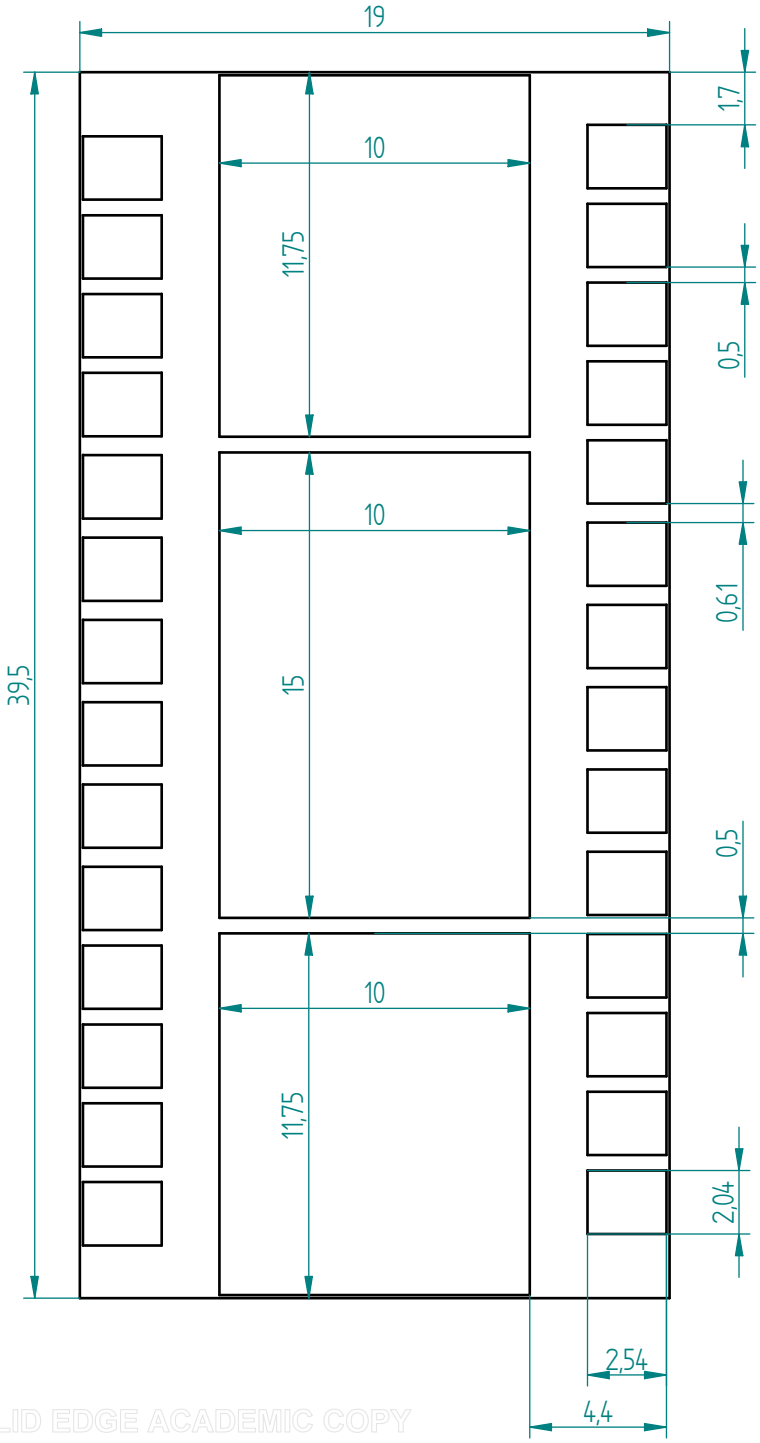

Figure A.6: *Technical drawing of the silicon device of the second generation with micro-sensors and heater pads.*

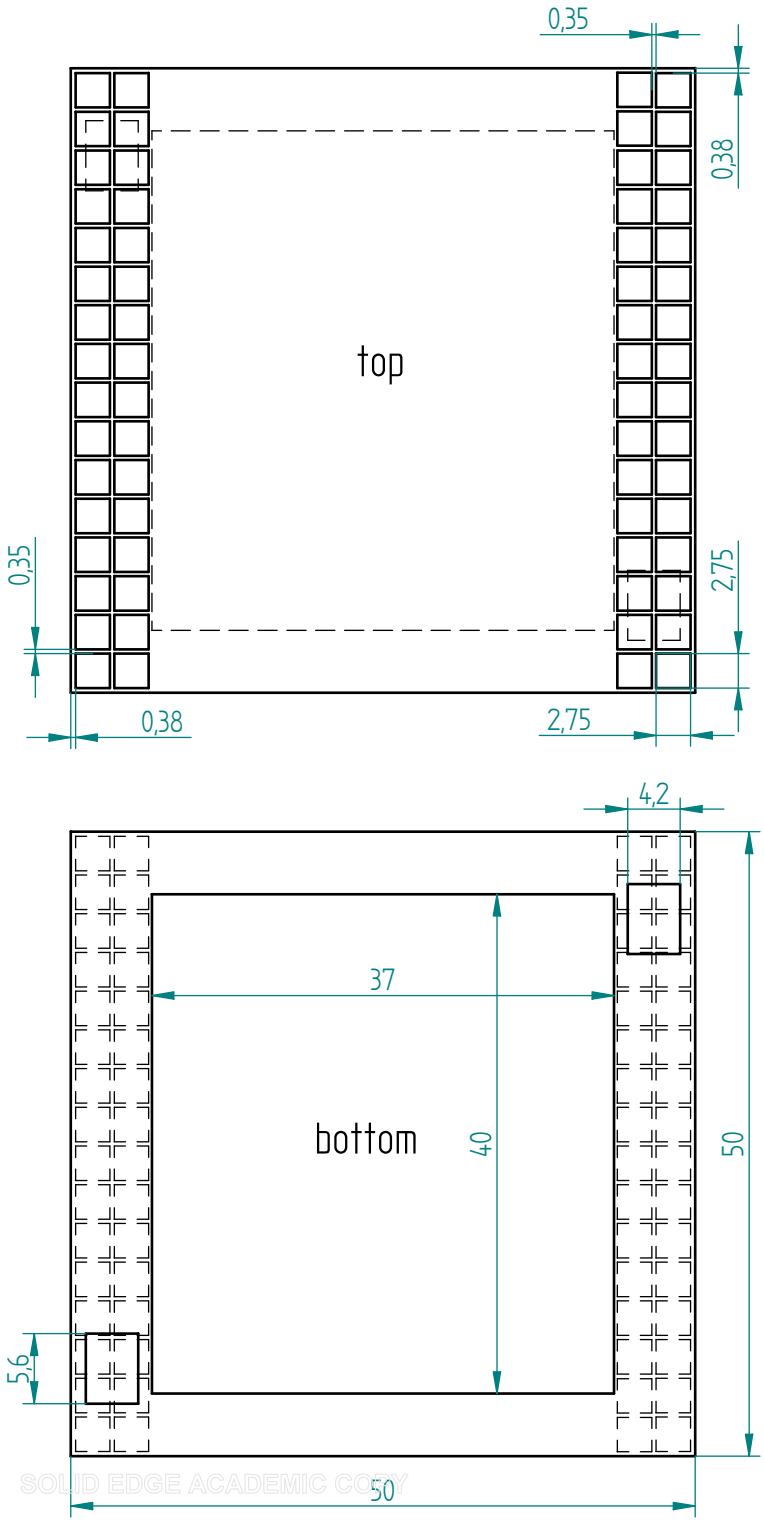

Figure A.7: *Technical drawing of the silicon device of the third generation with micro-sensors and heater pads.*

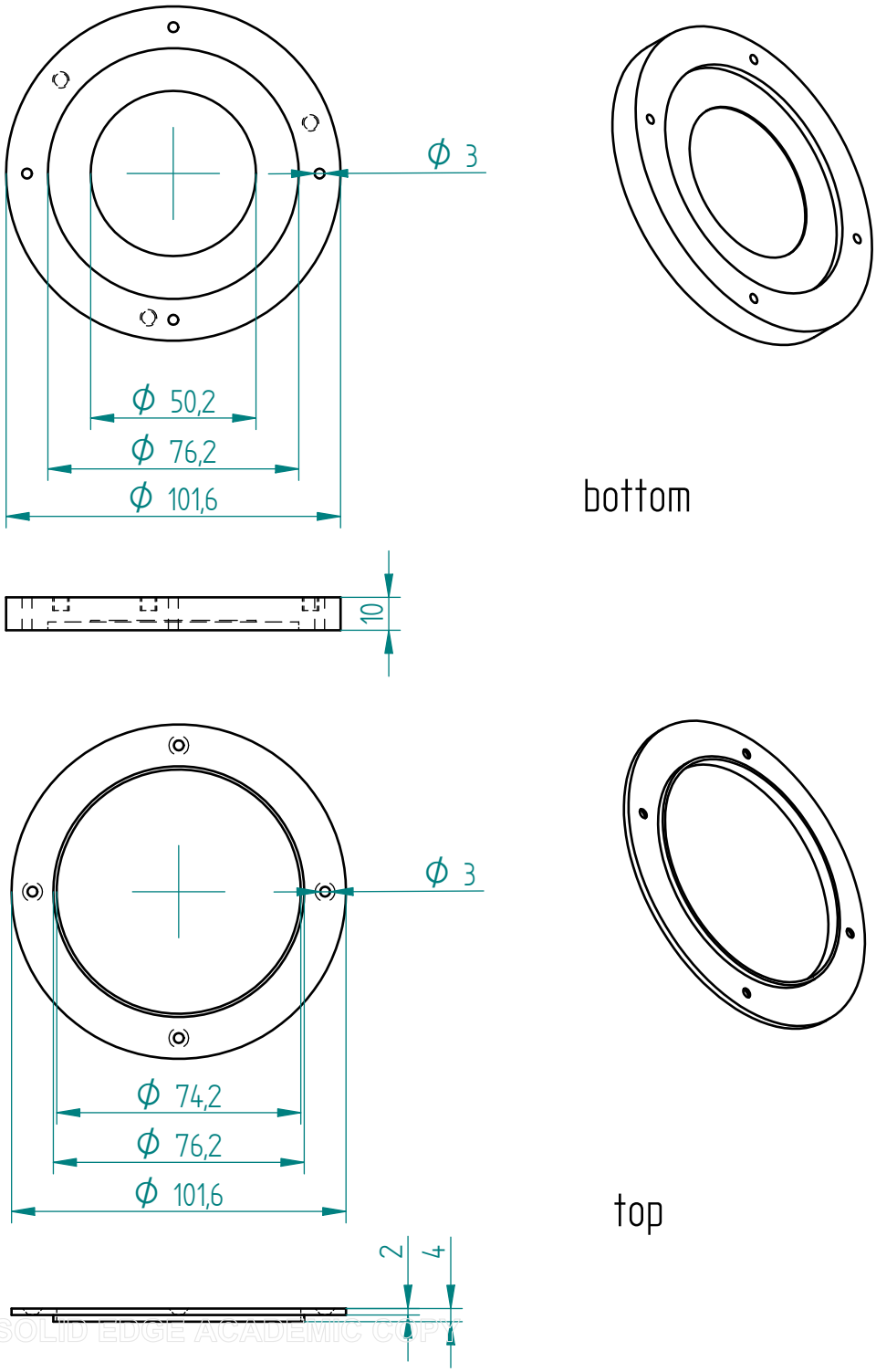

Figure A.8: *Technical drawing of the jig, holding the silicon device of the first generation in place.*

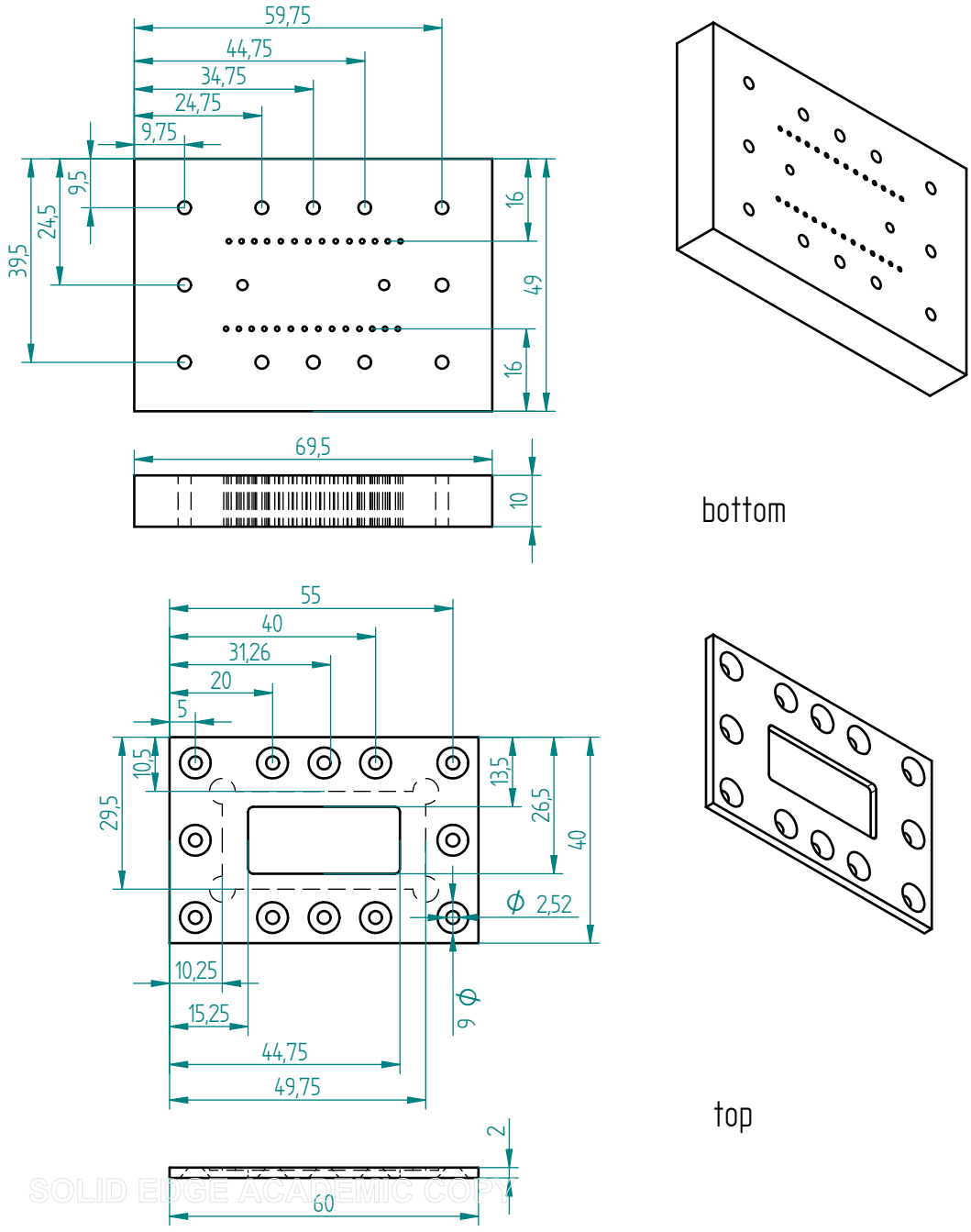

Figure A.9: *Technical drawing of the jig, holding the silicon device of the second generation in place.*

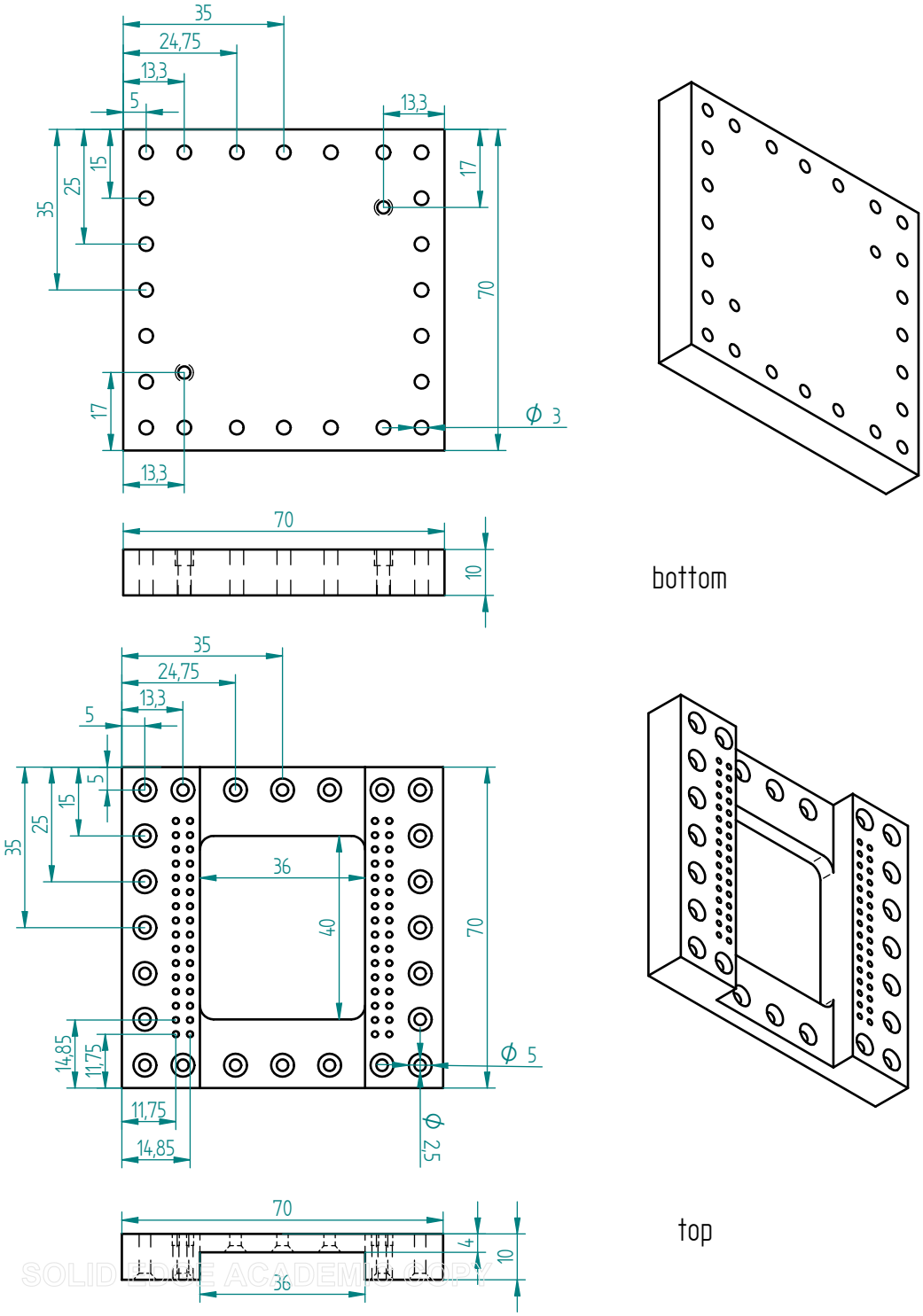

Figure A.10: *Technical drawing of the jig, holding the silicon device of the third generation in place.*

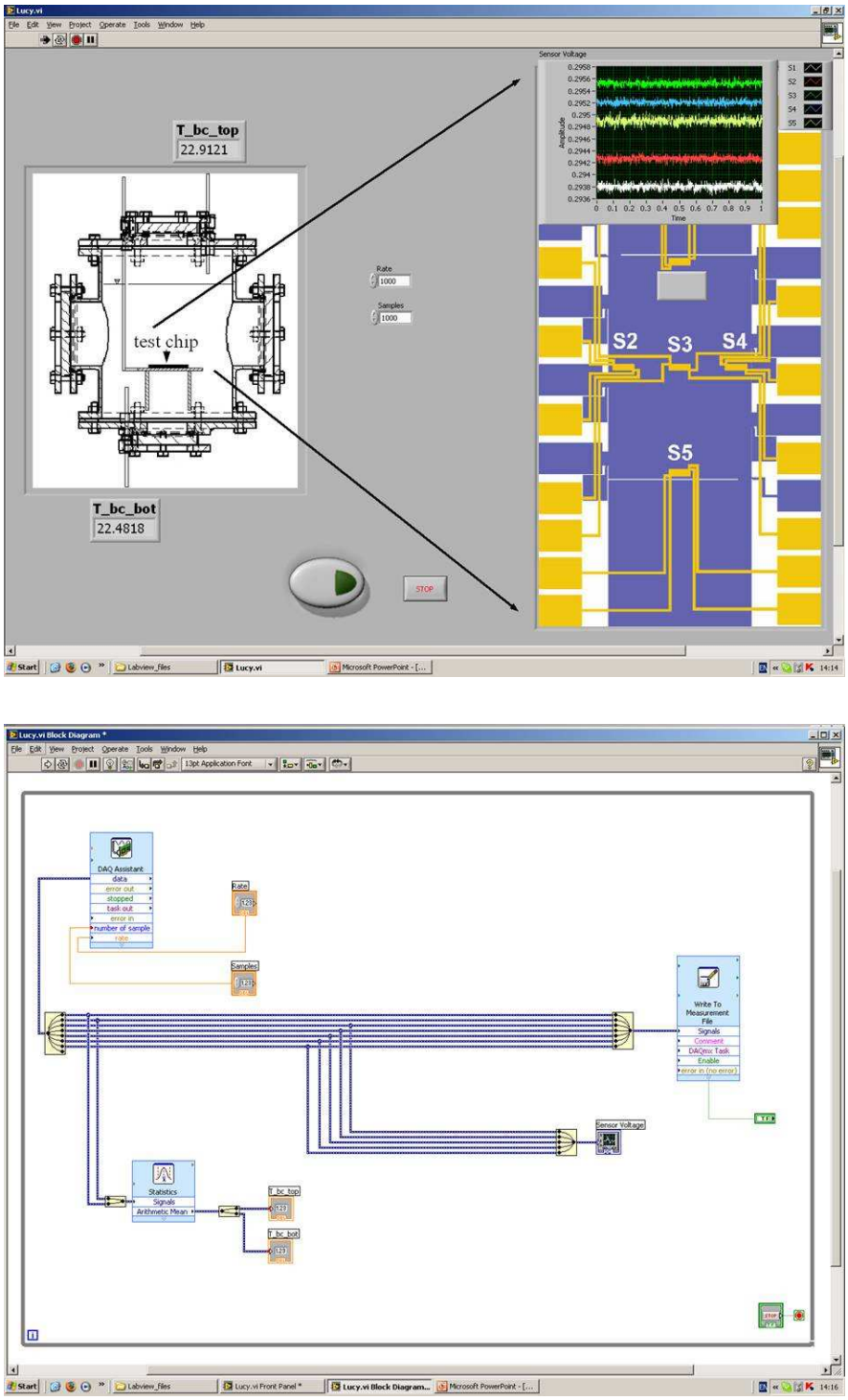

Figure A.11: *Top: LabVIEW user interface for DAQ for the second generation test section. Bottom: LabVIEW visual programming for the second generation test section.*

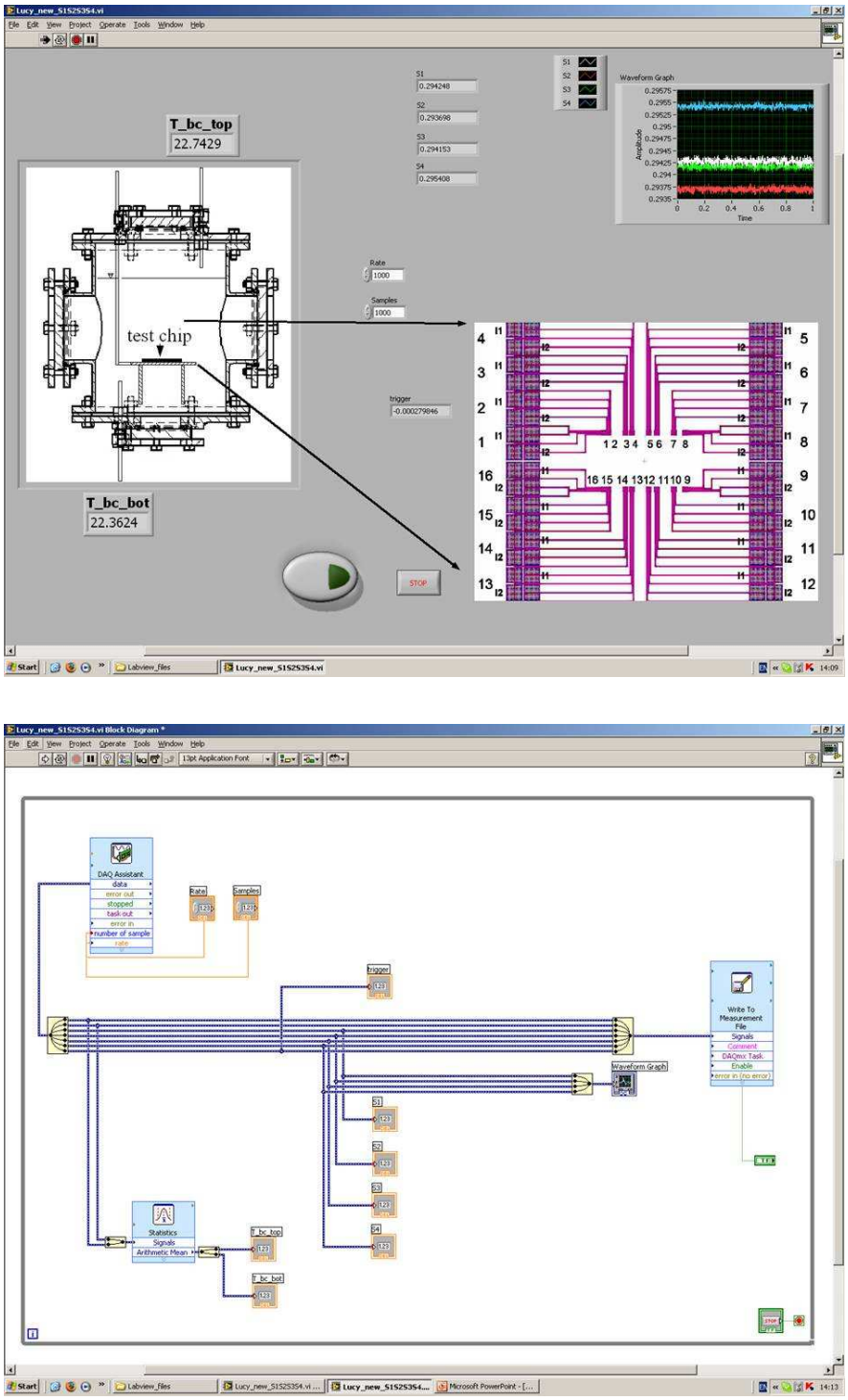

Figure A.12: *Top: LabVIEW user interface for DAQ for the third generation test section. Bottom: LabVIEW visual programming for the third generation test section.*

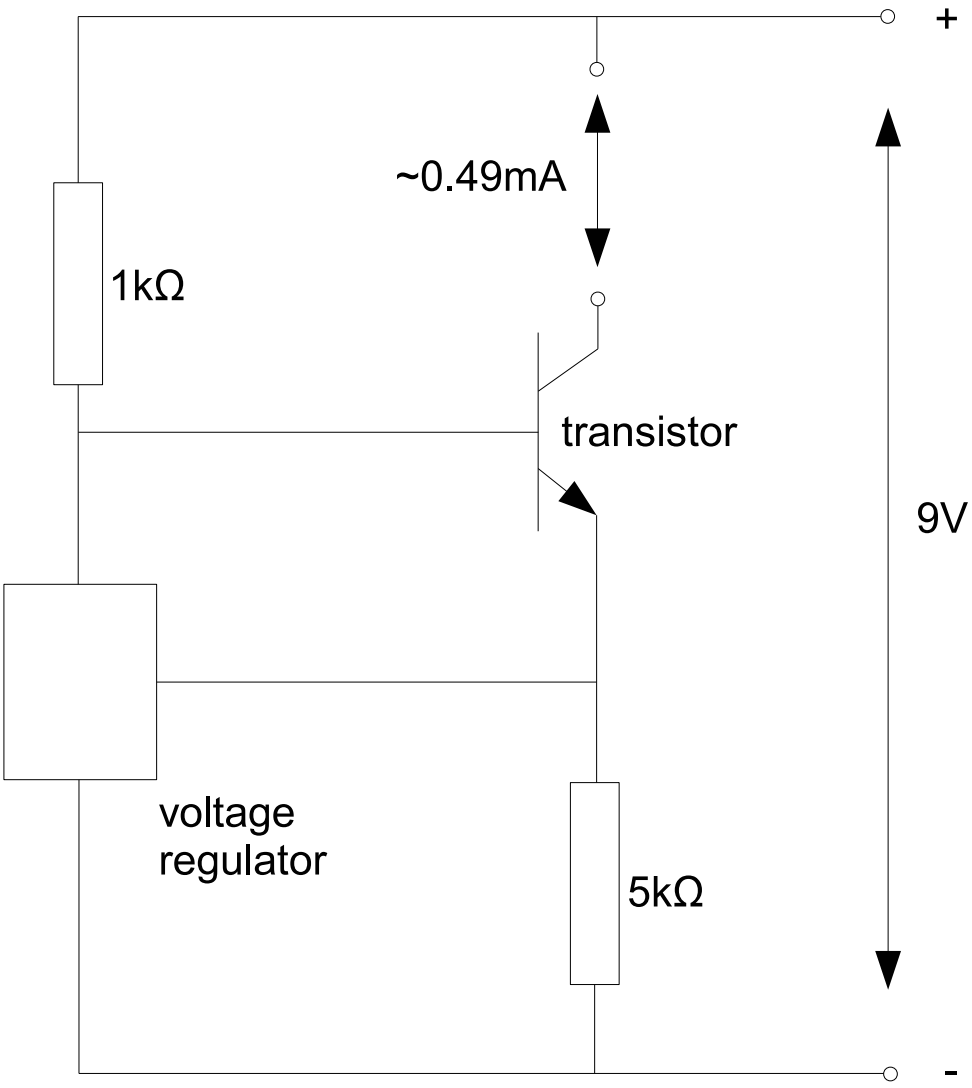

Figure A.13: *Drawing of the circuit of the self-made current source.*

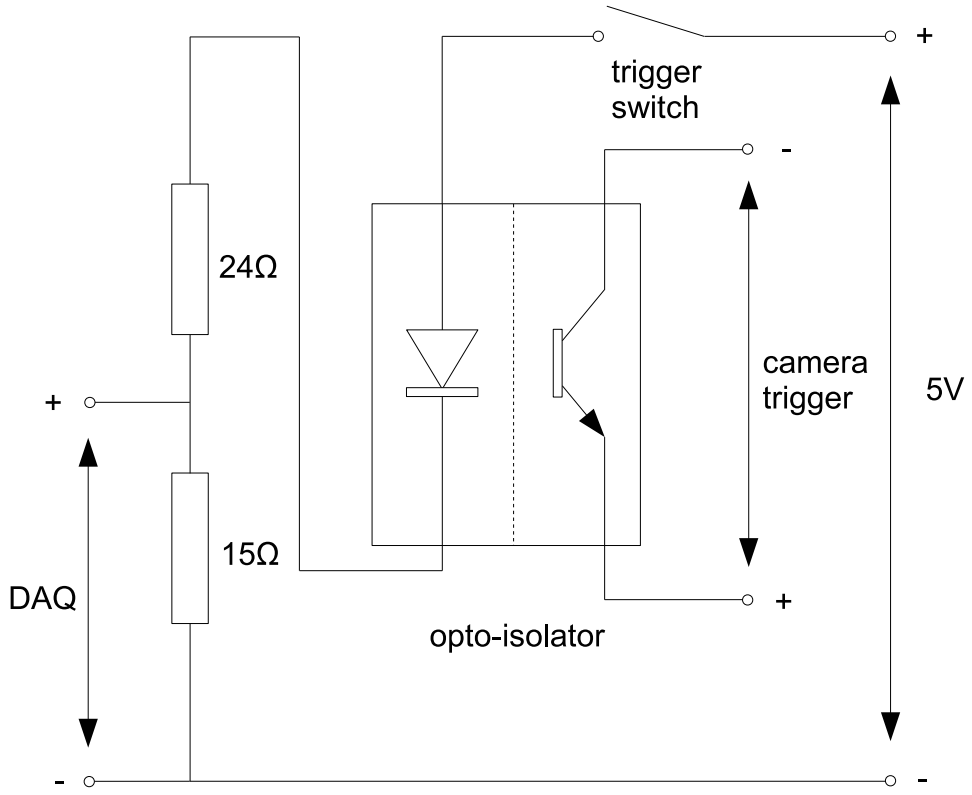

Figure A.14: *Drawing of the circuit of the self-made trigger to synchronise the high-speed imaging with the DAQ.*

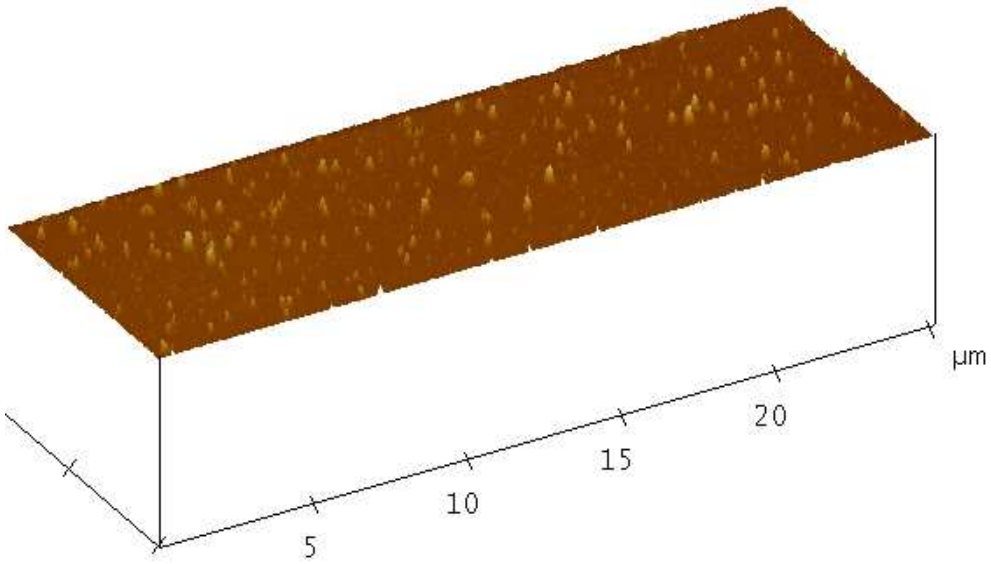

Figure A.15: *Surface roughness measurement results in 3D for the silicon device of the third generation.*

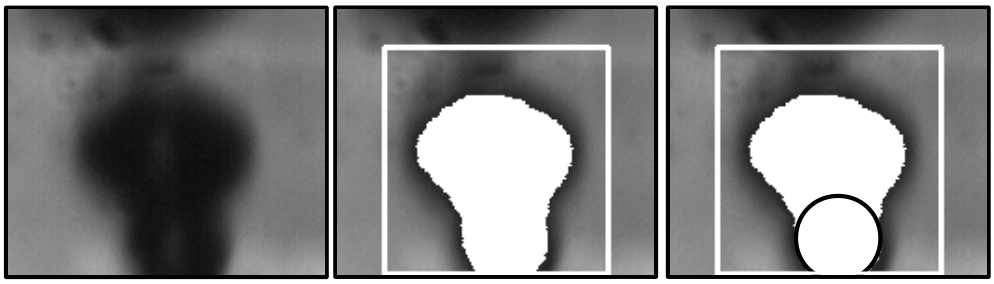

Figure A.16: *Three steps of image processing to identify the vapour volumes during vertical coalescence. Left: Original image during bubble growth with vertical coalescence. Middle: Processed picture with the assumed shape of the bottom bubble indicated. Right: Area measured with PCO Picture Viewer software. From this area the volume of revolution is calculated.*

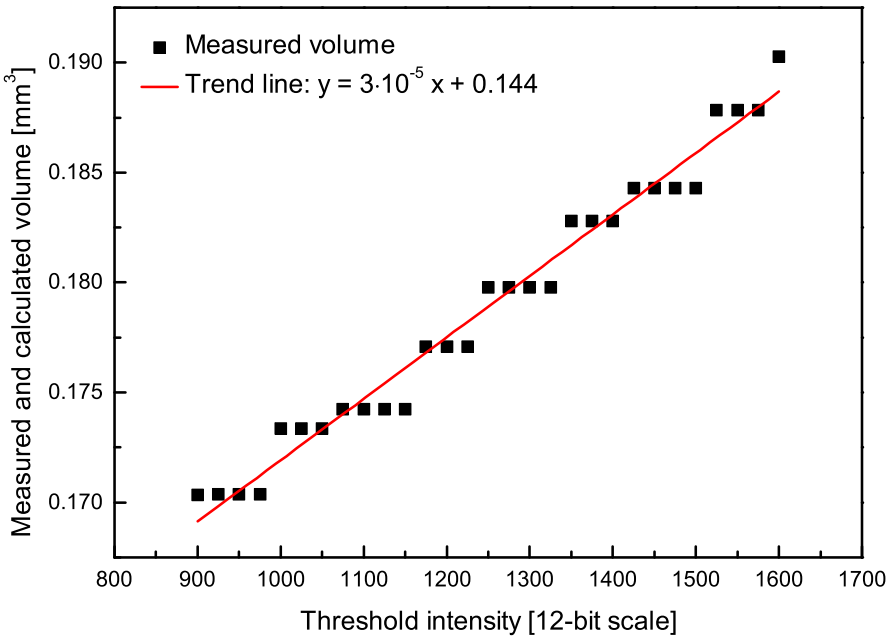

Figure A.17: *Influence of the choice of threshold intensity on the bubble volume calculation.*

Appendix B
General additional information

Table B.1: *Values of $C_{s,f}$ and n for various surface/liquid combinations ([21–23]).*

Surface liquid combination	$C_{s,f}$	n
Water / copper		
scored	0.0068	1.0
polished	0.0130	1.0
Water / stainless steel		
chemically etched	0.0130	1.0
mechanically polished	0.0130	1.0
ground and polished	0.0130	1.0
Water / brass	0.0060	1.0
Water / nickel	0.0060	1.0
water / platinum	0.0130	1.0
n-Pentane / copper		
polished	0.0154	1.7
lapped	0.0049	1.7
Benzene / chromium	0.0101	1.7
Ethyl alcohol / chromium	0.0027	1.7

Table B.2: *Thermal properties of nickel, silicon and titanium at 20 °C.*

		nickel	silicon	titanium
Density	ρ $\left[\mathrm{kg/m^3}\right]$	8.906	2.33	4.54
Specific heat capacity	c_p $\left[\mathrm{kJ/kg\ K}\right]$	0.4459	705.5	523
Thermal conductivity	k $\left[\mathrm{W/m\ K}\right]$	90	153	22
Thermal diffusivity	$\alpha \cdot 10^5$ $\left[\mathrm{m^2/s}\right]$	2.266	9.31	0.93

Table B.3: *Summary of the cases calculated with the numerical code.*

Case	R_d [mm]	t_g [ms]	ΔT_w [K]	f_{enh} [-]	$\dot{q}''$ [$^{kW}/_{m^2}$]	Test section
1	0.33	21	8.1	1.16	4.48	2
2	0.24	23	4.8	1.14	2.36	2
3	0.19	27	1.4	0.98	0.46	2
4	0.16	59	1.3	1.97	0.85	3
5	0.35	24	10.1	2.66	13.4	3

Table B.4: *Applied heat fluxes for experiments at 1, 1.25 and 1.5 atm and nominal cavity depths of 40, 80 and 100 μm and a diameter of 10 μm.*

	1 atm	1.25 atm	1.5 atm
40 μm	$1.35 - 18.20\,^{kW}/_{m^2}$	$1.33 - 13.33\,^{kW}/_{m^2}$	$1.36 - 12.50\,^{kW}/_{m^2}$
80 μm	$0.69 - 28.93\,^{kW}/_{m^2}$	$0.66 - 23.96\,^{kW}/_{m^2}$	$0.66 - 16.63\,^{kW}/_{m^2}$
100 μm	$0.85 - 36.00\,^{kW}/_{m^2}$	$0.83 - 32.00\,^{kW}/_{m^2}$	$0.67 - 28.75\,^{kW}/_{m^2}$

Table B.5: *Applied heat fluxes of experiments at 0.5, 0.75 and 1 bar and a nominal cavity depth of 80 μm and mouth diameter of 10 μm.*

Pressure	Applied heat flux
0.5 bar	$0.81 - 7.28\,^{kW}/_{m^2}$
0.75 bar	$0.51 - 7.29\,^{kW}/_{m^2}$
1 bar	$0.46 - 12.42\,^{kW}/_{m^2}$

Appendix C
Additional results

C.1 Preliminary results

In this short section preliminary results mainly from experiments conducted with the test section of the first generation are presented. Experiments with saturated gas-dissolved FC-72 at atmospheric pressure were conducted and bubble nucleation, growth and detachment were observed. The investigations focused on a single nucleation site. Fig. C.1 shows a sequence of images of two successive growing bubbles from the nucleation of the first to just before the detachment of the second one. The measured pressure was $1.01\,\mathrm{bar}$ and temperature $56.9\ (\pm 1.1)\,^{\circ}\mathrm{C}$, respectively. The power input from the background heater was $23.7\,\mathrm{W}$ ($11.7\,{}^{\mathrm{kW}}/_{\mathrm{m}^2}$). Because the nucleation process is very rapid, on the second image only a shadow appears and $1\,\mathrm{ms}$ later a bubble has already grown to a small sphere. The second flat bubble just below the round one is the reflection on the polished silicon surface and their intersection marks the contact line between bubble and silicon surface. The first growing bubble detaches after $18\,\mathrm{ms}$ and the succeeding bubble grows directly out of the remaining vapour on the surface. $18\,\mathrm{ms}$ later the second bubble is about to depart. During the growth of the first and the succeeding bubble the normalised diameter of the bubbles D_b' was estimated as follows

$$D_b' = {}^{D_b}/_{D_d} \tag{C.1}$$

where D_b is the bubble diameter measured at the bubble equator from the 2D high speed image sequence and D_d the bubble departure diameter, Fig. C.1.

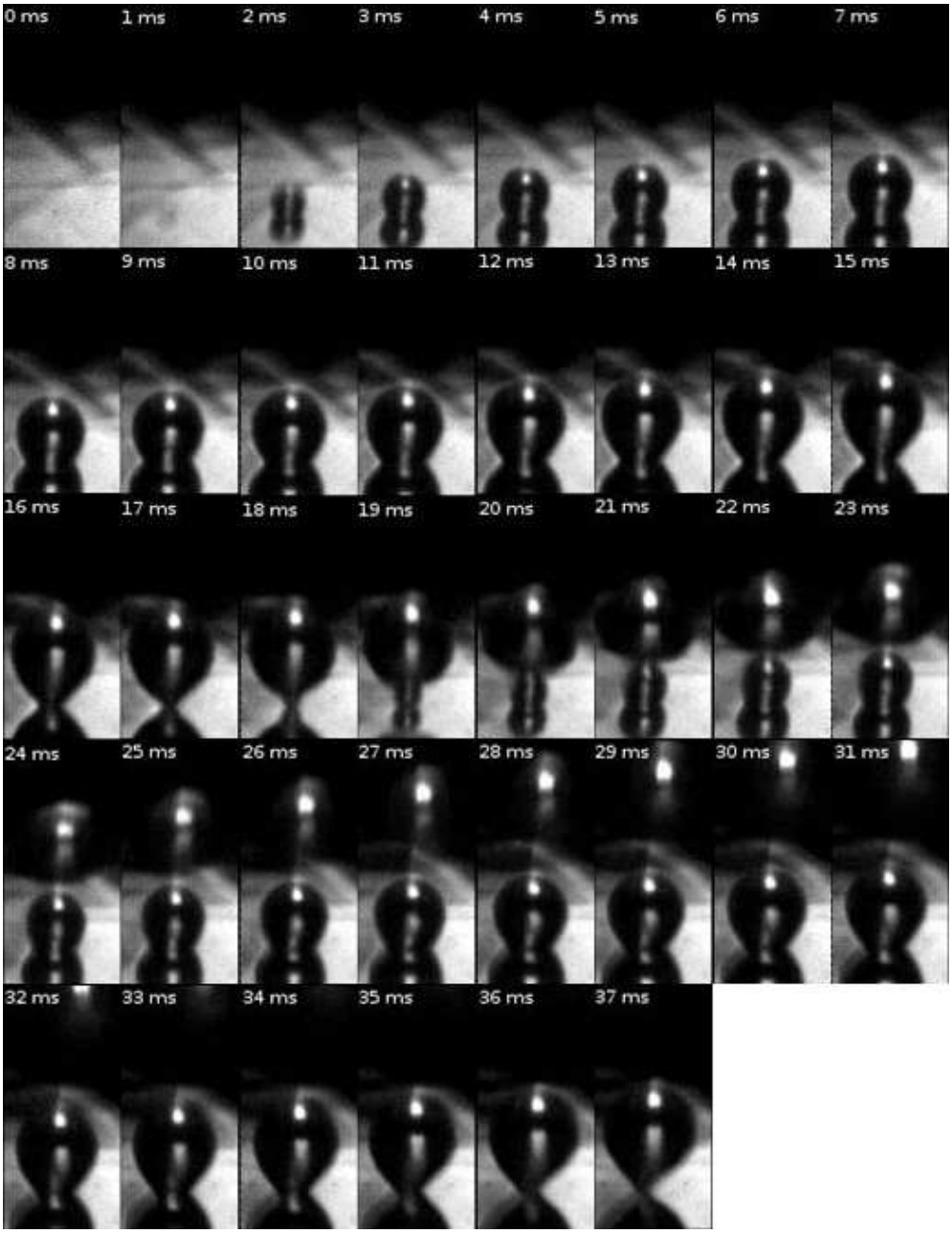

Figure C.1: *High-speed imaging sequence of bubble growth from the silicon device of the first generation in gas-dissolved saturated FC-72 at atmospheric pressure. Images were acquired at 1000 fps.*

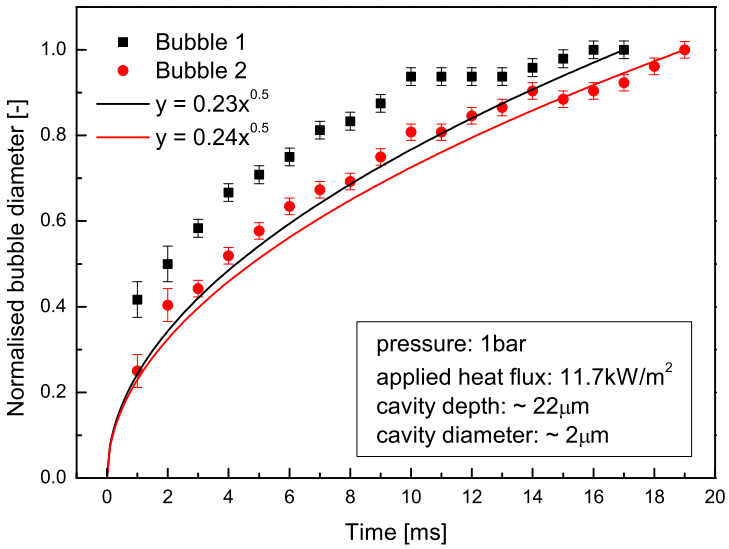

Figure C.2: *Bubble growth of successive bubbles at an applied heat flux of 11.7 kW/m² at 1.01 bar from an isolated cavity (S3) with a nominal mouth diameter of 2 μm and depth of around 22 μm. The data is compared to a correlation given by Mikic et al. [9], Eq. C.3.*

The error of the measurements was ± 2 pixels for the images 2 to $4\,\mathrm{ms}$ and 20 to $22\,\mathrm{ms}$, and ± 1 pixel for the remaining images, respectively. In Fig. C.2 the time dependence of the normalised bubble diameter of successive bubbles from the same nucleation site is shown. Mikic *et al.* [9] obtained a general bubble growth relation for two regions.

$$D_b \propto 2A \qquad \text{for} \quad t^+ << 1 \tag{C.2}$$

$$D_b \propto 2B\, t^{0.5} \qquad \text{for} \quad t^+ >> 1 \tag{C.3}$$

with

$$A = \left(b \, \frac{h_{lg} \, \rho_g \, \Delta T}{\rho_l \, T_{sat}} \right)^{1/2} \tag{C.4}$$

$$B = \left(\frac{12}{\pi} \alpha_l \right)^{1/2} \frac{\Delta T \, c_{p,l} \, \rho_l}{h_{lg} \, \rho_g} \tag{C.5}$$

and

$$t^+ = \frac{A^2 \, t}{B^2} \tag{C.6}$$

where b is $2/3$ for bubble growth in an infinite mass of liquid and $7/\pi$ for a sperical bubble growing attached to a surface. For $t^+ << 1$ the Rayleigh solution (Eq. C.2) applies (Rayleigh [150]) and for $t^+ >> 1$ the Plesset and Zwick relation (Eq. C.3) (Plesset and Zwick, [8]).

Initially the bubble growth rate is higher and decreases after $11\,\mathrm{ms}$. The break in gradient at $11\,\mathrm{ms}$ corresponds approximately to the maximum apparent contact radius, so there may be a change in heat transfer mechanism as the contact line recedes and the bubble starts to lift off. For FC-72 $t^+ >> 1$ is true for $1\,\mathrm{ms}$, the temporal resolution. The correlation of Plesset and Zwick only predicts the second bubble quite well, Eq. C.3, if the correlation is fitted to the experimentally measured bubble departure diameter. Comparison of the growth rates of the first and the succeeding bubble, however, showed only small differences and the influence of the growth of the first bubble on the succeeding one is negligible. The nucleation site is stable and produces similar bubbles.

C.2 Single bubble growth

C.2.1 Equilibrium superheat

Each artificial cavity has an equilibrium wall superheat which can be calculated theoretically from Eq. 2.3. Since in this study only cavities with the same nominal mouth diameter of $10\,\mu\mathrm{m}$ were used, the only changing parameter is the pressure and therefore the saturation temperature. The calculated equilibrium wall superheats are shown in Table C.1.

Table C.1: *Theoretically calculated equilibrium superheats for a hemispherical bubble at the mouth of the cavity with a nominal diameter of 10 μm.*

Pressure	[bar]	0.5	0.75	1	1.25	1.5
Saturation temperature	[°C]	37.53	48.8	57.3	64.21	70.08
Equilibrium superheat	[K]	1.96	1.28	0.93	0.73	0.58

C.2.2 Bubble growth rate

Figure C.3 and C.4 compare the experimentally measured bubble growth from an isolated cavity (S3) on the test section of the second generation with a nominal depth of $100\,\mu\mathrm{m}$ and a mouth diameter of $10\,\mu\mathrm{m}$ at two wall superheats 1.3 and $10.1\,\mathrm{K}$ at atmospheric pressure to an adjusted empirical correlation of Fritz and Ende [10]. If the constant $\sqrt{4/\pi}$ suggested by Fritz and Ende is multiplied by 1.29 to fit the experimentally measured final departure diameter, the correlation fails to follow the curve between 5 and $45\,\mathrm{K}$. For the experiment at $10.1\,\mathrm{K}$ Fritz and Ende's correlation was multiplied by 0.73, in which case the correlation predicts the bubble growth almost perfectly. The experimentally measured bubble growth from an isolated cavity (S8) on the test section of the third generation with a nominal depth of $80\,\mu\mathrm{m}$ and a mouth diameter of $10\,\mu\mathrm{m}$ at three wall superheats 1.4, 4.8 and $8.1\,\mathrm{K}$ at atmospheric pressure is compared to an adjusted empirical correlation of Fritz and Ende [10] and shown in Fig. C.5, C.6 and C.7. If the constant in Fritz and Ende's correlation was multiplied by 0.92, 1.05 and 2.23 to fit the final departure diameter, the agreement is satisfying.

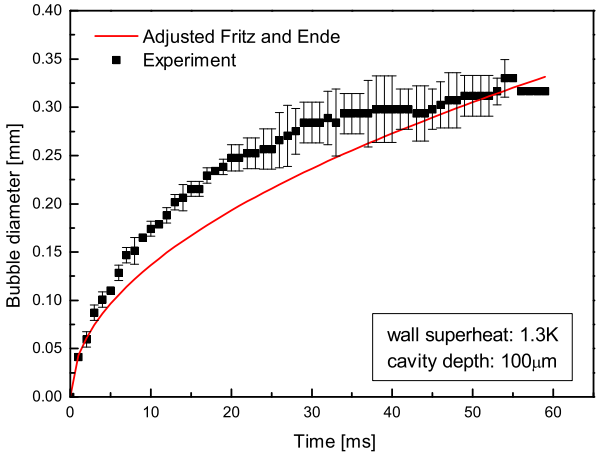

Figure C.3: *Comparison of experimental bubble growth from an isolated cavity (S3) with a nominal mouth diameter of 10 μm and a depth of 100 μm for a wall superheats of 1.3 K at atmospheric pressure with the adjusted empirical correlation of Fritz and Ende [10]. The constant suggested by Fritz and Ende was multiplied by 1.29.*

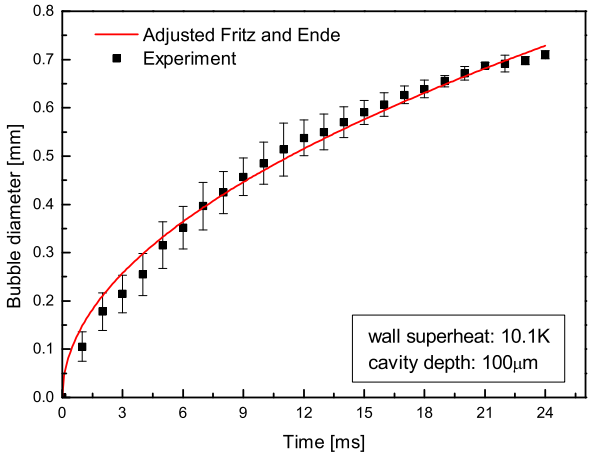

Figure C.4: *Comparison of experimental bubble growth from an isolated cavity (S3) with a nominal mouth diameter of 10 μm and a depth of 100 μm for a wall superheats of 10.1 K at atmospheric pressure with the adjusted empirical correlation of Fritz and Ende [10]. The constant suggested by Fritz and Ende was multiplied by 0.73.*

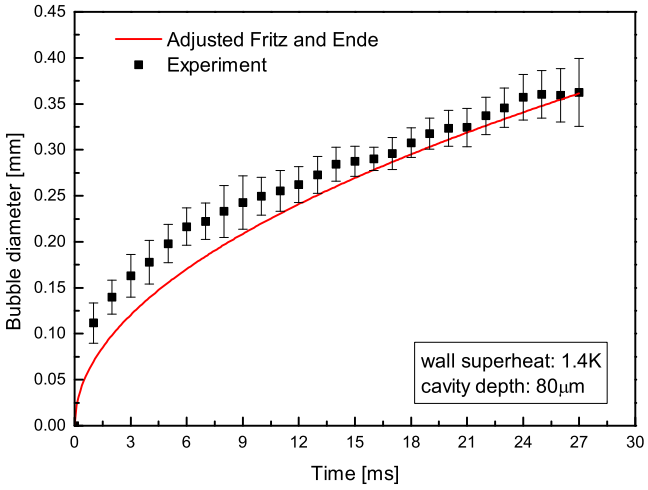

Figure C.5: *Comparison of experimental bubble growth from an isolated cavity (S8) with a nominal mouth diameter of 10 μm and a depth of 80 μm for a wall superheat of 1.4 K at atmospheric pressure with the adjusted empirical correlation of Fritz and Ende [10]. The constant suggested by Fritz and Ende was multiplied by 0.92.*

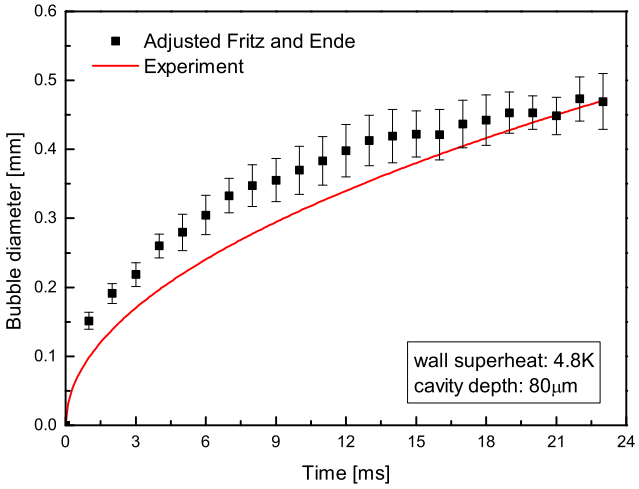

Figure C.6: *Comparison of experimental bubble growth from an isolated cavity (S8) with a nominal mouth diameter of 10 μm and a depth of 80 μm for a wall superheat of 4.8 K at atmospheric pressure with the adjusted empirical correlation of Fritz and Ende [10]. The constant suggested by Fritz and Ende was multiplied by 1.05.*

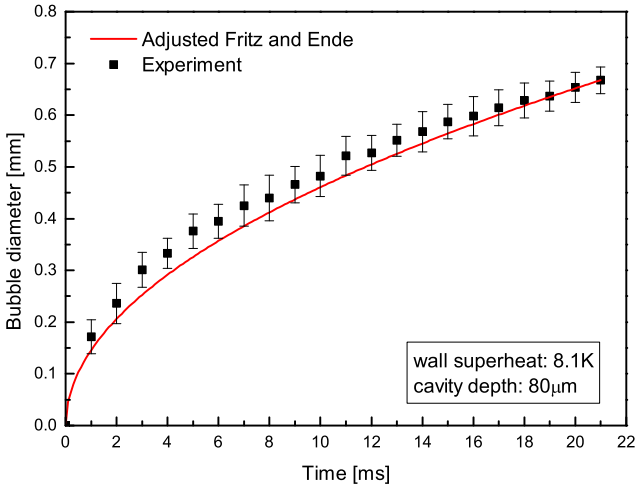

Figure C.7: *Comparison of experimental bubble growth from an isolated cavity (S8) with a nominal mouth diameter of 10 μm and a depth of 80 μm for a wall superheat of 8.1 K at atmospheric pressure with the adjusted empirical correlation of Fritz and Ende [10]. The constant suggested by Fritz and Ende was multiplied by 2.23.*

C.2.3 Bubble departure frequency and departure diameter

Jakob and Fritz [18], and Zuber *et al.* [19] suggested a constant product $f \cdot \overline{D_d}$ with increasing wall superheat, Fig. C.8, C.9 and C.10. The product calculated from experimental data is not constant and increases with increasing wall superheat in a near-linear fashion. Both correlations over predict even the largest value of the product of departure diameter and frequency determined from experiments. For the case of Jakob and Fritz this is not surprising, as the empirical correlation was given for experiments conducted in water and hydrogen.

As already mentioned in section 4.2 of chapter 4, only the range of wall superheats which all three curves cover are considered for the comparison of trend lines of the bubble departure diameter. At $1\,\mathrm{atm}$, Fig. C.11, the wall superheat ranges from 1.4 to $14.2\,\mathrm{K}$. At $14.2\,\mathrm{K}$ the departure diameters for the deepest and the most shallow cavities are very similar. Following the slopes of the curves the $40\,\mu\mathrm{m}$ cavity would produce the widest bubbles at higher wall superheats. At $1.25\,\mathrm{atm}$, Fig. C.12, the range of wall

superheats which all curves cover is from 1.1 to $11.1\,\mathrm{K}$. The bubble diameter for the three different cavity depths is behaving very similar as at $1\,\mathrm{atm}$ and the $40\,\mu\mathrm{m}$ deep cavity would also produce the largest bubbles at higher wall superheats, following the slope of the trend line. At $1.5\,\mathrm{atm}$, Fig. C.13, the range of covered wall superheat is between 1.1 and $9.5\,\mathrm{K}$. The $40\,\mu\mathrm{m}$ deep cavity produces the largest departing bubbles at $9.5\,\mathrm{K}$ and the smallest at $1.1\,\mathrm{K}$. The smallest difference in diameter for low wall superheats is $0.12\,\mathrm{mm}$ at $1\,\mathrm{atm}$ and the biggest $0.18\,\mathrm{mm}$ at $1.25\,\mathrm{atm}$. At high wall superheats the largest differences of $0.16\,\mathrm{mm}$ are at 1 and $1.5\,\mathrm{atm}$. At $1.25\,\mathrm{atm}$ the difference is $0.14\,\mathrm{mm}$.

If the bubble departure diameters for different pressures are compared, the differences between the different dimensioned cavities are with a maximum of $0.11\,\mathrm{mm}$ small, Fig. C.14, C.15 and C.16. For the $40\,\mu\mathrm{m}$ deep cavity departure diameters are always smallest for $1.25\,\mathrm{atm}$, however, the differences are within $0.05\,\mathrm{mm}$. With $0.02\,\mathrm{mm}$ for low wall superheats the difference in diameter is even smaller for the $80\,\mu\mathrm{m}$ deep cavity. For high wall superheats the diameter for bubbles from the $80\,\mu\mathrm{m}$ deep cavity increases with decreasing pressure and the bubbles produced at $1.5\,\mathrm{atm}$ are always the smallest. For the last cavity with a depth of $100\,\mu\mathrm{m}$ the diameter increases with decreasing pressure for high wall superheats and the largest bubbles are produced at $1\,\mathrm{atm}$ for all wall superheats.

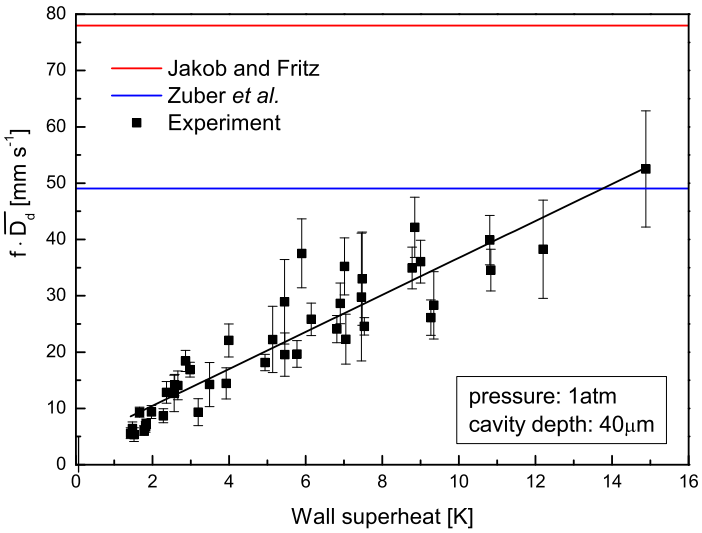

Figure C.8: *Comparison of the product $f \cdot \overline{D_d}$ from an isolated cavity (S3) with a nominal mouth diameter of 10 μm and a depth of 40 μm at 1 atm with correlations from Jakob and Fritz [18] and Zuber [19].*

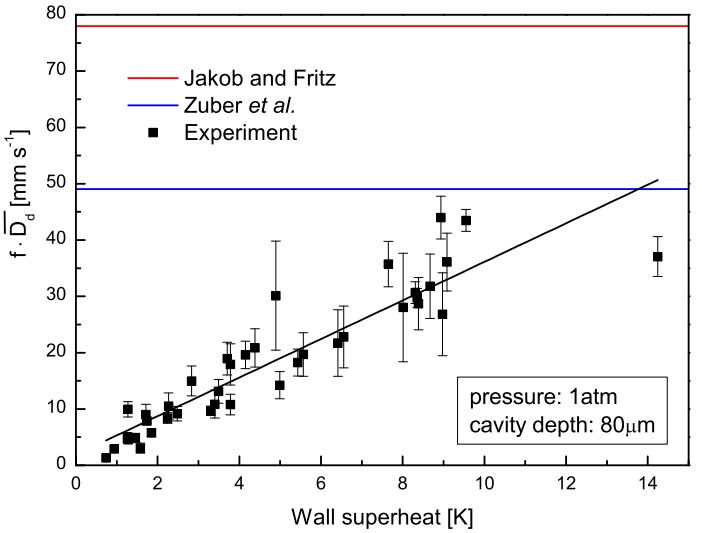

Figure C.9: *Comparison of the product $f \cdot \overline{D_d}$ from an isolated cavity (S3) with a nominal mouth diameter of 10 μm and a depth of 80 μm at 1 atm with correlations from Jakob and Fritz [18] and Zuber [19].*

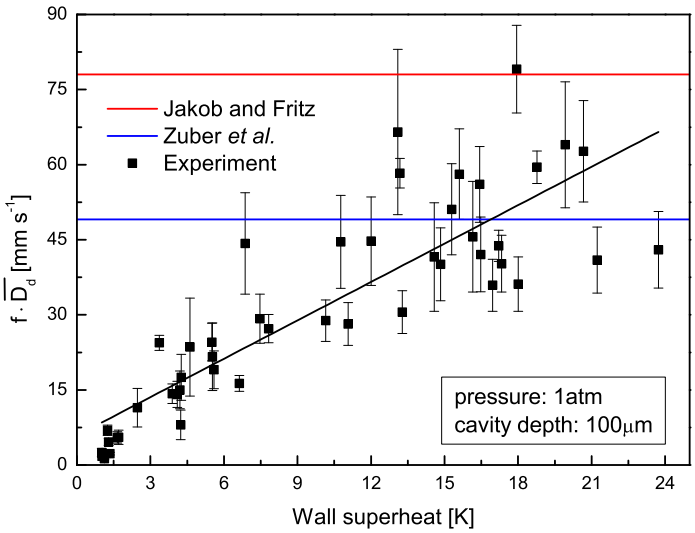

Figure C.10: *Comparison of the product $f \cdot \overline{D_d}$ from an isolated cavity (S3) with a nominal mouth diameter of 10 μm and a depth of 100 μm at 1 atm with correlations from Jakob and Fritz [18] and Zuber [19].*

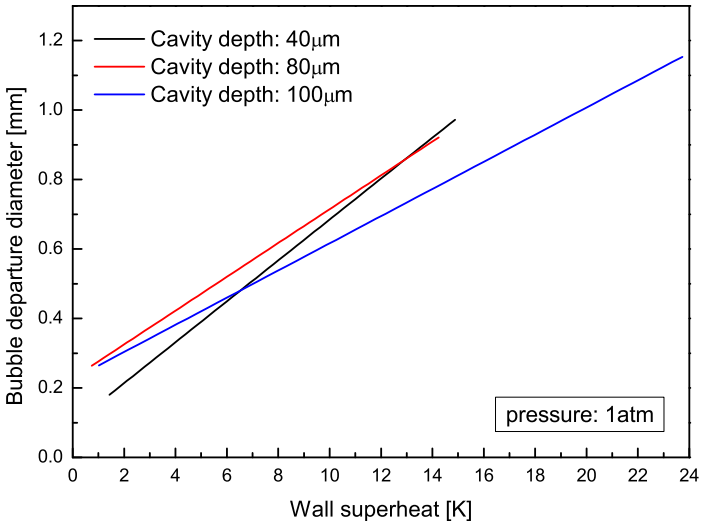

Figure C.11: *Comparison of the trend lines of the bubble departure diameter as a function of wall superheat for a pressure of 1 atm.*

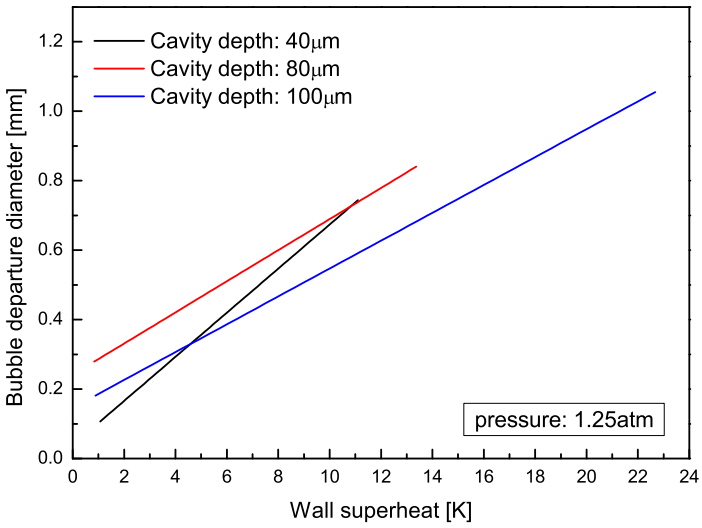

Figure C.12: *Comparison of the trend lines of the bubble departure diameter as a function of wall superheat for a pressure of 1.25 atm.*

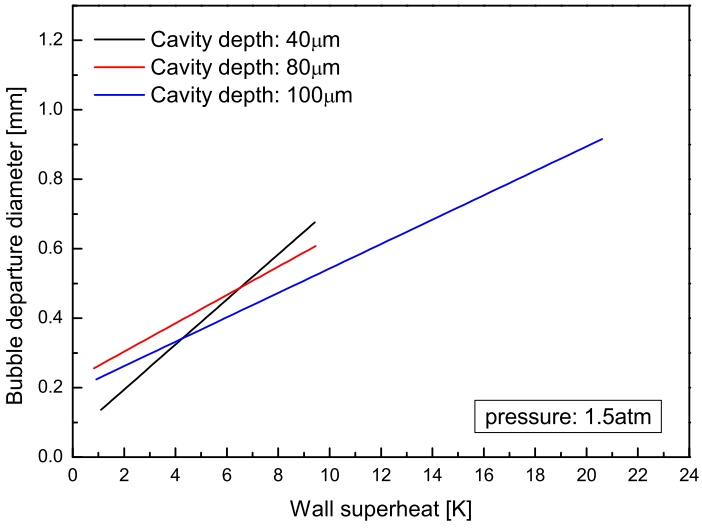

Figure C.13: *Comparison of the trend lines of the bubble departure diameter as a function of wall superheat for a pressure of 1.5 atm.*

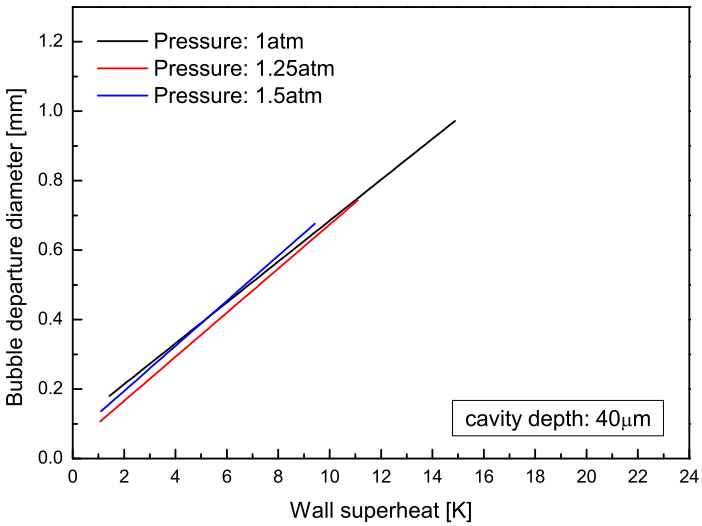

Figure C.14: *Comparison of the trend lines of the bubble departure diameter as a function of wall superheat for a nominal cavity depth of 40 μm.*

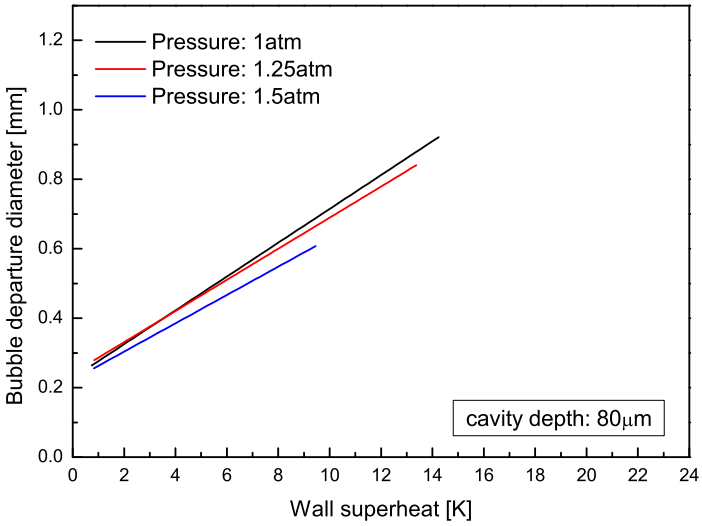

Figure C.15: *Comparison of the trend lines of the bubble departure diameter as a function of wall superheat for a nominal cavity depth of 80 μm.*

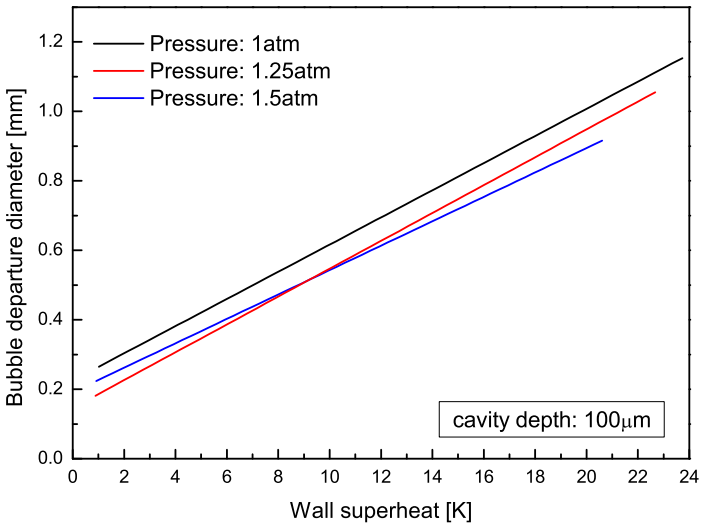

Figure C.16: *Comparison of the trend lines of the bubble departure diameter as a function of wall superheat for a nominal cavity depth of 100 μm.*

C.2.4 The waiting time

In Figure C.17 to C.25 the waiting time between two departing bubbles as function of wall superheat from cavities with a nominal depth of 40, 80 and $100\,\mu\mathrm{m}$ and for pressures of 1, 1.25 and $1.5\,\mathrm{atm}$ are presented. The waiting time is largest for wall superheats close to the equilibrium wall superheat and decreases rapidly with increasing wall superheat for all investigated cavity depths and set pressures. In general the maximum waiting time between two growing bubbles seems to increase with increasing cavity depth. The wall superheats, for which the waiting time is larger than the temporal resolution ($1\,\mathrm{ms}$), is varying strongly. For a nominal depth of $80\,\mu\mathrm{m}$ there was no waiting time detected above wall superheats between 4 to $5\,\mathrm{K}$. For the two other cavity depths the waiting time appears for much higher wall superheats, up to $17.5\,\mathrm{K}$. The error bars indicate the standard deviation between the average of the five measured bubbles. The waiting time between two bubbles can vary strongly for the same experimental conditions. No obvious influence of pressure was found in the presented results.

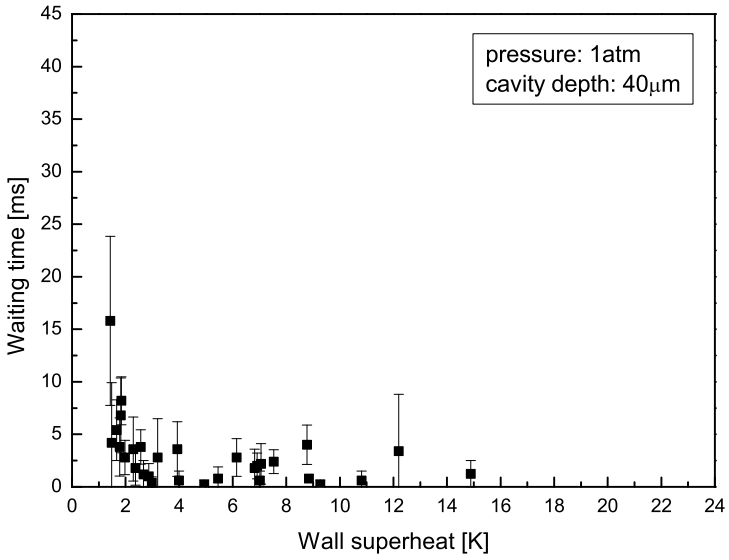

Figure C.17: *Waiting time during bubble growth as a function of wall superheat from an isolated cavity (S3) with a nominal mouth diameter of 10 μm and a depth of 40 μm at 1 atm.*

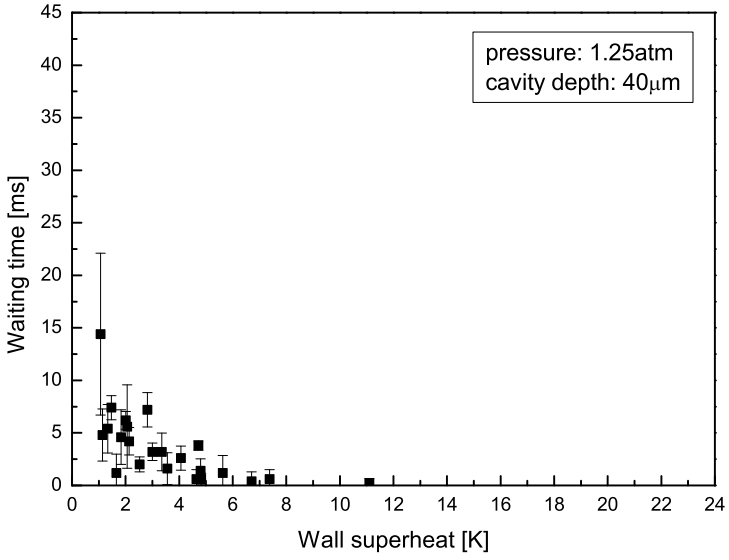

Figure C.18: *Waiting time during bubble growth as a function of wall superheat from an isolated cavity (S3) with a nominal mouth diameter of 10 μm and a depth of 40 μm at 1.25 atm.*

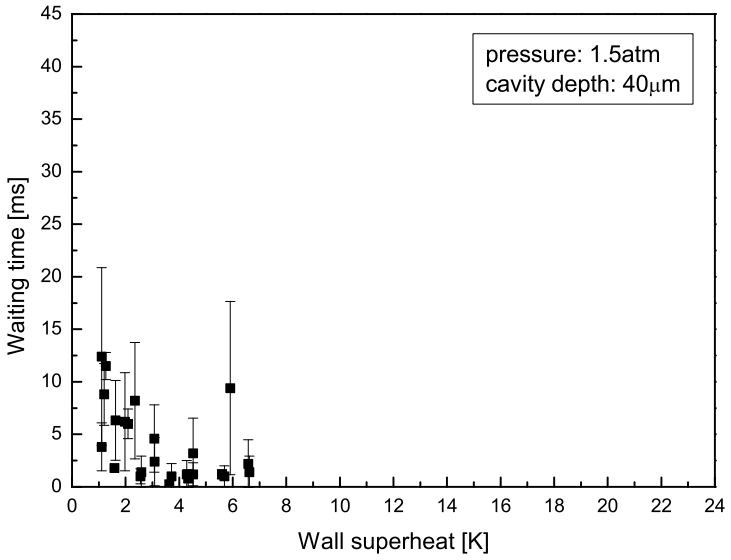

Figure C.19: *Waiting time during bubble growth as a function of wall superheat from an isolated cavity (S3) with a nominal mouth diameter of 10 μm and a depth of 40 μm at 1.5 atm.*

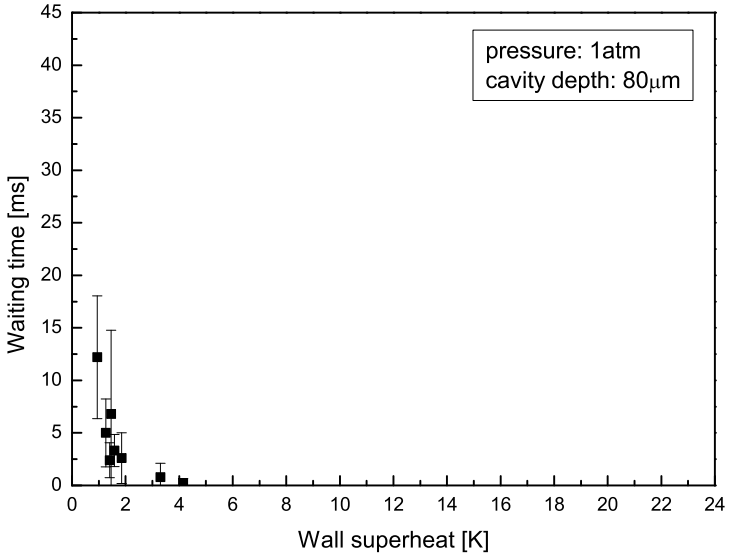

Figure C.20: *Waiting time during bubble growth as a function of wall superheat from an isolated cavity (S3) with a nominal mouth diameter of 10 μm and a depth of 80 μm at 1 atm.*

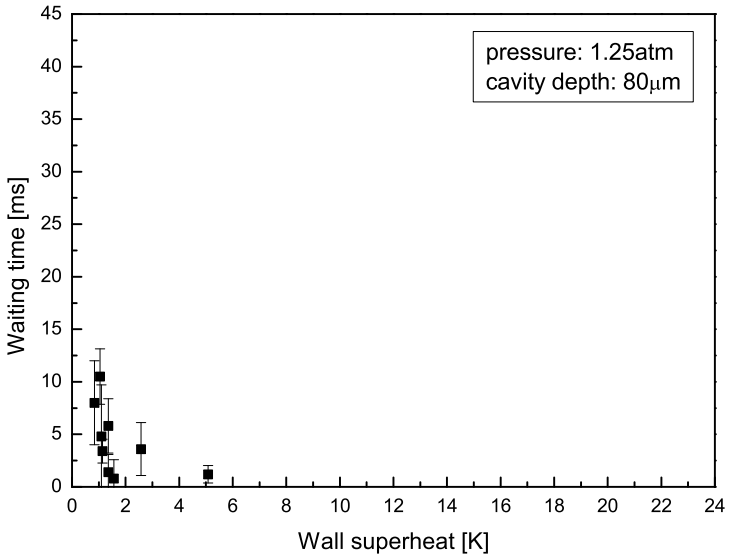

Figure C.21: *Waiting time during bubble growth as a function of wall superheat from an isolated cavity (S3) with a nominal mouth diameter of 10 μm and a depth of 80 μm at 1.25 atm.*

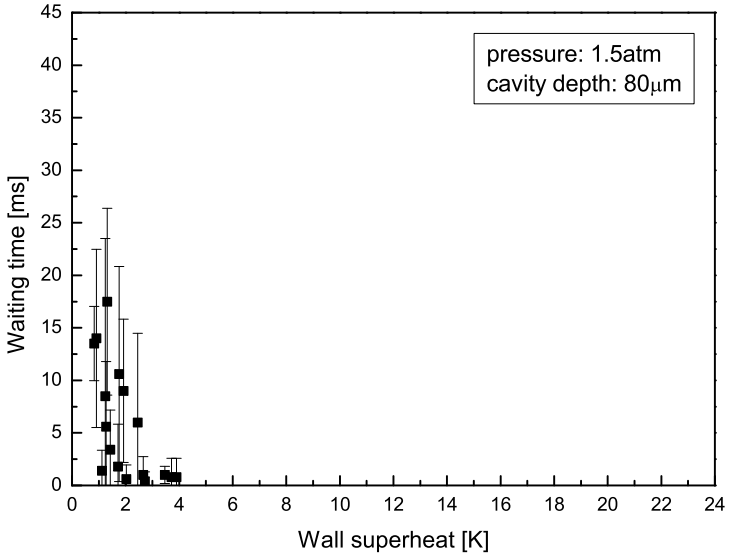

Figure C.22: *Waiting time during bubble growth as a function of wall superheat from an isolated cavity (S3) with a nominal mouth diameter of 10 μm and a depth of 80 μm at 1.5 atm.*

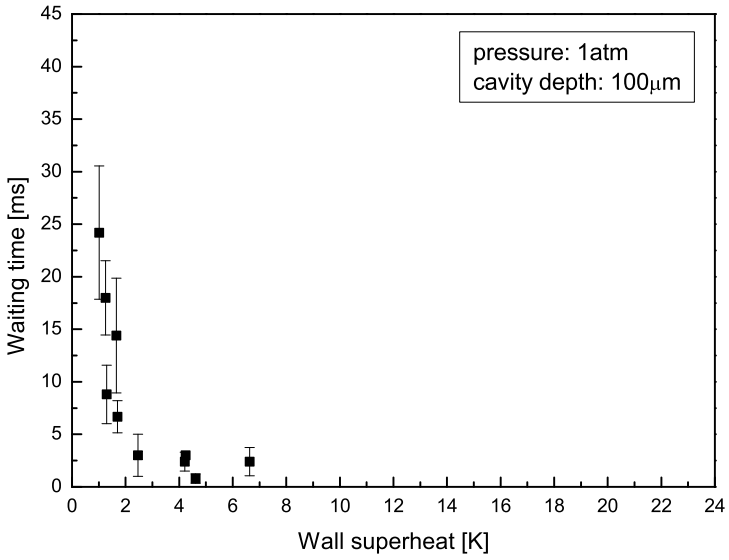

Figure C.23: *Waiting time during bubble growth as a function of wall superheat from an isolated cavity (S3) with a nominal mouth diameter of 10 μm and a depth of 100 μm at 1 atm.*

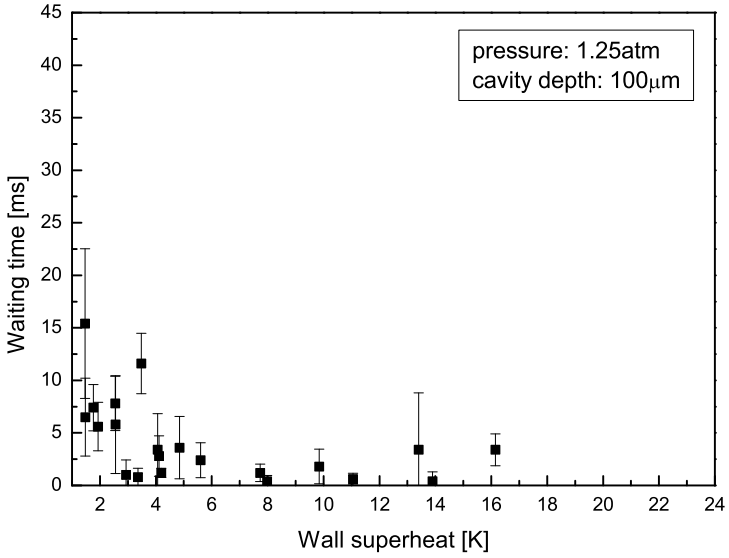

Figure C.24: *Waiting time during bubble growth as a function of wall superheat from an isolated cavity (S3) with a nominal mouth diameter of 10 μm and a depth of 100 μm at 1.25 atm.*

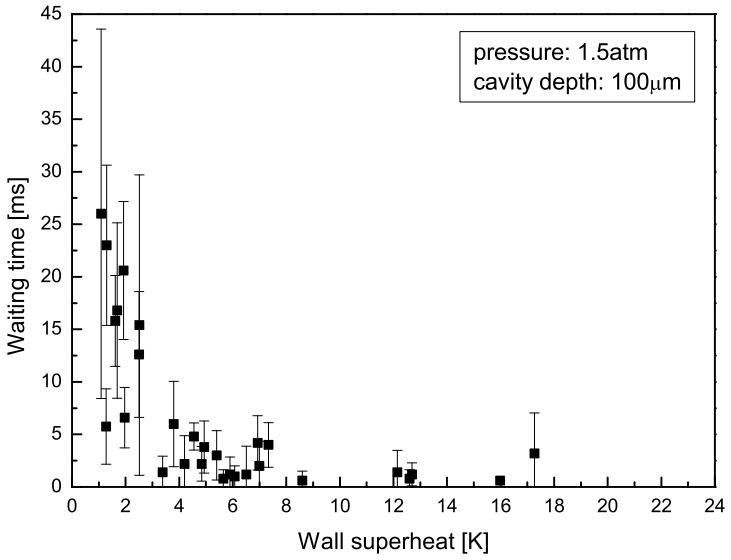

Figure C.25: *Waiting time during bubble growth as a function of wall superheat from an isolated cavity (S3) with a nominal mouth diameter of 10 μm and a depth of 100 μm at 1.5 atm.*

C.3 Vertical coalescence

In Figure C.26, C.27 and C.28 the average frequency of vertical coalescence is subtracted from the average nucleation frequency resulting in the bubble departure frequency. The number of departed bubbles per second like the number of bubble nucleations per second decreases with increasing pressure. With increasing wall superheat the bubble departure frequency initially increases sharply and seems to level off, with this behaviour being less pronounced compared to the nucleation frequency at $0.5\,\mathrm{bar}$. However, the results for 0.5 and $0.75\,\mathrm{bar}$ are rather scattered and for $1\,\mathrm{bar}$ the initial increase is less noticeable.

As for the pressures of 1, 1.25 and $1.5\,\mathrm{atm}$ in section 4.2 and 4.4 in chapter 4 the bubble departure diameter and the evaporative heat flux compared to the input heat flux as a function of wall superheat are presented in Fig. C.29, C.30, C.31, C.33, C.34 and C.35. The bubble departure diameter as a function of wall superheat represents the

averaged diameter of five bubbles for each wall superheat and the error bars represent the standard deviation. Only bubbles without prior vertical coalescence were considered. As the artificial cavity at S8 on the test section of the third generation has less spacing in between adjacent cavities than the cavity at S5 on the test section of the second generation, the regions of influence following Zhang and Shoji [6] were included in each plot. For all three pressure conditions the departure diameter is increasing in a near-linear fashion with increasing wall superheat. As previously shown in chapter 4, section 4.2, there is no obvious influence of pressure visible. However, if the trend lines are plotted together and compared with each other, small differences are revealed, Fig. C.32. Only the regions of wall superheat where all curves have data points are discussed. The slopes of the trend lines for 0.5 and $0.75\,\mathrm{bar}$ are very similar. The bubble departure diameter is largest at $0.5\,\mathrm{bar}$. For low wall superheats the departure diameter at $1\,\mathrm{bar}$ is in the middle and for high wall superheats diameters at 0.75 and $1\,\mathrm{bar}$ are almost the same. However, the slope of the trend lines indicates that for even higher wall superheats the expected behaviour of increasing bubble departure diameter with increasing pressure appears.

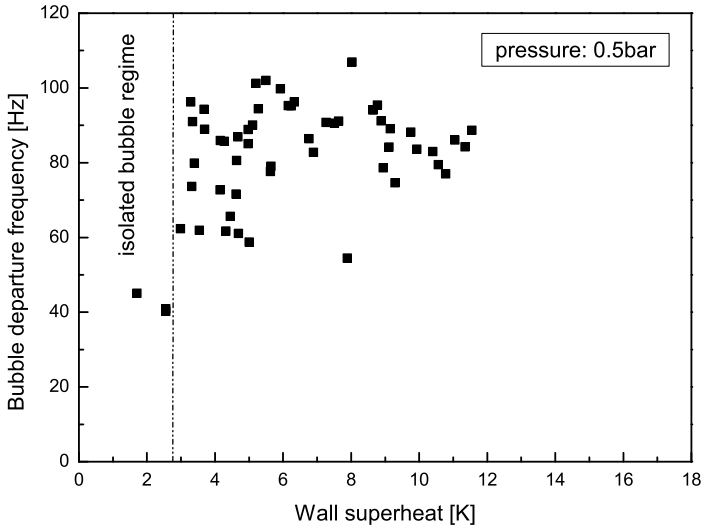

Figure C.26: *Bubble departure frequency as a function of wall superheat from an isolated cavity (S8) with a nominal mouth diameter of 10 μm and a depth of 80 μm at 0.5 bar.*

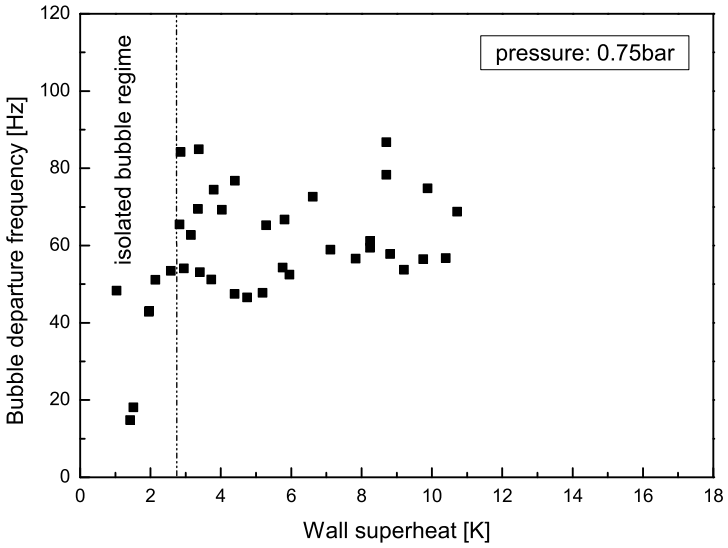

Figure C.27: *Bubble departure frequency as a function of wall superheat from an isolated cavity (S8) with a nominal mouth diameter of 10 μm and a depth of 80 μm at 0.75 bar.*

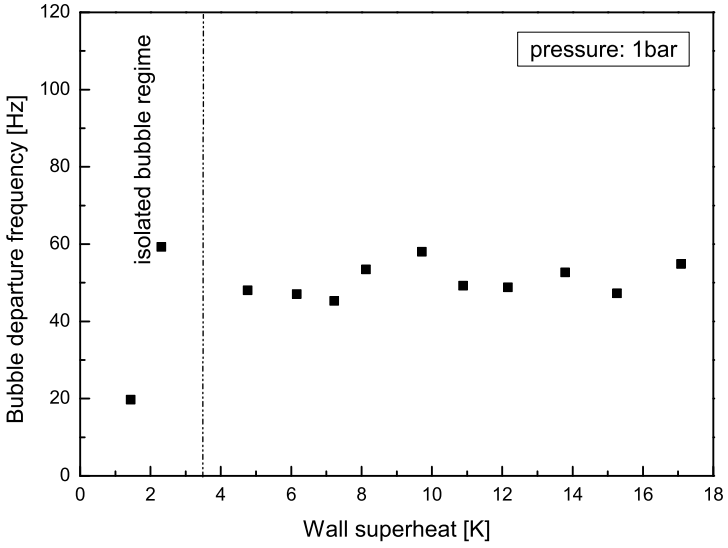

Figure C.28: *Bubble departure frequency as a function of wall superheat from an isolated cavity (S8) with a nominal mouth diameter of 10 μm and a depth of 80 μm at 1 bar.*

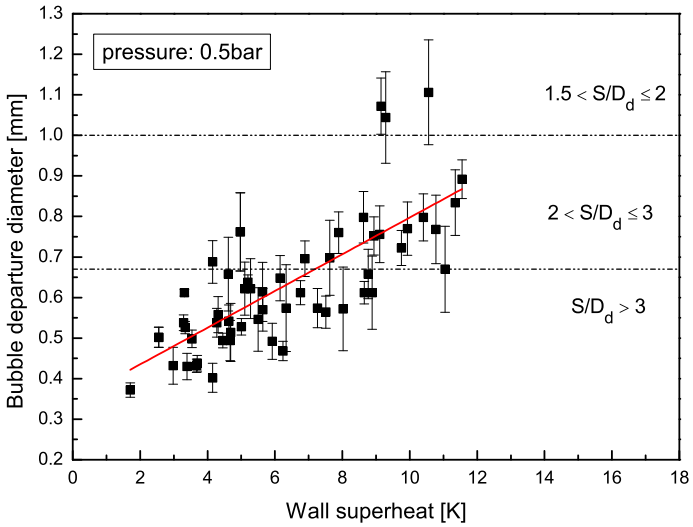

Figure C.29: *Bubble departure diameter as a function of wall superheat from an isolated cavity (S8) with a nominal mouth diameter of 10 μm and a depth of 80 μm at 0.5 bar. The regions of influence following Zhang and Shoji [6] are indicated. A linear trend line was fitted to the data.*

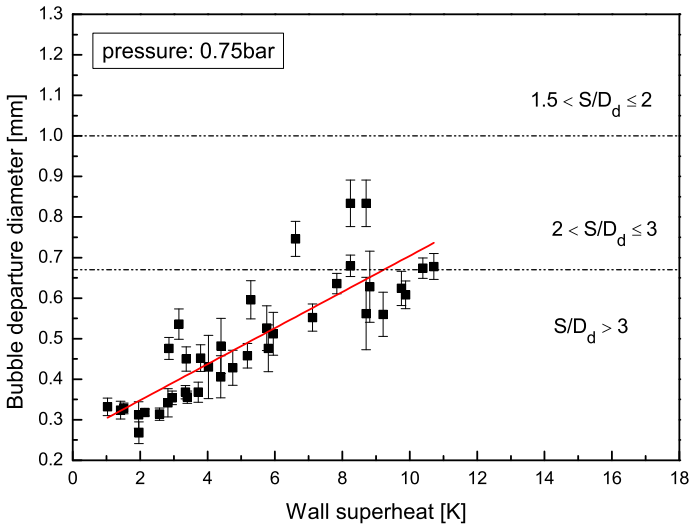

Figure C.30: *Bubble departure diameter as a function of wall superheat from an isolated cavity (S8) with a nominal mouth diameter of 10 μm and a depth of 80 μm at 0.75 bar. The regions of influence following Zhang and Shoji [6] are indicated. A linear trend line was fitted to the data.*

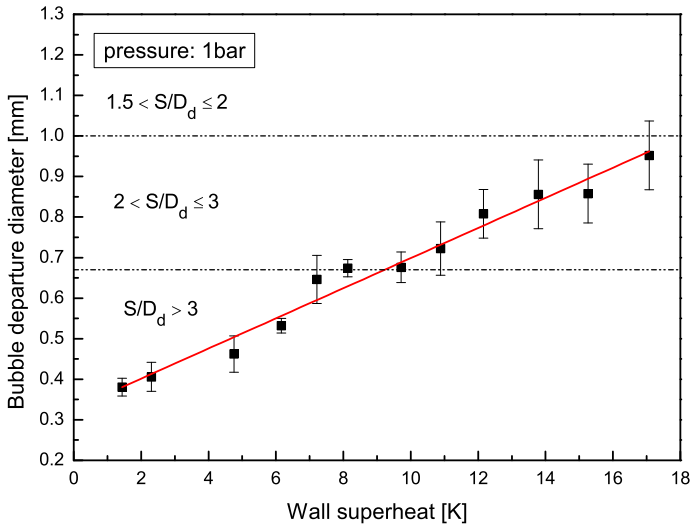

Figure C.31: *Bubble departure diameter as a function of wall superheat from an isolated cavity (S8) with a nominal mouth diameter of 10 μm and a depth of 80 μm at 1 bar. The regions of influence following Zhang and Shoji [6] are indicated. A linear trend line was fitted to the data.*

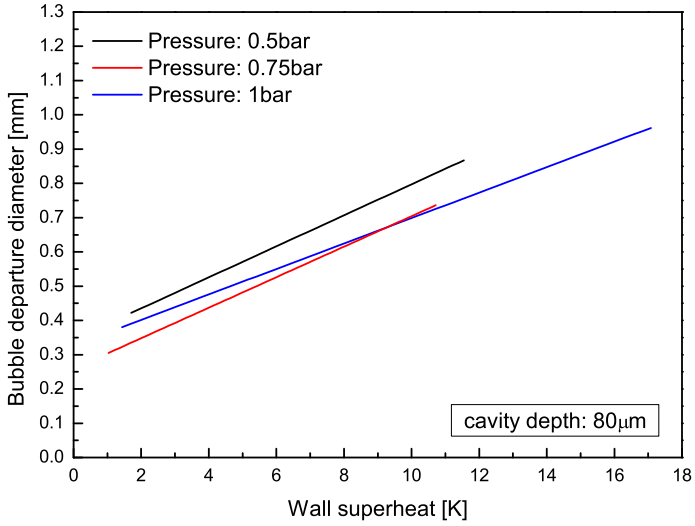

Figure C.32: *Comparison of the trend lines of the bubble departure diameter as a function of wall superheat from an isolated cavity (S8) with a nominal mouth diameter of 10 μm and a depth of 80 μm at 0.5, 0.75 and 1 bar.*

The transport of heat by latent heat of vaporisation is estimated from the product of the measured bubble frequency and the volume of a sphere of equivalent diameter to the bubble departure diameter, chapter 4, section 4.4. This is then expressed as an evaporative heat flux (based nominally on the projected area of the bubble), which is a factor N times the input heat flux. This evaporative heat flux can be calculated from Eq. 4.2 in section 4.4 of chapter 4. The input heat flux and the evaporative heat flux increase linearly with increasing wall superheat over a considerable range, with $N = 1$ and $N = 4$, Fig. C.33, C.34 and C.35. This behaviour is less obvious for $N = 1$ as the data expresses more scatter, especially at $0.75\,\mathrm{bar}$. The fitting lines on all plots have a slope of 0.6 and $1.4\,{}^{\mathrm{kW}}/_{\mathrm{m^2K}}$. Other than for the test section of the second generation, the projected bubble area had to be multiplied by 4. As the calculation of the evaporative heat flux for the second generation test section revealed previously, evaporation may not occur entirely at the triple contact line or micro-layer below a bubble. Some of the wall heat flux may be transferred to a layer of superheated liquid by bubble-induced convection and then to the dome of the bubble.

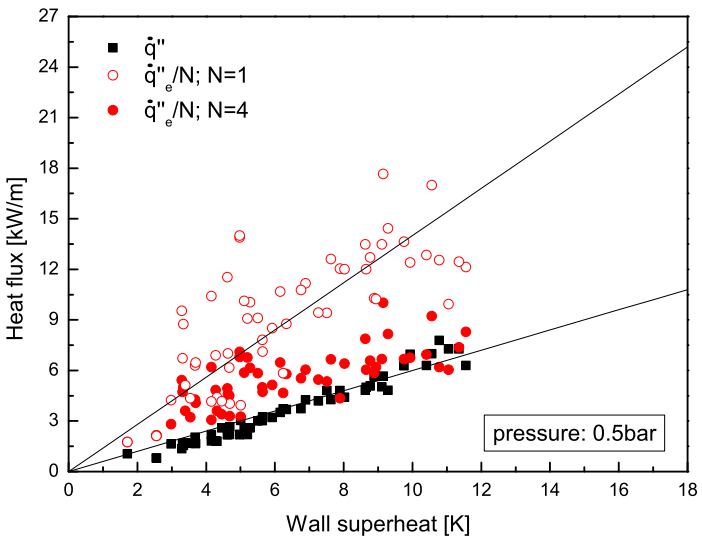

Figure C.33: *Evaporative heat flux $\dot{q}''_e$ and input heat flux $\dot{q}''$ with factor $N = 1$ and $N = 4$ as functions of wall superheat from an isolated cavity (S8) with a nominal mouth diameter of 10 μm and a depth of 80 μm at 0.5 bar.*

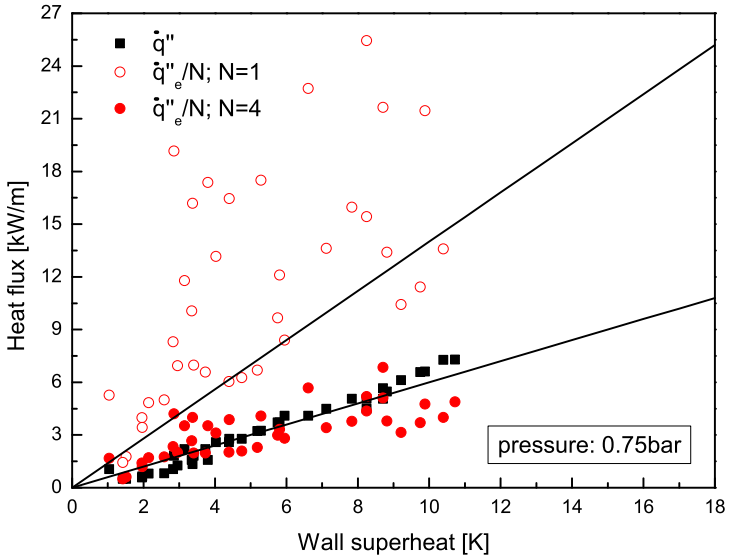

Figure C.34: *Evaporative heat flux $\dot{q}''_e$ and input heat flux $\dot{q}''$ with factor $N = 1$ and $N = 4$ as functions of wall superheat from an isolated cavity (S8) with a nominal mouth diameter of 10 μm and a depth of 80 μm at 0.75 bar.*

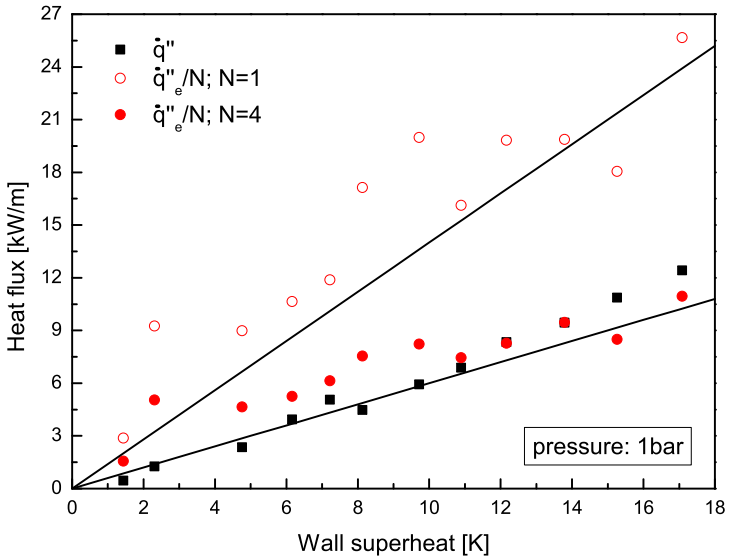

Figure C.35: *Evaporative heat flux $\dot{q}''_e$ and input heat flux $\dot{q}''$ with factor $N = 1$ and $N = 4$ as functions of wall superheat from an isolated cavity (S8) with a nominal mouth diameter of 10 μm and a depth of 80 μm at 1 bar.*

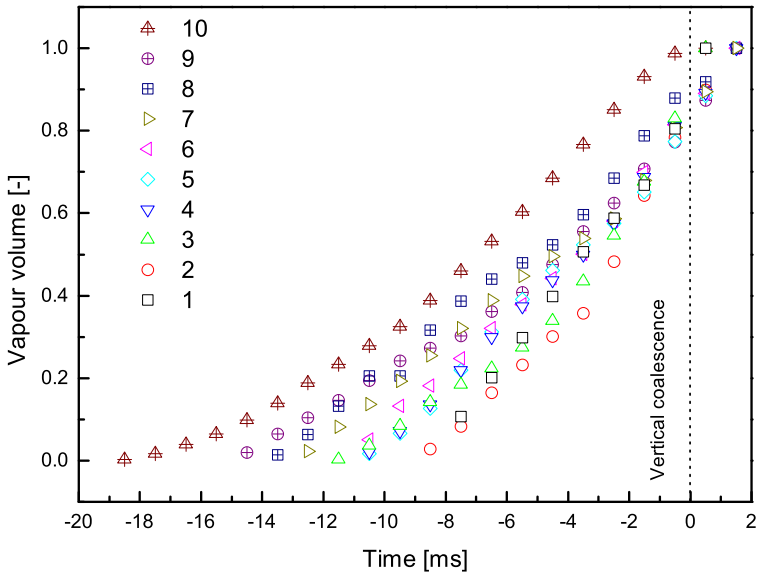

Figure C.36: *Vapour volume evolution from nucleation, over vertical coalescence to the departure of the coalesced bubble for 10 cases of vertical coalescence. The time at which coalescence occurs was set as the zero point and the vapour volume normalised with the volume of the merged bubbles at departure. Vapour production of an isolated cavity (S8) with a nominal mouth diameter of 10 μm and a depth of 80 μm at 0.5 bar and a wall superheat of 7.9 K (applied heat flux 4.8 $^{kW}/_{m^2}$).*

Vapour volume evolution starting from nucleation, over vertical coalescence to the departure of the coalesced bubble for ten cases of vertical coalescence with the time at which coalescence occurs set as the zero point was presented in Fig. 5.15 in chapter 5. To allow a better comparison between the different cases, the vapour volume was normalised with the volume of the merged bubbles at departure, Fig. C.36. The comparison reveals that for smaller bubbles the vapour volume is increasing faster to reach the normalised departure volume.

The bubble shapes of the images from 10 to 14 ms in Fig. 5.2 in chapter 5 were extracted with a suitable threshold. Assuming axial symmetry around the vertical axis the rotated shapes forming the bubble volumes are presented in Fig. C.37 to C.42. The inclination of the high frame rate camera of about 20 ° was not taken into account. At 10 ms, Fig. C.37, the bubble forms a geometry similar to a sphere connected to

the heated surface by a neck. One millisecond later, Fig. C.38, the bubble contact area starts to widen and the total volume is increasing with the top of the bubble not rising. At $12\,\mathrm{ms}$, Fig. C.39, the second nucleated bubble becomes visible at the bottom. The contact diameter reaches its maximum and the volume is naturally still increasing further. At $13\,\mathrm{ms}$, Fig. C.40, the second bubble merges with the preceding bubble and funnel-like geometry is formed, while the contact diameter is decreasing. In Figure C.41 the coalesced bubble is almost completely detached from the wall. The small amount of vapour remaining on the heated wall will grow to a new bubble as shown in Fig. C.42, where the contact area has already increased again. This newly nucleated bubble will not merge with its departed predecessor. The change of total bubble vapour, the maximum diameter, the diameter of the bubble base diameter and the location of the bubble apex with time are presented in Fig. C.43.

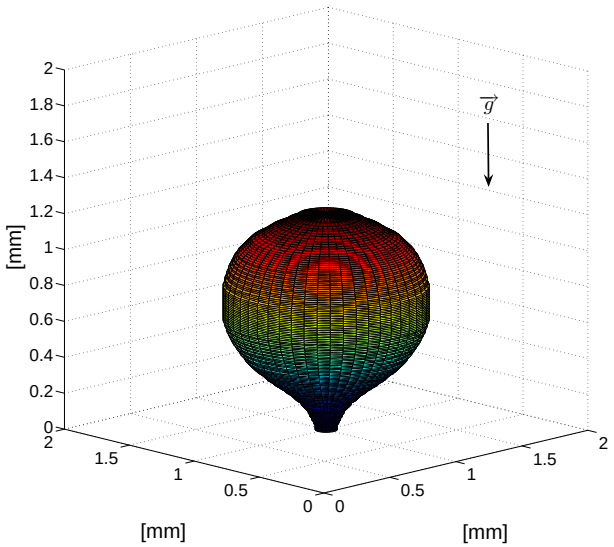

Figure C.37: *Three-dimensional view of the bubble formed by the two-dimensional bubble shape, extracted from the image at 10 ms in Fig. 5.2.*

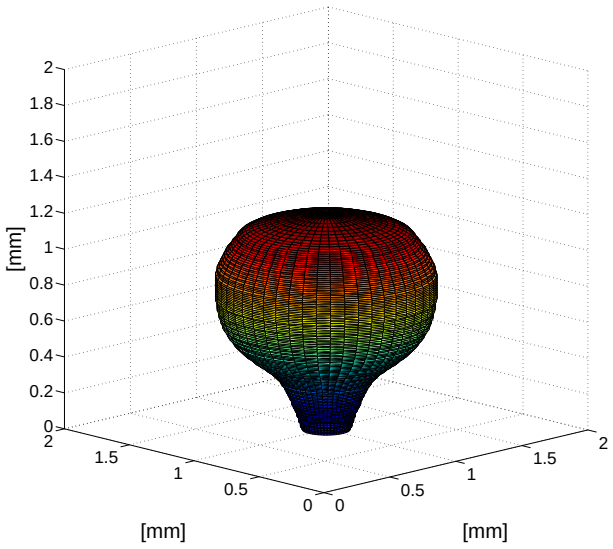

Figure C.38: *Three-dimensional view of the bubble formed by the two-dimensional bubble shape, extracted from the image at 11 ms in Fig. 5.2.*

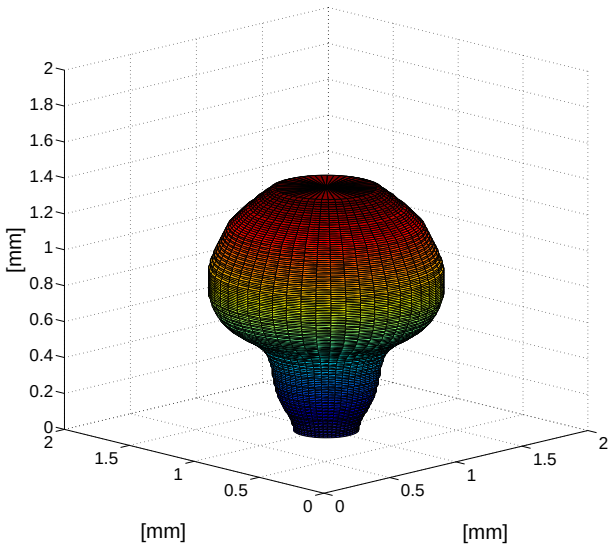

Figure C.39: *Three-dimensional view of the bubble formed by the two-dimensional bubble shape, extracted from the image at 12 ms in Fig. 5.2.*

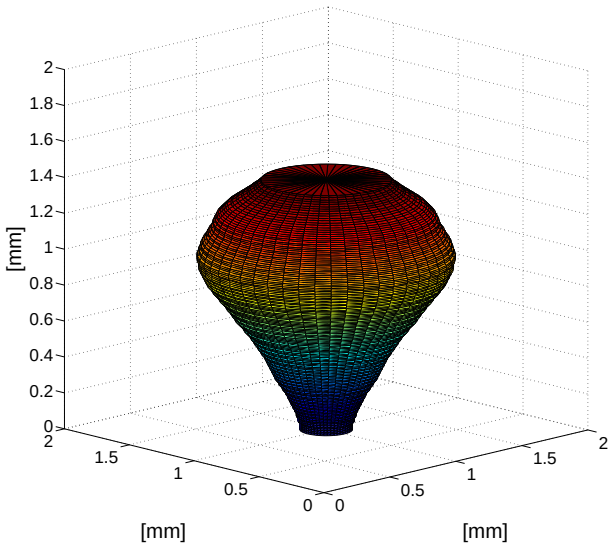

Figure C.40: *Three-dimensional view of the bubble formed by the two-dimensional bubble shape, extracted from the image at 13 ms in Fig. 5.2.*

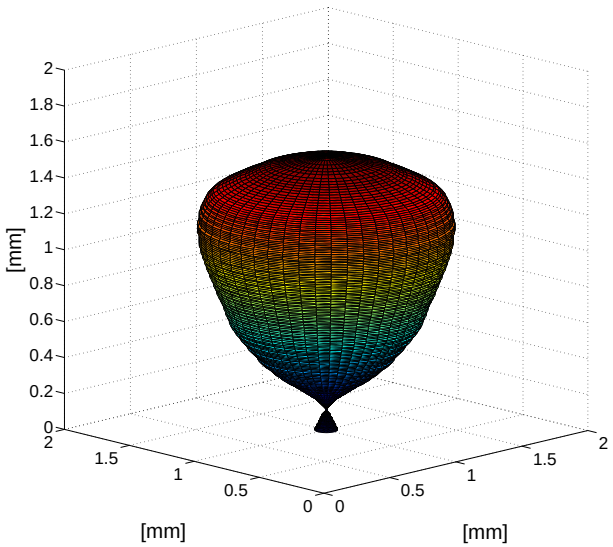

Figure C.41: *Three-dimensional view of the bubble formed by the two-dimensional bubble shape, extracted from the image at 14 ms in Fig. 5.2.*

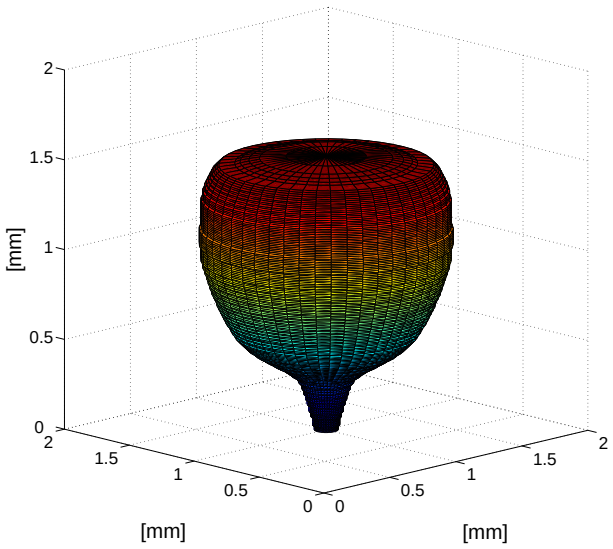

Figure C.42: *Three-dimensional view of the bubble formed by the two-dimensional bubble shape, extracted from the image at 15 ms in Fig. 5.2.*

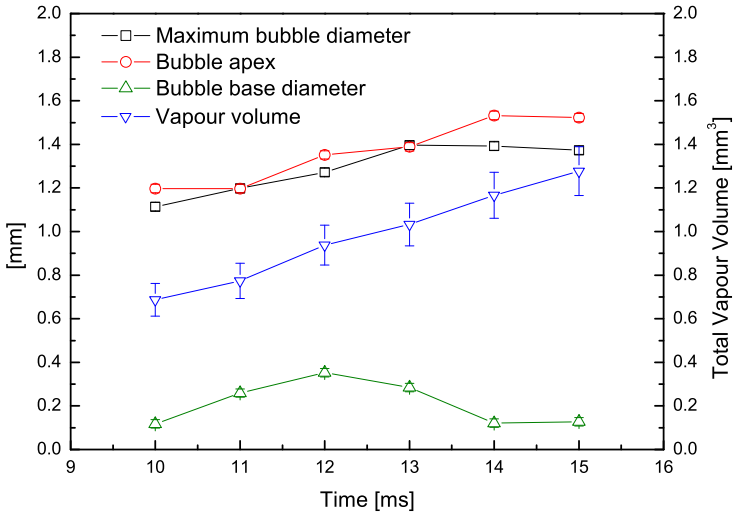

Figure C.43: *Maximum bubble diameter, location of the bubble apex, bubble base diameter and total vapour volume in time measured from Fig. C.37 to C.42.*

The above mentioned Figures have to be considered with care. The information extracted and presented in Fig. C.43 can also directly be extracted from 2D high-speed image sequences. The 3D illustrations presented in Fig. C.37 to C.42 are meant to give a better visualisation of vertical coalescence. There are many uncertainties which have to be considered, as the quality of the original images (especially close to the boiling substrate), the uncertainty introduced by image processing, the assumption of vertical axial symmetry (which is not perfect in 2D) and the possible existence of trapped liquid in between two merging bubbles.

C.4 Nucleation site interaction

C.4.1 Vertical coalescence

During bubble growth from two adjacent artificial cavities for spacings of 1.5, 1.2 and $0.84\,\mathrm{mm}$, at pressures of 0.5 and $1\,\mathrm{bar}$, vertical coalescence occurred. In Figure C.44 to C.49 the frequency of vertical coalescence as a function of wall superheat for the above experimental conditions is shown. At $0.5\,\mathrm{bar}$ vertical coalescence appears above wall superheats above $3\,\mathrm{K}$ for all three spacings, Fig. C.44, C.45 and C.46. After a rapid initial increase, the frequency of vertical coalescence seems to level off, before it starts to drop between 9 and $10\,\mathrm{K}$. This is less obvious for a cavity spacing of $1.5\,\mathrm{mm}$, as in this case measurements only up to around $10.5\,\mathrm{K}$ were possible. No influence of spacing is obvious or it may be hidden in the rather scattered data.

At $1\,\mathrm{bar}$ vertical coalescence starts to appear for wall superheats between 3 and $5\,\mathrm{K}$ for all cavity spacings, Fig. C.47, C.48 and C.49. Other than for a pressure of $0.5\,\mathrm{bar}$, the frequency increases slowly up to maximum values of $60\,\mathrm{Hz}$ and is far less scattered. All three cavity spacings behave quite similarly and only small differences are visible. The frequency of vertical coalescence is not influenced by the spacing between artificial cavities.

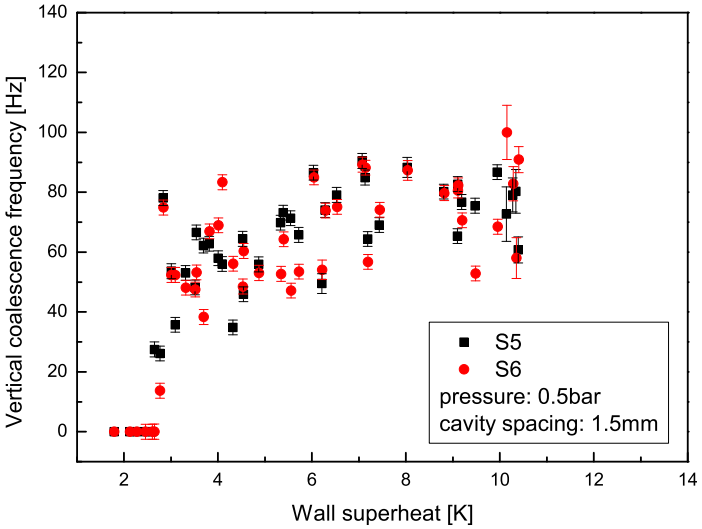

Figure C.44: *Frequency of vertical coalescence as a function of wall superheat with a spacing of 1.5 mm between the two cavities S5 and S6 at 0.5 bar.*

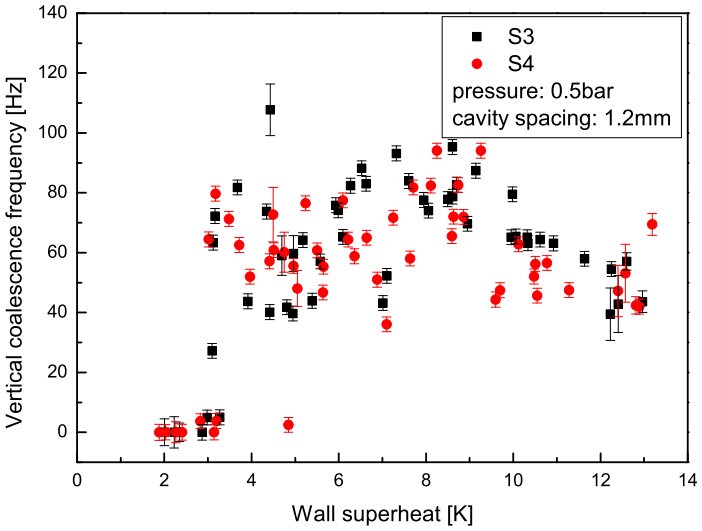

Figure C.45: *Frequency of vertical coalescence as a function of wall superheat with a spacing of 1.2 mm between the two cavities S3 and S4 at 0.5 bar.*

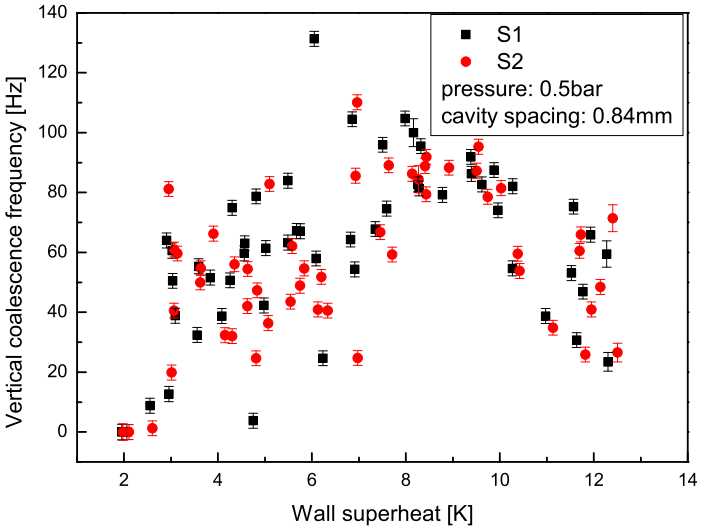

Figure C.46: *Frequency of vertical coalescence as a function of wall superheat with a spacing of 0.84 mm between the two cavities S1 and S2 at 0.5 bar.*

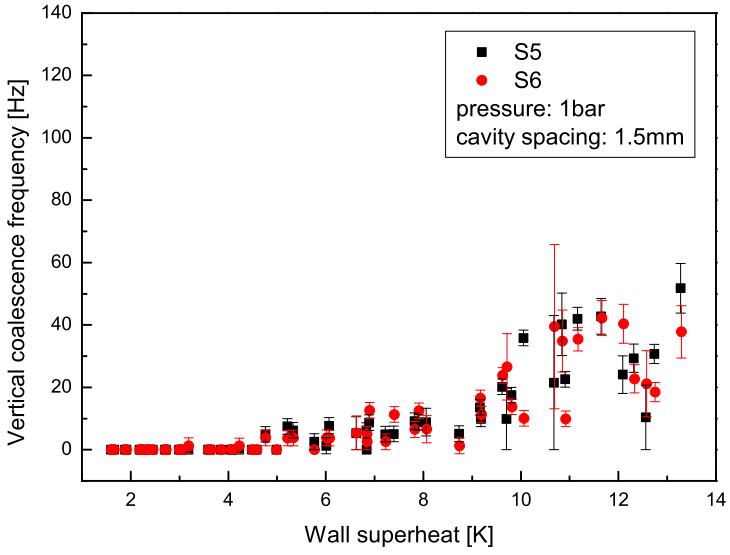

Figure C.47: *Frequency of vertical coalescence as a function of wall superheat with a spacing of 1.5 mm between the two cavities S5 and S6 at 1 bar.*

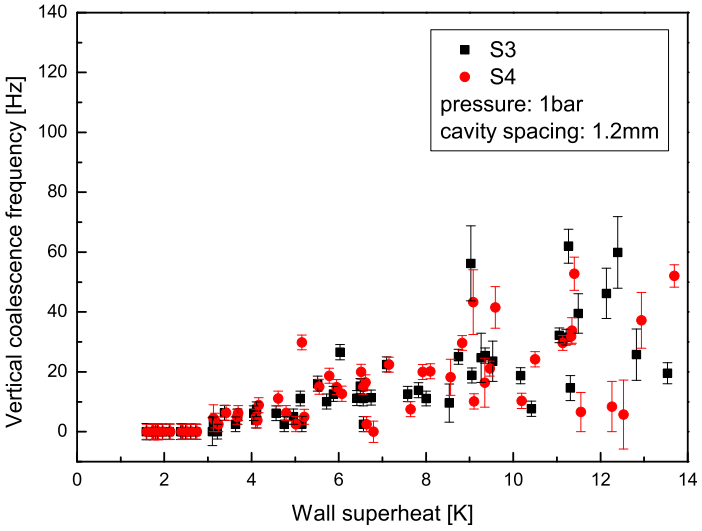

Figure C.48: *Frequency of vertical coalescence as a function of wall superheat with a spacing of 1.2 mm between the two cavities S3 and S4 at 1 bar.*

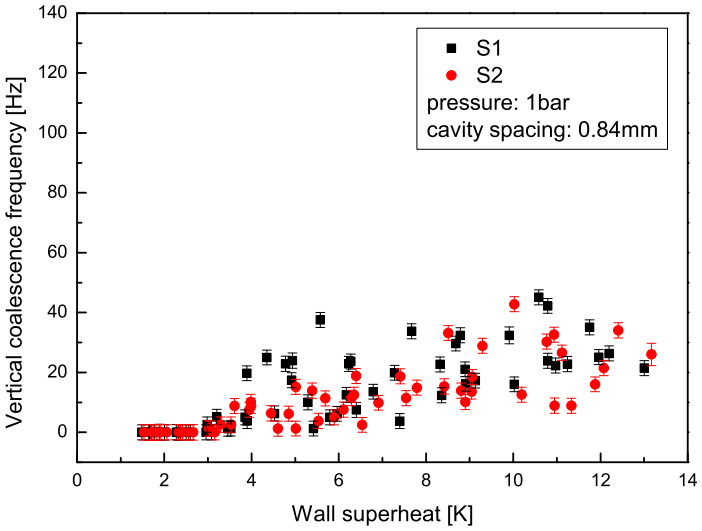

Figure C.49: *Frequency of vertical coalescence as a function of wall superheat with a spacing of 0.84 mm between the two cavities S1 and S2 at 1 bar.*

C.4.2 Bubble departure diameter

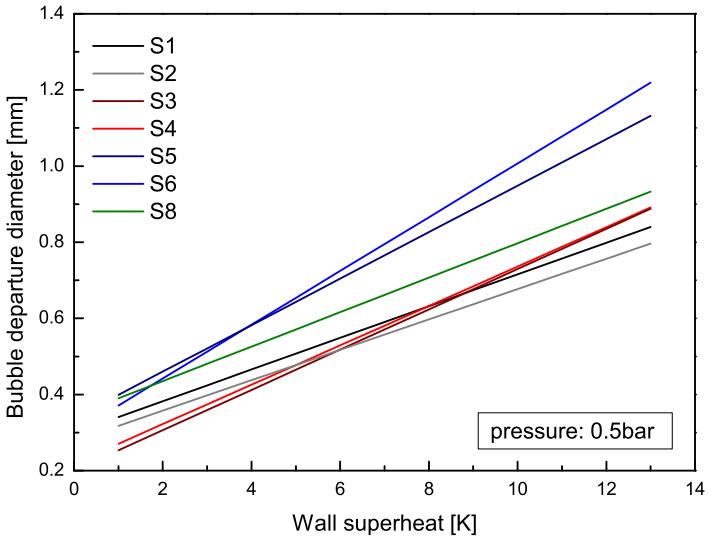

Figure C.50: *Comparison of the trend lines of the bubble departure diameter as a function of wall superheat for cavity spacings of 0.84 mm (S1 and S2), 1.2 mm (S3 and S4) and 1.5 mm (S5 and S6), and an isolated cavity (S8) at 0.5 bar.*

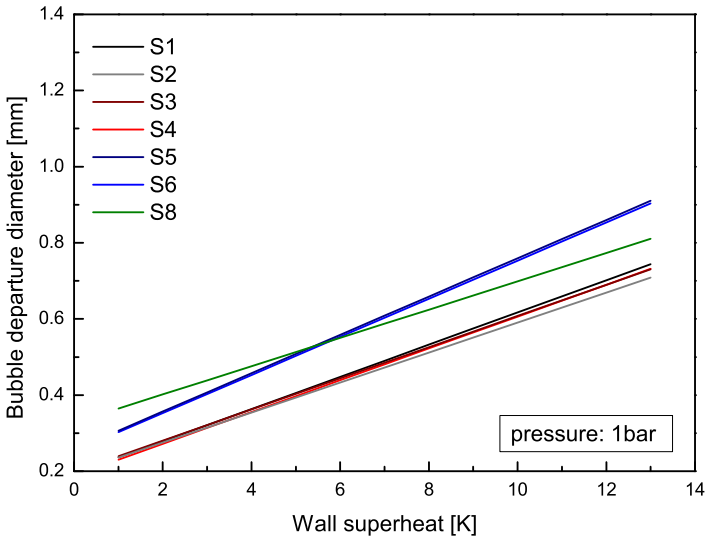

Figure C.51: *Comparison of the trend lines of the bubble departure diameter as a function of wall superheat for cavity spacings of 0.84 mm (S1 and S2), 1.2 mm (S3 and S4) and 1.5 mm (S5 and S6), and an isolated cavity (S8) at 1 bar.*

List of publications

The following papers were published during the present study so far.

Journal publications

1. A. Sanna, T. G. Karayiannis, D. B. R. Kenning, C. Hutter, K. Sefiane, A. J. Walton, I. Golobič, E. Pavlovič, R. A. Nelson, "Steps towards the development of an experimentally verified simulation of pool nucleate boiling on a silicon wafer with artificial sites", *Applied Thermal Engineering*, vol. 29, pp. 13271337, 2009.

2. C. Hutter, D. B. R. Kenning, K. Sefiane, T. G. Karayiannis, H. Lin, G. Cummins, A. J. Walton, "Experimental pool boiling investigations of FC-72 on silicon with artificial cavities and integrated temperature micro-sensors", *Experimental Thermal and Fluid Science*, 2009.

Conference proceedings

1. C. Hutter, K. Sefiane, A. J. Walton, T. G. Karayiannis, D. B. R. Kenning, "Pool boiling investigations on silicon with artificial cavities, immersed in FC-72.", *10th UK National Heat Transfer Conference*, Edinburgh, United Kingdom, 10-11 Sept., 2007.

2. A. Sanna, C. Hutter, T. G. Karayiannis, D. B. R. Kenning, R. A. Nelson, I. Golobič, E. Pavlovič, K. Sefiane, "A mechanistic model for pool nucleate boiling: Preliminary results and comparison with experiments", *46th European Two-Phase Flow Group Meeting*, Pisa, Italy, 28-30 May, 2008.

3. A. Sanna, C. Hutter, H. Lin, K. Sefiane, A.J. Walton, E. Pavlovič, I. Golobič, R. A. Nelson, T. G. Karayiannis, D. B. R. Kenning, "Simulation and experimental investigations of pool boiling on a silicon wafer with artificial nucleation sites", *5th European Thermal-Sciences Conference*, Eindhoven, The Netherlands, 18-22 May, 2008.

4. C. Hutter, G. Cummins, H. Lin, K. Sefiane, A. J. Walton, T. G. Karayiannis, D. B. R. Kenning, "Experimental pool boiling investigations of FC-72 on silicon with artificial cavities and integrated temperature micro-sensors", *21st Annual Scottish Fluid Mechanics Meeting*, Edinburgh, United Kingdom, 22 May, 2008.

5. C. Hutter, G. Cummins, H. Lin, T. G. Karayiannis, D. B. R. Kenning, K. Sefiane, A. J. Walton, "Experimental pool boiling investigations of FC-72 on silicon with artificial cavities and integrated temperature micro-sensors", *International Conference on Heat Transfer and Fluid Flow in Microscale*, Whistler, Canada, 21-26 Sept., 2008.

6. A. Sanna, C. Hutter, D. B. R. Kenning, T. G. Karayiannis, K. Sefiane, R. A. Nelson, "Design of a new silicon test section with micro-fabricated cavities during nucleate pool boling supported by numerical simulations", *7th International Conference on Boiling Heat Transfer*, Florianopolis, Brazil, 3-7 May, 2009.

7. C. Hutter, A. Sanna, K. Sefiane, D. B. R. Kenning, T. G. Karayiannis, R. A. Nelson, H. Lin, G. Cummins, A. J. Walton, "Experimental pool boiling investigations of vertical coalescence for FC-72 on silicon from an isolated artificial cavity", *7th World Conference on Experimental Heat Transfer, Fluid Mechanics and Thermodynamics*, Krakow, Poland, 28 June - 3 July, 2009.

8. C. Hutter, K. Sefiane, A. J. Walton, D. B. R. Kenning, T. G. Karayiannis, "Nucleation site interaction between artificial cavities during nucleate pool boiling on silicon with integrated micro-heater and temperature sensor", *11th UK Heat Transfer Conference*, London, UK, 6-8 Sep., 2009.

References

[1] S. Nukiyama, "Maximum and minimum values of heat Q transmitted from metal to boiling water under atmospheric pressure," *Journal of Japan Society of Mechanical Engineering*, vol. 37, p. 367, 1934.

[2] S. Nukiyama, "Maximum and minimum values of heat q transmitted from metal to boiling water under atmospheric pressure," *International Journal of Heat and Mass Transfer*, vol. 9, no. 12, p. 1419, 1966.

[3] Y. Y. Hsu and R. W. Graham, "An analytical and experimental study of the thermal boundary layer and ebullition cycle in nucleate boiling," Tech. Rep. NASA Technical note: D-594, NASA, 1961.

[4] D. B. R. Kenning, *Two Phase flow and Heat Transfer, Eds. Butterworth D. and Hewitt G. F.* Oxford: Oxford University Press, 1977.

[5] J. Kern and P. Stephan, "Theoretical model for nucleate boiling heat and mass transfer of binary mixtures," *Journal of Heat Transfer - Transactions of the ASME*, vol. 125, no. 6, pp. 1106–1115, 2003.

[6] L. Zhang and M. Shoji, "Nucleation site interaction in pool boiling on the artificial surface," *International Journal of Heat and Mass Transfer*, vol. 46, no. 3, pp. 513–522, 2003.

[7] H. K. Forster and N. Zuber, "Growth of a vapor bubble in a superheated liquid," *Journal of Applied Physics*, vol. 25, no. 4, pp. 474–478, 1954.

[8] M. S. Plesset and S. A. Zwick, "The growth of vapor bubbles in superheated liquids," *Journal of Applied Physics*, vol. 25, no. 4, pp. 493–500, 1954.

[9] B. B. Mikic, W. M. Rohsenow, and P. Griffith, "On bubble growth rates," *International Journal of Heat and Mass Transfer*, vol. 13, no. 4, pp. 657–666, 1970.

[10] W. Fritz and W. Ende, "Über den Verdampfungsvorgang nach kinematographischen Aufnahmen an Dampfblasen," *Physik Zeitschrift*, vol. 37, no. 11, pp. 391–401, 1936.

[11] M. G. Cooper, "The micro-layer and bubble growth in nucleate pool boiling," *International Journal of Heat and Mass Transfer*, vol. 12, no. 8, pp. 915–933, 1969.

[12] S. Siedel, S. Cioulachtjian, and S. Bonjour, "Experimental analysis of bubble growth, departure and interactions during pool boiling on artificial nucleation sites," *Experimental Thermal and Fluid Science*, vol. 32, no. 8, pp. 1504–1511, 2008.

[13] S. S. Kutateladze and I. I. Gogonin, "Growth rate and detachment diameter of a vapour bubble in free convection boiling of a saturated liquid," *High Temperature*, vol. 17, pp. 667–671, 1979.

[14] M. K. Jenson and G. J. Memmel, "Evaluation of bubble departure diameter correlations," in *Proceedings of the 8th International Heat Transfer Conference, San Francisco, USA*, vol. 4, (Washington, D.C., USA), pp. 1907–1912, Hemisphere Publishing Corp., 1986.

[15] R. Cole, "Bubble frequencies and departure volumes at subatmospheric pressures," *AIChE Journal*, vol. 13, no. 4, pp. 779–783, 1967.

[16] D. Gorenflo, V. Knabe, and V. Bieling, "Bubble density in surfaces with nucleate boiling - Its influence on heat transfer and burnout heat flux at elevated saturation process," in *Proceedings of the 8th International Heat Transfer Conference, San Francisco, USA*, vol. 4, (Washington, D.C., USA), pp. 1995–2000, Hemisphere Publishing Corp., 1986.

[17] B. B. Mikic and W. M. Rohsenow, "Bubble growth rates in non-uniform temperature field," *Progress in Heat and Mass Transfer; Monograph Series of the International Journal of Heat and Mass Transfer*, vol. 2, pp. 283–293, 1969.

[18] M. Jakob and W. Fritz, "Versuche über den Verdampfungsvorgang," *Forschungsgebiete des Ingenieurwesens*, vol. 2, pp. 435–447, 1931.

[19] N. Zuber, "Nucleate boiling. The region of isolated bubbles and the similarity with natural convection," *International Journal of Heat and Mass Transfer*, vol. 6, no. 1, pp. 53–60, 1963.

[20] 3M, "Speciality Materials, Fluorinert™ Liquid FC-72," *Product information*, 2006.

[21] W. M. Rohsenow, "A method of correlating heat transfer data for surface boiling of liquids.," *Journal of Heat Transfer - Transactions of ASME*, no. 74, pp. 969–976, 1952.

[22] W. M. Rohsenow, "Boiling," in *Handbook of Heat Transfer, Chapter 13* (W. M. Rohsenow and J. Hartnett, eds.), New York, USA: McGraw-Hill, 1973.

[23] R. I. Vachon, G. H. Nix, and G. E. Tanger, "Evaluation of constants for the Rohsenow pool boiling correlation," *Journal of Heat Transfer - Transactions of the ASME*, no. 90, pp. 239–247, 1968.

[24] G. E. Moore, "Cramming more components onto integrated circuits," *Electronics*, vol. 38, no. 8, pp. 114–117, 1965.

[25] S. Moghaddam, *Micro-scale study of nucleation process in boiling of low-surface tension liquids*. PhD thesis, University of Maryland, College Park, USA, 2006.

[26] A. Bar-Cohen, K. J. L. Geisler, and E. Rahim, "Boiling and two-phase flow in narrow gaps - with application to thermal packaging of chip stacks," in *7th World conference on Experimental Heat Transfer, Fluid Mechanics and Thermodynamics, Krakow, Poland*, pp. 99–119, 2009.

[27] K. O. Pasamehmetoglu and R. A. Nelson, "Cavity to cavity interaction in nucleate boiling: effect of heat conduction within the heater," *AIChE Symposium Series, 27th National Heat Transfer Conference, Minneapolis*, vol. 87, pp. 342–351, 1991.

[28] I. Golobič, E. Pavlovič, J. V. Hardenberg, R. A. Nelson, M. Berry, D. B. R. Kenning, and L. A. Smith, "Comparison of a mechanistic model for nucleate boiling with experimental spatio-temporal data," *Chemical Engineering Research and Design*, vol. 82, no. 8th UK National Heat Transfer Conference, pp. 435–444, 2004.

[29] A. Sanna, C. Hutter, H. Lin, K. Sefiane, A. J. Walton, E. Pavlocič, I. Golobič, R. A. Nelson, T. G. Karayiannis, and D. B. R. Kenning, "Simulation and experimental investigation of pool boiling on a silicon wafer with artificial nucleation sites," in *5th Eurotherm Conference on Thermal Science, Eindhoven, NL*, 2008.

[30] T. B. Drew and A. C. Mueller, "Boiling," *Transactions of the AIChE*, vol. 33, pp. 449–471, 1937.

[31] B. B. Mikic and W. M. Rohsenow, "A new correlation of pool-boiling data including effect of heating surface characteristics," *Journal of Heat Transfer - Transactions of the ASME*, vol. 91, no. 2, pp. 245–250, 1969.

[32] C. Y. Han and P. Griffith, "The mechanism of heat transfer in nucleate boiling - Part I: Bubble initiation, growth and departure," *International Journal of Heat and Mass Transfer*, vol. 8, no. 6, pp. 887–904, 1965.

[33] C. Y. Han and P. Griffith, "The mechanism of heat transfer in nucleate boiling - Part II: The heat flux-temperature difference relation," *International Journal of Heat and Mass Transfer*, vol. 8, no. 6, pp. 905–914, 1965.

[34] R. C. Hendricks and R. R. Sharp, "Initiation of cooling due to bubble growth on a heating surface," Tech. Rep. TN D-2290, NASA, 1964.

[35] M. G. Cooper and A. B. Lloyd, "Transient local heat flux in nucleate boiling," in *Proceedings of 3rd International Heat Transfer Conference*, (Chicago, USA), pp. 193–203, 1966.

[36] W. T. Brown, *Study of Flow Surface Boiling*. PhD thesis, Massachusetts Institute of Technology, Cambridge, USA, 1967.

[37] C. J. Rallis and H. H. Jawurek, "The mechanism of nucleate boiling," Tech. Rep. A/CONF.28/P/600, University of Witwatersrand, 1964.

[38] S. G. Bankoff, "Taylor instability of an evaporating plane interface," *AIChE Journal*, vol. 7, no. 3, pp. 485–487, 1961.

[39] D. E. Forster and R. Greif, "Heat transfer to a boiling liquid - Mechanisms and correlations," *Journal of Heat Transfer - Transactions of the ASME*, vol. 81C, no. 1, pp. 43–53, 1959.

[40] C. L. Tien, "A hydronamic model for nucleate pool boiling," *International Journal of Heat and Mass Transfer*, vol. 5, pp. 533–540, 1962.

[41] J. L. McGrew, F. L. Bamford, and T. R. Rehm, "Marangoni flow: An additional mechanism in boiling heat transfer," *Science*, vol. 153, no. 3740, pp. 1106–1107, 1966.

[42] Y. S. Kao and D. B. R. Kenning, "Thermocapillary flow near a hemispherical bubble on a heated wall," *Journal of Fluid Mechanics*, vol. 53, no. 4, pp. 715–735, 1972.

[43] R. L. Judd and H. Merte, "Evaluation of nucleate boiling heat-flux predictions at varying levels of subcooling and acceleration," *International Journal of Heat and Mass Transfer*, vol. 15, no. 5, pp. 1075–1096, 1972.

[44] V. K. Dhir, "Nucleate and transition boiling heat-transfer under pool and external flow conditions," *International Journal of Heat and Fluid Flow*, vol. 12, no. 4, pp. 290–314, 1991.

[45] Y. Fujita, "The state of the art - nucleate boiling mechanism," in *Engineering Foundation Conference on Pool and External Flow Boiling, ASME*, pp. 83–97, 1992.

[46] R. W. Graham and R. C. Hendricks, "Assessment of convection, conduction and evaporation in nucleate boiling," Tech. Rep. NASA-TN-D–3943, NASA, Lewis Research Center, 1967.

[47] R. L. Judd and K. S. Hwang, "Comprehensive model for nucleate pool boiling heat-transfer including micro-layer evaporation," *Journal of Heat Transfer - Transactions of the ASME*, vol. 98, no. 4, pp. 623–629, 1976.

[48] M. Shoukri and R. L. Judd, "Influence of surface conditions in nucleate boiling - Concept of bubble flux-density," *Journal of Heat Transfer - Transactions of the ASME*, vol. 100, no. 4, pp. 618–623, 1978.

[49] R. L. Judd and C. H. Lavdas, "The nature of nucleation site interaction," *Journal of Heat Transfer - Transactions of the ASME*, vol. 102, no. 3, pp. 461–464, 1980.

[50] D. D. Paul and S. I. Abdelkhalik, "A statistical-analysis of saturated nucleate boiling along a heated wire," *International Journal of Heat and Mass Transfer*, vol. 26, no. 4, pp. 509–519, 1983.

[51] V. K. Dhir, "Boiling heat transfer," *Annual Review of Fluid Mechanics*, vol. 30, pp. 365–401, 1998.

[52] Y. Heled, J. Ricklis, and A. Orell, "Pool boiling from large arrays of artificial nucleation sites," *International Journal of Heat and Mass Transfer*, vol. 13, no. 3, pp. 503–516, 1970.

[53] A. Luke, "Pool boiling heat transfer from horizontal tubes with different surface roughness," *International Journal of Refrigeration - Revue Internationale du Froid*, vol. 20, no. 8, pp. 561–574, 1997.

[54] D. B. R. Kenning and Y. Yan, "Pool boiling heat transfer on a thin plate: Features revealed by liquid crystal thermography," *International Journal of Heat and Mass Transfer*, vol. 39, no. 15, pp. 3117–3137, 1996.

[55] V. K. Dhir, "Mechanistic prediction of nucleate boiling heat transfer - Achievable or a hopeless task?," *Journal of Heat Transfer - Transactions of the ASME*, vol. 128, no. 1, pp. 1–12, 2006.

[56] R. Siegel and E. G. Keshock, "Effects of reduced gravity on nucleate boiling bubble dynamics in saturated water," *AIChE Journal*, vol. 10, no. 4, pp. 509–517, 1964.

[57] H. Merte, "Nucleate pool boiling: High gravity to reduced gravity; Liquid metals to cryogenics," in *Transaction of 5th Symposium on Space Nuclear Power Systems*, (Albuquerque, USA), pp. 437–442, 1988.

[58] M. Zell, J. Straub, and B. Vogel, "Pool boiling under microgravity," *Physicochemical Hydrodynamics*, vol. 11, no. 5-6, pp. 813–823, 1989.

[59] J. Kim, J. F. Benton, and D. Wisniewski, "Pool boiling heat transfer on small heaters: Effect of gravity and subcooling," *International Journal of Heat and Mass Transfer*, vol. 45, no. 19, pp. 3919–3932, 2002.

[60] T. D. Rule and J. Kim, "Heat transfer behavior on small horizontal heaters during pool boiling of FC-72," *Journal of Heat Transfer - Transactions of the ASME*, vol. 121, no. 2, pp. 386–393, 1999.

[61] J. Kim, C. Huh, and M. H. Kim, "On the growth behavior of bubbles during saturated nucleate pool boiling at sub-atmospheric pressure," *International Journal of Heat and Mass Transfer*, vol. 50, no. 17-18, pp. 3695–3699, 2007.

[62] K. Stephan and M. Abdelsalam, "Heat-transfer correlations for natural-convection boiling," *International Journal of Heat and Mass Transfer*, vol. 23, no. 1, pp. 73–87, 1980.

[63] X. Zhou and K. Bier, "Influence of the heat conduction properties of the wall material and of the wall thickness on pool boiling heat transfer," in *Proceedings of EUROTHERM Seminar No. 48: Pool Boiling 2*, (Paderborn, Germany), pp. 43–54, 1996.

[64] J. D. Jacobs and A. H. Shade, "Measurement of temperatures associated with bubbles in sub cooled pool boiling," *Journal of Heat Transfer - Transactions of the ASME*, vol. 91, no. 1, pp. 123–128, 1969.

[65] T. T. Robin and N. W. Snyder, "Bubble dynamics in subcooled nucleate boiling based on mass transfer mechanism," *International Journal of Heat and Mass Transfer*, vol. 13, no. 2, pp. 308–318, 1970.

[66] F. Demiray and J. H. Kim, "Micro-scale heat transfer measurements during pool boiling of FC-72: Effect of subcooling," *International Journal of Heat and Mass Transfer*, vol. 47, no. 14-16, pp. 3257–3268, 2004.

[67] J. L. Parker and M. S. El-Genk, "Enhanced saturation and subcooled boiling of FC-72 dielectric liquid," *International Journal of Heat and Mass Transfer*, vol. 48, no. 18, pp. 3736–3752, 2005.

[68] J. J. Wei and H. Honda, "Effects of fin geometry on boiling heat transfer from silicon chips with micro-pin-fins immersed in FC-72," *International Journal of Heat and Mass Transfer*, vol. 46, no. 21, pp. 4059–4070, 2003.

[69] J. H. Kim, S. M. You, and J. Y. Pak, "Effects of heater size and working fluids on nucleate boiling heat transfer," *International Journal of Heat and Mass Transfer*, vol. 49, no. 1-2, pp. 122–131, 2006.

[70] C. N. Ammerman and S. M. You, "Consecutive-photo method to measure vapor volume flow rate during boiling from a wire immersed in saturated liquid," *Journal of Heat Transfer - Transactions of the ASME*, vol. 120, no. 3, pp. 561–567, 1998.

[71] K. Nishikawa, Y. Fujita, S. Uchida, and H. Ohta, "Effect of surface configuration on nucleate boiling heat-transfer," *International Journal of Heat and Mass Transfer*, vol. 27, no. 9, pp. 1559–1571, 1984.

[72] C. P. Costello, J. M. Adams, and W. W. Clinton, "Improvement of burnout heat flux by orientation semicular heaters," *AIChE Journal*, vol. 8, no. 4, pp. 569–570, 1962.

[73] P. M. Githinji and R. H. Sabersky, "Some effects of the orientation of the heating surface in nucleate boiling," *Journal of Heat Transfer - Transactions of the ASME*, vol. 85, no. 4, p. 379, 1963.

[74] B. D. Marcus and D. Dropkin, "The effect of surface configuration on nucleate boiling heat transfer," *International Journal of Heat and Mass Transfer*, vol. 6, pp. 863–866, 1963.

[75] K. A. Joudi and D. D. James, "Surface contamination, rejuvenation, and the reproducibility of results in nucleate pool boiling," *Journal of Heat Transfer - Transactions of the ASME*, vol. 103, no. 3, pp. 453–458, 1981.

[76] C. Corty and A. S. Foust, "Surface variables in nucleate boiling," *Chemical Engineering Progress, Symposium Series*, vol. 51, no. 17, pp. 1–13, 1955.

[77] H. B. Clark, P. S. Strenge, and J. W. Westwater, "Active sites for nucleate boiling," *Chemical Engineering Progress, Symposium Series: Heat Transfer*, vol. 55, no. 29, pp. 103–110, 1959.

[78] S. G. Bankoff, "Entrapment of gas in the spreading of a liquid over a rough surface," *AIChE Journal*, vol. 4, no. 1, pp. 24–26, 1958.

[79] C. H. Wang and V. K. Dhir, "On the gas entrapment and nucleation site density during pool boiling of saturated water," *Journal of Heat Transfer - Transactions of the ASME*, vol. 115, no. 3, pp. 670–679, 1993.

[80] G. Barthau, "Active nucleation site density and pool boiling heat-transfer - an experimental study," *International Journal of Heat and Mass Transfer*, vol. 35, no. 2, pp. 271–278, 1992.

[81] D. B. R. Kenning, "Experimental methods: Looking closely at bubble nucleation," *Multiphase Science and Technology*, vol. 13, no. 3 and 4, pp. 1–33, 2001.

[82] Y. Y. Hsu, "On the size range of active nucleation site on a heating surface.," *Journal of Heat Transfer - Transactions of the ASME*, vol. 84, pp. 207–216, 1962.

[83] J. J. Wei, L. J. Guo, and H. Honda, "Experimental study of boiling phenomena and heat transfer performances of FC-72 over micro-pin-finned silicon chips," *Heat and Mass Transfer*, vol. 41, no. 8, pp. 744–755, 2005.

[84] Y. Y. Hsu and R. W. Graham, *Transport Processing in Boiling and Two Phase Systems*. Washington D.C., USA: Hemispheric Publishing Corp., 1976.

[85] G. Kocamustafaogullari and M. Ishii, "Interfacial area and nucleation site density in boiling systems," *International Journal of Heat and Mass Transfer*, vol. 26, no. 9, pp. 1377–1387, 1983.

[86] C. H. Wang and V. K. Dhir, "Effect of surface wettability on active nucleation site density during pool boiling of water on a vertical surface," *Journal of Heat Transfer - Transactions of the ASME*, vol. 115, no. 3, pp. 659–669, 1993.

[87] D. B. R. Kenning, "Wall temperature in in nucleate boiling," in *Proceedings EUROTHERM Seminar No.8: Advances on Pool Boiling Heat Transfer*, (Paderborn, Germany), pp. 1–9, 1989.

[88] T. G. Theofanous, J. P. Tu, A. T. Dinh, and T. N. Dinh, "The boiling crisis phenomenon - Part I: Nucleation and nucleate boiling heat transfer," *Experimental Thermal and Fluid Science*, vol. 26, no. 6-7, pp. 775–792, 2002.

[89] Y. S. Qi and J. F. Klausner, "Comparison of nucleation site density for pool boiling and gas nucleation," *Journal of Heat Transfer - Transactions of the ASME*, vol. 128, no. 1, pp. 13–20, 2006.

[90] T. L. Chen, J. F. Klausner, S. V. Garimella, and J. N. Chung, "Subcooled boiling incipience on a highly smooth micro-heater," *International Journal of Heat and Mass Transfer*, vol. 49, no. 23-24, pp. 4399–4406, 2006.

[91] R. J. Benjamin and A. R. Balakrishnan, "Nucleation site density in pool boiling of saturated pure liquids: Effect of surface micro-roughness and surface and liquid physical properties," *Experimental Thermal and Fluid Science*, vol. 15, no. 1, pp. 32–42, 1997.

[92] H. Gjerkeš and I. Golobič, "Pool boiling CHF on a laser heated thin plate," *International Journal of Heat and Mass Transfer*, vol. 43, no. 11, pp. 1999–2008, 2000.

[93] R. Rammig and R. Weiss, "Growth of vapor bubbles from artificial nucleation sites," *Cryogenics*, vol. 31, no. 1, pp. 64–69, 1991.

[94] B. K. Mori and W. D. Baines, "Bubble departure from cavities," *International Journal of Heat and Mass Transfer*, vol. 44, no. 4, pp. 771–783, 2001.

[95] M. Shoji and Y. Takagi, "Bubbling features from a single artificial cavity," *International Journal of Heat and Mass Transfer*, vol. 44, no. 14, pp. 2763–2776, 2001.

[96] S. Chatpun, M. Watanabe, and M. Shoji, "Experimental study on characteristics of nucleate pool boiling by the effects of cavity arrangement," *Experimental Thermal and Fluid Science*, vol. 29, no. 1, pp. 33–40, 2004.

[97] C. K. Yu, D. C. Lu, and T. C. Cheng, "Pool boiling heat transfer on artificial micro-cavity surfaces in dielectric fluid FC-72," *Journal of Micromechanics and Microengineering*, vol. 16, no. 10, pp. 2092–2099, 2006.

[98] F. Bošnjaković, "Verdampfung und Flüssigkeitsüberhitzung," *Technische Mechanik und Thermodynamik*, vol. 1, no. 10, p. 358, 1930.

[99] H. Beer, "Das dynamische Blasenwachstum beim Sieden von Flüssigkeiten," *Forschung Ingenieurwesen*, vol. 37, no. 3, pp. 85–90, 1971.

[100] N. R. Snyder and D. K. Edwards, "Summary of conference on bubble dynamics and boiling heat transfer," Tech. Rep. Memo 20-137, Jet Propulsion Laboratory, Pasadena, USA, 1956.

[101] F. D. Moore and R. B. Mesler, "The measurement of rapid surface temperature fluctuations during nucleate boiling of water," *AIChE Journal*, vol. 7, no. 4, pp. 620–624, 1961.

[102] M. G. Cooper and A. J. P. Lloyd, "Micro-layer in nucleate pool boiling," *International Journal of Heat and Mass Transfer*, vol. 12, no. 8, pp. 895–913, 1969.

[103] R. C. Lee and J. E. Nydahl, "Numerical calculation of bubble growth in nucleate boiling from inception through departure," *Journal of Heat Transfer - Transactions of the ASME*, no. 111, pp. 474–479, 1989.

[104] H. H. Jawurek, "Simultaneous determination of micro-layer geometry and bubble growth in nucleate boiling," *International Journal of Heat and Mass Transfer*, vol. 12, no. 8, pp. 843–848, 1969.

[105] M. S. Plesset and A. Prosperetti, "Flow of vapor in a liquid enclosure," *Journal of Fluid Mechanics*, vol. 78, pp. 433–444, 1976.

[106] S. Takagi and N. Yamamoto, "Behavior of a boiling bubble from a micro-scale heater," *Proceedings of the 11th Heat Transfer Conference, Kyongju, South Korea*, vol. 2, pp. 476–483, 1998.

[107] J. G. Myers, V. K. Yerramilli, S. W. Hussey, G. F. Yee, and J. Kim, "Time and space resolved wall temperature and heat flux measurements during nucleate boiling with constant heat flux boundary conditions," *International Journal of Heat and Mass Transfer*, vol. 48, no. 12, pp. 2429–2442, 2005.

[108] C. Sodtke, J. Kern, N. Schweizer, and P. Stephan, "High resolution measurements of wall temperature distribution underneath a single vapour bubble under low gravity conditions," *International Journal of Heat and Mass Transfer*, vol. 49, no. 5-6, pp. 1100–1106, 2006.

[109] P. Stephan and T. Fuchs, "Local heat flow and temperature fluctuations in wall and fluid in nucleate boiling systems," *Heat and Mass Transfer*, vol. 45, no. 7, pp. 919–928, 2009.

[110] S. Moghaddam and K. T. Kiger, "Physical mechanisms of heat transfer during single bubble nucleate boiling of FC-72 under saturation conditions - I. Experimental investigation," *International Journal of Heat and Mass Transfer*, vol. 52, no. 5-6, pp. 1284–1294, 2009.

[111] S. Moghaddam and K. T. Kiger, "Physical mechanisms of heat transfer during single bubble nucleate boiling of FC-72 under saturation conditions - II. Theoretical analysis," *International Journal of Heat and Mass Transfer*, vol. 52, no. 5-6, pp. 1295–1303, 2009.

[112] W. Fritz, "Maximum volume of vapor bubbles," *Physik Zeitschrift*, no. 36, pp. 379–384, 1935.

[113] Y. A. Buyevich and B. W. Webbon, "The isolated bubble regime in pool nucleate boiling," *International Journal of Heat and Mass Transfer*, vol. 40, no. 2, pp. 365–377, 1997.

[114] V. V. Chekanov, "Interaction of centers in nucleate boiling," *High Temperature*, vol. 15, no. 1, pp. 101–106, 1977.

[115] A. Calka and R. L. Judd, "Some aspects of the interaction among nucleation sites during saturated nucleate boiling," *International Journal of Heat and Mass Transfer*, vol. 28, no. 12, pp. 2331–2342, 1985.

[116] R. L. Judd, "On nucleation site interaction," *Journal of Heat Transfer - Transactions of the ASME*, vol. 110, no. 2, pp. 475–478, 1988.

[117] R. L. Judd and A. Chopra, "Interaction of the nucleation processes occurring at adjacent nucleation sites," *Journal of Heat Transfer - Transactions of the ASME*, vol. 115, no. 4, pp. 955–962, 1993.

[118] I. Golobič and H. Gjerkeš, "Interactions between laser-activated nucleation sites in pool boiling," *International Journal of Heat and Mass Transfer*, vol. 44, no. 1, pp. 143–153, 2001.

[119] N. D. Nimkar, S. H. Bhavnani, and R. C. Jaeger, "Effect of nucleation site spacing on the pool boiling characteristics of a structured surface," *International Journal of Heat and Mass Transfer*, vol. 49, no. 17-18, pp. 2829–2839, 2006.

[120] C. R. Williamson and M. S. El-Genk, "High-speed photographic analysis of saturated nucleate pool boiling at low heat flux," in *ASME Winter Annual Meeting, Paper 91-WA-HT-8*, 1991.

[121] Y. A. Buyevich and B. W. Webber, "Towards a new theory of nucleate boiling.," in *Proceedings of EUROTHERM: Thermal-Sciences Conference*, (Rome, Italy), 1996.

[122] Z. L. Yang, T. N. Dinh, R. R. Nourgaliev, and B. R. Sehgal, "Numerical investigation of bubble growth and detachment by the lattice-boltzmann method," *International Journal of Heat and Mass Transfer*, vol. 44, no. 1, pp. 195–206, 2001.

[123] J. Bonjour, M. Clausse, and M. Lallemand, "Experimental study of the coalescence phenomenon during nucleate pool boiling," *Experimental Thermal and Fluid Science*, vol. 20, no. 3-4, pp. 180–187, 2000.

[124] H. J. Goldsmid, *Applications of Thermoelectricity*. London, Great Britain: Butler and Tanner Ltd., 1960.

[125] A. W. Van Herwaarden and P. M. Sarro, "Thermal sensors based on the Seebeck effect," *Sensor and Actuators*, vol. 21-23, pp. 650–654, 1986.

[126] H. M. Tong, G. Arjavalingham, R. D. Haynes, G. N. Hyer, and J. J. Ritsko, "High-temperature thin film thermocouple with fast time response," *Review of Scientific Instrumentation*, vol. 58, no. 5, pp. 875–877, 1987.

[127] T. H. Herder, R. O. Olson, and J. S. Blakemore, "Diffused semiconductor low temperature thermometers," *Review of Scientific Instrumentation*, vol. 37, no. 10, pp. 1301–1305, 1966.

[128] H. F. Wolf, *Silicon Semiconductor Data*. New York, USA: Pergamon Press, 1969.

[129] F. J. Hyde, *Thermistors*. London, Great Britain: Iliffe, 1971.

[130] B. G. Cohen, W. B. Snow, and A. R. Tretola, "GaAs p-n junction diodes for wide range thermometry," *Review of Scientific Instrumentation*, vol. 34, no. 10, pp. 1091–1093, 1963.

[131] W. Beyer and J. Stuke, "Thermoelectric power of amorphous Ge and Si," *Amorphous and Liquid Semiconductors*, pp. 251–258, 1974.

[132] G. Urban, A. Jachimowicz, F. Kohl, H. Kuttner, F. Olcaytu, H. Kamper, F. Pitter, E. Mann-Buxbaum, T. Schalkhammer, O. Prohaska, and M. Schonauer, "High-resolution thin-film temperature sensor arrays for medical application," *Sensor and Actuators*, vol. 21-23, pp. 650–654, 1990.

[133] H. Kuttner, G. Urban, A. Jachimowicz, F. Kohl, F. Olcaytu, and P. Goiser, "Microminiaturized thermistor arrays for temperature gradient, flow and perfusion measurements," *Sensor and Actuators A*, vol. 2527, pp. 641–645, 1991.

[134] W. J. Miller, *Fabrication and calibration of micro temperature sensors on silicon for measurement of surface temperature during nucleate pool boiling in dielectric liquid*. PhD thesis, University of Pennsylvania, Philadelphia, USA, 1996.

[135] Z. Yin, A. Prosperetti, and J. Kim, "Bubble growth on an impulsively powered micro-heater," *International Journal of Heat and Mass Transfer*, vol. 47, no. 5, pp. 1053–1067, 2004.

[136] T. L. Chen and J. N. Chung, "Coalescence of bubbles in nucleate boiling on micro-heaters," *International Journal of Heat and Mass Transfer*, vol. 45, no. 11, pp. 2329–2341, 2002.

[137] T. L. Chen and J. N. Chung, "Heat-transfer effects of coalescence of bubbles from various site distributions," *Proceedings of the Royal Society of London Series A - Mathematical Physical and Engineering Sciences*, vol. 459, no. 2038, pp. 2497–2527, 2003.

[138] H. C. Lee, B. D. Oh, S. W. Bae, and M. H. Kim, "Single bubble growth in saturated pool boiling on a constant wall temperature surface," *International Journal of Multiphase Flow*, vol. 29, no. 12, pp. 1857–1874, 2003.

[139] J. B. Kim, B. D. Oh, and M. H. Kim, "Experimental study of pool temperature effects on nucleate pool boiling," *International Journal of Multiphase Flow*, vol. 32, no. 2, pp. 208–231, 2006.

[140] S. Moghaddam, K. T. Kiger, A. Modafe, and R. Ghodssi, "A novel benzocyclobutene-based device for studying the dynamics of heat transfer during the nucleation process," *Journal of Microelectromechanical Systems*, vol. 16, no. 6, pp. 1355–1366, 2007.

[141] I. G. Shekriladze, "Boiling heat transfer: mechanisms, models, correlations and the lines of further research," *The Open Mechanical Engineering Journal*, vol. 2, pp. 104–127, 2008.

[142] VDI - Gesellschaft Verfahrenstechnik und Chemieingenieurwesen, *VDI - Wärmeatlas*. Berlin and Heidelberg, Germany: Springer Verlag, 2006.

[143] D. B. R. Kenning, "Optical studies of boiling heat transfer: insights and limitations," *International Journal of Heat and Fluid Flow*, vol. 25, no. 2, pp. 209–222, 2004.

[144] M. Minnaert, *Light and colour in the open air*. London,UK: G. Bell and Sons Ldt., 1940.

[145] A. Sanna, T. Karayiannis, D. Kenning, C. Hutter, H. Lin, K. Sefiane, A. Walton, I. Golobič, E. Pavlocič, and R. Nelson, "Steps towards the development of an

experimentally verified simulation of pool nucleate boiling on a silicon wafer with artificial sites," *Applied Thermal Engineering*, vol. 29, no. 7, pp. 1327–1337, 2009.

[146] P. Stephan and J. Hammer, "A new model for nucleate boiling heat transfer," *Wärme- und Stoffübertragung*, vol. 30, no. 2, pp. 119–125, 1994.

[147] J. Golobič, Petkovsek, M. Baselj, A. Papez, and D. B. R. Kenning, "Experimental determination of transient wall temperature distribution close to growing vapor bubbles," *Heat Mass Transfer*, vol. 45, no. 7, pp. 857–866, 2009.

[148] S. Basic, J. Marn, and L. Skerget, "Velocity-field measurements around an isolated vapour bubble over an artificially produced nucleation site using the particle image velocimetry technique," *Strojniski Vestnik - Journal of Mechanical Engineering*, vol. 50, no. 9, pp. 413–426, 2004.

[149] J. T. Cieslinski, J. Polewski, and J. A. Szymczyk, "Flow field around growing and rising vapour bubble by piv measurement," *Journal of Visualization*, vol. 8, no. 3, pp. 209–216, 2005.

[150] L. Rayleigh, "Pressure due to collapse of bubbles," *Phil. Mag.*, vol. 94, 1917.